

**LOW PRESSURE INFRARED MULTIPLE-PHOTON DISSOCIATION  
DYNAMICS OF GASEOUS ION-MOLECULE COMPLEXES**

by

Darryl Scott Tonner

A thesis

presented to the University of Waterloo

in fulfilment of the

thesis requirement for the degree of

Doctor of Philosophy

in

Chemistry

Waterloo, Ontario, Canada, 1998

© Darryl Scott Tonner 1998



National Library  
of Canada

Acquisitions and  
Bibliographic Services

395 Wellington Street  
Ottawa ON K1A 0N4  
Canada

Bibliothèque nationale  
du Canada

Acquisitions et  
services bibliographiques

395, rue Wellington  
Ottawa ON K1A 0N4  
Canada

*Your file Votre référence*

*Our file Notre référence*

The author has granted a non-exclusive licence allowing the National Library of Canada to reproduce, loan, distribute or sell copies of this thesis in microform, paper or electronic formats.

The author retains ownership of the copyright in this thesis. Neither the thesis nor substantial extracts from it may be printed or otherwise reproduced without the author's permission.

L'auteur a accordé une licence non exclusive permettant à la Bibliothèque nationale du Canada de reproduire, prêter, distribuer ou vendre des copies de cette thèse sous la forme de microfiche/film, de reproduction sur papier ou sur format électronique.

L'auteur conserve la propriété du droit d'auteur qui protège cette thèse. Ni la thèse ni des extraits substantiels de celle-ci ne doivent être imprimés ou autrement reproduits sans son autorisation.

0-612-32863-5

The University of Waterloo requires the signatures of all persons using or photocopying this thesis. Please sign below, and give address and date.

## ABSTRACT

The infrared multiple photon dissociation (IRMPD) of gaseous cluster ions has been studied in the ultra-low pressure environment of a Fourier transform ion cyclotron resonance (FTICR) spectrometer. A bottleneck in the IRMPD kinetics of large isolated ions has been observed and tentatively identified as occurring in the upper levels of the vibrational manifold. A previous theory which proposed that IRMPD using low intensity, continuous wave, infrared laser radiation could be treated as a thermal unimolecular reaction has been disproven. Additionally, a new method of tandem mass spectrometry has been developed which uses IRMPD in place of traditional collisional activation to induce the fragmentation of large ions trapped in a FT-ICR spectrometer. The technique of IRMPD/FT-ICR has been combined with the previously developed method of black body radiation induced, thermal unimolecular dissociation to explore the dynamics of chloride-alkyl bromide  $S_N2$  reactions. The results of this study provide the first experimental verification of the theoretically predicted mode-specific behaviour of the  $Cl^- + CH_3Br$  reaction.

## ACKNOWLEDGEMENTS

I would like to express my gratitude to my supervisor, Terry McMahon for the advice and guidance he gave me but most importantly for allowing me the freedom to make my own mistakes (and throwing in some sarcastic comments to boot).

I would like to thank Bill Hase for providing me with unpublished vibrational frequencies for the  $\text{Cl}^-(\text{CH}_3\text{Br})$  complex and telling me which vibrational modes might yield modes specific behaviour (not that I had a lot of choice with a fixed frequency laser!). I am also thankful to Al Viggiano for helpful discussions concerning the non-statistical nature of the  $\text{S}_{\text{N}}2$  reaction dynamics.

Thanks also go out to Peter Bernath, John Hepburn, Jim Sloan and Ed Grant for discussions concerning the IRMPD chapter and the loan of assorted optical equipment which you don't know that I have.

I must also thank my FT-ICR compadres, Tim Hoffman, Jackie Jarvis and Graham McGibbon for all their help. Tim in particular deserves credit for coming up with the "SEX" acronym for the black body experiment which almost makes up for the horrible term "ZTRID." Jackie was extremely helpful with instrumental maladies and is the only other person to have truly suffered from the 6 month half-life of the "re-built" Balzers turbo pumps.

Last but not least, I would like to thank all the other members of the group who helped me with various tasks and favours during my Ph.D. tenure: Bogdan, Kim, Michael, Tania, Jeff, Pauline, Andrea, Greg and Jan.

**- To My Parents -**

## TABLE OF CONTENTS

1.	INTRODUCTION . . . . .	1
1.0	General Introduction . . . . .	1
1.1	Unimolecular Reactions Mechanisms . . . . .	3
1.3	References . . . . .	15
2.	INSTRUMENTATION . . . . .	16
2.1	Cyclotron Motion of a Charge in a Static Magnetic Field . . . . .	17
2.2	Application of a Radio Frequency Electric Field . . . . .	21
2.3	The FT-ICR Cell . . . . .	24
2.4	Ion Formation . . . . .	26
2.5	Ion Detection: ICR vs. Fourier Transform ICR Spectrometry . . . . .	32
2.6	Radio Frequency Isolation (Ion Ejection) . . . . .	38
2.7	Experimental Timing (FT-ICR Pulse Sequence) . . . . .	40
2.8	Continuous Wave Infrared CO <sub>2</sub> Laser and Bi-Stable Shutter . . . . .	44
2.9	References . . . . .	50
3.	INFRARED LASER PHOTODISSOCIATION OF CLUSTER IONS IN A FT-ICR SPECTROMETER . . . . .	52
3.1	Introduction . . . . .	52

3.1.1	Non-first Order Behaviour; Models and Kinetics . . . . .	60
3.1.3	Models for IRMPD . . . . .	68
3.1.3	Pulsed vs. CW IRMPD as a Tool for Elucidating Bottlenecking Mechanisms . . . . .	81
3.2	Experimental . . . . .	90
3.3	Results . . . . .	92
3.3.1	Proton Bound Dimer of Pentanone . . . . .	92
3.3.2	Proton Bound Dimer of Nonanone . . . . .	101
3.3.3	Proton Bound Dimer of Diethyl Ether . . . . .	105
3.3.4	Protonated Diethyl Ether . . . . .	108
3.4	Discussion . . . . .	110
3.4.1	Early vs. Late Bottleneck . . . . .	110
3.4.2	Non-Thermal Population Distribution . . . . .	128
3.5	Conclusions . . . . .	132
3.6	References . . . . .	134
4.	CONSECUTIVE INFRARED MULTIPHOTON DISSOCIATIONS OF THE PROTON BOUND DIMER OF DIETHYL ETHER . . . . .	138
4.1	Introduction . . . . .	139
4.2	Experimental . . . . .	144
4.3	Results and Discussion . . . . .	149



4.4	Conclusions . . . . .	157
4.5	References . . . . .	159
5.	THE DYNAMICS OF CHLORIDE-ALKYL BROMIDE $S_N2$ REACTIONS . . . . .	162
5.1	Introduction . . . . .	162
5.2	Experimental . . . . .	175
5.3	Results . . . . .	178
5.3.1	$Cl^-(CH_3Br)$ . . . . .	178
5.3.2	$Br^-(CH_3Cl)$ . . . . .	196
5.3.3	$Cl^-(C_2H_5Br)$ . . . . .	199
5.3.4	$Br^-(C_2H_5Cl)$ , $Cl^-(i-C_3H_7Br)$ and $Br^-(i-C_3H_7Cl)$ . . . . .	211
5.4	Discussion . . . . .	212
5.5	Conclusions . . . . .	225
5.6	References . . . . .	227
6.	SUMMARY AND FUTURE EXPERIMENTS . . . . .	230

## LIST OF FIGURES

Figure 1	The pressure dependence of the unimolecular rate constant as predicted by the Lindemann-Christiansen mechanism. <sup>6</sup> . . . . .	8
Figure 2	Pressure dependence of the $(\text{H}_2\text{O})_3\text{Cl}^-$ rate constant in various bath gasses. . . . .	12
Figure 3	The pressure dependence of the unimolecular dissociation rate when black body induced radiative dissociation is accounted for. <sup>6</sup> . . . . .	14
Figure 4	Schematic diagram of ion undergoing cyclotron motion in a magnetic field <b>B</b> . . . . .	19
Figure 5	Schematic representation of FTICR cell. . . . .	25
Figure 6	Schematic diagram of FTICR spectrometer with external ion source. . . . .	27
Figure 7	Detailed schematic diagram of the external high pressure ion source. . . . .	30
Figure 8	The sequence of detection steps in FTICR spectrometry. . . . .	34
Figure 9	Pulse sequence for unimolecular dissociation experiments. . . . .	41
Figure 10	Pulse sequence for laser induced dissociation experiments. . . . .	43
Figure 11	Apparatus for IRMPD experiments in a FTICR spectrometer. . . . .	45
Figure 12	Experimentally determined laser beam profile with Gaussian fit. . . . .	47
Figure 13	A plot of $[(\text{CH}_3\text{CH}_2)_2\text{O}]_2\text{H}^+$ ion intensity vs. time at 20 °C, . . . . .	

	2.4x10 <sup>-9</sup> mbar, I=9.7 W cm <sup>-2</sup> . Line a) is a 1st order fit, line b) was fit to equation 41. . . . .	59
Figure 14	Photodissociation kinetics for [(C <sub>2</sub> H <sub>5</sub> ) <sub>2</sub> O] <sub>2</sub> H <sup>+</sup> using pre-irradiation delays of 1 and 10 s. . . . .	65
Figure 15	Common schemes for representing the energy levels of a polyatomic molecule for multiphoton excitation. (see text for a description) . . . . .	71
Figure 16	Schematic illustration of population distributions for IRMPD and thermal unimolecular reactions. . . . .	80
Figure 17	FT-ICR Mass Spectrum of: a) Isolated [(C <sub>2</sub> H <sub>5</sub> ) <sub>2</sub> CO] <sub>2</sub> H <sup>+</sup> ion; b) Photoproducts after 10 s irradiation at I=9.9 W cm <sup>-2</sup> . . . . .	93
Figure 18	Plots of normalized [(CH <sub>3</sub> CH <sub>2</sub> ) <sub>2</sub> CO] <sub>2</sub> H <sup>+</sup> ion intensity vs. irradiation time at 20 °C for four different laser intensities. . . . .	94
Figure 19	Plots of normalized [(CH <sub>3</sub> CH <sub>2</sub> ) <sub>2</sub> CO] <sub>2</sub> H <sup>+</sup> ion intensity vs. irradiation time at 41 °C for four different laser intensities. . . . .	95
Figure 20	Plots of normalized [(CH <sub>3</sub> CH <sub>2</sub> ) <sub>2</sub> CO] <sub>2</sub> H <sup>+</sup> ion intensity vs. irradiation time at 58 °C for four different laser intensities. . . . .	96
Figure 21	Plots of normalized [(CH <sub>3</sub> CH <sub>2</sub> ) <sub>2</sub> CO] <sub>2</sub> H <sup>+</sup> ion intensity vs. irradiation time at 75 °C for four different laser intensities. . . . .	97
Figure 22	Plot of ln k <sub>2</sub> vs. T <sup>-1</sup> for the photodissociation of the proton bound dimer of pentanone at 20 °C. . . . .	99

Figure 23	A plot of the $[(C_4H_9)_2CO]_2H^+$ ion intensity vs. irradiation time at 20°C for laser intensities of 9.9, 4.6, 1.8 and 0.86 W cm <sup>-2</sup> . . . .	102
Figure 24	A logarithmic plot of $k_2$ vs. laser power for the photodissociation of $[(C_4H_9)_2CO]_2H^+$ ion at 20 °C. . . . .	103
Figure 25	Plots of normalized $[(CH_3CH_2)_2O]_2H^+$ ion intensity vs. irradiation time at 20 °C for six different laser intensities as indicated on the figure. . . . .	106
Figure 26	The photodissociation kinetics of $(C_2H_5)_2OH^+$ (prepared by the first stage of a double irradiation experiment) at 20 °C. . . . .	109
Figure 27	A plot of $[(CH_3CH_2)_2CO]_2H^+$ ion intensity as a function of laser fluence at 41 °C for laser intensities of 9.7, 4.6, 1.8, 0.91 W/cm <sup>2</sup> . . . . .	111
Figure 28	Photodissociation kinetics for $[(CH_3CH_2)_2CO]_2H^+$ at temperatures of 20 °C (a), 40 °C (b), 58 °C (c), 75 °C (d). $I=9.9$ W cm <sup>-2</sup> . . .	116
Figure 29	The effect of ion size on IRMPD kinetics. $I=9.8\pm0.1$ W cm <sup>-2</sup> . . . . .	118
Figure 30	The pressure dependence of the dissociation kinetics for $[(CH_3CH_2)_2O]_2H^+$ with various bath gasses added to the FT-ICR cell. . . . .	122
Figure 31	The photodissociation kinetics of $[(CH_3CH_2)_2O]_2H^+$ obtained from a double irradiation experiment. . . . .	125
Figure 32	The photodissociation kinetics of $[(CH_3CH_2)_2CO]_2H^+$ obtained	

	from a double irradiation experiment. . . . .	126
Figure 33	Schematic representation of the apparatus used for IRMPD MS <sup>n</sup> experiments in a FTICR spectrometer. . . . .	146
Figure 34	The FTICR pulse sequence which controls the timing of MS <sup>n</sup> experiments. This example illustrates the MS <sup>3</sup> experiment used to obtain the mass spectrum shown in Figure 35d). . . . .	148
Figure 35	Series of spectra illustrating the progression of the sequential photodissociation reactions of [(C <sub>2</sub> H <sub>5</sub> ) <sub>2</sub> O] <sub>2</sub> H <sup>+</sup> ion. . . . .	151
Figure 36	MS <sup>4</sup> spectra obtained by fragmenting the isolated C <sub>2</sub> H <sub>5</sub> OH <sub>2</sub> <sup>+</sup> ion using a) IRMPD; b) CID. . . . .	154
Figure 37	Schematic Representation of the Ion Reaction Sequence used in IRMPD-MS <sup>n</sup> experiments . . . . .	156
Figure 38	Schematic representation of the double minimum potential energy surface for a S <sub>N</sub> 2 reaction. . . . .	169
Figure 39	The potential energy surface for the Cl <sup>-</sup> + CH <sub>3</sub> Br reaction. . . .	171
Figure 40	The potential energy surface for the Cl <sup>-</sup> + C <sub>2</sub> H <sub>5</sub> Br reaction. . . .	173
Figure 41	The potential energy surface for the Cl <sup>-</sup> + i-C <sub>3</sub> H <sub>7</sub> Br reaction. . .	174
Figure 42	Un-ejected FT-ICR mass spectrum of ions produced in the high pressure external ion source during the Cl <sup>-</sup> + CH <sub>3</sub> Br reaction. .	179
Figure 43	FT-ICR mass spectrum of the Cl <sup>-</sup> (CH <sub>3</sub> Br) complex after rf isolation. . . . .	180

Figure 44	Black body dissociation kinetics of $\text{Cl}^-(\text{CH}_3\text{Br})$ at 21 °C. . . . .	182
Figure 45	Arrhenius plot of $\ln k_{\text{Br}^-}$ vs. $T^{-1}$ for black body induced dissociation of $\text{Cl}^-(\text{CH}_3\text{Br})$ . . . . .	185
Figure 46	Arrhenius plot of $\ln k_{\text{Cl}^-}$ vs. $T^{-1}$ for black body induced dissociation of $\text{Cl}^-(\text{CH}_3\text{Br})$ . . . . .	186
Figure 47	FT-ICR mass spectra resulting from 15 s exposure of isolated $\text{Cl}^-(\text{CH}_3\text{Br})$ to a) 9.9 $\text{W cm}^{-2}$ IR laser radiation; b) black body radiation, 20 °C. . . . .	188
Figure 48	Difference spectrum (laser ON-laser OFF) for $\text{Cl}^-(\text{CH}_3\text{Br})$ photodissociation. . . . .	189
Figure 49	Dissociation kinetics of $\text{Cl}^-(\text{CH}_3\text{Br})$ from; a) 9.9 $\text{W cm}^{-2}$ IR laser radiation; b) black body IR radiation at 20 °C. . . . .	192
Figure 50	Kinetics plot for the bimolecular reaction of $\text{Cl}^- + \text{CH}_3\text{Br}$ at 20 °C. The uncorrected ion gauge pressure of $\text{CH}_3\text{Br}$ was $1.1 \times 10^{-7}$ mbar. . . . .	193
Figure 51	FT-ICR spectrum recorded after 60 s exposure of $\text{Br}^-(\text{CH}_3\text{Cl})$ to a) black body radiation; $T=21$ °C, b) IRMPD; laser intensity= $9.9 \text{ W cm}^{-2}$ . . . . .	197
Figure 52	Kinetics plots for the dissociation of $\text{Br}^-(\text{CH}_3\text{Cl})$ by a) black body infrared radiation; $T=21$ °C, b) IRMPD; laser intensity= $9.9 \text{ W/cm}^2$ . . . . .	198

Figure 53	FT-ICR mass spectrum of the $\text{Cl}^-(\text{C}_2\text{H}_5\text{Br})$ complex after rf isolation. ....	201
Figure 54	Black body dissociation kinetics of $\text{Cl}^-(\text{C}_2\text{H}_5\text{Br})$ at 31 °C. ....	202
Figure 55	Arrhenius plot of $\ln k_{\text{Br}}$ vs. $T^{-1}$ for black body induced dissociation of $\text{Cl}^-(\text{C}_2\text{H}_5\text{Br})$ . ....	204
Figure 56	Arrhenius plot of $\ln k_{\text{Cl}}$ vs. $T^{-1}$ for black body induced dissociation of $\text{Cl}^-(\text{C}_2\text{H}_5\text{Br})$ . ....	205
Figure 57	IRMPD kinetics of $\text{Cl}^-(\text{C}_2\text{H}_5\text{Br})$ at a laser intensity of 9.9 $\text{W}/\text{cm}^2$ . ....	208
Figure 58	IRMPD kinetics of $\text{Cl}^-(\text{C}_2\text{H}_5\text{Br})$ at a laser intensity of 3.3 $\text{W}/\text{cm}^2$ . ....	209
Figure 59	Low energy CID of $\text{Cl}^-\text{CH}_3\text{Br}$ ion in $1.6 \times 10^{-8}$ mbar neon. ....	220

## LIST OF TABLES

Table 3.1	Photodissociation Data for the Proton Bound Dimer Ion of Pentanone . . . . .	100
Table 3.2	Photodissociation Data for the Proton Bound Dimer Ion of Nonanone. . . . .	104
Table 3.3	Photodissociation Data for the Proton Bound Dimer Ion of Diethyl Ether . . . . .	107
Table 5.1	Data obtained from the dissociation kinetics of $\text{Cl}^-(\text{CH}_3\text{Br})$ . . . .	195
Table 5.2	Data Obtained from the Dissociation kinetics of $\text{Cl}^-(\text{C}_2\text{H}_5\text{Br})$ . .	210



## 1. INTRODUCTION

*"Great spirits have always encountered violent opposition from mediocre minds."*

Albert Einstein

### 1.0 General Introduction

For the last five years, the study of unimolecular dissociation reactions of gaseous ions has dominated the research interests of the Fourier transform ion cyclotron resonance (FT-ICR) group at the University of Waterloo. The discovery of black body radiation induced unimolecular dissociation in 1994 by McMahon and co-workers<sup>1,2</sup> led to a re-examination of the historical "radiation theory" of unimolecular reactions. Since the original discovery, there have been extensive experimental<sup>3,4,5,6</sup> and theoretical<sup>7</sup> treatments of thermal unimolecular reactions induced by black body radiation and at least one review<sup>8</sup>. However, in the infancy of the "modern" black body radiation experiments, one of the main questions was: How could such a weak infrared (IR) source affect dissociation of ions? Dunbar had previously shown that infrared photodissociation of ions by low intensity continuous wave (CW) CO<sub>2</sub> laser radiation could be treated as if the ions were being irradiated by a black body source.<sup>9,10,11</sup> Thus, some of the proof for the black body mechanism was found by comparison with Dunbar's existing theory. The black body radiative dissociation mechanism was termed zero-pressure thermal radiatively induced dissociation (ZTRID)

for reasons which will be explained in section 1.1 of this thesis.

The goal of this thesis was not to study the ZTRID mechanism further but instead to build upon the existing knowledge of thermal unimolecular reactions and to explore the connection between ZTRID and low intensity infrared multiple photon dissociation (IRMPD). The IR laser could then be used to dissociate ions which did not dissociate by ZTRID at the temperatures accessible in our laboratory. Since Dunbar had already shown that a low intensity IR laser was equivalent to a black body source, the laser power could be calibrated to a ZTRID temperature and the IRMPD process could be treated as a thermal unimolecular dissociation. Like so many experiments in science, the further one digs the more complex the problem becomes and, in fact, the initial experiments indicated that the IRMPD kinetics did *not* behave like a thermal unimolecular dissociation. Chapter 3 of this thesis is devoted to the study of the IRMPD dynamics of gaseous ions in the low pressure regime of a FT-ICR spectrometer.

The study of IRMPD mechanisms led to two related experiments. The first presents a new method for studying ion structure by multiple IR photodissociation events. This IRMPD equivalent to previous tandem mass spectrometry ( $MS^n$ ) experiments which used collision induced dissociation (CID), is presented in chapter 4 of this thesis. It is hoped that, in the future, application of this new technique to the field of biological mass spectrometry could dramatically improve the current ability to perform *in situ* sequencing of DNA and oligopeptides using a FT-ICR spectrometer.

The IRMPD/FT-ICR technique, developed in chapter 3, was applied to the study of chloride-alkyl halide  $S_N2$  reaction dynamics. This study uses both IRMPD and ZTRID methods to probe the dissociation dynamics of bound  $S_N2$  reaction intermediates and is presented in chapter 5 of this thesis. The predicted non-statistical dynamics of the  $Cl^- + CH_3Br$  reaction was of particular interest.

A detailed introduction to the experiments presented in chapters 3-5 is included at the beginning of each of the chapters. As mentioned above, the discussion of thermal unimolecular reactions *via* black body radiation is not the primary subject of this work. However, the historical evolution of unimolecular reaction mechanisms, including the modern radiative mechanism, is presented in the following section for the sake of completeness and because some experiments in this thesis will draw comparisons between IRMPD and black body dissociation results.

## 1.1 Unimolecular Reactions Mechanisms

Unimolecular reactions are characterized by the decomposition of a single reactant molecule, A, into two or more product molecules (or atoms), B and C.

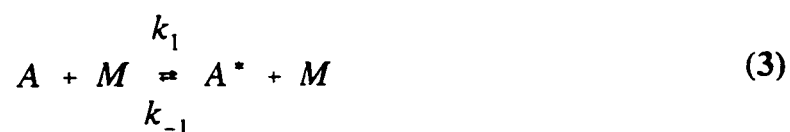


Since the reaction rate depends only upon the concentration of the initial reactant molecule, the integrated rate equation for a unimolecular reaction is one of the simplest cases in chemical kinetics.

$$[A] = [A]_0 e^{-k_{\text{unf}} t} \quad (2)$$

The simplicity of the unimolecular rate equation belies the fact that for many years the mechanism of energization of A remained a mystery. In 1919 Perrin reasoned that, since the reaction rate did not depend upon the concentration of surrounding molecules, the energy necessary for the reaction to proceed must be coming from the radiation emitted from the hot reaction vessel.<sup>12</sup> It was known that all objects emit radiation with a spectral density characteristic of their temperature.<sup>13</sup> The radiation emitted is known as black body radiation and its maximum emission wavelength occurs in the infrared for objects at ambient temperatures and shifts to shorter wavelengths for objects at higher temperatures. This is the basis of the modern day term "heat signature" used to describe the infrared emission which allows night vision or missile tracking equipment to "see" objects which are ordinarily invisible to the naked eye. Perrin's "radiation hypothesis" was rejected primarily because of the arguments of Langmuir, who argued that the bond dissociation energy of certain molecules would require the frequency of the radiation to be in the visible region of the spectrum and that, since these gasses were colourless, they did not absorb visible

light.<sup>14</sup> Langmuir also argued that the energy density of black body radiation, at visible wavelengths, was insufficient to provide the activation energy necessary for reaction. The radiation hypothesis remained an issue of debate until Lindemann<sup>15</sup> and separately, Christiansen<sup>16</sup> proposed that A is energized by collisions with surrounding molecules, M, and that the overall mechanism could be represented by a two-step reaction sequence involving collisional energization of A and deactivation of the energized A<sup>\*</sup>.<sup>17</sup>



If steady state is assumed for A<sup>\*</sup> as indicated in Equation (5), then the resultant rate equation is given by Equation (6).

$$\frac{\partial[A^*]}{\partial t} = 0 = k_1[A][M] - (k_{-1}[M] + k_d) \cdot [A^*] \quad (5)$$

$$\frac{-\partial[A]}{\partial t} = \frac{\partial[B]}{\partial t} = k_d[A^*] = \frac{k_1 k_d}{k_{-1}[M] + k_d} [M][A] \quad (6)$$

The rate can be expressed as a simple, first order equation

$$\frac{\partial[A]}{\partial t} = -k_{uni}[A] \quad (7)$$

or in the integrated form

$$\ln \frac{[A]}{[A]_0} = -k_{uni} \cdot t \quad (8)$$

where  $k_{uni}$  is now a pseudo-first order, unimolecular rate constant which can be determined experimentally by monitoring the abundance of the parent species  $[A]$  with respect to time. It can be seen from Equation (8) that  $-k_{uni}$  is equal to the slope of a plot of the natural logarithm of  $[A]$  vs time.

A consequence of the Lindemann-Christiansen (LC) mechanism is that the kinetics are first order at high pressure when the rate of de-energization is much greater than the rate of dissociation of the excited species  $A^*$ . Comparing Equation (9) with Equation (7) yields the observed, first order rate constant in the high pressure regime which is given by Equation (10).

At high pressure,  $k_{-1}[M] \gg k_d$

$$\frac{-\partial[A]}{\partial t} = \frac{k_1 k_d}{k_{-1}} [A] \quad (9)$$

$$k_{uni} = \frac{k_1 k_d}{k_{-1}} \quad (10)$$

At low pressure collisional stabilization is slow and nearly all excited species dissociate. The overall rate of reaction is approximately equal to the rate of formation of  $A^*$  and the kinetics become second order overall. Comparing Equation (12) with Equation (7) yields the observed, pseudo-first order rate constant in the low pressure regime which is given by Equation (12).

At low pressure,  $k_d \gg k_{-1}[M]$

$$k_{uni} = k_1 [M] \quad (11)$$

$$\frac{-\partial[A]}{\partial t} = k_1 [M][A] \quad (12)$$

The low pressure rate constant is termed pseudo first order because the observed rate of decomposition of A will be first order provided that the pressure of M remains constant throughout the reaction. The experimentally observed rate constant,  $k_{uni}$ , will be linearly dependent on the pressure of M at low pressure and independent of [M] at high pressure. Since the energization of A depends on collisions with M, the rate constant will be zero at zero pressure. A plot of  $k_{uni}$  vs. [M] is presented in Figure 1.

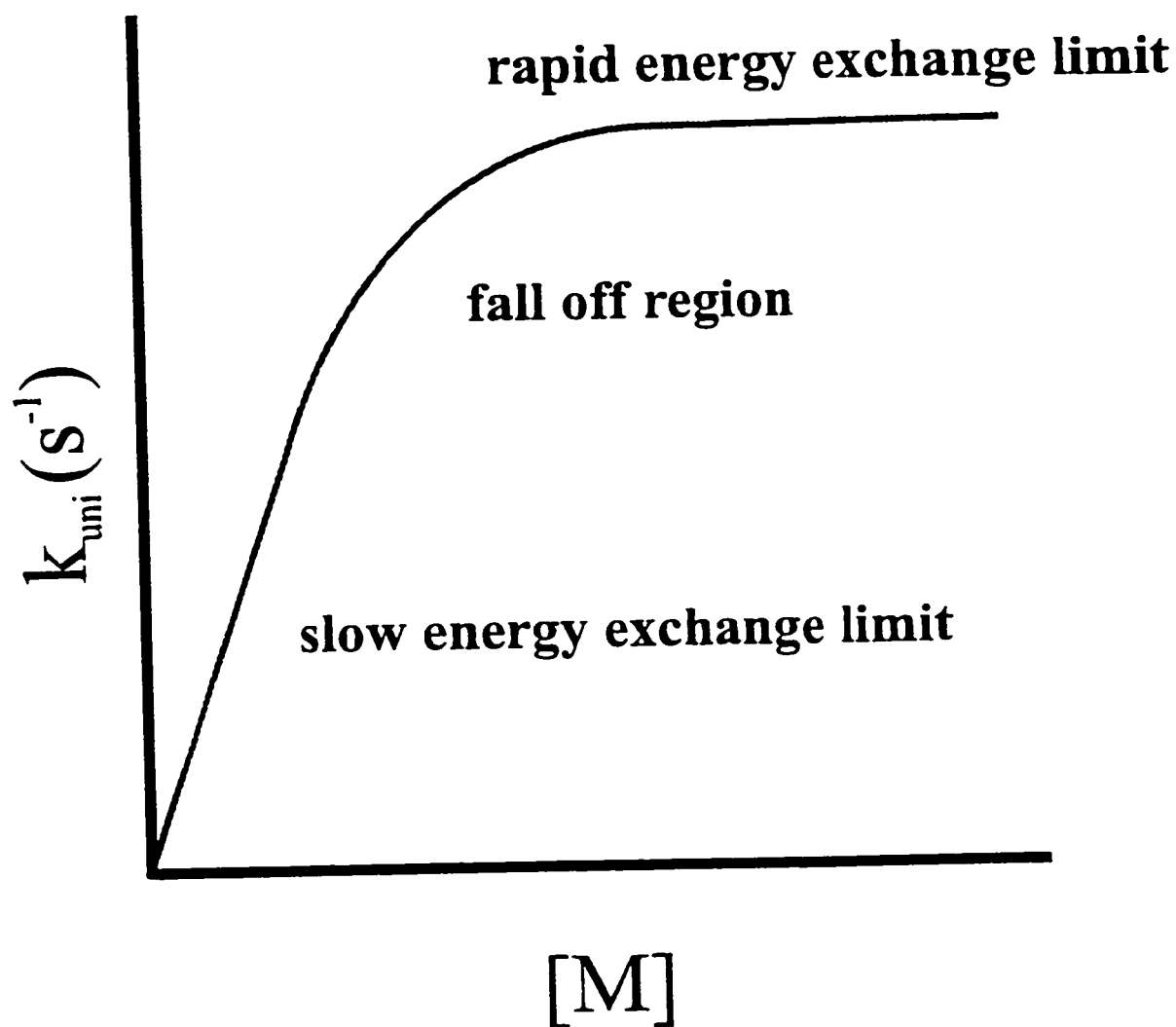


**Figure 1** The pressure dependence of the unimolecular rate constant as predicted by the Lindemann-Christiansen mechanism.<sup>6</sup>

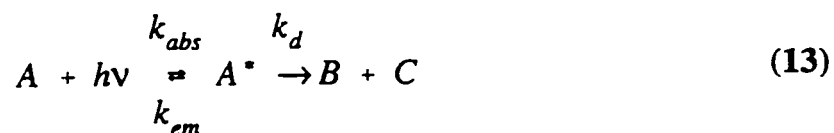


All known examples of unimolecular reactions for the next 70 years obeyed the Lindemann-Christiansen model and exhibited a fall-off in reaction rate at low pressures. Modern kinetics textbooks only included the radiation hypothesis in order to point out its fallacy. Steinfeld *et al.* did point out that Langmuir's paper did not refute the radiation hypothesis because he neglected to consider that molecules could absorb multiple infrared photons rather than a single visible one and that the black body radiation curve peaks in the infrared.<sup>18</sup> Steinfeld *et al.* go on to reject the radiation hypothesis on the basis of the thermodynamic argument that the walls cannot do chemical work on the system if the two are in thermal equilibrium. They further point out that an infrared source at a higher temperature (such as an infrared laser) can induce a radiative unimolecular reaction. An interesting variation on this point was suggested by Quack<sup>19</sup> in 1980, who pointed out that IR radiative unimolecular dissociation of molecules might be barely observable in the collisionless environment of a molecular beam.

In 1994, the radiation hypothesis was revitalized by the first observation of a unimolecular reaction which was truly independent of collision gas pressure. McMahon and co-workers<sup>1</sup> observed a true unimolecular dissociation of trapped ions which was induced by the ambient black body radiation field surrounding the ions. The observation of this phenomenon was facilitated by a unique experimental apparatus. A high pressure cluster ion source was coupled to a Fourier transform ion cyclotron resonance (FT-ICR) spectrometer which operated at  $\leq 10^{-9}$  torr. The

combination of having weakly bound cluster ions trapped for long periods of time in the ultralow pressure environment of the FT-ICR spectrometer proved to be exactly the experimental conditions necessary for the observation of black body induced unimolecular dissociation. This observation has been verified by extensive experimental<sup>3,4,5</sup> and theoretical<sup>7</sup> explorations of thermal unimolecular reactions induced by black body radiation.

The "modern" radiation mechanism is summarized by the reaction shown below, where the term  $(h\nu)$  represents photon density.



If we assume steady state for  $A^*$  as in Equation (14), then the resultant rate equation is give by Equation (15).

$$\frac{\partial[A^*]}{\partial t} = 0 = k_{abs}[A](h\nu) - k_{em}[A^*] - k_d[A^*] \quad (14)$$

$$\frac{-\partial[A]}{\partial t} = \frac{\partial[B]}{\partial t} = k_d[A^*] = \frac{k_{abs}k_d}{k_{em} + k_d}(h\nu)[A] \quad (15)$$

The rate can be expressed by the same simple, first order equation which governed the LC collisional mechanism.

$$\frac{-\partial[A]}{\partial t} = k_{uni} [A] \quad (16)$$

Comparison of Equation (15) and Equation (16) reveals the true form of  $k_{uni}$  for the limiting cases of slow energy exchange (SEX) in Equation (17) and rapid energy exchange (REX) in Equation (18).

$$\text{If } k_d \gg k_{em} ; \quad k_{uni} = k_{abs} \cdot (h\nu) \quad (17)$$

$$\text{If } k_{em} \gg k_d ; \quad k_{uni} = \frac{k_{abs} k_d}{k_{em}} \cdot (h\nu) \quad (18)$$

For simplicity, only spontaneous emission has been included in the radiative mechanism described above. If the mechanism in equation (13) is modified to account for stimulated emission, the photon term ( $h\nu$ ) drops out of the rate constant expression for the (REX) limit by direct analogy to the  $[M]$  term in the LC mechanism. In the initial experiments of McMahon and co-workers,<sup>1</sup> the rate constant was observed to have a pressure dependent slope accompanied by a finite, zero pressure intercept which represented the true radiative rate constant. This is shown in Figure 2.<sup>2</sup> Thus the process of black body induced unimolecular dissociation was termed zero-pressure thermal radiatively induced dissociation (ZTRID). More recent studies<sup>7,5</sup> have shown

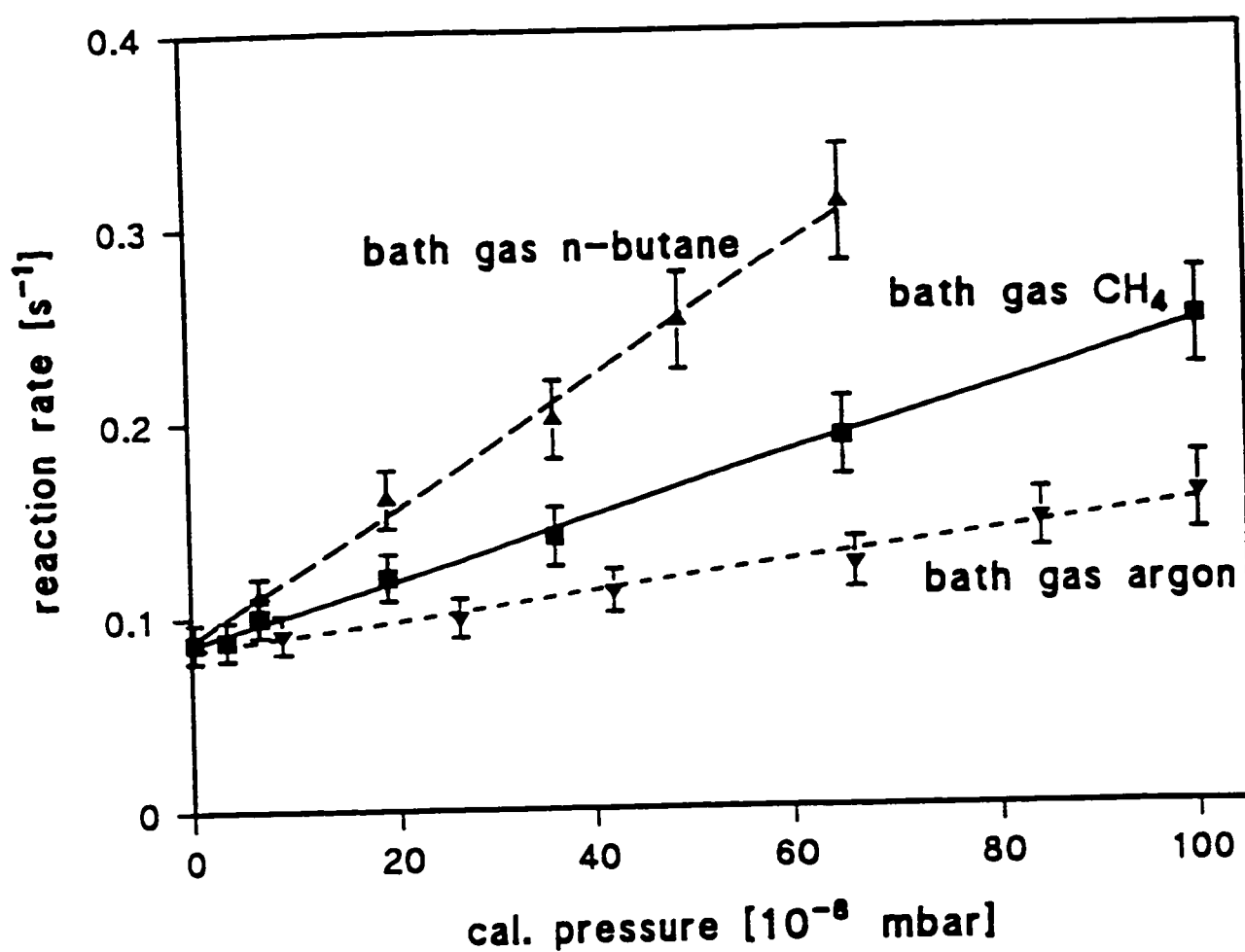


**Figure 2** Pressure dependence of the  $(\text{H}_2\text{O})_3\text{Cl}^-$  rate constant in various bath gases.

that complete pressure independence can be observed in the dissociation of very large ions at higher temperatures, which have many oscillators to absorb the IR radiation and slow  $k_d$  values. These species are said to be in the REX limit of the radiative mechanism which is directly analogous to the high pressure limit in the LC mechanism. When the LC mechanism is modified to account for radiative dissociation, the dependence of the unimolecular dissociation rate constant on pressure is now given by Figure 3.

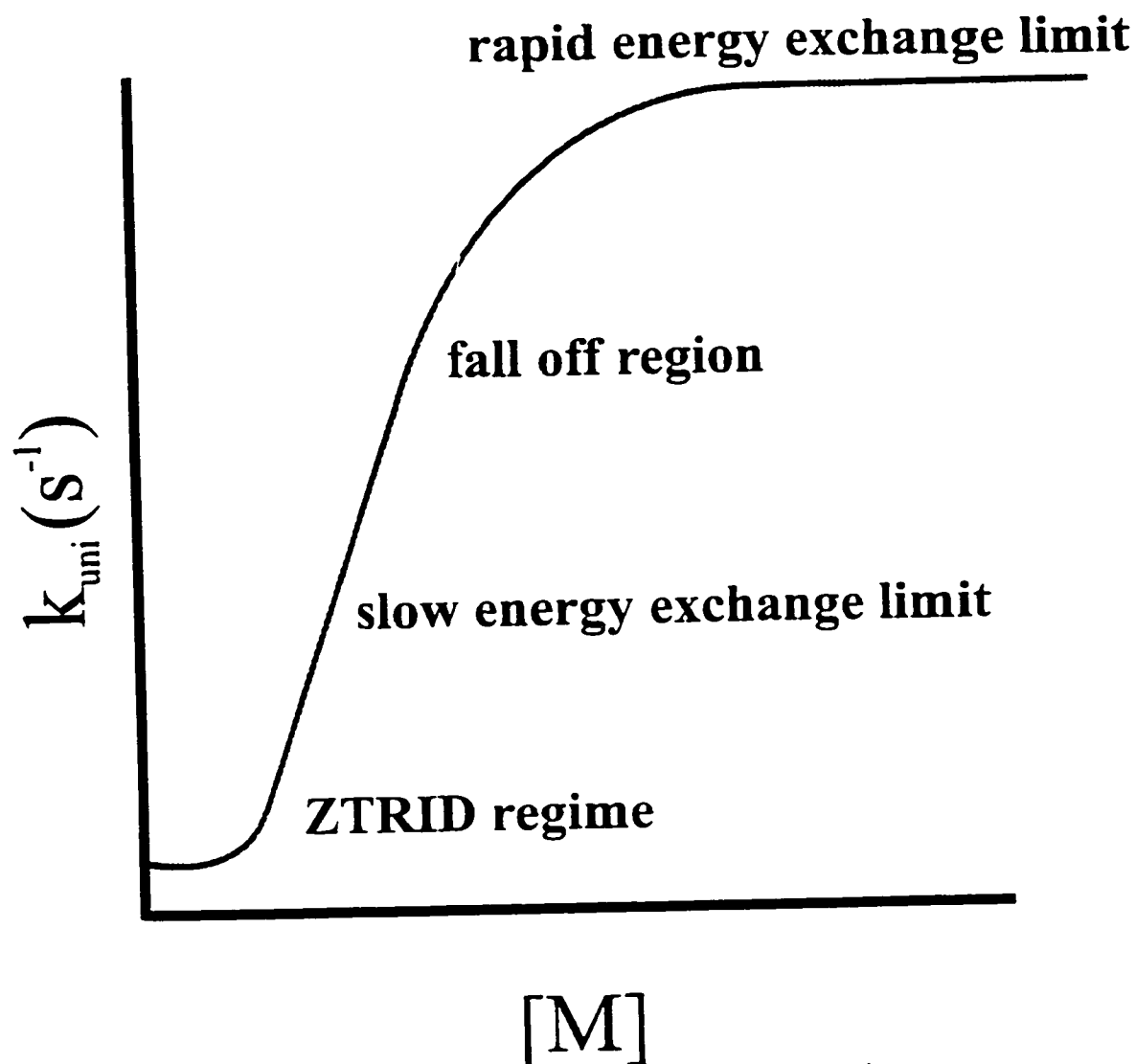


**Figure 3** The pressure dependence of the unimolecular dissociation rate when black body induced radiative dissociation is accounted for.<sup>6</sup>

### 1.3 References

1. Thölmann, D.; Tonner, D. S.; McMahon, T. B. *J. Phys. Chem.* **1994**, 98, 2002.
2. Tonner, D. S. *M.Sc. thesis*, University of Waterloo, **1994**.
3. Tonner, D. S.; Thölmann, D.; McMahon, T. B. *Chem. Phys. Lett.* **1995**, 233, 324.
4. Tonner, D. S.; Thölmann, D.; McMahon, T. B. *Chem. Phys. Lett.* **1995**, 223, 324-330.
5. Price, W. D.; Schnier, P. D.; Williams, E. R. *Anal. Chem.* **1996**, 68, 859-866.
6. Hoffman, T. L.; *M.Sc. thesis*, University of Waterloo, **1997**.
7. Dunbar, R. C. *J. Phys. Chem.* **1994**, 98, 8705-8712.
8. Dunbar, R. C.; McMahon, T. B. *Science* **1998**, 279, 194.
9. Dunbar, R. C. *J. Chem. Phys.* **1991**, 95, 2537.
10. Dunbar, R. C.; Zaniwski, R. C. *ibid.* **1992**, 96, 5069.
11. Uechi, G. T.; Dunbar, R. C. *ibid.* 8897.
12. Perrin, J.; *Ann. Phys.* **1919**, 11, 5.
13. The spectral density of black body radiation is given by the Planck relation which is described in any introductory physics textbook.
14. Langmuir, I. *J. Amer. Chem. Soc.* **1920**, 42, 2190.
15. Lindemann, F. A.; *Trans. Faraday Soc.* **1922**, 17, 598.
16. Christiansen, J. A.; Ph.D. thesis, University of Copenhagen, Copenhagen, Denmark, **1921**.
17. For a discussion of the Lindemann-Christiansen hypothesis see; K.J. Laidler, *Chemical Kinetics*, 3<sup>rd</sup> ed. (Harper and Row, 1987) 152.
18. Steinfeld, J. I.; Francisco, J. S.; Hase, W. L. *Chemical Kinetics and Dynamics*; Prentice-Hall, Englewood Cliffs: NJ, **1989**.
19. Quack, M.; *Personal Communication*.

## 2. INSTRUMENTATION

*God runs electromagnetics by wave theory on Monday, Wednesday and Friday, and the Devil runs them by quantum theory on Tuesday, Thursday and Saturday.*

William Bragg

All of the experiments reported in this thesis were performed on a Bruker Spectrospin CMS 47 Fourier transform ion cyclotron resonance (FT-ICR) spectrometer. The CMS 47 is equipped with a 4.7 T, 15 cm horizontal bore, superconducting magnet. A 6 cm x 6 cm diameter cylindrical cell rests inside the bore of the magnet within a vacuum system which is pumped by a magnetically shielded Balzers 300 L/s turbomolecular pump. The base pressure in the FT-ICR cell is typically in the  $10^{-10}$  mbar range as measured by a magnetically shielded Balzers IMR 312 ionization gauge. A Silicon Graphics Inc. INDY computer controls the instrument. The FT-ICR in our laboratory has been modified by the addition of an external, high pressure, ion source so that weakly bound cluster ions can be generated in a region of high pressure before being trapped at low pressure in the FT-ICR cell. Details of both the CMS 47 and the external ion source have been published previously.<sup>1,2</sup> Neutral gas samples were introduced into the ICR cell through Balzers molecular leak valves for the purpose of collisional thermalization of the ions or for performing ion-molecule reactions. For black body induced unimolecular experiments, the FT-ICR cell heaters were powered



with a 200 W DC variable power supply rather than the standard AC supply because of the interference observed while using alternating current inside the magnet bore. The light source for the infrared laser photodissociation experiments was a 10 W Synrad Inc. 48-0-15W, continuous wave (CW) CO<sub>2</sub> laser operating at or near 10.6  $\mu\text{m}$ .

## 2.1 Cyclotron Motion of a Charge in a Static Magnetic Field

Ion cyclotron resonance (ICR) spectrometry is based upon the periodic circular motion of charged particles in a static magnetic field. The experiment is conducted at very low pressure ( $\sim 10^{-9}$  torr) to minimize collisions so that the coherence of the ion motion can be maintained for times on the order of a second. The effects of electric and magnetic fields on a charged particle are governed by the Lorentz force equation which is shown in equation (19).<sup>3</sup>

$$\mathbf{F} = q [\mathbf{E} + (\mathbf{v} \times \mathbf{B})] \quad ; \quad q = ez \quad (19)$$

The Lorentz force equation gives the total force on a moving charge expressed as the vector sum of the forces from the electric and magnetic fields, where  $q$  is the net charge on the particle, ( $e$  is the charge on an electron,  $z$  is the integer number of charges)  $\mathbf{v}$  is the velocity of the particle,  $\mathbf{E}$  is the electric field strength and  $\mathbf{B}$  is the magnetic field strength. In the absence of an electric field, the Lorentz equation

reduces to equation (20).

$$\mathbf{F} = q [(\mathbf{v} \times \mathbf{B})] \quad (20)$$

The motion resulting from a uniform magnetic field is most easily seen if the velocity of the moving charges is separated into velocity components which are parallel,  $v_z$ , and perpendicular,  $\mathbf{v}_{xy} \equiv \mathbf{v}_x + \mathbf{v}_y$ , to the magnetic field direction.

$$\mathbf{v} = v_z + \mathbf{v}_{xy} \quad (21)$$

The force resulting from the interaction of  $\mathbf{v}_{xy}$  and  $\mathbf{B}$  produces a circular ion motion in the xy plane normal to  $\mathbf{B}$ . It is this circular motion which is exploited for ICR spectrometry. The parallel velocity component,  $v_z$ , is not affected by the magnetic field and thus, for most discussions of ICR, ion motion along the z axis can be ignored or treated separately. Since the z-axis motion can be separated out, equation (20) can be reduced to a scalar equation (22) with the resultant force directed inward toward the center of the circular trajectory, perpendicular to  $\mathbf{B}$ , as shown in Figure 4 for a positively charged ion. Negatively charged ions rotate in the opposite direction.

$$F = qBv_{xy} \quad ; \text{ where } v_{xy} = |\mathbf{v}_{xy}| \quad (22)$$

From Newton's laws of motion, the centripetal force of an orbiting object is related

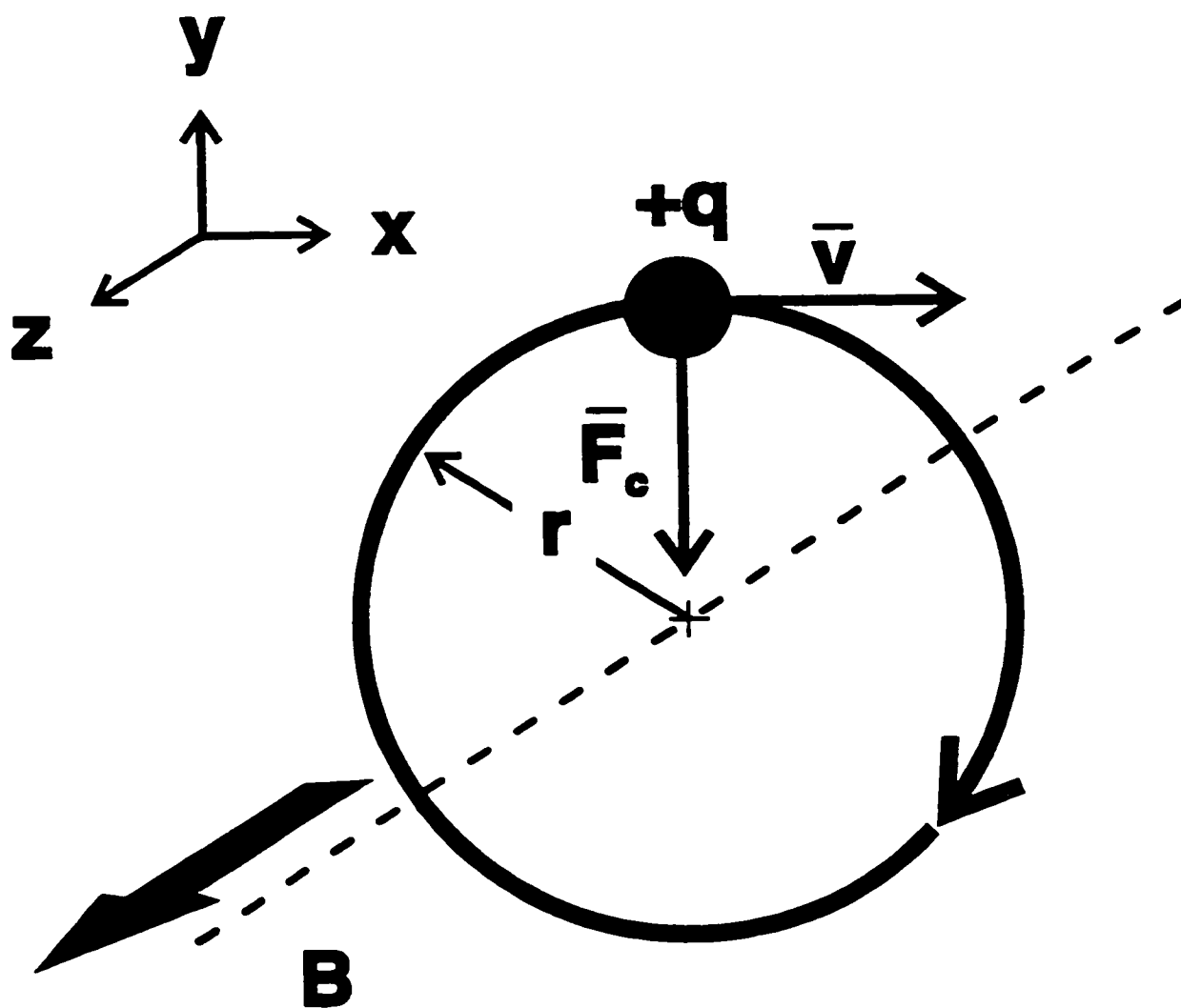


**Figure 4** Schematic diagram of ion undergoing cyclotron motion in a magnetic field  $\mathbf{B}$ .

to its velocity by equation (23), where  $r$  is the radius of the circular trajectory and  $a$  is the radial acceleration.

$$F = ma = \frac{mv_{xy}^2}{r} \quad (23)$$

Comparison of equations (22) and (23) yields solutions for the radius and the angular frequency of the cyclotron motion.

$$r = \frac{mv_{xy}}{qB} \quad (24)$$

$$\omega_c = \frac{v_{xy}}{r} = \frac{qB}{m} = \frac{eB}{m/z} \quad (25)$$

Equation (25) is often referred to as the cyclotron equation. It is evident from equations (24) and (25) that the radius depends on  $v_{xy}$  but the cyclotron frequency depends only on the mass-to-charge ratio ( $m/z$ ) of the ion in a constant magnetic field. Thus, a measured spectrum of ion cyclotron frequencies can immediately be converted into a mass spectrum. Section 2.2 describes how the cyclotron frequencies of ions can be measured.

## 2.2 Application of a Radio Frequency Electric Field

It can be seen from equation (24) that the radius of the ion cyclotron motion depends on the velocity and, hence, the kinetic energy of the ion. Re-arranging equation (24) to solve for  $v_{xy}$  in equation (26) leads to the expression for the two dimensional kinetic energy of the ion in the xy plane ( $K_{xy}$ ) shown in equation (27).

$$v_{xy} = \frac{qBr}{m} \quad (26)$$

$$K_{xy} = \frac{m v_{xy}^2}{2} = \frac{q^2 B^2 r^2}{2m} \quad (27)$$

Almost all ICR techniques rely upon an alternating, radio frequency electric field to excite the cyclotron motion of the ions prior to detection. The ion motion is still described by the Lorentz force equation but the electric field ( $\mathbf{E}$ ) is now non-zero. The electric field near the centre of the cell is given by:

$$\mathbf{E} = E_{rf} \sin(\omega t + \phi) \mathbf{i} + E_T \mathbf{k} \quad (28)$$

where  $\phi$  is the phase angle between the oscillating field and the initial cyclotron motion of the ion,  $E_T$  is the magnitude of the electric field from the end trapping plates and  $E_{rf} = V_p/d$  ( $V_p$  is the base to peak voltage and  $d$  is the cell diameter). Far from the centre of the cell this approximation breaks down because the rf electric field lines

curve towards the end plates (and vice versa) rather than running directly between the plates. The Bruker Infinity<sup>TM</sup> cell used in these experiments attempts to correct for this effect using graduated potentials on the trapping plates. Since the radius of ions with thermal translational energy is  $\sim 0.05$  mm, equation (28) represents the electric field "felt" by the ions in the center of the cell. For ions with large translational energy, such as products of collisional induced dissociation (CID), the effective electric field may not be adequately represented by equation (28). The  $E_T \mathbf{k}$  term in equation (28) may be ignored during rf excitation since the voltage on the end plates is small ( $\leq 2$  V) and approximately symmetric about the centre of the cell. Thus, only the radio frequency electric field applied perpendicularly to  $\mathbf{B}$  through the excitation plates is pertinent to the ion excitation process. Only those ions whose cyclotron frequencies are resonant with the applied rf field are translationally excited. As these ions are accelerated, the radius of the cyclotron motion increases and the ions pass closer to a pair of detector plates which are mounted orthonormal to both the excitation plates and the magnetic field. The motion of the ions past the stationary plates induces an oscillating image current, at frequency  $\omega_c$ , in the plates. The magnitude and frequency of this current yield the intensity and mass-to-charge ratio of the excited ions respectively.

The effect of a rf electric field on the energy of the ions has been discussed by Bowers *et al.*<sup>4</sup> The instantaneous power absorption,  $A$ , is the dot product of the electric force ( $\mathbf{F}$ ) and the ion velocity in the xy plane:

$$A = \mathbf{F} \cdot \mathbf{v}_{xy} = q\mathbf{E} \cdot \mathbf{v}_{xy} \quad (29)$$

Both Comisarow<sup>5</sup> and Dunbar<sup>6</sup> have solved equation (29) with the simplifying assumptions that the frequency of de-energizing collisions is much less than  $\omega_c$  and that  $\omega_c$  is approximately the same as the excitation frequency,  $\omega$  (ie. near resonance). In the low pressure limit where collisional damping is not important, the instantaneous power absorption is given by equation (30), where  $t_{rf}$  is the length of the rf excitation pulse.

$$A(t_{rf}) = \frac{q^2 E_{rf}^2 t_{rf}}{4m} \quad (30)$$

Since the excitation is a resonant process, there are lineshape/linewidth factors to consider in the actual power absorption equations. These and other factors relating to ICR power absorption, including the high pressure limit, are discussed by Bowers *et. al.*<sup>4</sup> with the appropriate derivations being referenced therein. The average kinetic energy imparted to the ions by the rf field may be found by integrating the instantaneous power absorption over the irradiation time.

$$\langle K \rangle = \int_0^{t_{rf}} A(t_{rf}) dt_{rf} \quad (31)$$

Thus the kinetic energy in excess of thermal is given by equation (32).

$$\langle K \rangle = \frac{q^2 E_{rf}^2 t_{rf}^2}{8m} \quad (32)$$

A comparison of equations (27) and (32) provides an expression for the radius of the ion as a function of the rf amplitude and irradiation time.

$$r = \frac{E_{rf} t_{rf}}{2B} \quad (33)$$

The radius of thermal cyclotron motion depends upon the mass of the ion; as shown in equation (24). The radius of the ion trajectory during the rf excitation/detection events, however, does not. Since the amplitude of the image current induced in the receiver plates depends upon the proximity of the ion to the surface of the plate, mass discrimination would be a significant problem *if* the radius *were* mass dependent.

### 2.3 The FT-ICR Cell

The central part of an FT-ICR spectrometer is the cell which consists of a pair each of trapping plates, rf transmitter plates and rf receiver plates as shown in Figure 5. The repulsive potentials on the endplates of the FT-ICR cell contain the ion motion along the z axis. Motion in the xy plane is restricted by the cyclotron motion.



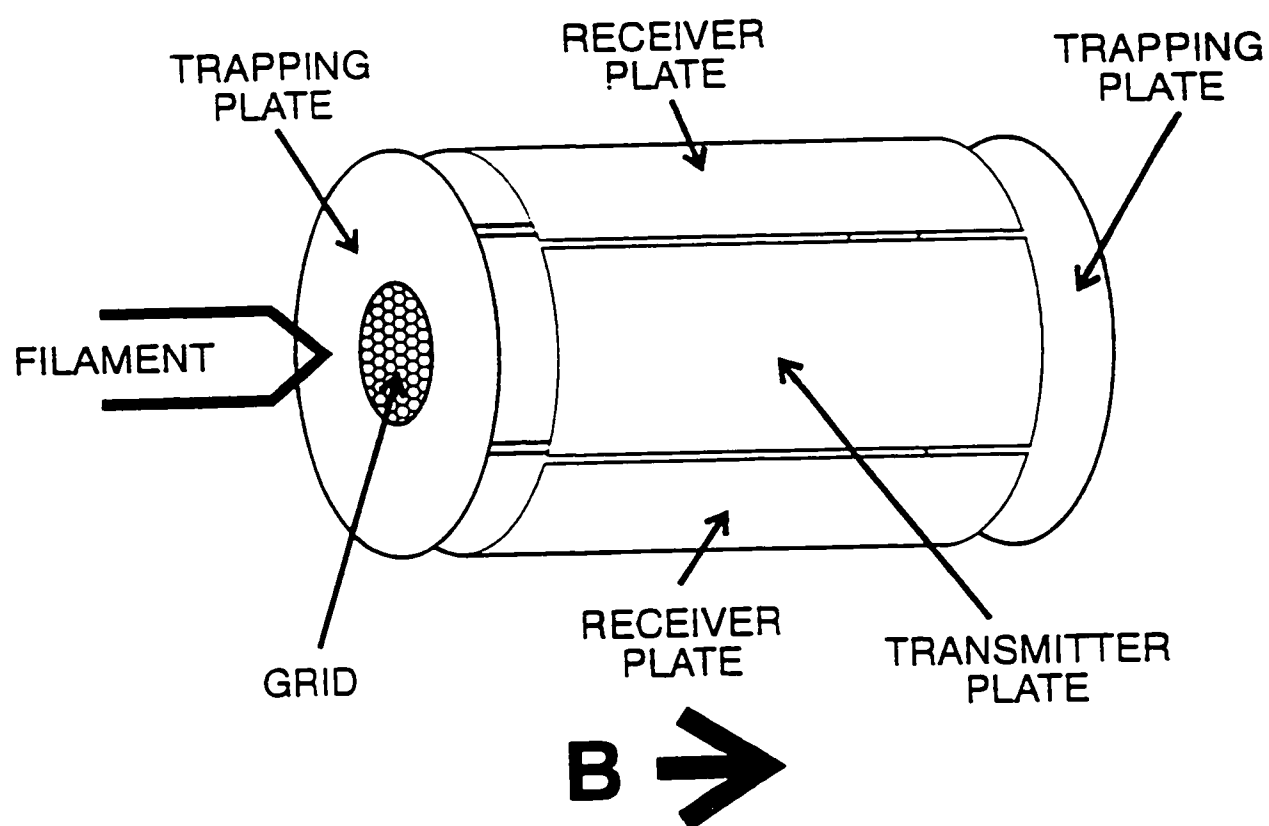


**Figure 5** Schematic representation of FTICR cell.

Hence, the FT-ICR cell is a three dimensional ion trap. A computer controlled rf synthesizer with pulse shaping capabilities generates radio frequency signals of variable length, frequency, and intensity. Amplification of these signals produces the desired electric field waveform on the excitation plates of the FT-ICR cell to excite the ions translationally. The oscillating image current induced in the receiver plates is amplified and detected so that the cyclotron frequencies of the ions can be determined and a mass spectrum produced. Figure 6 is a schematic diagram of the FT-ICR with the external ion source which is described in the next section. The FT-ICR cell rests inside the bore of a 4.7 Tesla superconducting magnet. The ion path from the source to the FT-ICR cell is co-linear with the magnetic field along the z axis. Since the ions were generated in the external high pressure ion source, the internal ionization filament shown in Figure 5 was not required for these experiments and was replaced with a infrared transparent ZnSe window through which the CO<sub>2</sub> laser beam enters the cell.

## **2.4 Ion Formation**

The Bruker CMS 47 FT-ICR spectrometer has the capability of generating ions inside the FT-ICR cell by 70 eV pulsed electron impact ionization of the neutral gas, in a process referred to as "internal ionization." The electrons are produced from a rhenium filament mounted outside of the ICR cell. Internal ionization was not used in these experiments, because it requires higher neutral gas pressures in the FT-ICR

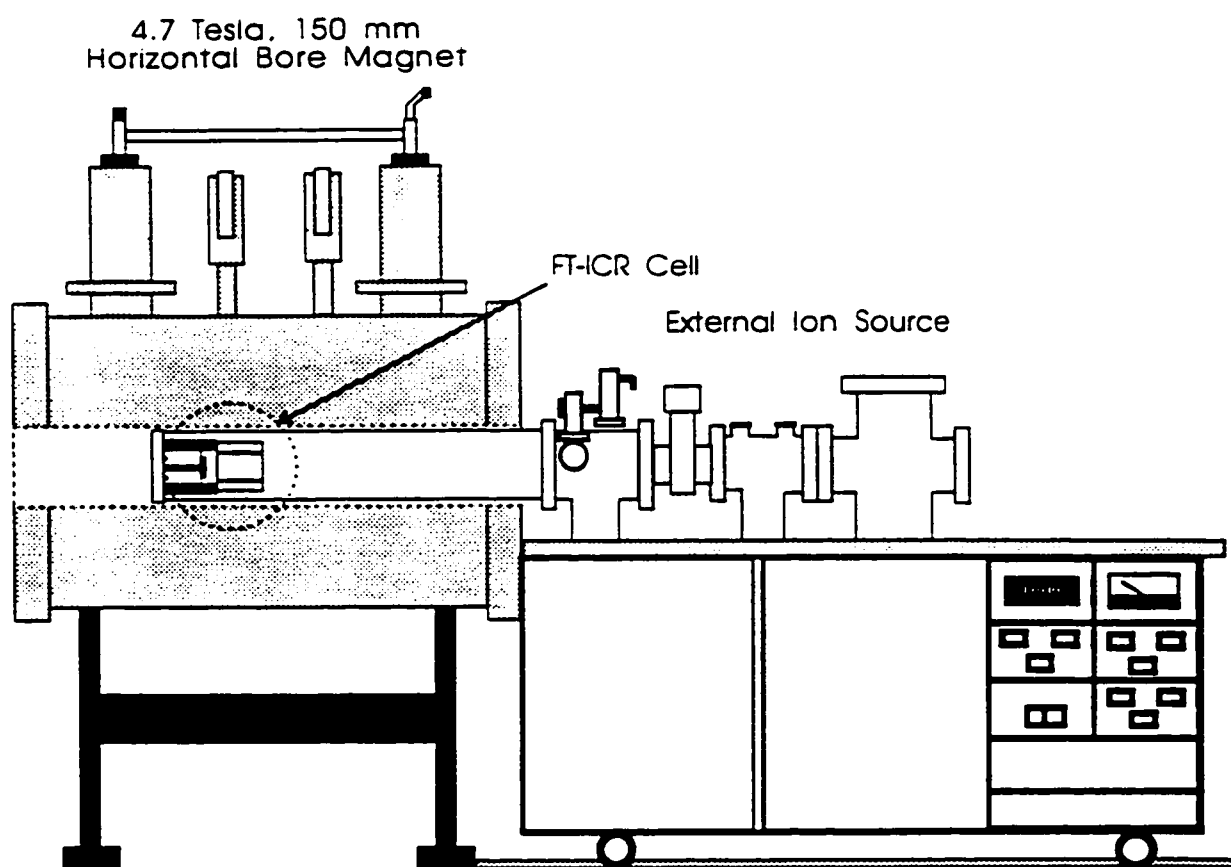


**Figure 6** Schematic diagram of FTICR spectrometer with external ion source.

cell and does not necessarily produce thermal ions. An additional problem with internal generation of ions in the Bruker spectrometer is the incompatibility with laser photodissociation experiments because the vacuum feedthrough for the rhenium filament must be replaced with a ZnSe window for the laser beam to enter the cell. Therefore, all of the ions (both positive and negative) studied here were generated in an external high pressure ion source built at the University of Waterloo. The source is similar to that found in a High Pressure Mass Spectrometer (HPMS). HPMS is a technique which was pioneered by Paul Kebarle<sup>7</sup> to study the thermochemistry of ion-molecule reactions. An excellent review of HPMS has been published by Kebarle.<sup>7</sup> The experiments presented in this thesis attempt to probe reaction kinetics and dynamics rather than ion thermochemistry, however, there is an important commonality between the two experiments. Both HPMS and the high pressure ion source on the Waterloo FT-ICR produce weakly bound cluster ions which have undergone  $\sim 10^5$  collisions with the excess bath gas before diffusing out of the ion source. The large number of collisions in the source allow the formation of bound ion-molecule complexes and cluster ions because termolecular collisions stabilize the association complex before it can re-dissociate to reactant ion and neutral. A consequence of the collisions with the bath gas is that ions leaving the source have a thermal internal energy distribution. Thus mating a high pressure source to the ultra-high vacuum (UHV) FT-ICR instrument, provides a unique experimental environment for the study of ion-molecule reaction kinetics and dynamics because ions with a thermal energy

distribution, produced in the high pressure source, can be trapped and then reacted or photodissociated under nearly collision free conditions. An additional benefit of using the high pressure source to produce the ions for the FT-ICR studies is that the thermochemistry of the ion can be determined on one of the HPMS instruments in our laboratory. This information complements, and is often essential to, the interpretation of the dynamical data obtained from the FT-ICR experiment. Figure 7 is a schematic diagram of the external high pressure ion source built at the University of Waterloo. A description of it has been given by Kofel and McMahon.<sup>2</sup> In an HPMS instrument, the ions are accelerated and focussed through a series of ion optics, then mass selected by either a magnetic sector or a quadrupole mass filter and finally detected. In the FT-ICR apparatus, the ions leave the acceleration region of the ion optics and then pass through a gate valve into a deceleration region and finally into the FT-ICR cell where they are trapped. The entire ion generation and transfer process is triggered by a TTL pulse which controls the length of the 2 kV electron beam pulse which enters the ion source through a 200  $\mu\text{m}$  electron microscope aperture. During the ionization pulse and post-ionization delay ( $\sim 0.2$  s), the ions are accelerated to 2 kV through the series of ion optics which provide spatial focussing. The ions are decelerated to  $< 2$  Volts prior to entering the FT-ICR cell. The strong magnetic field outside the FT-ICR cell, effectively contains the ions by inducing cyclotron motion during deceleration. In the absence of the magnetic field, ions could not be decelerated without significant radial dispersion which would negate the previous ion

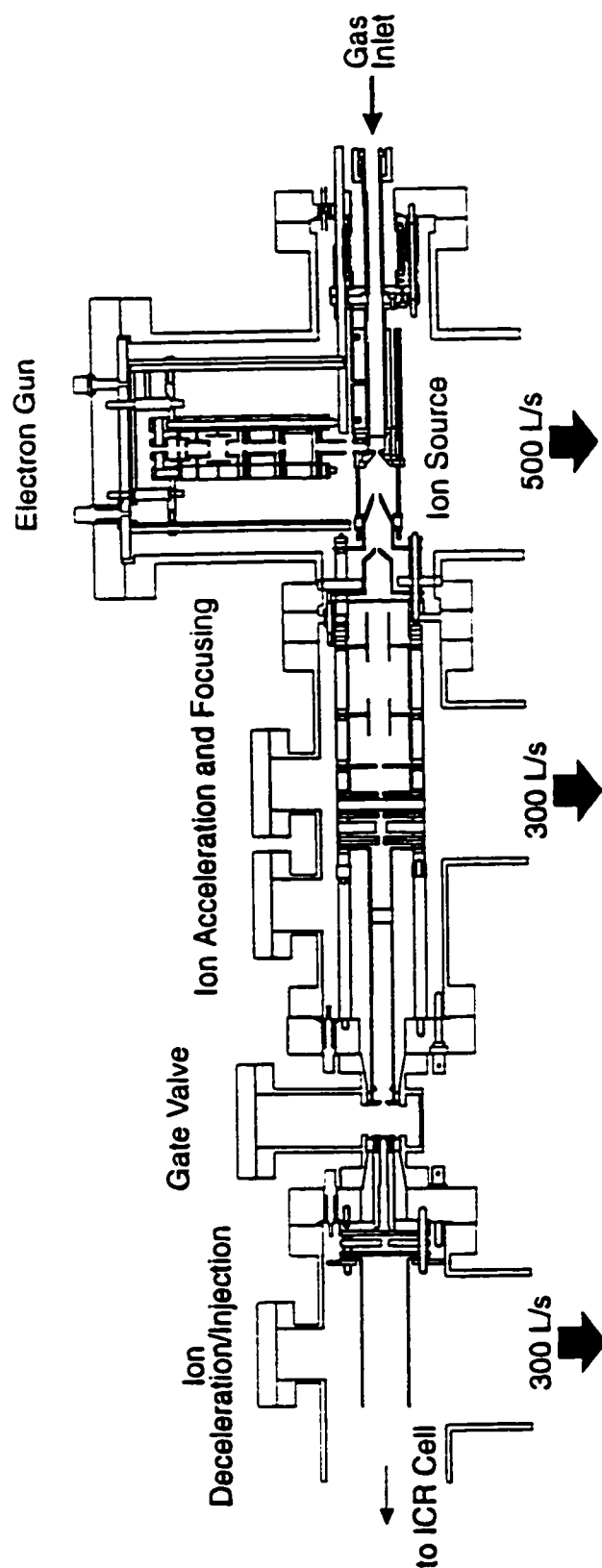


**Figure 7** Detailed schematic diagram of the external high pressure ion source.

focussing and result in very few ions reaching the cell. As the ions enter the cell they are deflected in the x direction by applying a potential across the two hemispherical halves of the 5.5 mm wide circular cell opening. This off-axis motion is necessary to induce cyclotron motion. The magnitude of the voltage across the deflector plates is variable from -16 to +16 V and is tuned to achieve maximum ion signal in the cell. Inside the cell, the ions are trapped in the z-direction by a repulsive potential of approximately 1-2 Volts on the end plates of the FT-ICR cell.

The positive ion clusters were formed by electron impact on methane. A series of well characterized reactions generate  $\text{CH}_5^+$  which subsequently transfers a proton to the neutral solvent molecule(s) to form protonated molecules, proton bound dimers or protonated cluster ions. Negative ions may be formed by resonant electron capture, dissociative electron capture, or ion-pair production. The negatively charged  $\text{S}_{\text{N}}2$  complexes were formed by association reactions of  $\text{Cl}^-$  onto alkyl halide neutrals. The chloride ions were produced by dissociative electron impact ionization of carbon tetrachloride. Termolecular collisions carry away energy and allow the  $\text{S}_{\text{N}}2$  complex to be stabilized in a potential well rather than having the reaction proceed directly to products. Detailed descriptions of the experimental ionization conditions precede the results of each individual experiment. The relevant reaction thermochemistry and potential energy surfaces are also provided in the results sections.

## 2.5 Ion Detection: ICR vs. Fourier Transform ICR Spectrometry

As discussed in Section 2.2, ion detection in an ICR spectrometer requires resonant excitation of the ion cyclotron motion. When the diameter of the circular motion becomes sufficiently large that the ions pass close to the detection plates, an oscillating image current on the order of 10 nA is induced in the plates. A conventional ICR excites trapped ions by scanning the frequency of the alternating electric field through the radio frequency region of approximately 2 kHz to 5 MHz, depending on the mass region of interest. When the applied rf frequency comes into resonance with the cyclotron frequency of an ion, that ion is accelerated and detected. The typical ICR spectrometer used either a marginal oscillator or capacitance bridge detector. Whether the observed signal arose from a change in capacitance across the detection plates or induced image current has been a topic of some debate.<sup>8</sup> Monitoring the intensity of the signal on the detection plates as a function of the rf excitation frequency, produces a frequency spectrum which is directly converted into a mass spectrum via equation (25). At low pressures, the ion motion persists long after the rf excitation ceases. This is an important consideration when scanning the rf excitation through the cyclotron frequencies of 2 closely spaced ions. If the motion of the first ion has not decayed prior to the excitation of the second ion, the two ions will not be resolved. This is because there is no frequency discrimination built into the detection. Hence, the resolution and sensitivity capabilities of traditional ICR spectrometers are limited by the rate of the rf sweep in addition to the physical factors



such as magnetic field strength, pressure, etc. Several early ICR cell configurations<sup>9</sup> were developed which make use of the ion drift which occurs in crossed electric and magnetic fields to improve resolution.

Fourier transform ICR differs from conventional ICR in that the electric field is rapidly swept through the entire frequency range (usually  $\sim 2$  kHz to 5 MHz) and then turned off. The coherent motion of the resulting ion packet, containing *all* ions whose  $m/z$  falls within the rf excitation bandwidth, induces an oscillating image current on the receiver plates. The observed time domain or "transient" signal results from the superposition of the individual waveforms from each  $m/z$  group of ions. If all of the ions had the same mass to charge ratio, the resultant signal would resemble a sine wave of frequency  $\omega_c$ . Collisions cause the ion radius to decay, therefore, the intensity of the transient appears "damped." The duration of the signal depends on the pressure in the FT-ICR cell as well as the tuning of the potentials on the FT-ICR cell plates. The uncertainty principle dictates that better resolution requires longer transients and therefore, optimum resolution is observed under UHV conditions. At pressures of  $\sim 10^{-9}$  torr, coherent ion motion can last for 1 s or longer after the rf excitation. Therefore, the signal can be sampled and digitized for up to 1 s provided the data collection system has sufficient capacity. Fast Fourier transform of the detected, time domain signal produces a frequency domain spectrum which is then converted to a mass spectrum using equation (25). Figure 8 illustrates the sequence of operations necessary to determine a mass spectrum with FT-ICR.

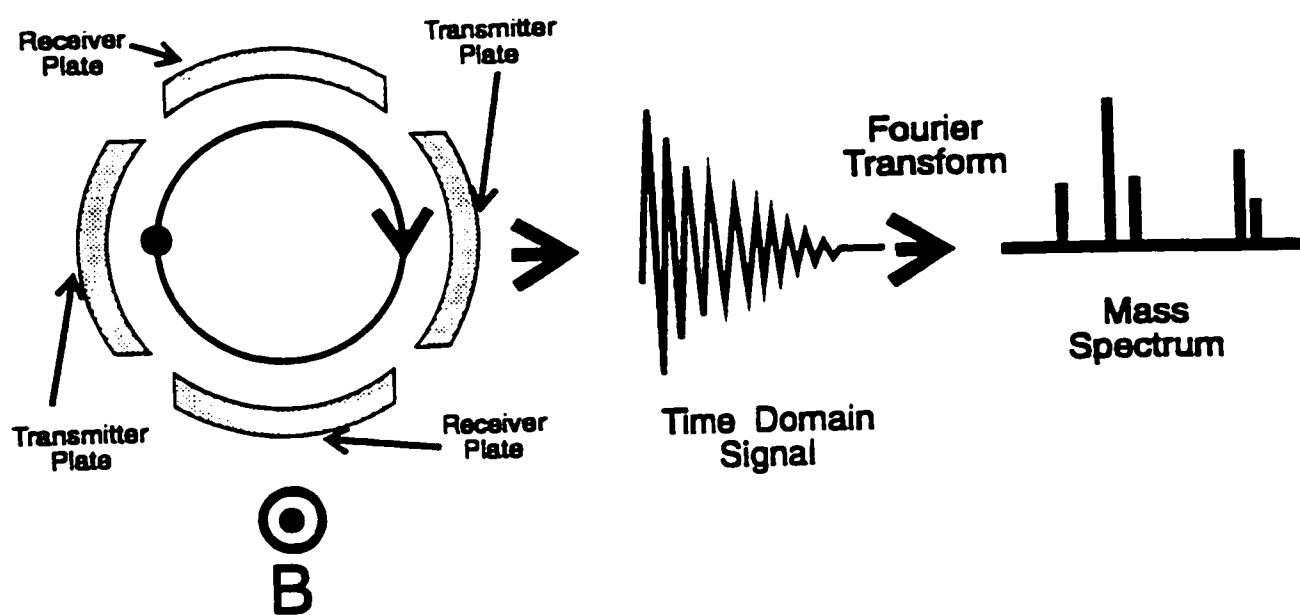


**Figure 8** The sequence of detection steps in FTICR spectrometry.

Sweeping the entire frequency range rapidly can be done in one of two ways. A rectangular rf pulse with period,  $T$ , in the time domain will produce a *sinc* function with a frequency bandwidth of  $\sim 1/T$ . Therefore, a very short pulse will have the broad frequency range desired, but since it is so brief, the corresponding intensity of the pulse needs to be greater to achieve the same excitation radius, as shown by equation (33). In their early work on FT-ICR, Comisarow and Marshall<sup>10</sup> realized that in order to sweep a wide frequency range of  $\sim 2$  MHz, using a short rectangular pulse, the length of the pulse would have to be  $\sim 10^{-7}$  s and the amplitude  $> 10^4$  V. Instead, they developed the "chirp" excitation which scans a frequency range of  $\sim 2$  MHz in a period of approximately 1 ms and, hence, requires an amplitude of about 1-100 V.<sup>11</sup>

Since FT-ICR detects all frequencies simultaneously, it benefits from the same multiplex advantages as other Fourier transform techniques. For a spectrum with  $n$  channels, the multiplexing instrument will take  $1/n$  of the time of a scanning spectrometer to achieve the same signal to noise (S/N) ratio in the spectrum. Alternately, a multiplexing instrument will have  $n^{1/2}$  better signal to noise than a scanning spectrometer. This is known as the Fellgett advantage.<sup>12</sup> Since unimolecular dissociation experiments can require delays of 5000 s or longer for each scan, this advantage in speed can be significant. Also, if  $M$  transients are collected and summed, the S/N ratio increases as  $M^{1/2}$ . One of the most important features of FT-ICR is its ultra-high resolution capabilities. A resolution of  $m/\Delta m > 10^8$  has been recorded for  $\text{H}_2\text{O}^+$  ion from 1 scan which was digitized for 51 s.<sup>13</sup> As mentioned

earlier, the longer the transient is sampled, the better the resolution *and* the sensitivity. This differs from sector mass spectrometers which experience a trade-off between decreased sensitivity and increased resolution as the slits are narrowed. According to Freiser,<sup>14</sup> the resolution of a FT-ICR spectrometer is given by equation (34) with the sampling time,  $t$  in seconds,  $B$  in tesla ( $10^4$  Gauss), and  $m$  in atomic mass units (amu).

$$R = \frac{m}{\delta m} = \frac{\omega}{\delta \omega} \leq 1.7 \times 10^7 \frac{z B t}{m} \quad (34)$$

Thus, the resolution increases with increasing magnetic field strength, sampling time and unit electronic charge ( $z$ ) but decreases with increasing mass. Despite this limitation, FT-ICR still produces the highest resolution mass spectra of very large multiply charged, biomolecules. However, for obtaining mass spectra of the very large, singly charged ions produced by matrix assisted laser desorption ionization (MALDI), time of flight (TOF) mass spectrometry is a better choice. Another interesting point is that, despite the instrumental similarities between ICR and NMR, only the former gains resolution by going to the Fourier transform experiment.<sup>14</sup>

An important feature of FT-ICR (and FT-NMR) is that the time domain signal can be mathematically apodized.<sup>15</sup> For transients which decay substantially during the sampling period, multiplication by an increasing or decreasing function will increase resolution (with poorer S/N) or improve signal to noise (at the expense of resolution) respectively. However, the greatest use of apodization in FT-ICR is to

narrow the baseline width and "ringing" of Lorentian peak shapes. This is accomplished by multiplying the transient by a Gaussian function prior to performing the fast Fourier transform (FFT).

As noted earlier, the resolution of FT-ICR is often limited by the memory capacity of the data system rather than by experimental apparatus. The Nyquist criterion dictates that the transient must be digitized at least twice as fast as the highest frequency in the signal. Since the low mass limit is 14 amu (5 MHz), a broad band chirp from 14- $\infty$  amu must be digitized at  $\geq 10$  MHz. If the transient persists for 1 s (easily attainable at pressures  $\leq 10^{-9}$  torr), 10 Mb of fast memory would be required. There are some methods to get around this limitation, such as "zero-filling" to make 128 k spectra from smaller data sets, but the most powerful tool for obtaining high resolution spectra from modern FT-ICR spectrometers is high resolution mode (also referred to as mixer mode or narrow band mode). This is a rf heterodyne experiment in which the transient is mixed with a reference frequency. In FT-ICR, the difference between the transient and the reference frequency is what is actually digitized. If the reference frequency is chosen to be close to the actual frequency, the resulting difference frequency is much less than the frequency of the original signal and therefore, the digitization rate and memory requirements are less. After digitization, the reference frequency is re-added to the signal. This is analogous to an optical heterodyne experiment in which the frequency of the light source is measured by mixing it with a stable frequency reference laser and detecting the microwave signal produced from

the difference in the optical frequencies. In FT-ICR, the mixer mode technique is capable of producing spectra with extremely high resolution but the mass range is greatly reduced (approximately 1-5 amu) compared to broad band experiments.

## **2.6 Radio Frequency Isolation (Ion Ejection)**

Radio frequency ejection is often used to isolate one or more ionic species from the distribution produced during ionization. "Shots" and "sweeps" are the two basic methods for performing rf ejection, with pulse and frequency shaping variations of both being available. Both methods use frequency specific rf excitation to accelerate unwanted ions to a radius larger than that of the FT-ICR cell. The ions, therefore, strike the walls and are neutralized. Ejection "shots" consist of a sequence of narrow bandwidth, rf pulses of approximately 1-3 ms in duration. Each pulse has a frequency resonant with a single  $m/z$  group, hence, a list of the ions to be ejected must be compiled from the mass spectrum. The pulse length and attenuator setting (controlling rf amplitude) are user-defined variables in the Bruker software and are optimized for each individual experiment. Ejection "sweeps" are similar to the chirped, broad band rf excitation, discussed in Section 2.5, except that a "notch" is cut into the frequency distribution around the desired ion. The spectral width of this frequency notch is a variable parameter in the Bruker software and is called the "Ejection Safety Belt." As with shots, the amplitude and length of the sweep ejection event are user-controlled.

Sweep ejection is simpler to implement than shots because only the mass of the ion to be isolated has to be input rather than all of the other masses. Ideally, even very congested spectra coming out of the ion source can be reduced to only one ion of interest without having to use a list of >100 shots at the masses of the individual ions. The drawback of using sweep ejection is that there is a trade-off between clean isolation with a narrow safety belt and translational excitation (and possible fragmentation) of the ion to be isolated. To minimize this, the Bruker software inverts the phase of the rf on either side of the ejection window. Thus, any translational excitation from nearby frequencies to the "red" of the ion should be cancelled by the phase inverted frequencies to the "blue." Even with this technique there may still be some kinetic energy imparted to the ion. Therefore, ejection shots are used for experiments which are sensitive to the ion kinetic energy, or whenever the number of species to be ejected (and hence the number of shot frequencies to be input) is manageably small. There are "correlated" versions of both the shot and sweep ejections which tailor the excitation rf so that the frequency of the ion to be isolated corresponds to a node in the excitation waveform. This technique is particularly useful for attempting to isolate one ion from a nearby neighbour. Correlated ejections were not used in these experiments because the ions studied were usually only close to their isotopic analogues. It was more reliable to simply normalize all of the isotopes when calculating rates. An additional reason is that a preliminary evaluation of the correlated shots technique revealed *more* fragmentation of the ion to be isolated. Thus

more translational excitation was occurring than with traditional shot ejection. A thorough study of the capabilities of the correlated ejections could improve their utility.

## **2.7 Experimental Timing (FT-ICR Pulse Sequence)**

The basic FT-ICR experiment is performed using a series of digital pulses and delays to control the timing. Figure 9 illustrates the FT-ICR pulse sequence used in the determination of unimolecular dissociation kinetics. The initial step is the quench pulse in which residual ions are repelled from the cell by a potential difference applied across the trapping plates for 7 ms. A quench delay of approximately 0.1 s follows to allow the ions to leave the cell. The next step is ion formation. For all of the experiments performed in this thesis, the ions are generated in the high pressure external ion source discussed in section 2.4. The length of the digital pulse controls the length of the 2 kV electron beam pulse which enters the ion source through the electron microscope aperture. During the ionization pulse (4-10 ms) and post-ionization delay ( $\sim 0.2$  s), the ions are accelerated to 2 kV through a series of ion optics and then decelerated to  $< 2$  Volts and trapped in the FT-ICR cell. Radio frequency ejection is used to isolate 1 or more desired ions from the equilibrium distribution coming out of the high pressure source. Combinations and permutations of the shot and sweep excitation methods (or the analogous correlated ejections) may be used. Following isolation, a relaxation delay is introduced to allow the ions to



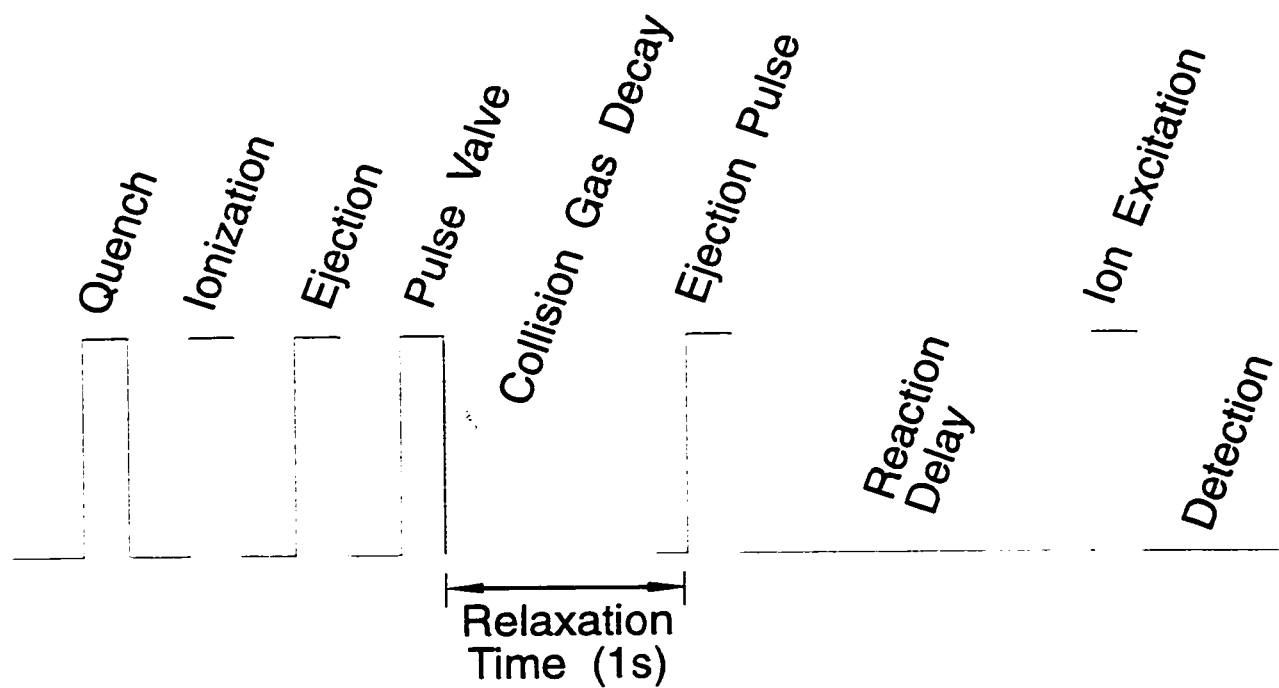
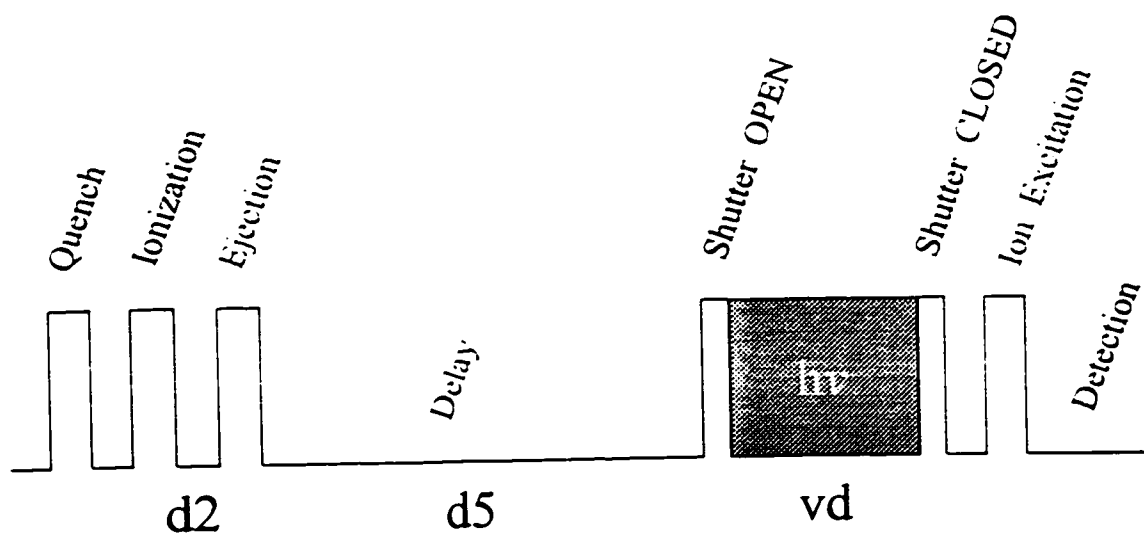


**Figure 9** Pulse sequence for unimolecular dissociation experiments.

undergo collisions with a neutral background gas to relax them translationally and/or to regain a thermal internal energy distribution by allowing any "hot" ions to dissociate. A second ejection removes ion fragments formed during the relaxation delay. The ions present in the FT-ICR at this time are mass selected and can be represented by a thermal energy distribution. A variable reaction delay of approximately 1 to 500 s then occurs, during which the extent of unimolecular dissociation is determined. Finally, an ion excitation chirp is applied and the induced image current is detected. If reaction kinetics are desired, the experiment is repeated using a series of reaction delays such as {0.001, 1,2,4,6,8,10,20,50,80,100 s}. Monitoring the ion intensities as a function of reaction time produces a kinetic plot for the dissociation of the parent ion, from which the dissociation rate constant(s) may be obtained. (see chapter 3)

The pulse sequence for the low power infrared multi-photon dissociation (IRMPD) experiments is essentially the same as for the unimolecular dissociation experiments except that a CO<sub>2</sub> laser beam is used to irradiate the ions instead of the ambient black body radiation. The length of the irradiation period is still variable as with the unimolecular experiments. The actual irradiation period is controlled by two separate digital outputs from the Bruker Aspect 3000 computer to the logic electronics controlling the bi-stable shutter. One positive going pulse opens the shutter and after a variable delay, another closes the shutter. Figure 10 shows schematically the pulse sequence for IRMPD of ions in the FT-ICR. The photodissociation experiments are

a) Single Laser Irradiation Stage; MS/MS Experiment:



b) 2 Laser Irradiation Stages; MS<sup>3</sup> Experiment:

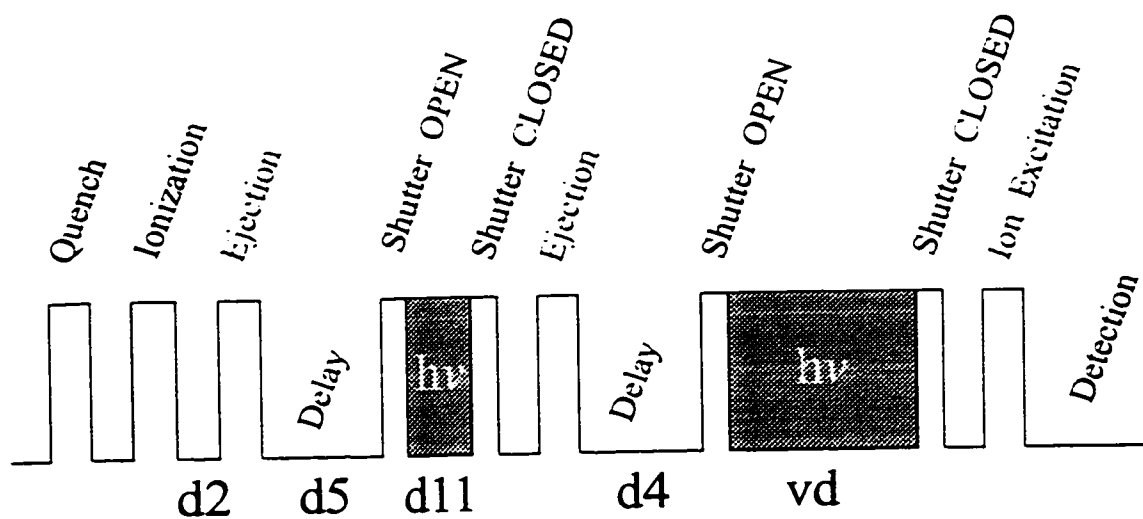


**Figure 10** Pulse sequence for laser induced dissociation experiments.

usually performed with a fixed series of reaction delay times and the extent of dissociation monitored for each time with the laser on and off. Subtraction of the "ON" minus "OFF" signals can be performed. This description of pulse sequences is intended as a general overview since each experiment requires an individual scheme. For example, the MS<sup>n</sup> experiments described in Chapter 4, may require up to four separate stages of laser irradiation, all of different length. The specific pulse sequence for each experiment is described in the "Experimental" sections of Chapters 3-5.

## **2.8 Continuous Wave Infrared CO<sub>2</sub> Laser and Bi-Stable Shutter**

As a complement to the study of unimolecular dissociation caused by black body radiation, the dissociation produced by a low power infrared laser was also studied. The complete apparatus for the IRMPD experiments is illustrated schematically in Figure 11. All IRMPD experiments were done with a SYNRAD Inc. 48-0-15W, CO<sub>2</sub> laser operating CW in TEM<sub>00</sub> modes with frequency at or near 10.6  $\mu\text{m}$  (10.55 to 10.65  $\mu\text{m}$ ).<sup>16</sup> Output power can be controlled up to a maximum of 10 W by changing the duty cycle from 5 to 98%. For most experiments, the duty cycle was fixed at approximately 40% so that the output laser power was 3.9 W. Further attenuation of laser power was accomplished by passing the beam through a static pressure (~1-10 torr) of ethylene gas contained in an attenuation cell equipped with AR coated zinc selenide windows (>99% transmission at 10.6  $\mu\text{m}$ ). The beam continues through a Newport 846HP bi-stable shutter with a 5.6 mm aperture. The shutter blade

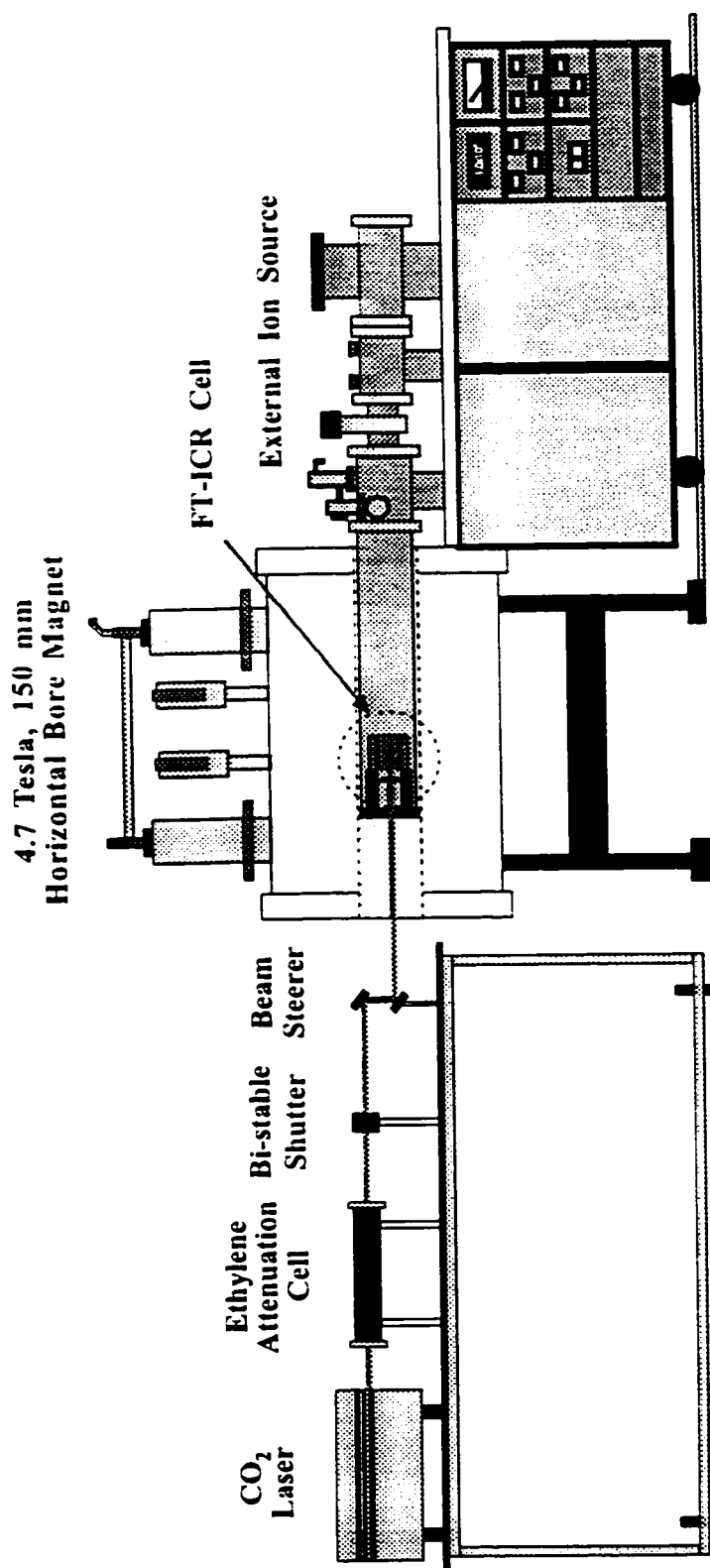


**Figure 11** Apparatus for IRMPD experiments in a FTICR spectrometer.

is capable of blocking a maximum incident beam power of 5 W without being consumed. Positioning of the beam in the FTICR cell is accomplished with a Newport beam steerer using coated, first surface aluminum mirrors. Finally, the laser beam enters the rear of the FTICR cell through a 3x25.4 mm AR coated ZnSe window (> 99% transmission at 10.6  $\mu\text{m}$ ) and passes through 5.6 mm restrictions at both the front and rear of the cell before being dissipated in the ion optics of the external source.

The laser beam profile at<sup>17</sup> the FT-ICR cell was determined by translating a 1 mm diameter aperture across the beam and measuring the transmitted power. The aperture was mounted on a two dimensional translation stage and an origin was defined as the position of maximum power transmission. The recorded power was plotted in Figure 12 as a function of horizontal aperture displacement from the origin. The resultant data was fit to a Gaussian beam profile and a full width half maximum (FWHM) diameter of 0.66 cm was obtained from the fit. During these measurements the two most sensitive ranges of the power meter were used. It was difficult to obtain a consistent zero and no absolute reference calibration was attempted. Thus, the small values of transmitted laser power recorded for the beam profile measurements may have a significant systematic error. The limited range of the translation stage prevented the position of zero laser intensity from being recorded. Thus, the Gaussian profile was fit to the data points in Figure 12 assuming that the absolute value of measured laser power at the maximum was correct. Since there may be significant error in the absolute readings and, since the FWHM value determined from the fit is

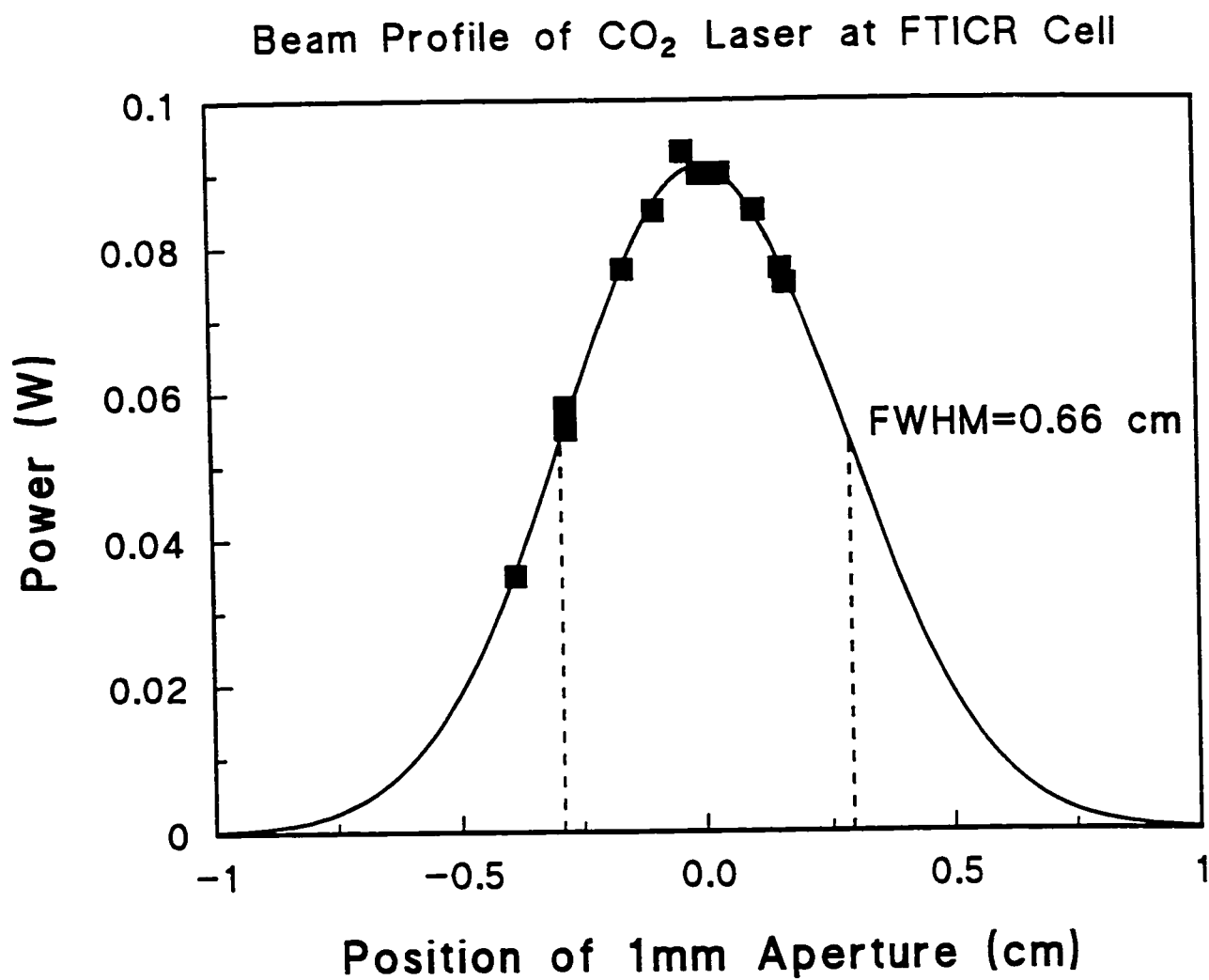


**Figure 12** Experimentally determined laser beam profile with Gaussian fit.

sensitive to absolute measurements, some error is expected in the FWHM beam diameter value. This would be a concern if absolute absorption cross sections were being reported but not for determining relative intensity effects since the beam diameter will be a constant. It should be noted that the laser intensity calculated using the FWHM beam radius will differ slightly from an intensity value determined using the definition of beam waist (the radial distance at which the electric field amplitude has decreased by  $1/e$ ).<sup>18</sup> Laser power was measured directly behind the bi-stable shutter with a Coherent 210 power meter. The laser power at the FTICR cell was calculated by multiplying the power measured behind the shutter by a correction factor of 0.87. This factor was used to correct the measured laser power for atmospheric absorptions and losses from the optics. The overall infrared laser intensity was determined by dividing the corrected laser power at the cell by the beam area (FWHM). For example, a laser power of 3.9 W (behind the shutter) translates into an intensity of  $10 \text{ W/cm}^2$ . It should be noted that the power cannot be measured during the photodissociation event. Power readings are taken before and after the photolysis spectra are collected. Every attempt to stabilize the laser power before the experiment is made and any experiments for which the post-experiment reading is substantially different than the initial power is discarded. Nevertheless, there can be a substantial drift in the output laser power which is thought to be the limiting factor in the reproducibility of the individual data points. Five to ten replicate photodissociation yields were collected to determine the relative error of each data point. The relative



error fluctuated from  $\pm 2\%$  to  $\pm 5\%$  of the raw value on a day to day basis. These values were used to assign the error bars on the graphs.

The optical shutter was coupled to the Bruker data collection system via home-built electronics such that a TTL pulse from one auxiliary output would open the shutter which remains in this position until a TTL pulse from a second auxiliary output closes the shutter. Using this design, the shutter could be opened at any point in the experimental sequence and left open for any duration longer than 100 ms which was the minimum reliable opening time determined by the shutter control logic and the power supply rise time. Accurate time response was confirmed by passing a helium-neon (HeNe) laser beam through the shutter aperture and observing the signal produced by a fast optical detector using a pre-amplifier and an oscilloscope. By adding additional isolation and irradiation events with the appropriate delays to the software, multiple stage photodissociation experiments were accomplished.

## 2.9 References

1. M. Alleman, H. Kellerhalls and K-P Wanczek, *Int. J. Mass Spectrom. Ion Phys.*, **46** (1983) 139.
2. P. Kofel and T.B. McMahon, *Int. J. Mass Spectrom. Ion Proc.*, **98** (1990) 1.
3. See any text on E&M. for instance: A.F. Kip, *Fundamentals of Electricity and Magnetism*, 2<sup>nd</sup> Ed., McGraw-Hill (1969) 507.
4. Kemper, P. R. and Bowers, M. T. *Techniques for the Study of Ion-Molecule Reactions*, Chpt. I, W. Saunders and J.M. Farrar (Eds.), Wiley Interscience, New York, (1988) 9, 15.
5. Comisarow, M. B. *J. Chem. Phys.* **1971**, 55, 205.
6. Dunbar, R. C. *J. Chem. Phys.* **1971**, 54, 711.
7. P. Kebarle, *Techniques for the Study of Ion-Molecule Reactions*, Chpt. V, W. Saunders and J.M. Farrar (Eds.), Wiley Interscience, New York, (1988) 221.
8. Wronka, J. *Private communication*.
9. a) McMahon, T. B. and Beauchamp, J. L. *Rev. Sci. Instrum.* **1972**, 43, 509. b) McIver, R. T. *Rev. Sci. Instrum.* **1970**, 41, 555.
10. Comisarow, M. B. and Marshall, A. G. *Chem. Phys. Lett.* **1974**, 25, 282.
11. Comisarow, M. B. and Marshall, A. G. *Chem. Phys. Lett.* **1974**, 26, 489.
12. A.G. Marshall, *Fourier, Hadamard and Hilbert Transforms in Chemistry*, Plenum Press (1982).
13. Alleman, M.; Kellerhals, Hp. and Wanczek, C.-P. *Int. J. Mass Spectrom. Ion Phys.* **1983**, 56, 2744.
14. Freiser, B. S. *Techniques for the Study of Ion-Molecule Reactions*, Chpt. II, W. Saunders and J.M. Farrar (Eds.), Wiley Interscience, New York, **1988**.
15. a) Marshall, A. G. *Acc. Chem. Res.* **1985**, 18, 316. b) Lee J. P. and Comisarow, M. B. *Appl. Spectrosc.* **1987**, 41, 93.
16. SYNRAD Inc. *Infrared Gas Lasers Instruction Manual*.
17. Note: The physical dimensions of the FT-ICR cell and its location inside the bore of the superconducting magnet prevent the power meter from being located inside the cell for these measurements. Therefore, the beam profile and power correction were obtained by

re-directing the laser beam away from the cell (with a gold coated first surface mirror,  $\geq 99\%$  reflective) and placing the power meter such that the original path length of the beam was conserved.

18. Svelto, O.; *Principles of Lasers* 3<sup>rd</sup> Ed., 1989, Plenum Press, New York, p.178.

### 3. INFRARED LASER PHOTODISSOCIATION OF CLUSTER IONS IN A FT-ICR SPECTROMETER

*"If a guy tells me the probability of failure is 1 in  $10^5$ ,  
I know he's full of crap.*

Richard P. Feynman

#### 3.1 Introduction

Since Isenor<sup>1,2</sup> first demonstrated that high power, CO<sub>2</sub> laser pulses could induce infrared multiphoton dissociation (IRMPD) of molecules in 1971, many researchers have reported both experimental measurements and theoretical attempts to explain the photophysics of this phenomenon. The potential uses of IRMPD included mode selective and isotope selective photofragmentation and much of the research effort in this area during the 1970's and early 1980's was driven by these goals. Mode selective IRMPD was shown to be untenable because of the complete randomization of excitation energy throughout the vibrational modes of the molecule prior to decomposition.<sup>3</sup> Conversely, isotopically selective IRMPD was shown to be quite facile.<sup>4,5,6,7</sup> Substantial effort was devoted to fundamental studies of IRMPD but the ultimate motivation was to selectively enhance uranium isotopes by photofragmentation of UF<sub>6</sub>. The practical use of this technique, was limited by the large energy deposition which often produced multiple fragmentation pathways and, in some cases, secondary photodissociation of the highly excited products of the initial

decomposition reaction.<sup>3</sup> The efficient separation of isotopes from multiple products can be problematic. For these reasons, the technique of resonance enhanced multiphoton ionization (REMPI) of pure uranium vapour was adopted for industrial isotope enhancement and some of the interest in IRMPD waned. During the same period that the pulsed laser IRMPD studies of neutral molecules was occurring, Beauchamp *et al.* demonstrated for the first time that IRMPD could be accomplished with a relatively low intensity ( $<10 \text{ W cm}^{-2}$ ), continuous wave (CW),  $\text{CO}_2$  laser.<sup>8,9</sup> These experiments were aided by the capability of the ion cyclotron resonance (ICR) spectrometer to trap ions for a period of time ranging from seconds to minutes at pressures as low as  $10^{-8}$  torr. These unique experimental conditions allowed ion irradiation for periods of several seconds with only a small number of collisions occurring during that time. The laser fluence obtained from a low intensity CW laser over a period of 1 s, is the same as that of a nanosecond laser pulse  $\sim 10^9$  times more intense. At approximately the same time, Brauman and co-workers were performing IRMPD studies of ions in an ICR spectrometer using pulsed  $\text{CO}_2$  lasers, and produced a comparative investigation of CW vs. pulsed laser photodissociation of the  $[(\text{C}_2\text{H}_5)_2\text{O}]_2\text{H}^+$  ion using both their data and Beauchamp's.<sup>10</sup>

Since these pioneering experiments, substantial effort has been devoted to the study of infrared multiphoton dissociation of ions trapped in an ICR spectrometer using both pulsed and continuous wave (cw) lasers.<sup>11</sup> A significant amount of information regarding the structure of the precursor ion and the bond energies of the dissociation

pathway(s) can be obtained from these studies. A renewed interest in infrared photodissociation of ions in a FT-ICR spectrometer has arisen because of the application of the technique to the analysis of biologically significant molecules. The combination of the "soft" fragmentation produced by CW IRMPD and the high mass resolution capabilities of modern FT-ICR spectrometers is ideally suited to the study of large, multiply protonated ions produced from an electrospray ion source (ESI). This technique has received even more attention since the ability of IRMPD/FT-ICR to directly sequence DNA and large protein molecules was demonstrated.<sup>12,13</sup> A novel extension of the IRMPD experiment has been developed for the purpose of performing multiple mass spectrometry ( $MS^n$ ) in a FT-ICR spectrometer.<sup>14</sup> This experiment is presented in Chapter 4. When applied to ions generated by ESI, this method should simplify the structural interpretation of these large complex ions and promises to improve the capabilities of IRMPD/FT-ICR even further.

In this chapter, the Waterloo FT-ICR with its external high pressure ion source was used to investigate the IRMPD of proton bound dimer ions using a continuous wave, fixed frequency  $CO_2$  laser of relatively low power. The FT-ICR instrument and the methodology used in these experiments was similar to that used to show for the first time that ambient black body radiation could, in fact, cause dissociation of isolated cluster ions<sup>15,16,17</sup>. Both experiments expose the ions to a continuous infrared radiation source for a variable duration of time. The difference is that the IRMPD experiment uses monochromatic infrared laser radiation instead of the broad

distribution of infrared frequencies which are produced from a black body emitter. It should be noted that the laser radiation used for IRMPD experiments does not replace the black body infrared radiation, but is usually much more intense at ambient temperatures. For ions with a weak absorption cross section at the laser wavelength, or experiments at high temperatures, the black body dissociation rate may be comparable to the IRMPD rate. In these cases, background subtraction must be performed to separate the laser and black body contributions.

Both IRMPD<sup>12</sup> and black body<sup>18</sup> induced dissociation of the ions derived from large bio-polymers are being actively investigated in many laboratories. Both techniques provide a very "soft" method (*i.e.* one that favours the lowest energy pathway) for fragmenting ions in tandem mass spectrometry (MS<sup>2</sup>) experiments. This method is useful for determining ion structure but, to determine bond energies, theoretical modelling is needed which may or may not be reliable for ions of this size. A comparative study of the two methods, on systems where the thermochemistry was known or could be determined by PHPMS in our laboratory, was desired. The IRMPD experiments presented in this chapter were initially undertaken with this goal in mind. The first evidence of black body induced dissociation was obtained at the University of Waterloo on cluster ions. Dunbar's master equation modelling of the black body dissociation process<sup>19,20</sup> was a key piece of evidence in establishing that the radiation mechanism of unimolecular reactions was viable. Dunbar had experience with both the theory and experiments of laser photodissociation of molecular ions in

a FT-ICR spectrometer. He was, in fact, the first person to observe photodissociation of an ion in an ICR instrument.<sup>21</sup> Black body dissociation was shown to be a thermal unimolecular process characterized by first order kinetics and a Boltzmann distribution of internal energies. A unimolecular, or "first order", reaction is characterized by the following rate equation:

$$\frac{d[A]}{dt} = -k_{uni} [A] \quad (35)$$

First order refers to the fact that the reaction rate depends only on the concentration of the parent species, A. The integrated form of the rate equation is:

$$[A]_t = [A]_0 e^{-k_{uni} t} \quad (36)$$

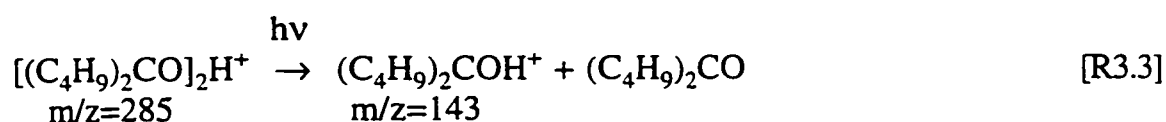
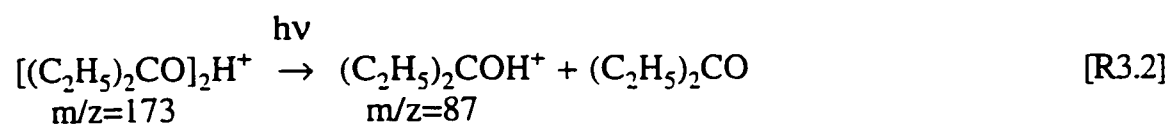
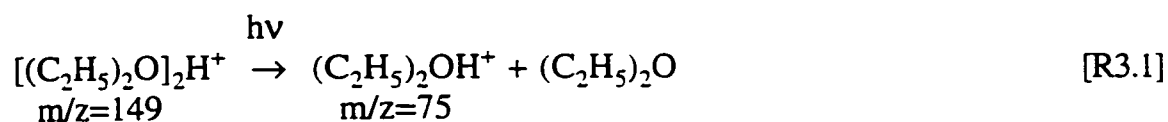
In several publications,<sup>22,23,24</sup> Dunbar states that irradiation of large ions with a relatively low intensity CW infrared laser can be treated as thermal activation and is, therefore, equivalent to irradiation with a black body source. The basis for this statement is that large ions have many absorption modes in the infrared and that the coupling of all modes *via* intramolecular vibrational energy redistribution (IVR) is rapid compared to the rate of dissociation. Such processes should then be expected to yield first order dissociation kinetics as were observed for the black body experiments. Some preliminary examples of photodissociation of the weakly bound



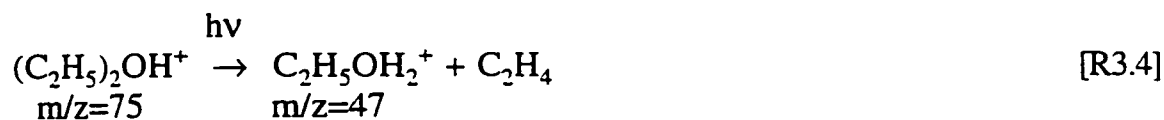
cluster ion  $\text{H}_3\text{O}^+(\text{H}_2\text{O})_3$  indicated what appeared to be approximately first order kinetics.<sup>15</sup>

It was important to verify first order kinetics for all IRMPD experiments. A photodissociation yield at a single time can then be extrapolated to determine a rate constant. First order kinetics may also signify the existence of a thermal population of ions which could be assigned an effective temperature, dependent upon laser power. Thus the IRMPD process could then be treated as a thermal unimolecular reaction and perhaps bond thermochemistry could be obtained for ions which were too strongly bound to dissociate at the temperatures accessible in a normal FT-ICR instrument. A thermal model of IRMPD has the advantage that it does not require knowledge of all of the state-to-state transition probabilities which are required for using a master equation approach such as Quack's.<sup>25</sup> The proton bound dimer ion of diethyl ether was chosen as a good IRMPD test-case because of the litany of work on this system by Beauchamp *et al.*<sup>26,27</sup> It was also being investigated as part of a concurrent study of black body dissociation and thermochemistry of proton bound ether and ketone ions occurring in this laboratory by Hoffman.<sup>28</sup> The proton bound dimers of 3-pentanone and 5-nonanone were subsequently studied because they had similar bond dissociation enthalpies to the diethyl ether dimer and, therefore, the effect of ion size on the reaction kinetics could be examined. The experimental results show that all three dimer ions undergo loss of a neutral ligand molecule as the exclusive photodissociation reaction channel. The dissociation reactions for the proton-bound

dimer ions of diethyl ether, 3-pentanone and 5-nonanone are summarized in reactions R1-R3 respectively.



There is also a secondary dissociation of the protonated diethyl ether ion produced from reaction R1. This reaction was found to proceed exclusively by ethylene elimination (reaction R4) and the kinetics of this reaction were also studied.



In contrast to the thermal picture of IRMPD proposed by Dunbar, the photodissociation

kinetics, of all of the ions studied here deviate markedly from the expected single exponential decay as shown in Figure 13. Perhaps this should not have been so surprising since Quack<sup>25</sup> states: "Comparison with thermal unimolecular reactions shows that collisionless unimolecular reactions induced by monochromatic infrared radiation (URIMIR) are quite different in all respects." The results presented in this chapter attempt to elucidate the physical factors responsible for the non-first order kinetics observed at low pressures. Section 3.1.1 addresses the concern of whether the kinetic deviations are the result of some experimental or chemical imperfections in the method. Examples of these would be incomplete overlap of the laser beam with the ion packet and isomeric contamination of the ions, respectively. If the non-first order behaviour cannot be attributed to experimental artefacts, then the alternative is to look for explanations in the microscopic properties of isolated ions in a monochromatic radiation field. In the remainder of this introduction, models of IRMPD and the possible causes of non-first order kinetics are discussed.

Experiments were performed in which parameters, such as temperature, laser intensity and pressure were varied in an attempt to determine the mechanism responsible for the observed non-first order behaviour. The results are presented in section 3.3 of this chapter. It is hoped that the knowledge gained from the study of large, polyatomic ion photodissociation reactions will increase our understanding of IRMPD in general and the ability to model such processes.

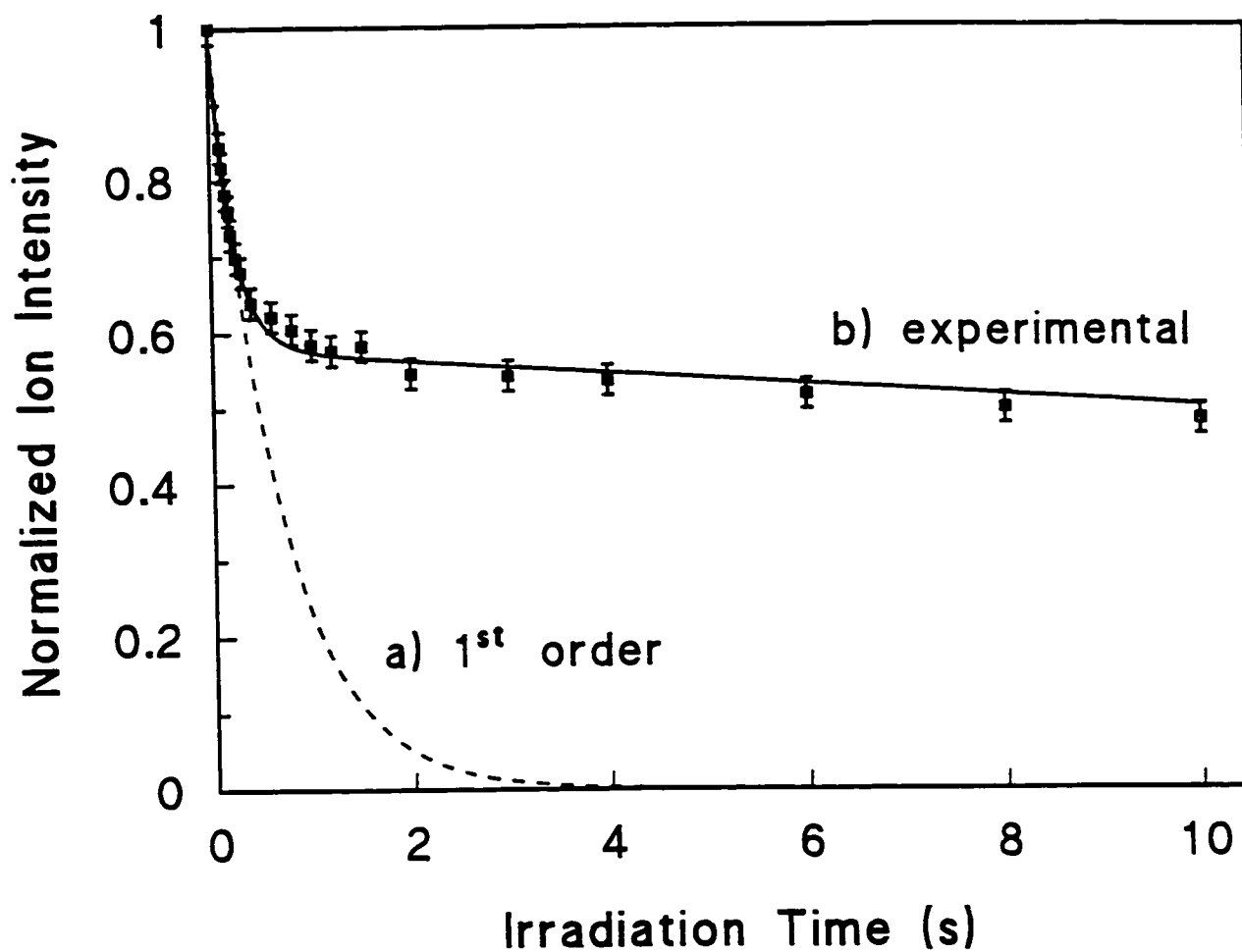


**Figure 13** A plot of  $[(\text{CH}_3\text{CH}_2)_2\text{O}]_2\text{H}^+$  ion intensity vs. time at  $20^\circ\text{C}$ ,  $2.4 \times 10^{-9}$  mbar,  $I=9.7 \text{ W cm}^{-2}$ . Line a) is a 1st order fit, line b) was fit to equation 41.

### 3.1.1 Non-first Order Behaviour; Models and Kinetics

The experimentally observed dissociation curve in Figure 13 begins to deviate from first order at irradiation times greater than approximately 0.5 s. There are two possible ways in which this behavior could be caused by an incomplete overlap of the laser beam with the ions. If a fraction of the ions is initially trapped with a cyclotron radius larger than the radius of the laser beam or if some of the ions are gradually increasing their radius, the behavior in Figure 13 could be observed. Thus, two experimental questions need to be answered: 1) are *ALL* of the ions being irradiated; 2) are they being irradiated for the *ENTIRE* duration of the experiment? The difference between the two scenarios should be evident in the long time behavior of the kinetics curve. If a fraction of the ions were never irradiated because their trajectories in the FT-ICR cell keep them outside the cross sectional area of the laser beam, the resulting kinetics plot would be expected to appear first order initially and then reach a flat plateau. The data in Figure 13 does not plateau but, instead has a small but non-zero slope at long times. The scatter on the points is significant, therefore, the observation of a slope is not, by itself, sufficient evidence of incomplete ion irradiation. The equations of FT-ICR ion motion are well characterized (see Chapter 2). Therefore, the magnitude of the ion cyclotron radius can be calculated and compared to the laser radius. The laser beam profile was determined to be approximately Gaussian with FWHM diameter equal to 6.6 mm at the FT-ICR cell. The procedure for measuring the beam diameter and profile has been described in

section 2.8. The effective cross sectional area (C.S.A.) of the laser beam within the ICR cell is less than the FWHM beam C.S.A., reported in section 2.8, because the laser entrance hole in the rear trapping plate is only 5.6 mm in diameter. Therefore, the ion packet will be fully irradiated provided the ion cyclotron radius does not exceed 2.8 mm. The diameter of the ion cyclotron motion may be calculated from equation 24 in chapter 2. For ions with thermal translational energy at 300 K (0.04 eV), the cyclotron radius of an ion with a  $m/z$  ratio of 150 is 0.1mm. The ions must possess between 1 and 2 eV of forward kinetic energy in order to overcome the potential on the entrance trapping plate and still be stopped by the rear trapping plate. The repulsive potential well causes the ions to execute a slow oscillatory motion along the  $z$ -axis until this forward kinetic energy is damped by collisions. This velocity is perpendicular to the cyclotron motion and, therefore, does not affect the cyclotron radius. In order to induce cyclotron motion of the ions coming into the cell directly on axis with the magnetic field, a deflection voltage,  $V_{DEV2}$ , is applied across the pair of hemispherical plates that form the ion entrance hole. This potential difference is adjusted to obtain maximum signal but has a maximum value of 16 V ( $\pm 8$  V) across the 5.6 mm diameter opening. Ions passing through the centre of the opening are given a maximum translational energy ( $K_{xy}$ ) of 8 eV. The radius calculated for ions with  $m/z=150$  in a 4.7 T magnetic field, possessing 8.0 eV translational energy is 1.06 mm ( $r=1.5$  mm for  $m/z=300$ ). Ions which just graze the deflector plates could approach  $K_{xy}=16$  eV. The cyclotron radius of a  $m/z=150$  ion with such a trajectory

is  $r=1.5$  mm ( $r=2.1$  mm for  $m/z=300$ ). These values serve as absolute maxima for the cyclotron radii and are still within the maximum allowable radius for full ion illumination by the laser. It should be noted that the actual kinetic energies of the ions must be much lower. Hop *et al.* showed that the centre of mass (COM) threshold for collision induced dissociation (CID) for the proton bound dimer ion of diethyl ether was approximately 1.2 eV.<sup>29</sup> Since no fragmentation in the presence of argon collision gas was observed in these experiments, the translational energy of the ions in the laboratory frame must be less than 6 eV. The actual ion trajectory results from a combination of cyclotron and magnetron motion which is more difficult to estimate. Gäumann<sup>30</sup> *et al.* have previously measured the ion volume as approximately 1 mm<sup>3</sup> in a similar FT-ICR spectrometer. Therefore, the observed kinetic deviations are, almost certainly, not caused by incomplete overlap of the laser beam with the ions. This assertion is further supported by the observation of nearly complete, albeit slow, dissociation of  $(\text{CH}_3\text{CH}_2)_2\text{OH}^+$ .

If the kinetic behavior observed in Figure 13 is due to the ions gradually moving away from the centre of the cell, then most of the ions would have to have acquired radii larger than 2.8 mm within 1 s of the onset of the laser irradiation period. The most likely cause of this effect would be collisions increasing the radius of the magnetron motion of the ions. The fraction of ions which have moved outside a given radius will depend only upon the length of time between ionization and detection events, *NOT* on the irradiation time. Since the start of the irradiation event is

controlled by the shutter, it is simple to collect photodissociation kinetics for two experiments which have significantly different pre-irradiation delays. If the kinetic behavior appears similar for the two experiments, then the gradual motion of the ions due to increasing magnetron motion can be ruled out. The photodissociation kinetics of  $[(\text{CH}_3\text{CH}_2)_2\text{O}]_2\text{H}^+$  were obtained with pre-irradiation delays of 1 and 10 s and the results are presented in Figure 14. The two plots differed by less than the 5% error associated with each point due to laser intensity fluctuations. Since the kinetics plot is essentially unaffected by the presence of a 10 s delay, we are able to exclude the possibility that the previously observed "break" in the slope is caused by ions gradually moving away from the centre of the cell due to increasing magnetron motion with time. Also, if the effect were this severe within 1 s, ions would not be trapped and detected efficiently at times longer than ~5-10 s since detection is optimal for ions very near the centre of the cell. This is not the case and trapping times of 1000 s are routinely obtained in this instrument.

Since complete overlap of the laser beam with the ion packet has been established, it follows that the ion population is interacting inhomogeneously with the radiation (ie. not all ions are photodissociated at the same rate). There may be microscopic reasons why individual ions within an ensemble would exhibit this behaviour. These will be discussed in the following sections 3.1.2 and 3.1.3. Another explanation could be the existence of two isomeric structures for the proton bound dimer of diethyl ether and this issue will be addressed in the remainder of this section.



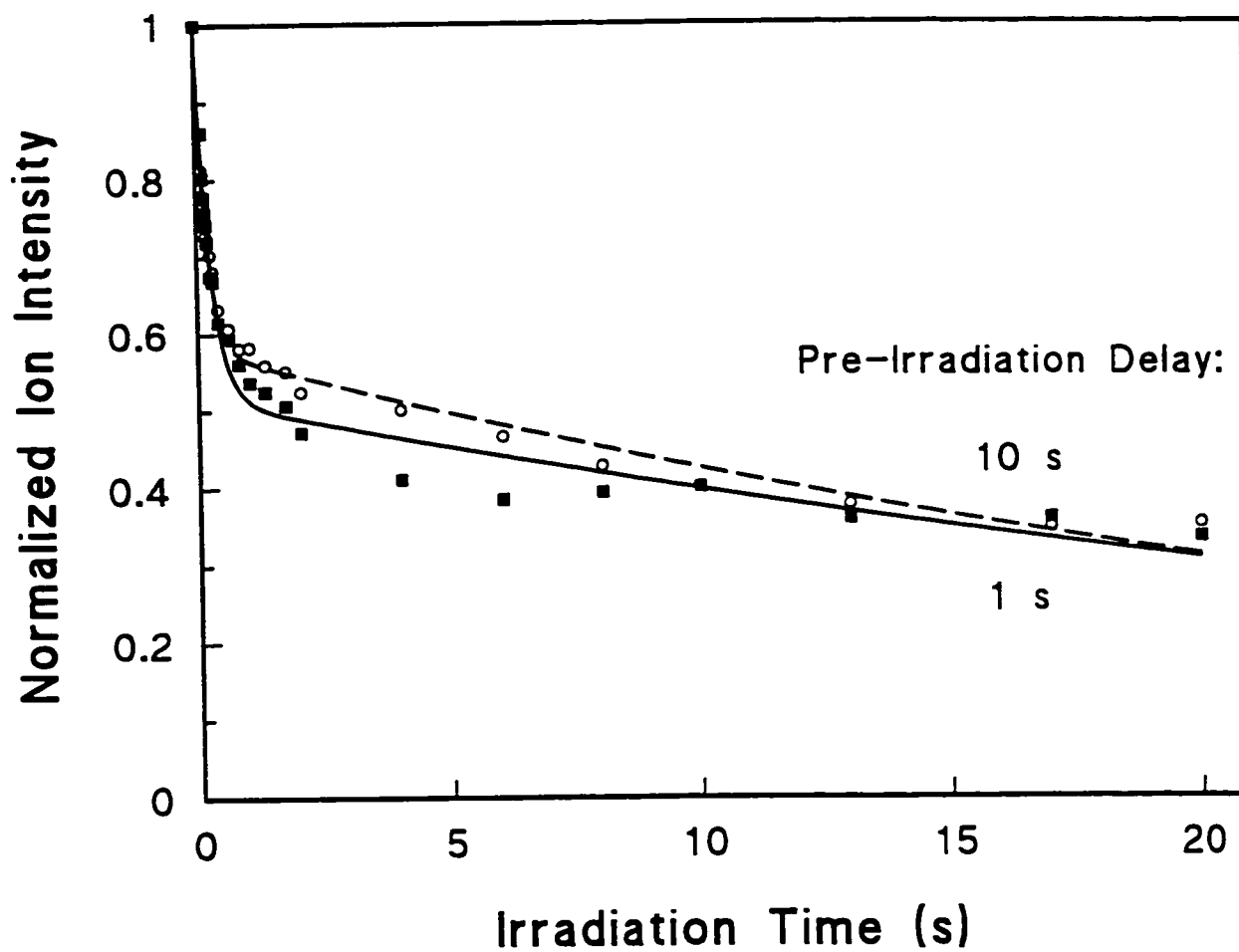
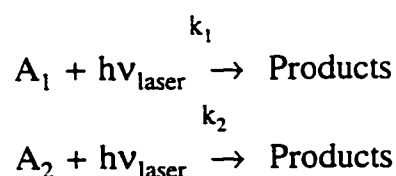


**Figure 14** Photodissociation kinetics for  $[(\text{C}_2\text{H}_5)_2\text{O}]_2\text{H}^+$  using pre-irradiation delays of 1 and 10 s.

If there are two stable isomeric forms of the ion, each with a distinct rate of photodissociation, the abrupt change in slope seen in the kinetics would result. Since ions are detected only by their mass and not structure, it is not possible to directly probe the existence of isomers. However, it is possible to test the fit of the data to the rate equation for parallel unimolecular dissociation reactions of two distinct, isobaric ions.  $A_1$  and  $A_2$  are chosen to represent the two species of ions whose photodissociation rate constants are  $k_1$  and  $k_2$  respectively, as shown in Reaction Scheme 1.



**Reaction Scheme 1:**

Reaction Scheme 1 yields the following integrated rate equation (subject to the condition that  $[A_1]_0 + [A_2]_0 = [A]_0$ ):

$$\frac{A(t)}{A_0} = [A_1]_0 e^{-k_1 t} + [A_2]_0 e^{-k_2 t} \quad (37)$$

The intensity of the  $[(\text{CH}_3\text{CH}_2)_2\text{O}]_2\text{H}^+$  ion was plotted vs. irradiation time in Figure 13. A least squares fit of Equation (37) to the data from Figure 13, yields the values  $k_1=2.2 \times 10^{-2} \text{ s}^{-1}$ ,  $k_2=5.0 \text{ s}^{-1}$ ,  $[A_1]_0=0.59$  and  $[A_2]_0=0.41$  if  $A_2$  is arbitrarily chosen to be the strongly absorbing species and  $A_1$  the weakly absorbing species. The line through the data in Figure 13 was calculated from Equation (37) with these values. Inspection

of the Figure indicates that the resulting curve correctly describes the behaviour of the data. In order to explain the large difference in the dissociation rates of  $A_1$  and  $A_2$ , however, the two isomers would have to differ substantially in either bond strength or photon absorption rate at 10.6  $\mu\text{m}$ . This would further suggest that the isomeric parent ions have markedly different structures but still yield the same photoproducts, which is unlikely. The results presented in section 3.3 will show that the proton bound dimers of pentanone and nonanone also exhibit the same non-first order photodissociation kinetics as  $[(\text{CH}_3\text{CH}_2)_2\text{O}]_2\text{H}^+$ . Thus if isomers are causing this behaviour, all three species must have two isomeric forms of the dimer ions which is also unlikely. Previous studies, performed on a pulsed high pressure mass spectrometer (PHPMS), have demonstrated that PHPMS can be used to distinguish isomeric ions with different thermochemical properties *via* a change in slope of the Van't Hoff plot ( $\ln K_{\text{eq}}$  vs.  $T^{-1}$ ).<sup>31</sup> A detailed PHPMS study<sup>32</sup> has shown that no such "break" exists for the species studied here. It should be noted that the PHPMS experiments were conducted at relatively high temperatures ( $\geq 300^\circ\text{C}$ ) in order to obtain sufficient intensity in the protonated monomer ion that the equilibrium constant ( $K_{\text{eq}}$ ) for the clustering reaction between the monomer and dimer ions could be determined. Whether an ion exists in an isomeric form may depend upon the internal energy of the ion. The absence of evidence for isomers in PHPMS at high temperature does not absolutely eliminate the possibility that such a species exists in the lower temperature regime of the present experiments. Optical spectroscopy is often a

powerful tool for revealing the existence of isomers. Infrared spectroscopy of ions is extremely difficult and absorptions for large molecules or ions are usually characterized by broad absorption bands rather than distinct lines. Beauchamp<sup>9, 21</sup> *et al.* have shown that photodissociation of  $[(\text{CH}_3\text{CH}_2)_2\text{O}]_2\text{H}^+$  has little wavelength dependence between 920-980  $\text{cm}^{-1}$ . It, therefore, seems unlikely that one isomeric structure of an ion this large would absorb infrared strongly while the other structure was infrared transparent (or very weakly absorbing). Therefore, a pair of isomeric structures could explain the observed kinetics but a thorough experimental search has revealed no evidence for their existence.

A process of elimination has revealed that the non-uniform interaction of the ion population with the infrared laser radiation is being caused by the molecular properties of the ions. For small molecules it is understood that the absorption of narrow bandwidth laser light will depend on the quantum state of the molecule. It is less clear that the microscopic properties of an ensemble of large ions should separate individual ions into "absorbing" and "non-absorbing" classes in a continuous IR radiation field. The following sections will be devoted to exploring the microscopic properties of ions during the IRMPD process. A review of the models of IRMPD will be presented in section 3.1.2. Sources of bottlenecks and their application to the current experiment will be discussed in section 3.1.3. Processes such as rotational hole burning, thermal vibrational bottlenecks and population inversion (saturation) will be discussed with the goal of explaining the observed non-first order kinetics.

### 3.1.3 Models for IRMPD

Although the details of the individual models are the subject of some controversy, the qualitative aspects of the IRMPD process are thought to be well understood.<sup>33</sup> The basic concept is simple. A sequential absorption of photons increases the energy of the molecule until the dissociation threshold is exceeded and unimolecular decomposition of the molecule occurs. The microscopic mechanism of this process is more complex. IRMPD cannot occur within a single vibrational mode because, even with a high powered pulsed IR laser, the power broadening is not sufficient to overcome the anharmonicity of the vibrations. Some current experiments are attempting to use femtosecond infrared laser pulses, which are frequency "chirped" from blue to red wavelengths, to overcome the anharmonicity and increase the photolysis yield in agreement with theoretical predictions.<sup>34</sup> Collisional energy redistribution among the many ro-vibrational states of a polyatomic molecule can overcome this limitation.<sup>35</sup> Thus, it was initially thought that collisions played an essential role in the IRMPD process and this theory was supported by several examples of enhanced photodissociation yield in the presence of a collision gas.<sup>36,37</sup> However, Lee and co-workers demonstrated that IRMPD could occur under molecular beam conditions where collisions were not a significant factor.<sup>3</sup> The reason that purely radiative IRMPD occurs in polyatomic molecules is the presence of many other vibrational modes which form a set of background states. At higher excitation energies, there is a strong interaction of normal mode states due to anharmonic

coupling. This is shown by the complete randomization of the excitation energy throughout the vibrational modes of the molecule prior to decomposition even when the dissociation occurs rapidly ( $\leq 100$  ns).<sup>3</sup> When the "pumped" normal mode becomes non-resonant with the laser radiation, due to anharmonicity, rapid coupling to other modes allows the excitation process to continue even in the absence of collisions. A schematic model for the IRMPD process is presented in Figure 15a). The ladder of ro-vibrational energy levels, through which the molecular energy is "pumped," is often referred to as the "vibrational manifold." The energy levels are categorized by three energy regimes which correspond to very different dynamical behaviour. The low lying region of the energy diagram is characterized by discrete ro-vibrational states for which the energy levels are quantized and therefore, could potentially be determined by molecular spectroscopy. Correspondingly a quantum mechanical approach is required to describe the IR transition rate through these states. Higher up the vibrational manifold, in between the discrete region and the dissociation continuum, lies a region of intermediate behavior termed the "quasicontinuum." As the internal energy of the molecule increases, the density of states also increases due to the anharmonicity in the vibrational potential energy. At some point the average spacing between the energy levels becomes less than the linewidth of the laser and the quasicontinuum is reached. Black *et al.* state: "The key property of the quasicontinuum is that at a sufficiently high density of states,  $\rho(E)$ , Fermi's Golden Rule becomes valid."<sup>38</sup> The Fermi Golden Rule governs non-radiative transitions.

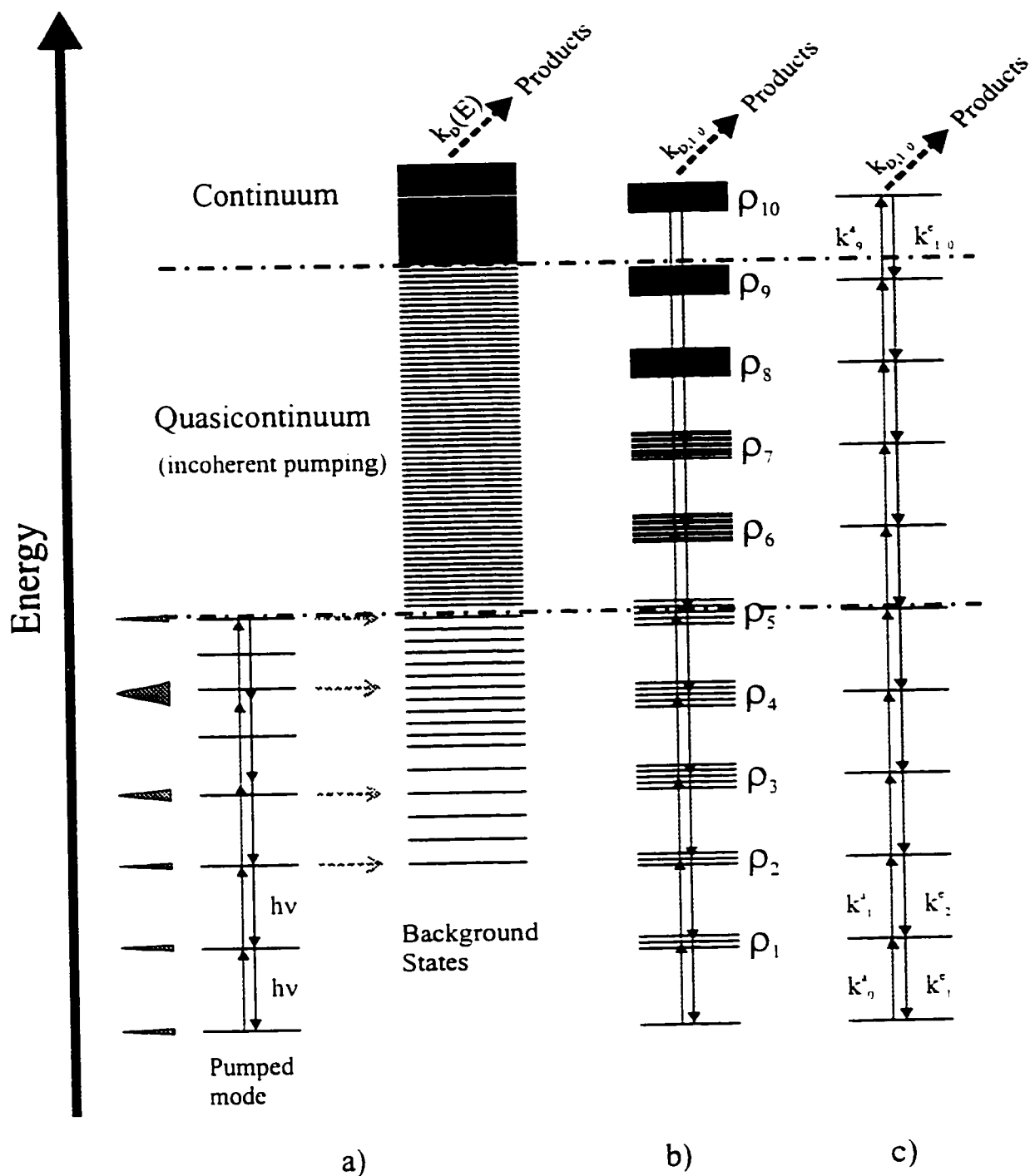


**Figure 15** Common schemes for representing the energy levels of a polyatomic molecule for multiphoton excitation. (see text for a description)

For coupling between vibrational states it may be expressed as:<sup>35</sup>

$$\Gamma_n = 2\pi g \rho(E=nh\nu) \quad (38)$$

where  $\Gamma_n$  is the coupling rate (actually an inverse lifetime) of a state with energy equal to  $n$  excitation photons in the "pumped" vibrational mode to all background modes;  $g$  is the electric dipole matrix element coupling the "pumped" state to the background states and  $\rho(E=nh\nu)$  is the density of states at energy,  $E$ . Since the coupling is proportional to  $\rho(E)$ , highly excited vibrational states will be fully coupled to the background modes. This results in complete energy randomization, prior to dissociation, as was observed by Grant *et al.*<sup>39</sup>. This allows pumping through the quasicontinuum to be treated as a series of incoherent single photon absorptions. However, strong optical selection rules may still apply to transitions within the quasicontinuum, as shown by the observation of phenomenon such as rotational hole-burning, which will be discussed in section 3.1.3. Therefore, treating all states as degenerate may substantially overestimate the allowed transition rates in the quasicontinuum. It is also important to note that the definition of the onset of the quasicontinuum is relative and depends upon both the molecule and the laser linewidth. Above the dissociation threshold lies the true dissociation continuum where the intramolecular potential becomes asymptotic and an infinite number of states exists. For molecules with energies substantially above the dissociation threshold,



decomposition is rapid and may be represented by an energy dependent dissociation rate constant,  $k_d(E)$ . For very large molecules or those just at the dissociation limit, the lifetime  $[k_d(E \geq E_{th})]^{-1}$  may be infinitely long.

The dynamics of the multi-photon excitation process are, therefore, summarized by three events: 1) putting the molecules into the quasicontinuum. This is referred to as overcoming the "discrete-state barrier" by Grant *et al.*<sup>39</sup> 2) Pumping the internal energy of the molecule through the quasicontinuum. The continuous nature of the quasicontinuum should result in a uniform rate of excitation between all states in this region and there should not be significant rate fluctuations or large bottlenecks in the up-pumping process. 3) The rate of dissociation of molecules with energy above the dissociation limit governed by  $k_d(E)$ .

A complete description of the multistep excitation process must include transitions between all molecular energy states. For a molecule with  $i$  such states, the rate of change of the population in each state,  $p_i$ , can be described by a first order differential equation. A set of  $i$  such equations describes the kinetic evolution of the population of  $i$  states. In matrix notation, this may be expressed by the linear rate equation:

$$\dot{p} = K \cdot p \quad (39)$$

where  $\dot{\mathbf{p}}$  denotes the time derivative of the vector  $\mathbf{p}$ , containing all  $p_i$ , and  $\bar{\mathbf{K}}$  is the coupling matrix containing the rate constants,  $K_{fi}$ , which govern transitions between pairs of states. Equation (39) is termed a "master equation." Many groups proposed theoretical models of IRMPD and perhaps the only point of universal agreement was the validity of the master equation approach. The various theories begin to differ with respect to the practical implementation of this method. Quack has provided perhaps the most complete overview of solutions for the master equation derived from strictly microscopic arguments starting from the Schrödinger equation.<sup>25,40,41</sup> Jortner *et al.* adopted a similar approach.<sup>42</sup> Exact solutions of these equations, however, require an accurate knowledge of the coupling co-efficients between all states for polyatomic molecules. Quack calls the problem of deducing the master equation from the Schrödinger equation, "the *hard* problem of statistical mechanics."<sup>25</sup> In 1978, he stated:<sup>25</sup> "With the most advanced computational techniques it appears to be out of the question to solve such a problem exactly, even for ozone, which would be one of the most favourable examples as far as the size of the problem is concerned." Thus, approximations had to be made in the theory and the applicability of the approximations to real systems is not always clear. Even with current computational methods, it would be exceedingly difficult to obtain reliable state-to-state transition rates for molecules or ions which are as large as those which appear in this study. Thus, quantitative modelling of the IRMPD experiments presented here will not be attempted.

A modified approach to solving the master equation adopts a strictly phenomenological approach to the determination of rate co-efficients. Since a molecule can only undergo absorption and emission between states separated by the photon energy, states may be grouped together into "levels" separated by  $h\nu$  as shown in Figure 15b). Grant *et al.* initially proposed that "infrared multiphoton excitation of a molecule can be described by stepwise incoherent one-photon transitions among a set of equally spaced energy levels; the degeneracy factor of each level is given by the corresponding molecular density of states which can be calculated."<sup>39</sup> Thus, if  $j$  represents the maximum number of photons absorbed (note:  $j h\nu$  can be greater than the bond energy if excitation is rapid compared to  $k_D(E_{th})$ ) before dissociation occurs, then the entire process of IRMPD may be described by transitions between  $j$  levels as shown in Figure 15c). If only single photon transitions are allowed, the complex problem of solving equation (39) for a very large number of ro-vibrational states may be reduced to a set of  $j$  coupled differential equations of the form:

$$\frac{dP_n}{dt} = k_{n-1}^a P_{n-1} + k_{n+1}^e P_{n+1} - (k_n^a + k_n^e) P_n - k_{Dn} P_n \quad (40)$$

where  $k_n^a$  is the absorption rate constant from level  $n$  to  $n+1$ ,  $k_n^e$  is the emission rate constant from level  $n$  to  $n-1$ , and  $k_{Dn}$  is the dissociation rate constant. (for levels below the dissociation energy,  $E_{th}^{diss}$ ,  $k_{Dn}=0$ , and  $k_0^e=0$ ) This treatment was used by many groups in their treatment of IRMPD of both neutral molecules<sup>38,43,44</sup> and

ions.<sup>45,46,47</sup> It should be pointed out that this model is really just a simplified case of the rigorously derived result put forth by Quack,<sup>25</sup> but using phenomenologically determined rate constants. The requirement of incoherent single-photon pumping between levels does not apply to the low energy states in the discrete regime of the vibrational manifold. A common model is that one or more photons are resonantly absorbed into the low-lying vibrational states and then incoherent pumping dominates once the quasicontinuum is reached. However, pulsed laser IRMPD has been observed in molecules which do not have resonant absorptions. In the modelling of Grant *et al.*,<sup>39</sup> the initial one-step multiphoton transition over the discrete states is ignored since their laser intensity is above the threshold required to overcome the "discrete state barrier" for pulsed laser experiments. This minimum intensity is required either to power broaden the transition until one or more resonant absorptions are possible or to increase the probability of a non-linear absorption (*ie.*  $\geq 2$  photons simultaneously) process. Thus, in their model, it is assumed that the absorption of the first few photons to reach the quasicontinuum is not the rate determining step or "bottleneck" and that the dissociation rate is determined by the transitions in the quasicontinuum region. It may seem irrelevant to talk about this approach since the laser intensities used in the current experiments are far too low, however, the enormous density of states of the ions being studied effectively eliminates the low energy bottleneck in much the same way as power broadening would. If the thermal energy of the ions is large enough that a majority of the ions are within 1 photon of the quasicontinuum

threshold,  $E_{th}^{quasi}$ , then there is always an upper state and a low energy bottleneck is not expected. Beauchamp refers to this as the large molecule category where IRMPD is made facile by the large density of vibrational states at low energies.<sup>48</sup> This concept will be expanded upon in section 3.1.3 of this thesis.

If the laser intensity is too low for power broadening and the molecules are smaller than the large molecule limit, there may be no initial resonant absorption into low  $v$  vibrational states. Thus, only molecules which possess sufficient internal energy to populate the quasicontinuum initially will dissociate. After the high energy fraction of an ensemble of molecules dissociates, the IRMPD rate will plateau. If there is a weakly resonant absorption into a normal vibrational mode, the IRMPD rate will slow down rather than plateau. This process, called a "vibrational bottleneck," will be discussed in detail in section 3.1.3. If the ions studied here are in the large molecule limit, vibrational bottlenecking is not expected.

The picture of uniform excitation through the entire vibrational manifold may be complicated by the existence of resonances within the quasicontinuum. Resonances in the true continuum above the ionization limit are well known in zero kinetic energy (ZEKE) photoelectron spectroscopy. In the quasicontinuum, not all pairs of states which are separated by the laser frequency will exhibit the same transition probability. Thus, absorptions through the quasicontinuum can mimic the behaviour of a discrete absorption process and ions which appear to be in the large molecule limit may exhibit a behavior resembling low energy vibrational bottlenecking, due to quasicontinuum

resonances.

The role of collisions in IRMPD has been studied extensively but still may not be fully understood. Both enhancements and decreases in IRMPD yields have been reported. Wittig *et al.* state that "collisions are expected to promote rotational relaxation, dephasing of coherent absorption processes and randomization and quenching of vibrational energy."<sup>36</sup> Stone *et al.* also reported "collisional hole filling" at lower pressures and collisional deactivation at higher pressures.<sup>49</sup> The rotational relaxation time due to collisions has been experimentally estimated at 20 ns torr for low vibrational levels of C<sub>2</sub>H<sub>4</sub>,<sup>37</sup> and Jetter and co-workers have measured the rotational relaxation time, T<sub>1</sub>, at 10 ns torr for <sup>13</sup>CH<sub>3</sub>F using time resolved, microwave-IR, double resonance techniques.<sup>50</sup> Additionally, Setser *et al.* have examined the collisional deactivation of highly vibrationally excited CH<sub>3</sub>CF<sub>3</sub> by many bath gasses and found that simple collision gasses such as argon, helium and methane remove ~1-3 kcal mole<sup>-1</sup> per collision.<sup>51</sup>

The validity of the kinetic master equation may be generally agreed upon, but the population distribution of molecular eigenstates that results from infrared multiphoton excitation (IRMPE) is not. Yablonovitch *et al.* proposed that IRMPD could be modelled by assuming a thermal distribution of internal energies and assigning an effective temperature, T<sub>eff</sub>, to the ensemble of molecules.<sup>38,52</sup> The kinetics could then be treated using the well established theory of thermal unimolecular reactions. Some reasonable agreement with experiments was initially demonstrated.

The "thermal model" of Yablonovitch *et al.* included the assumptions that 1) all vibrational modes were degenerate, 2) the thermal population was not significantly perturbed, 3) the classical equipartition theorem is valid and 4) inhomogeneous effects such as hot bands, rotational state selection rules and doppler broadening could be ignored. Many other groups disagreed with the validity of these assumptions. Barker states: "It will be shown that although the Yablonovitch "thermal" model was derived using a non-physical and inaccurate expression for the density of states, compensating errors give rough agreement with the exact EGMA (energy grained master equation) when certain restrictive conditions are met."<sup>44</sup> Lee and co-workers demonstrated that the population distribution produced by pulsed laser IRMPD of SF<sub>6</sub> was substantially different from a thermal distribution with the same average energy.<sup>39</sup> Furthermore they show that the use of the classical equipartition theorem,  $\langle E \rangle = 15kT_{\text{eff}}$ , as used by Yablonovitch and co-workers produces a thermal population with temperature,  $T_{\text{eff}}$ , which grossly underestimates the real population of states. Quack<sup>25</sup> has also presented steady state vibrational state distributions which are qualitatively the same as those of Lee. Quack has also stated that collisionless IRMPD is different from thermal unimolecular reactions in all respects and, therefore, there is no justification for using a Boltzmann distribution. He suggests that the idealized distribution for IRMPD is microcanonical. Figure 16 shows the qualitative differences between the population produced by IRMPD and a thermal population with the same average energy.<sup>25,39</sup> The IRMPD distribution tends to be narrower and symmetric. An important consideration

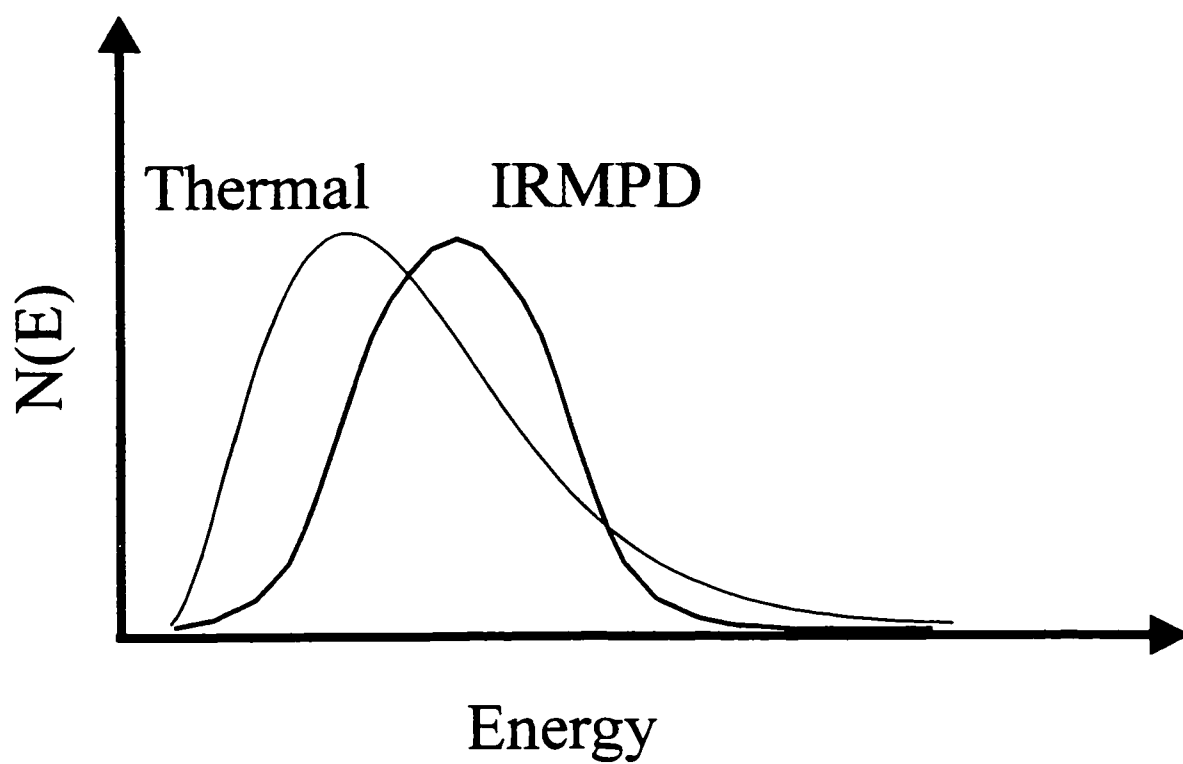


**Figure 16** Schematic illustration of population distributions for IRMPD and thermal unimolecular reactions.



is that several calculations<sup>25,39</sup> indicate the existence of steady state distributions in multilevel systems. Time evolution trajectories for three and five level systems, obtained by random walk methods, show features such as recurrences, oscillations and steady state behaviour even when excitation is by short, high intensity laser pulses. Consider a system of  $n=11$  levels separated by photon energy ( $943\text{ cm}^{-1}$ ), where only the upper state may dissociate ( $E_{11} \geq E_{\text{th}}^{\text{diss}}$ ) and  $k_{D\ 11}$  is slow. There is also rapid quenching from levels near  $E_{\text{th}}^{\text{diss}}$ , and all ions may be excited because the density of states satisfies the "big molecule" criteria. The results of Quack<sup>25</sup> and Lee<sup>39</sup> suggest that such a system could exhibit a steady state population distribution similar to that shown in Figure 16 for URIMIR. The distribution becomes narrower than a Boltzmann distribution and the maximum is shifted to higher  $n$ . The effect of this population inversion may be similar to saturation in a two level system. The system described above should crudely describe the IRMPD process observed in the experiments presented in this thesis. Without master equation modelling, it is difficult to say whether this type of saturation effect could result in the non-first order kinetics observed here. It is certain that high intensity pulsed laser IRMPD produces a non-thermal distribution of internal energy and it seems probable that the unique experimental conditions of the present experiment may also result in a distribution which is not Boltzmann. Therefore, the kinetics may not necessarily be expected to behave as though a thermal unimolecular reaction were occurring.

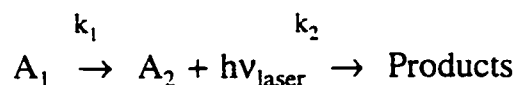
### 3.1.3 Pulsed vs. CW IRMPD as a Tool for Elucidating Bottlenecking Mechanisms

A process of elimination has revealed that the non-first order kinetics observed in these experiments must be the result of structurally identical ions exhibiting dissimilar interaction with the laser radiation field. In order to determine why the population of ions might interact inhomogeneously with a monochromatic IR source, the microscopic properties of the ensemble must be considered. An enhanced infrared multi-photon absorption cross section is often exhibited by ions in excited vibrational levels. As mentioned in section 3.1.2, a common assumption of IRMPD models is that the initial absorption of photons in the discrete regime is the rate limiting step because of the low probability of having discrete transitions exactly matching the laser frequency. The production of "hot" ions by-passes this slow step in the IRMPD process and the subsequent excitation through the upper levels is rapid due to the increased density of states. Since the level of vibrational excitation determines whether a molecule is above or below the threshold for rapid dissociation, this process will be referred to as a "vibrational bottleneck." Since the rate limiting step occurs at low energy, this example falls into the broader category of an "early bottleneck" as defined by Quack.<sup>25</sup> Non-thermal ionization conditions may produce ions in excited vibrational states. IRMPD of relatively small ions, produced under these conditions, may exhibit an extreme vibrational bottleneck because the separation of vibrational states is large. The IRMPD rate would be expected to slow down (or halt) at some time, indicating the depletion of the hot ions and slow (or non-existent) repopulation

of the excited vibrational levels. The observation of ion relaxation over time (*via* collisional quenching or radiative emission) indicates the presence of hot ions. Brauman has shown that increasing the relaxation delay between ion generation and pulsed laser IRMPD of  $\text{F}(\text{CH}_3\text{OH})$  changed the appearance of the logarithmic reactant fluence (LRF) plots.<sup>53</sup> The LRF plot is a plot of  $-\ln(1-F_D)$  vs. Fluence, where  $F_D$  is the fraction of ions dissociated. A change in slope or "break" in the LRF plot signifies a bottleneck just as a break in the kinetics plots presented here does. Since the CW fluence is the product of intensity and irradiation time,  $F=I \cdot t$ , the kinetic plots presented here provide equivalent information to logarithmic reactant fluence (LRF) plots used by Quack<sup>25,54</sup> and Brauman<sup>53</sup> in previous discussions of IRMPD processes. The full kinetic plots, however, have the advantage of monitoring the entire time evolution of the ion population rather than merely observing the fraction dissociated at a given time which may or may not be representative of the actual dissociation rate. The existence of a "roll-over" or negative change in slope was replaced by a linear slope for longer relaxation delays. This indicates that the hot ions, made *in situ* in a conventional ICR spectrometer, are relaxing and that the initially rapid photolysis of the hot ions is replaced by slower, uniform dissociation of ions in lower vibrational states.

The change in the slope of the kinetic plot in Figure 13 could indicate the presence of a vibrational bottleneck in the present experiments. The external ion source used here, however, produces ions which are in thermal equilibrium with the

surroundings (unlike Brauman's experiment), therefore, time dependent relaxation should not be observed. The internal energy contained in the very large ions investigated here, may be sufficient to thermally populate vibrational levels above a bottleneck. Thus, only the high energy fraction of the population would be rapidly dissociated and a truncated Boltzmann distribution of internal energies would result. With the long time scale of this experiment, however, some ions will be converted from the low energy, non-absorbing species to the strongly absorbing (rapidly dissociating) species by collisional (and/or black body radiative) energy exchange. This mechanism can be described by a modified version of Reaction Scheme 1. In Reaction Scheme 2, two species,  $A_1$  and  $A_2$ , of the same ion are defined according to their interaction with the IR radiation. The ionic species  $A_2$  can absorb laser photons and dissociate, but  $A_1$  ions cannot dissociate directly.  $A_1$  can, however, slowly interconvert to  $A_2$  which then rapidly dissociates.



**Reaction Scheme 2:**

In this scheme,  $k_1 = k'_1 [M]$  for collisional energy exchange and  $k_1 = k''_1 [h\nu]$  for radiative energy exchange. Reaction Scheme 2 yields the following integrated rate equation (subject to the condition that  $[A_1]_0 + [A_2]_0 = [A]_0$ ):

$$\frac{A(t)}{A_0} = [A_1]_0 e^{-k_1 t} + [A_2]_0 e^{-k_2 t} + [A_1]_0 \frac{k_1}{k_2 - k_1} (e^{-k_1 t} - e^{-k_2 t}) \quad (41)$$

A least squares fit of the data in Figure 13 to Equation (41), yields the same values ( $k_1 = 2.2 \times 10^{-2} \text{ s}^{-1}$ ,  $k_2 = 5.0 \text{ s}^{-1}$ ,  $[A_1]_0 = 0.59$  and  $[A_2]_0 = 0.41$ ) as the previous fit to Equation (37) which indicates that the last term in Equation (41) is negligible when  $k_1 \ll k_2$ . Scheme 2 has been proposed to explain enhanced dissociation of vibrationally excited ions, however, this reaction scheme and the accompanying kinetic equation, apply equally well to any system which has two species dissociating at different rates. The remainder of this section will address other sources of bottlenecking which may have relevance to the IRMPD kinetics observed here. The applicability of each will be addressed in the discussion section (3.4).

Another type of bottleneck is related to molecular vibrational modes. For molecules with energy below the quasicontinuum threshold, the initial absorption of photons will be into a single, or several degenerate, normal mode(s) which are resonant with the laser frequency. As mentioned in section 3.1.2, IRMPD requires coupling of the pumped vibrational modes to the background vibrational states to overcome anharmonicity effects. It was also shown that complete energy randomization occurs for molecules as small as  $\text{SF}_6$  at high levels of excitation. Thus, it is possible for the molecule to absorb several photons into the resonant mode and then randomly distribute the energy to the other modes. If the molecule absorbs more photons,

IRMPD will occur but there is also the possibility that the molecule will spontaneously emit photons and relax into a discrete, low  $v$ , state of another vibrational mode which is optically dark. Poor coupling between the pumped and dark vibrational modes, at low vibrational excitation, could result in molecules being trapped as "non-absorbers". This is an example of "vibrational hole-burning." The bottleneck observed in the current experiments cannot be caused by vibrational hole burning because intramolecular vibrational energy redistribution (IVR) would cause vibrational hole filling and the IVR rate is expected to be at least nine orders of magnitude faster than the observed  $A_1 \rightarrow A_2$  conversion rate ( $k_1 \sim 0.01 \text{ s}^{-1}$ ). The ions studied here are very large and fluctional, with a substantial amount of thermal energy "floating" around. Thus, it is unlikely that vibrational modes could be entirely "de-coupled" from one another and the discussion of vibrational bottlenecking is only presented here for the sake of completeness. It is worth noting that the trapping mechanism proposed above could be regarded as an infrared optical pumping mechanism by analogy to a 3 level laser system in which the  $\text{CO}_2$  laser pumps the  $1 \rightarrow 2$  transition, and then level 2 rapidly decays to level 3.<sup>55</sup> Since there is no laser resonant with the  $3 \rightarrow 1$  transition to stimulate emission, the population is trapped in level 2 except for the much slower process of spontaneous emission.

A third type of early bottleneck can be caused by the selection rules governing ro-vibrational transitions. The concept is best illustrated by considering a small linear molecule with a distribution of thermally populated rotational states,  $J''$ , in the ground

vibrational state. For a ro-vibrational transition induced by a very narrow laser line, only absorption from a single  $J''$  state can occur. Subsequent IRMPD of the absorbing molecules depletes the population of that rotational state and the process is called "rotational hole burning." The rate of IRMPD product formation will depend upon the rate of "rotational hole filling" (*ie.* the rate of re-populating the depleted  $J''$  state). Thus, rotational hole burning may also be described by Scheme 2. In contrast to the sharp rotational lines observed in the molecular spectra of small molecules, large molecules are known to produce only broad, featureless bands with no rotational structure, even at low temperature. The question then arises as to why a rotational bottleneck should be relevant to the study of the IRMPD of very large ions presented here. It is important to remember that the broad spectroscopic bands do not necessarily result from broad ro-vibrational transitions. Instead, the individual transitions overlap simply because there are many populated rotational states in many vibrational modes. The basis of the quasicontinuum concept is that the individual states are replaced by energy levels which represent the superposition of all states with that energy. This is expected to be perfectly valid for thermal unimolecular reactions resulting from collisional or broad-band IR excitation, but is not necessarily true for IRMPD from a narrow bandwidth laser. Angular momentum must be rigidly conserved in a collisionless process. Therefore, absorption or emission of a photon must be accompanied by a change in the angular momentum of the molecule by -1 or +1 angular momentum unit, respectively. Thus, even in very large molecules which

are devoid of any spectroscopic rotational structure, conservation of angular momentum may restrict the radiative re-population of rotational states. The proton bound dimer ions are asymmetric tops for which no formal selection rules apply, however, it should be noted that a rotational bottlenecking mechanism for such large molecules would certainly involve more than one rotational state as discussed in the simplified example above. Multiple vibrational modes, K splittings and a broad laser line (100-200 MHz) all suggest that a hole burning mechanism would involve a band of many rotational states. However, the same argument applies to the depletion of a group of rotational states as applies to one. This point is addressed in more detail in the discussion section (3.4) of this chapter. Collisional energy exchange with a polyatomic bath gas must also conserve the total angular momentum of the system. Unlike radiative transitions, however, a molecule undergoing collisional energy transfer is not limited to a unit change in angular momentum. Thus, collisions are an efficient method of re-populating depleted rotational states. At a pressure of  $10^{-9}$  torr, which is typical for these FT-ICR experiments, the collision rate is approximately  $0.05\text{ s}^{-1}$ . Thus, even with a strong collision assumption, the rate of rotational re-population will be slow for these low pressure experiments. However, the long time rate constant,  $k_1$ , is on the order of  $0.01\text{ s}^{-1}$ , for many of the kinetics plots obtained. Therefore, rotational hole burning must be considered and the pressure dependence of the photodissociation kinetics are explored in section 3.4.

Brauman *et al.* have reported evidence of rotational hole burning in the IRMPD



of benzyl anion,  $\text{C}_6\text{H}_5\text{CH}_2^-$ .<sup>53</sup> Increasing the relaxation delay between ion formation and pulsed laser photolysis did not result in the LRF plot changing from bent to linear, as observed for  $\text{F}^-(\text{CH}_3\text{OH})$ . Thus, a vibrational bottleneck was not suspected. A comparison of CW and pulsed laser LRF plots showed *greater* yield for the CW laser photodissociation at the same fluence despite the much lower intensity. Since the CW laser had approximately  $10^6$  less intensity than the pulsed laser, the CW irradiation times were on the order of several hundred milliseconds. At their experimental pressure of  $5 \times 10^{-7}$  torr, collisions begin to be important after  $\sim 40$  ms. Thus rotational hole filling in the IRMPD of ions was demonstrated.

Quack also addresses the master equation modelling of systems with the rate limiting step occurring very near threshold.<sup>25</sup> The existence of a "late bottleneck" may be caused by the rate of de-activation of highly vibrationally excited molecules becoming competitive with the rate of up pumping. This effect will be most noticeable for molecules with slow dissociation rates (governed by  $k_D$ ) and relatively fast collisional quenching or spontaneous emission. Very large molecules or ions will have long excited state lifetimes and correspondingly, small values for  $k_D$ . Spontaneous emission in the infrared is quite slow ( $A_{21} \sim 0.1$ -1 s) compared to visible transitions but on the timescale of this experiment could be quite important. An investigation of the pressure dependence of IRMPD kinetics will be used to probe collisional quenching and a comparison of the observed kinetics, as a function of ion size may help to elucidate the role of spontaneous emission in quenching processes.

The population distribution of energy levels during IRMPD have been discussed in section 3.1.2. Quack has calculated population distributions for some model systems with a late bottleneck and the results show that a kind of multilevel saturation effect may be achieved.<sup>25</sup> As mentioned previously, it is difficult to say whether the non-first order kinetics observed in this study could result from such a distribution without master equation modelling. Thus, only the qualitative aspects of the late bottleneck will be discussed.

### 3.2 Experimental

All experiments were performed on a Bruker CMS 47 Fourier transform ion cyclotron resonance (FTICR) spectrometer equipped with a 4.7 T superconducting magnet and a Bruker Infinity cell. The Waterloo FTICR spectrometer has been modified by the addition of an external, high pressure ion source similar to that found in a high pressure mass spectrometer (HPMS). A detailed treatment of HPMS has been published by Kebarle.<sup>56</sup> The high pressure ion source permits the generation of weakly bound ion-molecule complexes which are thermalized by many collisions ( $\sim 10^5$ ) before exiting the source. Details of the CMS 47,<sup>57</sup> the external ion source<sup>58</sup> and the CO<sub>2</sub> laser are discussed in section 2.4 of this thesis. Differential pumping is accomplished with 3 Balzers turbomolecular pumps. With 3.5 torr in the ion source, the pressure outside the source region is  $\sim 2 \times 10^{-4}$  torr while the base pressure in the

FTICR cell is on the order of  $1 \times 10^{-9}$  torr at 20°C. Pressure dependence experiments were performed with a static pressure of methane or diethyl ether collision gas in the FTICR cell. The proton-bound dimer ions were generated in the external ion source from a mixture of ~1% reagent grade solvent in methane. The gas mixture was flowed into the ion source at a pressure of ~3-5 torr and was ionized by secondary electron impact ionization from 2 keV electrons.  $\text{CH}_5^+$  and  $\text{C}_2\text{H}_5^+$  ions are formed under the high pressure conditions of the source. These ions subsequently proton transfer to the neutral solvent molecules in a chemical ionization (CI) process. Room temperature ionization conditions produced almost exclusively dimer ions. The proton bound dimer ions dominate the equilibrium distribution coming out of the ion source. Thus, complete isolation of the desired ion, prior to photodissociation, was readily accomplished using the standard r.f. ejection shots described in section 2.6. In some experiments, the  $^{13}\text{C}$  carbon isotopes were left unejected to prevent unintentional near-resonant excitation of the desired parent ion. For all of the experiments, test-delays were inserted after the ion ejection event to ensure that no accidental CID of the parent ion was occurring. The complete apparatus for the IRMPD experiments is described in section 2.4.

### 3.3 Results

#### 3.3.1 Proton Bound Dimer of Pentanone

The photodissociation of the proton bound dimer of pentanone produced exclusively protonated pentanone. No further dissociation products were observed regardless of increases in laser power or irradiation time. The FT-ICR mass spectrum of the isolated  $[(C_2H_5)_2CO]_2H^+$  ion prior to irradiation is shown in Figure 17a). The two peaks occurring at  $m/z=173$  and  $m/z=174$  correspond to the  $^{12}C$  and  $^{13}C$  isotopes, respectively. The ions were produced from approximately 2% reagent grade 3-pentanone in a methane bath gas. The ion source pressure ( $P_{IS}$ ) was  $\sim 3.5$  torr. The FT-ICR cell pressure ( $P_{ICR}$ ) increases with increasing cell temperature due to outgassing from the chamber walls. At the experimental temperatures of 20, 41, 58 and 75 °C, ( $P_{ICR}$ ) was 2.0, 2.4, 2.9 and  $4.3 \times 10^{-9}$  mbar, respectively. The preceding pressure values are uncorrected ionization gauge readings. Black body dissociation of  $[(C_2H_5)_2CO]_2H^+$  was not observed at 20 °C or at 41 °C. The photodissociation experiments were conducted using the following relaxation delays in this order: {ionization,  $d2=1$  s, shot ejection,  $d5=2$  s, shot ejection,  $d4=1$  s, laser ON,  $vd$ , laser OFF, detection}. Irradiation of the ion for  $vd=10$  s at a laser intensity of  $9.9 \text{ W cm}^{-2}$  produced the mass spectrum in Figure 17b). Kinetic plots of  $[(C_2H_5)_2CO]_2H^+$  ion intensity vs. irradiation time were obtained at temperatures of 20, 41, 58 and 75 °C and are presented Figure 18, Figure 19, Figure 20, and Figure 21, respectively. At each of the four temperatures, kinetic plots were obtained at four different laser intensities

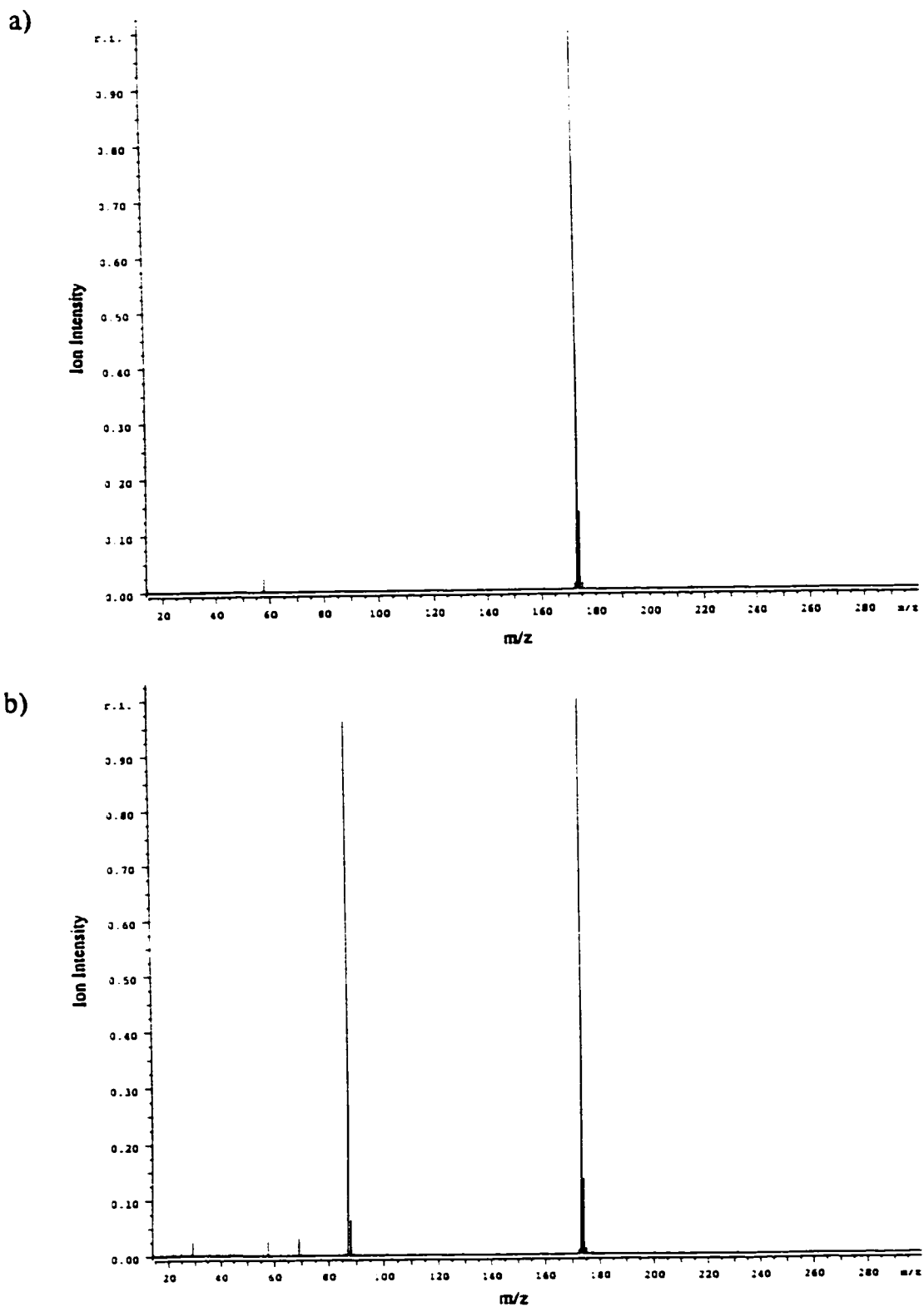


**Figure 17** FT-ICR Mass Spectrum of: a) Isolated  $[(C_2H_5)_2CO]_2H^+$  ion; b) Photoproducts after 10 s irradiation at  $I=9.9 \text{ W cm}^{-2}$ .

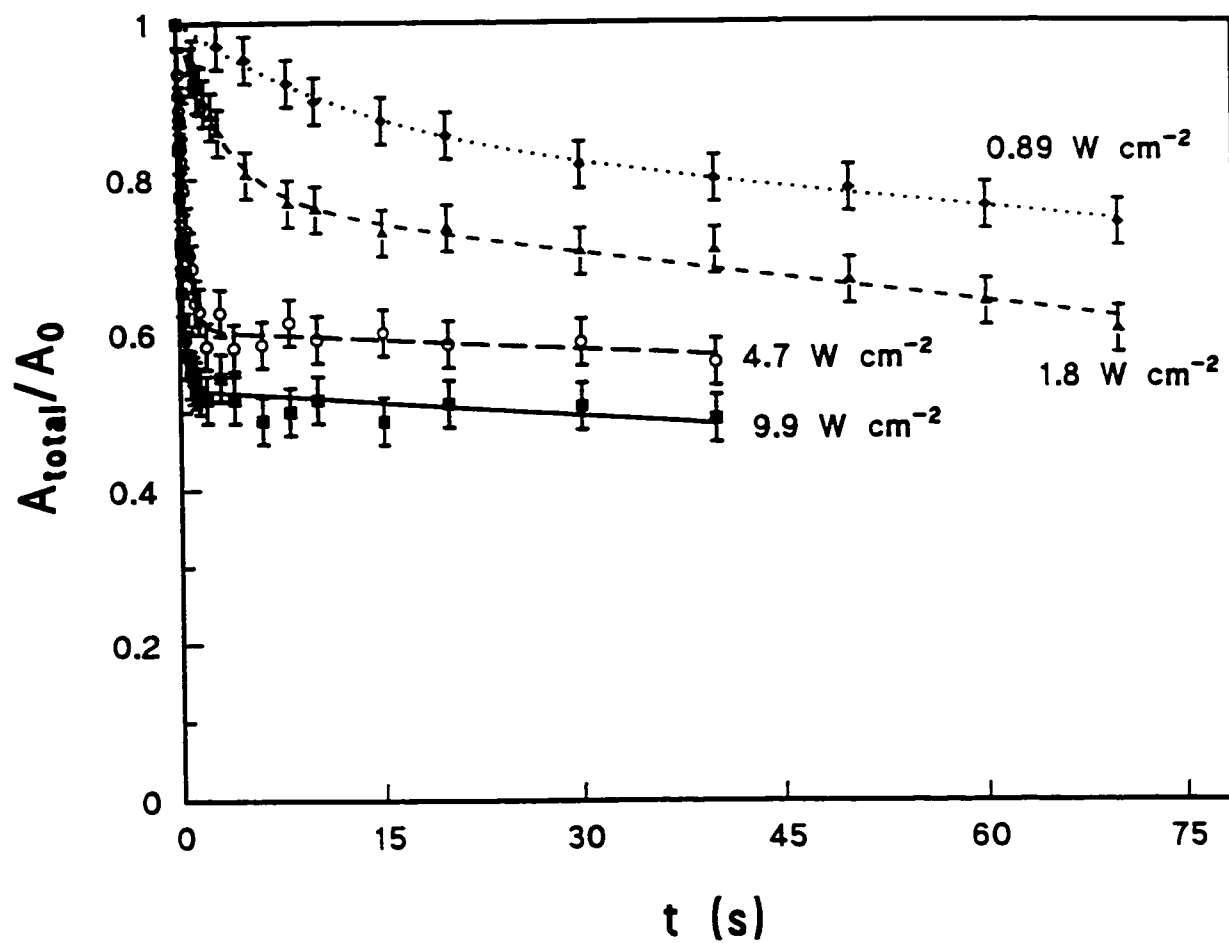


**Figure 18** Plots of normalized  $[(\text{CH}_3\text{CH}_2)_2\text{CO}]_2\text{H}^+$  ion intensity vs. irradiation time at  $20^\circ\text{C}$  for four different laser intensities.

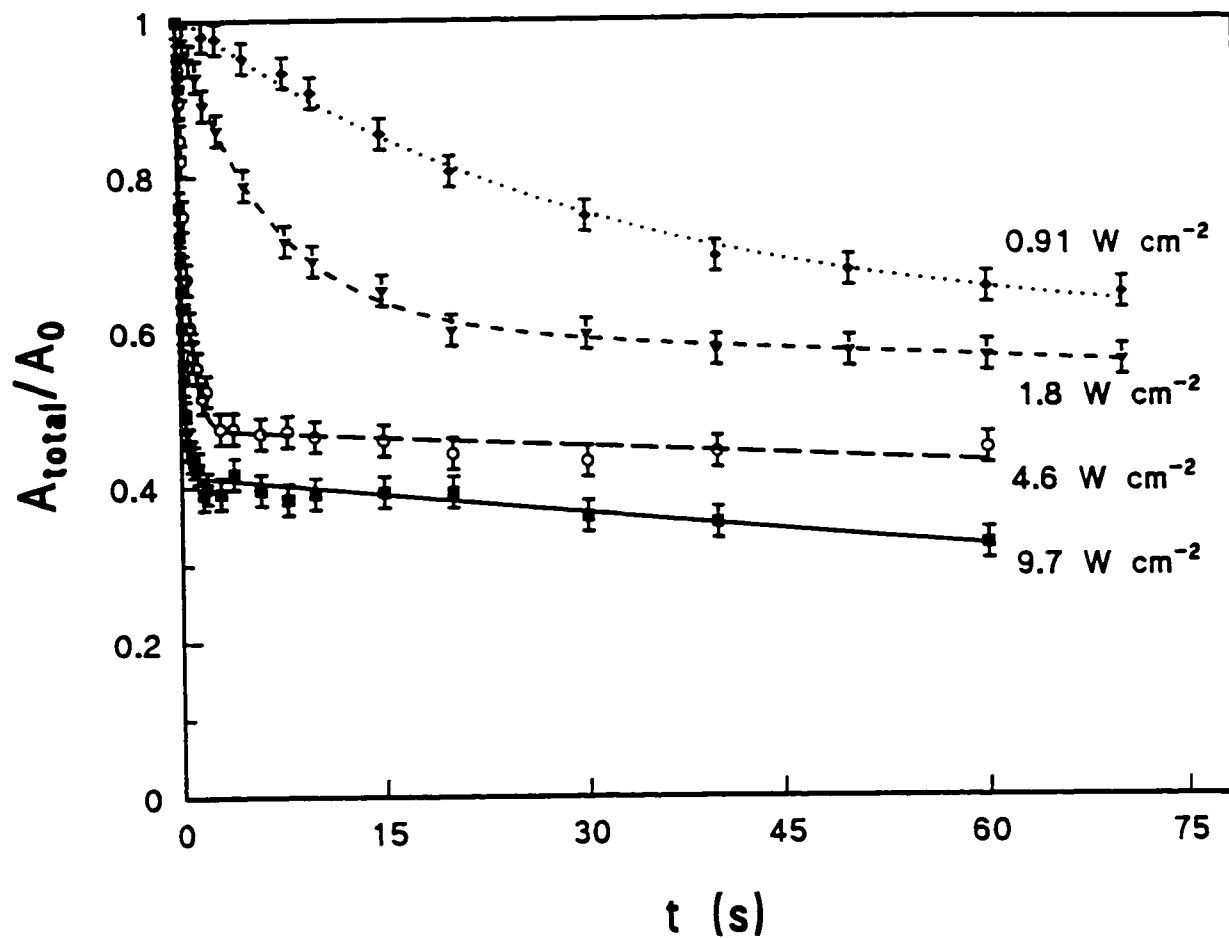


**Figure 19** Plots of normalized  $[(\text{CH}_3\text{CH}_2)_2\text{CO}]_2\text{H}^+$  ion intensity vs. irradiation time at 41 °C for four different laser intensities.

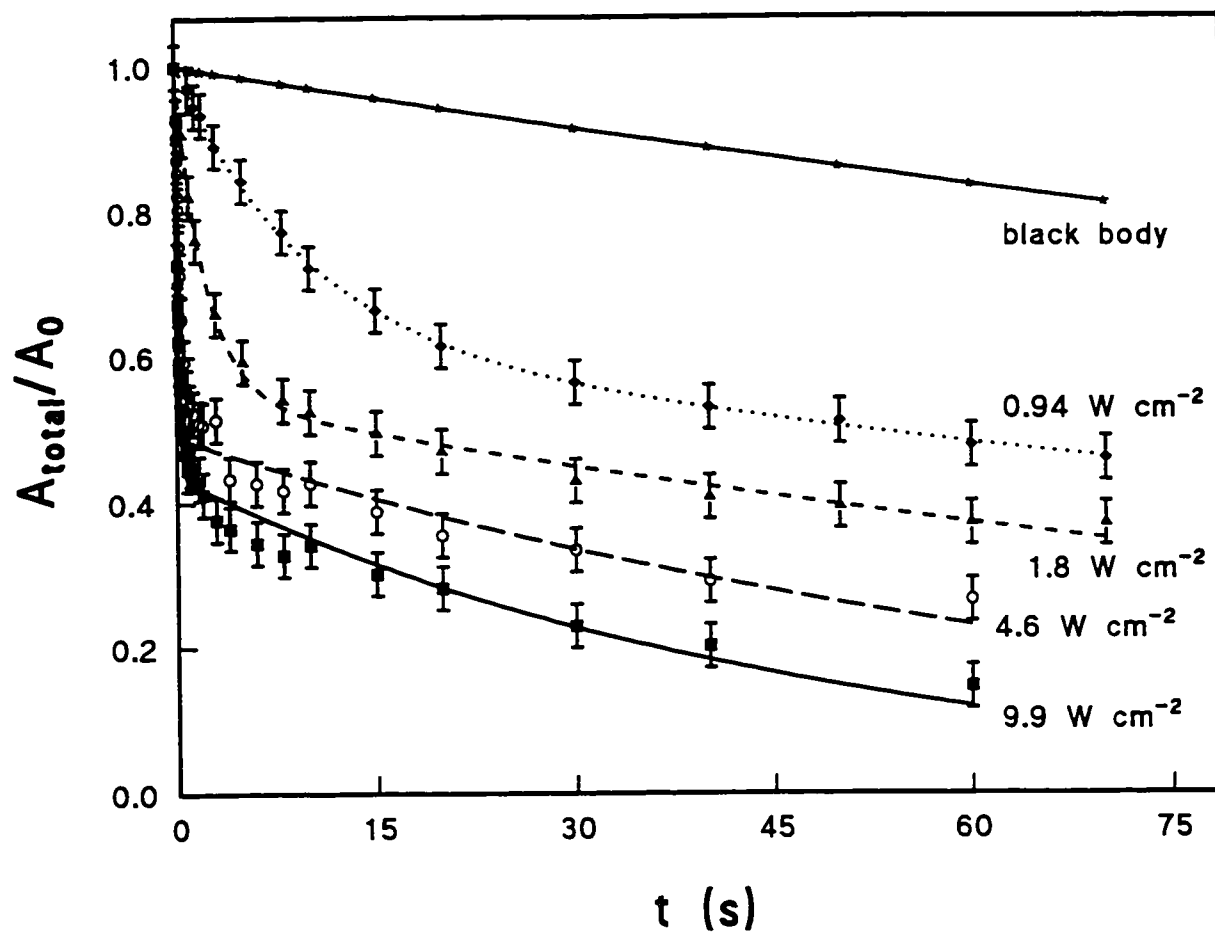


**Figure 20** Plots of normalized  $[(\text{CH}_3\text{CH}_2)_2\text{CO}]_2\text{H}^+$  ion intensity vs. irradiation time at 58 °C for four different laser intensities.



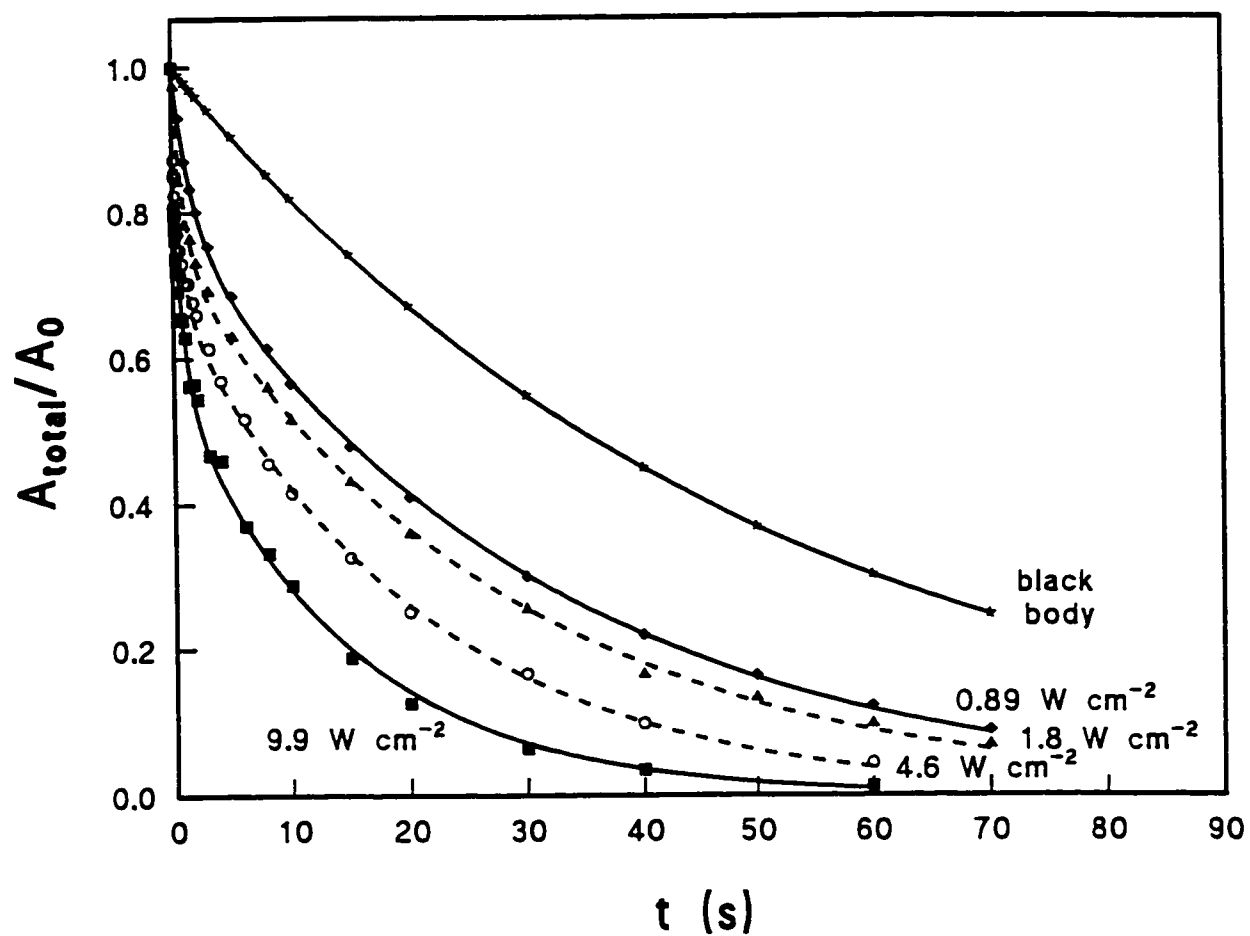


**Figure 21** Plots of normalized  $[(\text{CH}_3\text{CH}_2)_2\text{CO}]_2\text{H}^+$  ion intensity vs. irradiation time at 75 °C for four different laser intensities.

(approximately 9.9, 4.6, 1.8 and 0.86 W cm<sup>-2</sup>). The photodissociation rate constants and relative abundances of the A<sub>1</sub> and A<sub>2</sub> species are obtained by fitting each of the curves in the figures to equation (41). The results are tabulated in Table 3.1. Logarithmic plots of the photodissociation rate constant,  $k_2$ , vs. laser power at each of the four temperatures were obtained. The 20 °C plot is presented in Figure 22 as a representative example. The equation of the linear fit to the data is shown on the figure. For the simultaneous absorption of  $n$  photons, the slope of the log-log power dependence plot should reveal the order of the reaction with respect to photon flux ( $n$ ). For the sequential absorption of multiple photons, the meaning of this slope is less clear. At all four temperatures, the log-log power dependence plots displayed a slope between 1 and 2 which would indicate that the IRMPD observed here requires 1-2 photons. This is consistent with the slope of 0.9 obtained previously from IRMPD studies of H<sup>+</sup>(H<sub>2</sub>O)<sub>4</sub>.<sup>15</sup> Since the total number of IR photons required to dissociate [(C<sub>2</sub>H<sub>5</sub>)<sub>2</sub>CO]<sub>2</sub>H<sup>+</sup> is ~11, the logarithmic power dependence plots do not reveal the overall photon order for this reaction but may indicate something about the order of the rate limiting absorption step.

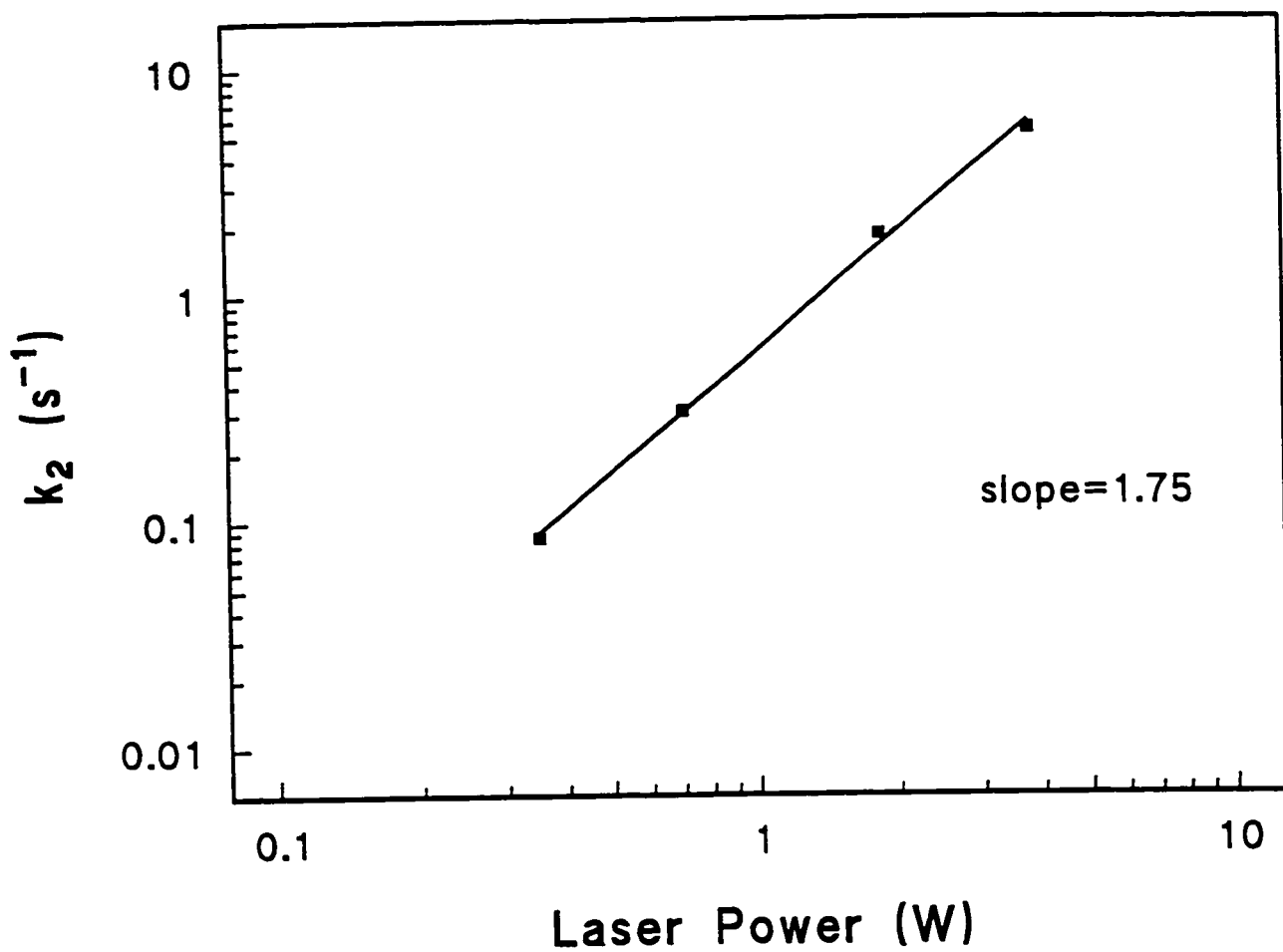


**Figure 22** Plot of  $\ln k_2$  vs.  $T^{-1}$  for the photodissociation of the proton bound dimer of pentanone at 20 °C.

**Table 3.1 Photodissociation Data for the Proton Bound Dimer Ion of Pentanone**

- Values were determined from fitting the data to equation (41)

Temperature (°C)	Laser Intensity (W cm <sup>-2</sup> )	k <sub>1</sub> (s <sup>-1</sup> )	k <sub>2</sub> (s <sup>-1</sup> )	A <sub>1</sub>	A <sub>2</sub>
20	9.7	2.2x10 <sup>-3</sup>	5.3	0.53	0.47
	4.7	1.3x10 <sup>-3</sup>	1.8	0.60	0.39
	1.8	3.2x10 <sup>-3</sup>	0.31	0.77	0.24
	0.89	2.1x10 <sup>-3</sup>	0.085	0.84	0.16
41	9.9	6.9x10 <sup>-3</sup>	5.5	0.45	0.54
	9.7	4.1x10 <sup>-3</sup>	5.3	0.41	0.58
	4.6	1.6x10 <sup>-3</sup>	1.6	0.47	0.56
	1.8	1.2x10 <sup>-3</sup>	0.15	0.60	0.40
	0.91	≤ 1x10 <sup>-3</sup>	0.033	0.60	0.42
58	9.9	2.2x10 <sup>-2</sup>	6.4	0.44	0.55
	4.6	1.3x10 <sup>-2</sup>	2.6	0.49	0.54
	1.8	6x10 <sup>-3</sup>	0.43	0.54	0.46
	0.94	4.2x10 <sup>-3</sup>	0.10	0.59	0.41
75	9.9	8.8x10 <sup>-2</sup>	6.5	0.66	0.33
	4.6	5.5x10 <sup>-2</sup>	5.9	0.74	0.26
	1.8	3.7x10 <sup>-2</sup>	1.6	0.74	0.26
	0.89	3.2x10 <sup>-2</sup>	0.59	0.74	0.26

### 3.3.2 Proton Bound Dimer of Nonanone

The photodissociation of the proton bound dimer of nonanone produced exclusively protonated nonanone. No further dissociation products were observed regardless of increases in laser power or irradiation time, as was observed for the pentanone experiments. The  $[(C_4H_9)_2CO]_2H^+$  ion was isolated and photodissociated in the FT-ICR cell in the same way described in section 3.3.1 for the proton bound dimer of pentanone. The experimental conditions for the generation of ions were: FT-ICR cell temperature (T) of 20 °C, ions source pressure ( $P_{IS}$ ) of 3.7 torr and FT-ICR cell pressure ( $P_{ICR}$ ) of  $2.0 \times 10^{-9}$  mbar. No dissociation of the  $[(C_4H_9)_2CO]_2H^+$  ion due to black body radiation was observed at this temperature. The photodissociation experiments were conducted using the following relaxation delays in this order: {ionization, d2=1 s, shot ejection, d5=5 s, shot ejection, d4=1 s, laser ON, vd, laser OFF, detection}. A plot of  $[(C_4H_9)_2CO]_2H^+$  ion intensity vs. irradiation time (vd) at laser intensities of 9.9, 4.6, 1.8 and 0.86 W cm<sup>-2</sup> is presented in Figure 23. The photodissociation rate constants and relative abundances of the A<sub>1</sub> and A<sub>2</sub> species are obtained by fitting each of the curves in the figure to equation (41). The results are tabulated in Table 3.2. The dependence of the photodissociation rate constant,  $k_2$ , upon laser power at 20 °C is represented graphically in Figure 24. A linear fit to the data yields a slope of 1.21, a y-intercept of 0.343 and a regression co-efficient,  $r^2=0.97$ .

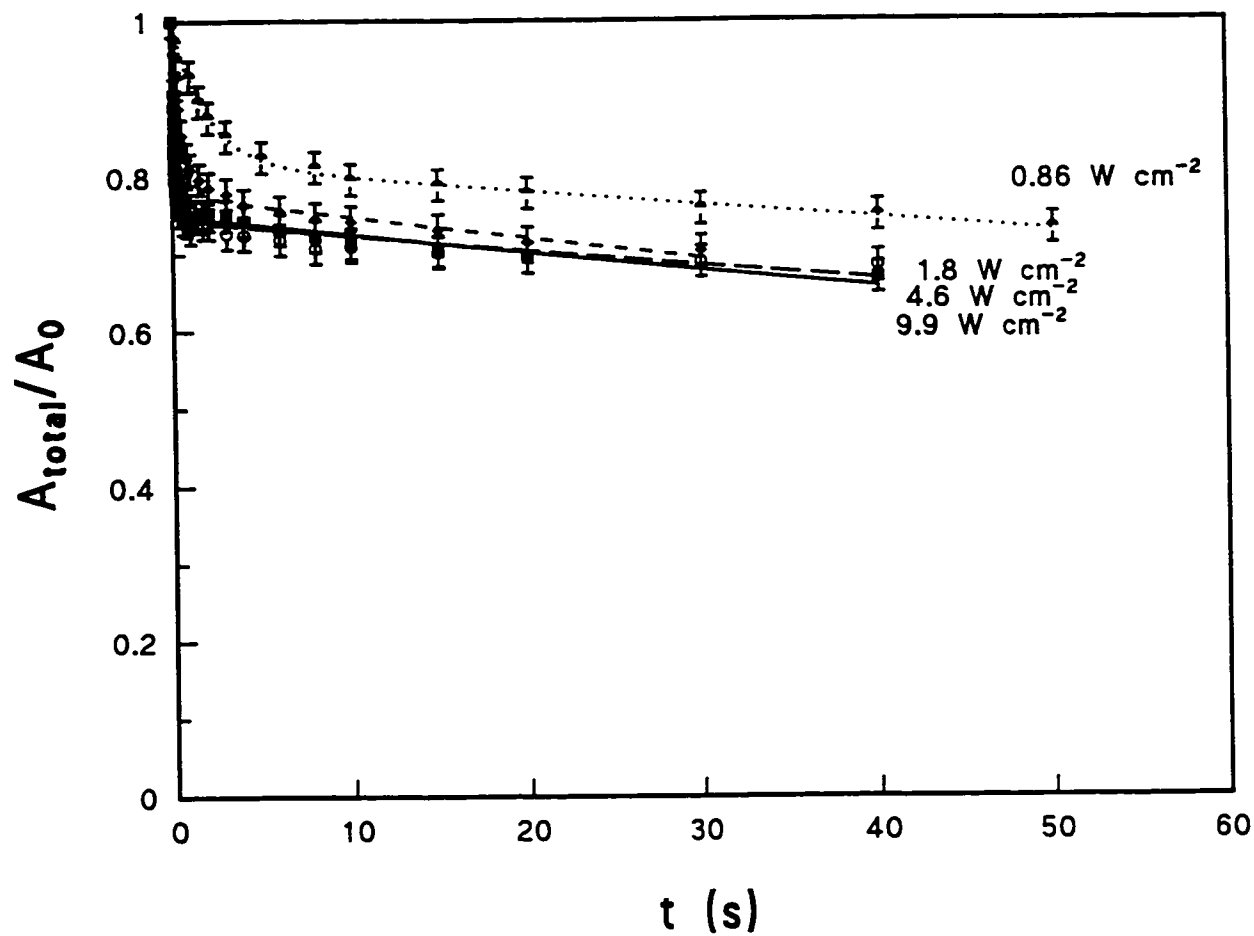


**Figure 23** A plot of the  $[(\text{C}_4\text{H}_9)_2\text{CO}]_2\text{H}^+$  ion intensity vs. irradiation time at  $20^\circ\text{C}$  for laser intensities of 9.9, 4.6, 1.8 and  $0.86 \text{ W cm}^{-2}$ .

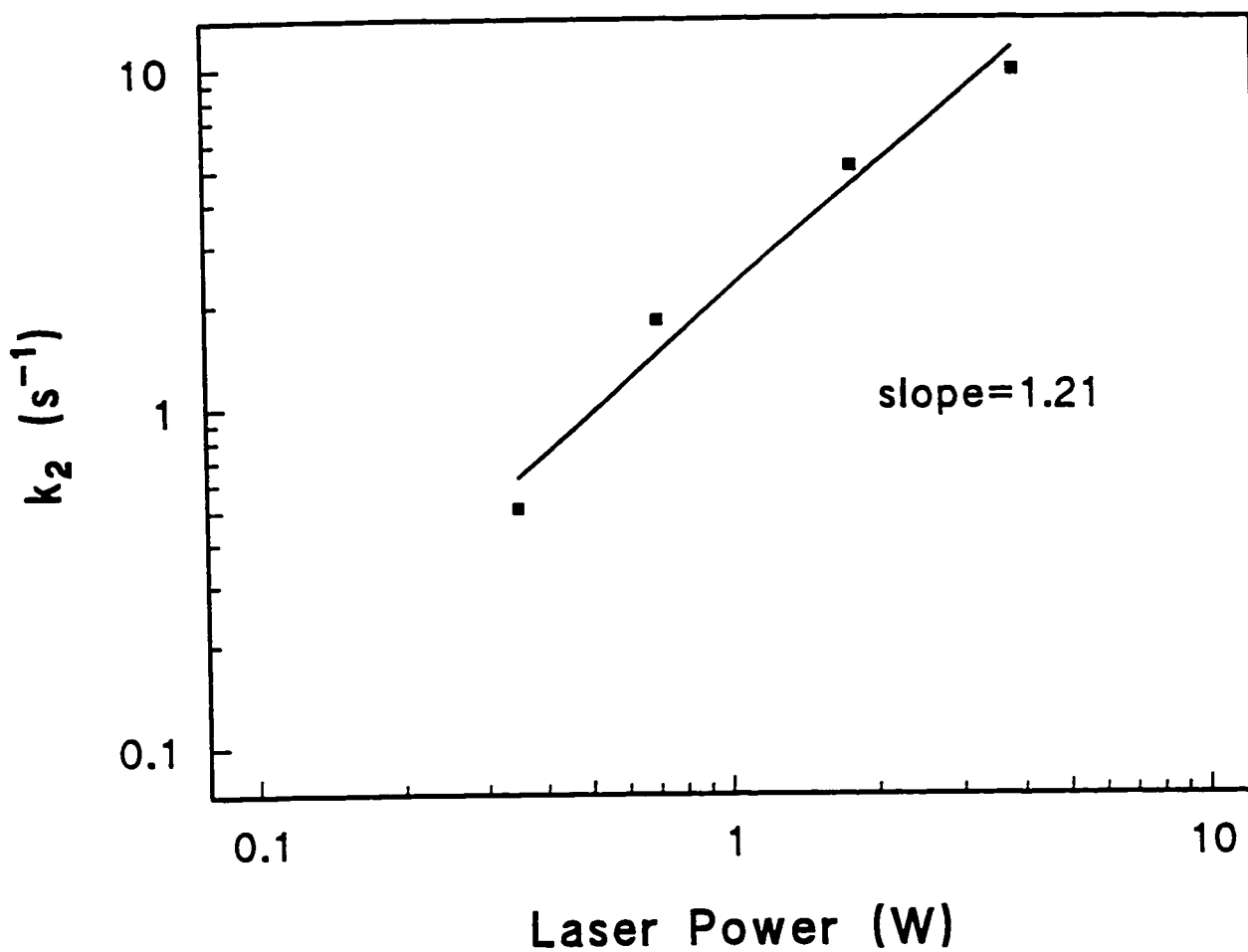


**Figure 24** A logarithmic plot of  $k_2$  vs. laser power for the photodissociation of  $[(\text{C}_4\text{H}_9)_2\text{CO}]_2\text{H}^+$  ion at 20 °C.

**Table 3.2 Photodissociation Data for the Proton Bound Dimer Ion of Nonanone.**

- Values were determined from fitting the data to equation (41).

Temperature (°C)	Laser Intensity (W cm <sup>-2</sup> )	k <sub>1</sub> (s <sup>-1</sup> )	k <sub>2</sub> (s <sup>-1</sup> )	A <sub>1</sub>	A <sub>2</sub>
20	9.9	3.3x10 <sup>-3</sup>	9.8	0.75	0.25
	4.6	2.7x10 <sup>-3</sup>	5.1	0.74	0.25
	1.8	3.7x10 <sup>-3</sup>	1.8	0.77	0.24
	0.86	2.2x10 <sup>-3</sup>	0.51	0.81	0.19



### 3.3.3 Proton Bound Dimer of Diethyl Ether

The photodissociation of the proton bound dimer of diethyl ether produced protonated ether which undergoes subsequent photolysis. The FT-ICR mass spectrum of the isolated  $[(C_2H_5)_2O]_2H^+$  ion and all of the resulting photoproducts are shown in Chapter 4 of this thesis. The ions were produced from approximately 2% reagent grade diethyl ether in a methane bath gas. The ion source pressure ( $P_{IS}$ ) was  $\sim 3.5$  torr. At the experimental temperatures of 20, 30, 43 and 66 °C,  $P_{ICR}$  was 2.0, 2.3, 2.5 and  $3.5 \times 10^{-9}$  mbar, respectively. The preceding pressure values are uncorrected ionization gauge readings. No dissociation of the  $[(C_2H_5)_2O]_2H^+$  ion due to black body radiation was observed at the experimental temperatures. The photodissociation kinetics were obtained using the following relaxation delays in this order: {ionization,  $d_2=1$  s, shot ejection,  $d_5=2$  s, shot ejection,  $d_4=1$  s, laser ON,  $vd$ , laser OFF, detection}. At each of the four temperatures, kinetic plots of  $[(C_2H_5)_2O]_2H^+$  ion intensity vs. irradiation time were obtained with laser intensities ranging between 9.9 and 0.9 W cm<sup>-2</sup>. The photodissociation kinetics of  $[(C_2H_5)_2O]_2H^+$  at laser intensities of 0.9, 1.8, 3.3, 6.9, 8.9 and 10 W cm<sup>-2</sup> is shown in Figure 25. Similar plots were obtained at the other experimental temperatures and were not included here for the sake of brevity. The photodissociation rate constants and relative abundances of the  $A_1$  and  $A_2$  species are obtained by fitting each of the curves in the figure to equation (41). The results are tabulated in Table 3.3.

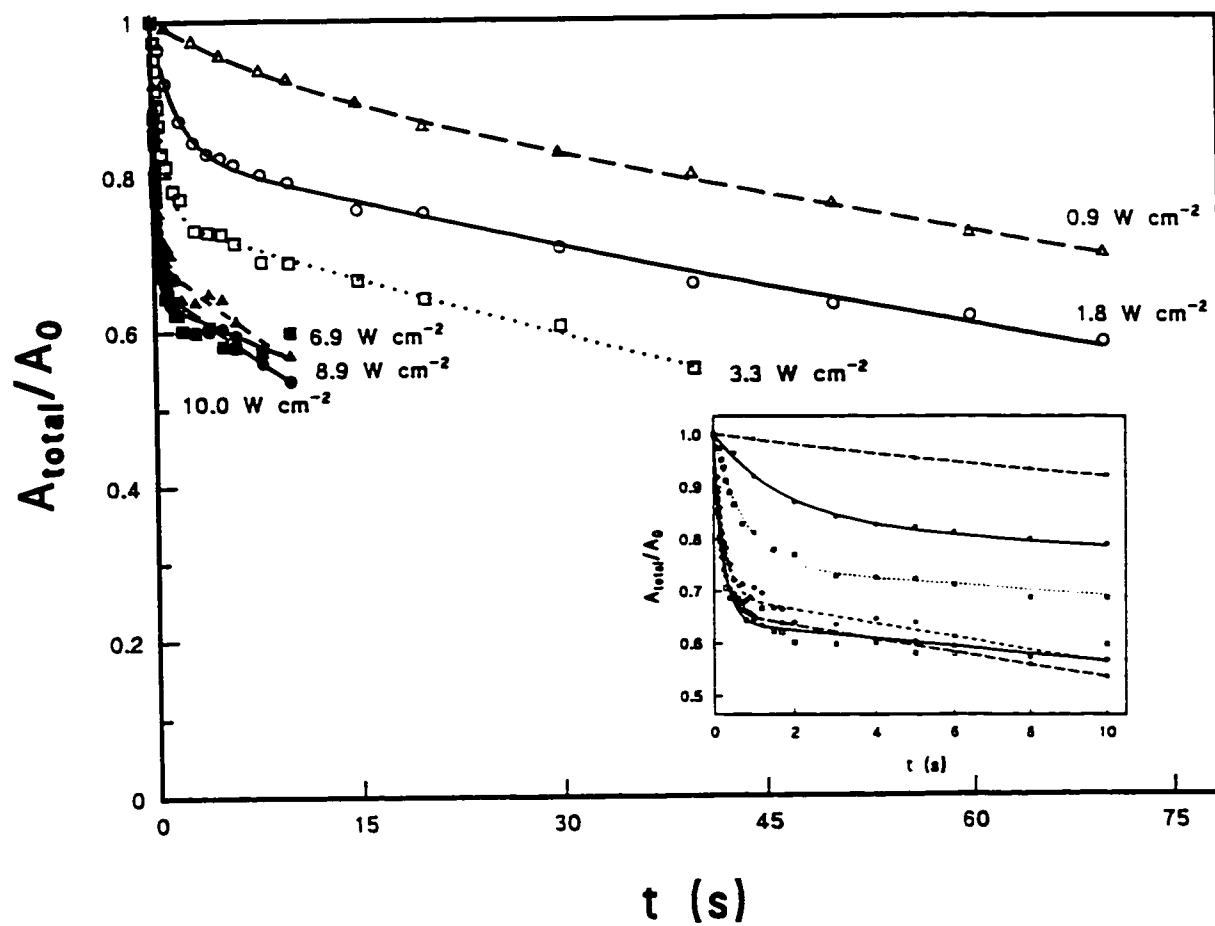


**Figure 25** Plots of normalized  $[(\text{CH}_3\text{CH}_2)_2\text{O}]_2\text{H}^+$  ion intensity vs. irradiation time at 20 °C for six different laser intensities as indicated on the figure.

**Table 3.3 Photodissociation Data for the Proton Bound Dimer Ion of Diethyl Ether**

- Values were determined from fitting the data to equation (41)

Temperature (°C)	Laser Intensity (W cm <sup>-2</sup> )	k <sub>1</sub> (s <sup>-1</sup> )	k <sub>2</sub> (s <sup>-1</sup> )	A <sub>1</sub>	A <sub>2</sub>
20	10	1.2x10 <sup>-2</sup>	4.4	0.64	036
	8.9	2.1x10 <sup>-2</sup>	5.1	0.66	034
	6.9	2.0x10 <sup>-2</sup>	4.3	0.69	032
	3.3	7.5x10 <sup>-3</sup>	1.3	0.74	026
	1.8	5.2x10 <sup>-3</sup>	0.57	0.82	018
	0.9	4.4x10 <sup>-3</sup>	0.11	0.91	010
30	10	1.3x10 <sup>-2</sup>	3.4	0.61	036
	7.6	1.1x10 <sup>-2</sup>	2.8	0.64	034
	4.6	8.0x10 <sup>-3</sup>	1.3	0.68	029
	1.8	5.1x10 <sup>-3</sup>	0.65	0.82	018
	0.86	3.7x10 <sup>-3</sup>	0.14	0.89	011
43	9.9	1.4x10 <sup>-2</sup>	4.0	0.55	043
	4.7	9.8x10 <sup>-3</sup>	1.7	0.64	035
	1.8	5.6x10 <sup>-3</sup>	0.61	0.77	024
66	9.8	2.2x10 <sup>-2</sup>	3.7	0.55	042
	4.3	1.3x10 <sup>-2</sup>	1.7	0.65	032
	1.8	9.5x10 <sup>-3</sup>	0.72	0.73	027

### 3.3.4 Protonated Diethyl Ether

The protonated diethyl ether ion,  $(\text{C}_2\text{H}_5)_2\text{OH}^+$  was not produced in any appreciable quantity from the high pressure ion source. The ion may be produced by photodissociation of  $[(\text{C}_2\text{H}_5)_2\text{O}]_2\text{H}^+$ , as seen in the previous section of this thesis. The use of the double laser irradiation technique allowed the production of  $(\text{C}_2\text{H}_5)_2\text{OH}^+$ , in the first irradiation stage and then isolation and subsequent photolysis. The photodissociation of  $(\text{C}_2\text{H}_5)_2\text{OH}^+$  produced  $\text{C}_2\text{H}_5\text{OH}_2^+$ , which can be further photodissociated to form exclusively  $\text{H}_3\text{O}^+$  *via* ethylene elimination. The reaction sequence resulting from the photodissociation of the proton bound dimer of diethyl ether is the subject of Chapter 4. The spectra of the isolated  $(\text{C}_2\text{H}_5)_2\text{OH}^+$  ion as well as the products are also presented in Chapter 4. The photodissociation kinetics were obtained at 20 °C and are plotted in Figure 26. The curve displayed in the figure is the result of fitting the data to Equation (41). The values obtained from the fitting are:  $k_1=0.025 \text{ s}^{-1}$ ,  $k_2=0.48 \text{ s}^{-1}$ ,  $A_1=0.33$ ,  $A_2=0.68$ .

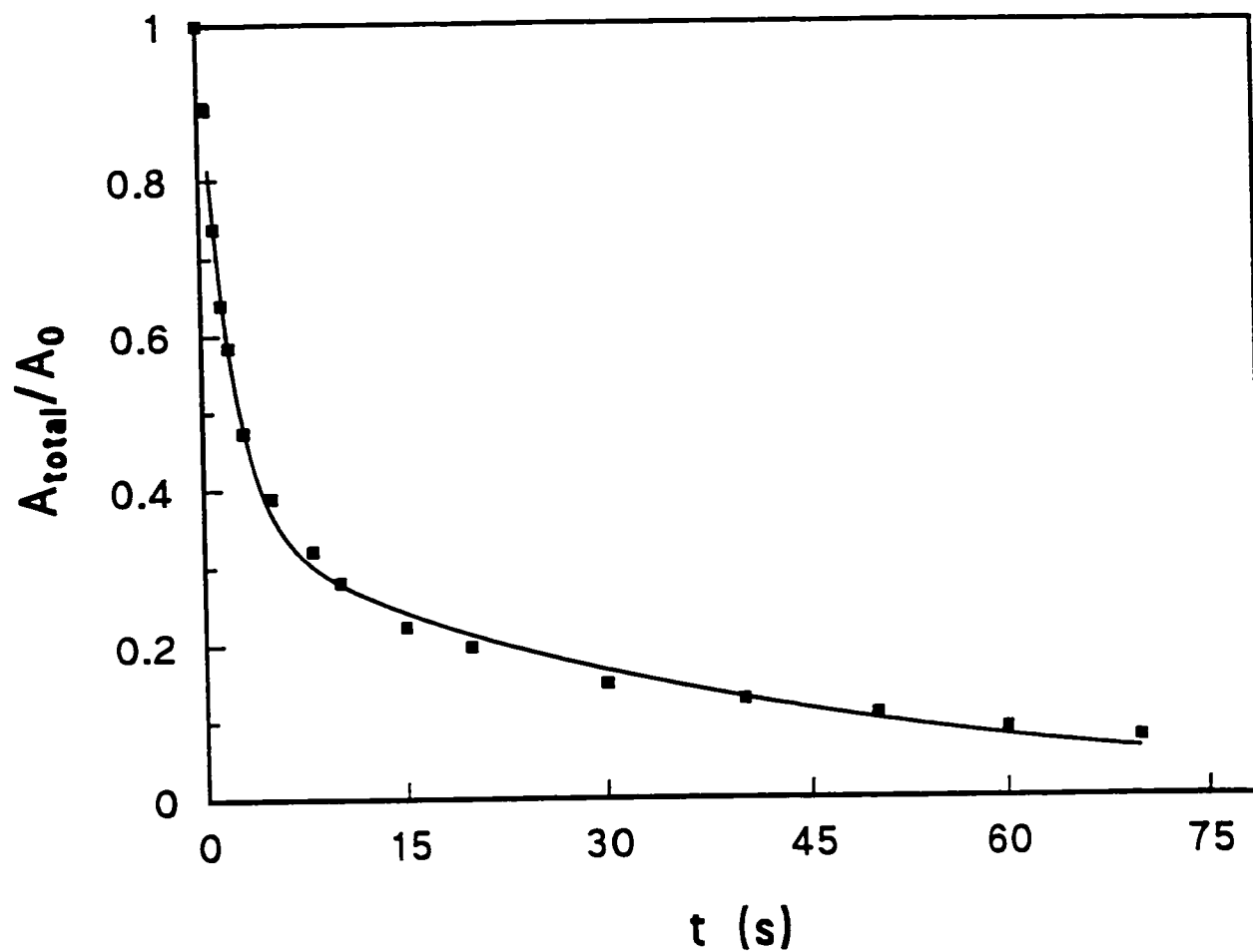


**Figure 26** The photodissociation kinetics of  $(\text{C}_2\text{H}_5)_2\text{OH}^+$  (prepared by the first stage of a double irradiation experiment) at 20 °C.

### 3.4 Discussion

#### 3.4.1 Early vs. Late Bottleneck

The occurrence of a slow, rate limiting step in the absorption of the initial photon(s) is the most commonly accepted cause of a bottleneck in IRMPD experiments. However, the experiments presented here represent a new and unique regime of large molecular size and long irradiation time, therefore, the relevance of current models of IRMPD must be considered carefully. The effects of temperature, pressure, laser intensity, ion size, and density of states will be discussed in this section. This evidence will be used to investigate the mechanism or mechanisms responsible for the observed non-first order kinetics and to ascertain whether kinetics are consistent with an early or late bottleneck, as defined in Section 3.1.3 of this thesis. Early bottlenecks are discussed in terms of the specific underlying cause, either vibrational bottlenecking or rotational hole burning.

*Intensity Dependence.* The photodissociation kinetics for the proton bound dimer of pentanone,  $[(\text{CH}_3\text{CH}_2)_2\text{CO}]_2\text{H}^+$ , at 4 different laser intensities were presented in Figure 23. The results are re-plotted in Figure 27 as a plot of the normalized parent ion abundance vs. laser fluence to illustrate both the fluence AND intensity dependence of the data. The data were fit to Equation (41). It may be seen from Figure 27 that both the fraction of the absorbing species,  $A_2$ , and the initial dissociation rate constant,  $k_2$ , increase with increasing laser intensity. Many IRMPD models predict that the rate

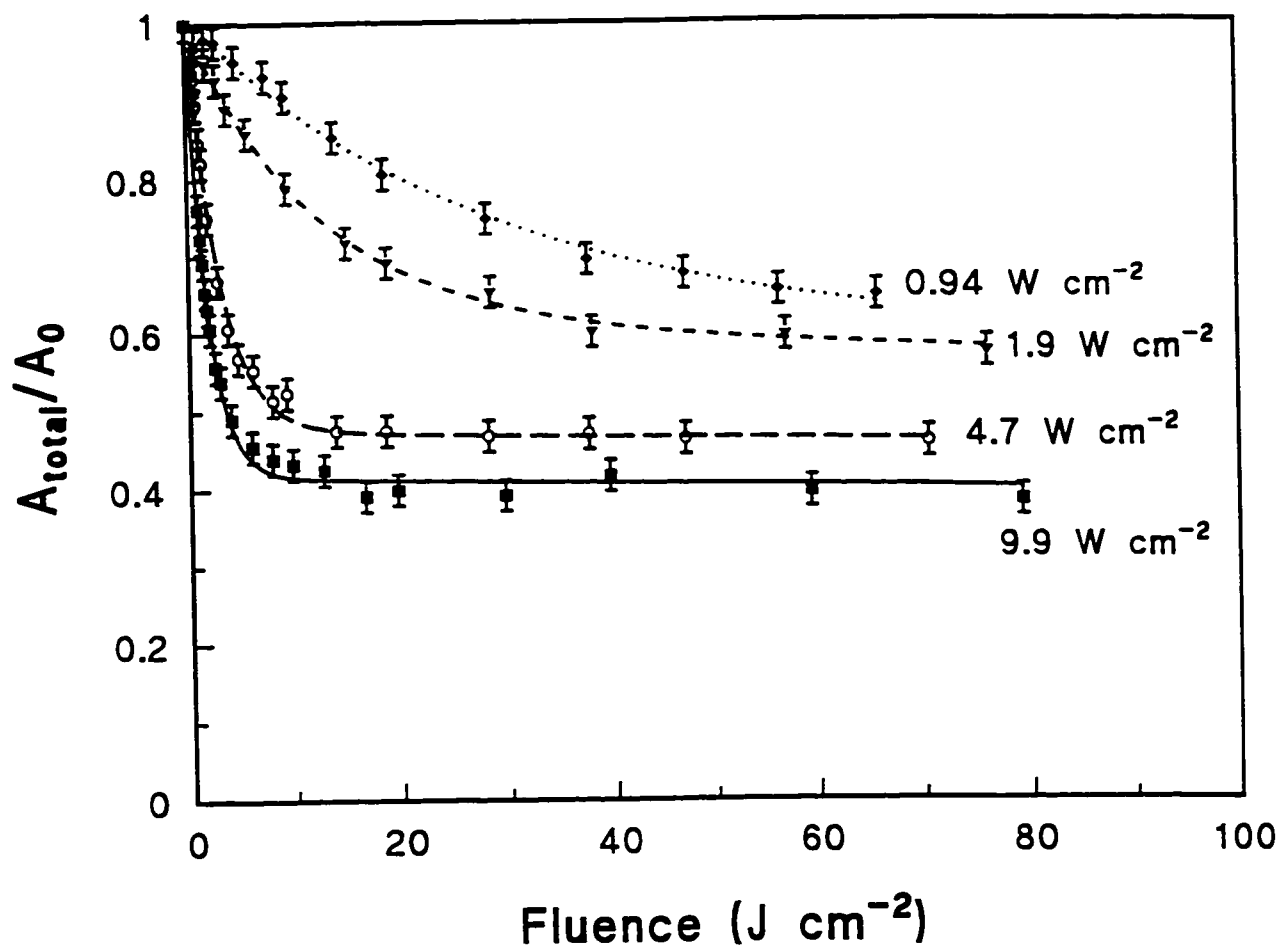


**Figure 27** A plot of  $[(\text{CH}_3\text{CH}_2)_2\text{CO}]_2\text{H}^+$  ion intensity as a function of laser fluence at  $41^\circ\text{C}$  for laser intensities of 9.7, 4.6, 1.8,  $0.91 \text{ W cm}^{-2}$ .

of photon absorption in the quasi-continuum will depend only on laser fluence, while photon absorption through discrete transitions should be intensity controlled.<sup>59</sup> Quack has suggested that IRMPD should show strong intensity dependence for the explicit case of low intensity radiation and an early bottleneck due to off-resonant transitions.<sup>25</sup> Thus, the observed intensity dependence would indicate that the bottleneck occurs in a discrete region of the ro-vibrational manifold, consistent with a rotational hole burning mechanism. Although the laser intensities used here are small compared to pulsed laser IRMPD experiments, power broadening may still be the dominant<sup>60</sup> homogenous line broadening mechanism due to the extremely narrow intrinsic linewidth of these transitions, for the typical conditions of the FT-ICR experiment. The greater fraction of ions dissociated with increased laser intensity would then be consistent with an increased number of individual transitions which overlap the bandwidth of the laser.

A point of clarification should be made regarding the rotational hole burning mechanism discussed above. Such a process would likely correspond to a depletion of a *band* of rotational states, rather than a single J state. The laser linewidth is sufficiently narrow to encompass only a few discrete ro-vibrational transitions at most. However, there are over 100 rotational states populated at room temperature and dissociation of only those ions with some  $J \pm 3$  would hardly be sufficient to account for 50% dissociation yields. Since the Rabi frequency<sup>61</sup> is on the order of  $10^6 \text{ s}^{-1}$  and the observed dissociation rates are  $<10 \text{ s}^{-1}$ , there would be a rapid cycling of the



ions up and down the vibrational manifold. Each transition can change the total angular momentum by  $\Delta J = \pm 1$  and therefore the absorbing state can be repopulated from rotational states up to  $J \pm 20$  (since the dissociation threshold is  $\sim 11$  photons above the zero point energy) through this optical pumping mechanism. When overtones and coupling between states are accounted for, this rotational hole burning mechanism could potentially account for the observed yields. There are, however, conflicting reports and opinions concerning the intensity dependence of IRMPD rates. Additionally, the validity of Quack's limiting cases is based upon knowledge of the coupling matrix elements,  $V_{IJ}$  which are not known for the current systems. Thus, a cautious interpretation of the intensity dependence data is advised. Quack also predicts a strong intensity dependence for the case of a late bottleneck caused by a slow dissociation rate for molecules above the dissociation threshold ( $E_{th}^{diss}$ ). The importance of this result will become clear in the discussion of late bottlenecks which follows.

*Density of States.* For the rotational hole burning mechanism discussed above to be responsible for the IRMPD bottleneck, the initial photon absorption must take place between TWO discrete states. A large fraction of the ions studied here, however, possess thermal internal energy either above, or within one photon of, the quasi-continuum threshold energy ( $E_{th}^{quasi}$ ) initially. By definition, ions with internal energy greater than  $E_{th}^{quasi}$  must always have an upper state resonant with the laser line and, hence, the entire process of IRMPD occurs within the quasi-continuum region.

Ions with less energy than  $E_{\text{th}}^{\text{quasi}}$  do not dissociate or are much slower. Thus, a thermal vibrational bottleneck occurs as described in section 3.1.3. It is, therefore, useful to determine the fraction of ions which have energy in excess of  $E_{\text{th}}^{\text{quasi}}$ . For the proton bound dimer of diethyl ether, the average energy spacing between states has been estimated<sup>9, 21</sup> from the Whitten-Rabinovitch approximation<sup>62</sup> to be  $0.008 \text{ cm}^{-1}$  and  $10^{-5} \text{ cm}^{-1}$  at  $1000 \text{ cm}^{-1}$  and  $2000 \text{ cm}^{-1}$  above the zero point energy, respectively. Since the laser linewidth is estimated to be on the order of  $0.003 \text{ cm}^{-1}$ , the onset of the quasi-continuum region should be between  $1000 \text{ cm}^{-1}$  and  $2000 \text{ cm}^{-1}$ . Dunbar has shown<sup>63</sup> that for molecules with 90 degrees of freedom, (the approximate size of diethyl ether or pentanone dimer ions) approximately 30 % of the ions, in a 300 K thermal distribution, possess internal energy in excess of  $2000 \text{ cm}^{-1}$  and about 70% have internal energy greater than  $1000 \text{ cm}^{-1}$ . We can, therefore, estimate that 30-70% of the ions should be rapidly dissociated by incoherent pumping through the quasi-continuum. These ions are represented by  $A_2$  in Reaction Scheme 2 and the rate constant for the dissociation is  $k_2$ . The ions in lower vibrational states with energy less than  $E_{\text{th}}^{\text{quasi}}$  are represented by  $A_1$  in Reaction Scheme 2. These ions are essentially unaffected by the laser and a truncated Boltzmann energy distribution results. The  $A_1$  species may gain enough energy to move into the quasicontinuum either by absorption of ambient black body radiation or collisional energy transfer from neutral molecules. The rate constant,  $k_1$ , will reflect the rate of the dominant energy transfer process. The value of  $A_2=30\text{-}70\%$ , estimated above, qualitatively agrees with

the fraction of ions dissociated before the plateau in all of the kinetic plots. Thus, the calculated density of states provides a strong indication that the observed kinetics are caused by a thermal vibrational bottleneck. Before rotational hole burning is excluded, it should be noted that the above estimates are based on classical arguments. Optical selection rules and angular momentum constraints have been ignored. Therefore, the threshold for the onset of the "effective" quasicontinuum may be much higher than the density of states predicts and absorptions into discrete lower states may still be the rate limiting step for ions which appear to be in the large molecule limit.

*Temperature Dependence.* The photodissociation kinetics of  $[(\text{CH}_3\text{CH}_2)_2\text{CO}]_2\text{H}^+$  for four different temperatures ranging from 20 - 75 °C are shown in Figure 28. Increasing the temperature substantially increases the fraction of ions which is initially dissociated ( $A_2$ ) and increases the rate constant ( $k_2$ ) to a lesser extent. This is consistent with a thermal vibrational bottleneck and the rapid burning-off of the ions with internal energy above the onset of the quasicontinuum. The rate constant for dissociation at long time,  $k_1$ , increases with increasing temperature as well and complete dissociation of the parent ion is observed at 60 s at 75 °C. Since the intensity of black body radiation increases with increasing temperature, it is tempting to interpret the increase in  $k_1$  as the result of an increase in the rate of repopulation of the energy levels above the quasicontinuum threshold. At this temperature, however, the black body unimolecular dissociation rate is approaching the laser dissociation rate and the resultant curve is a convolution of the two processes. Thus, the increasing

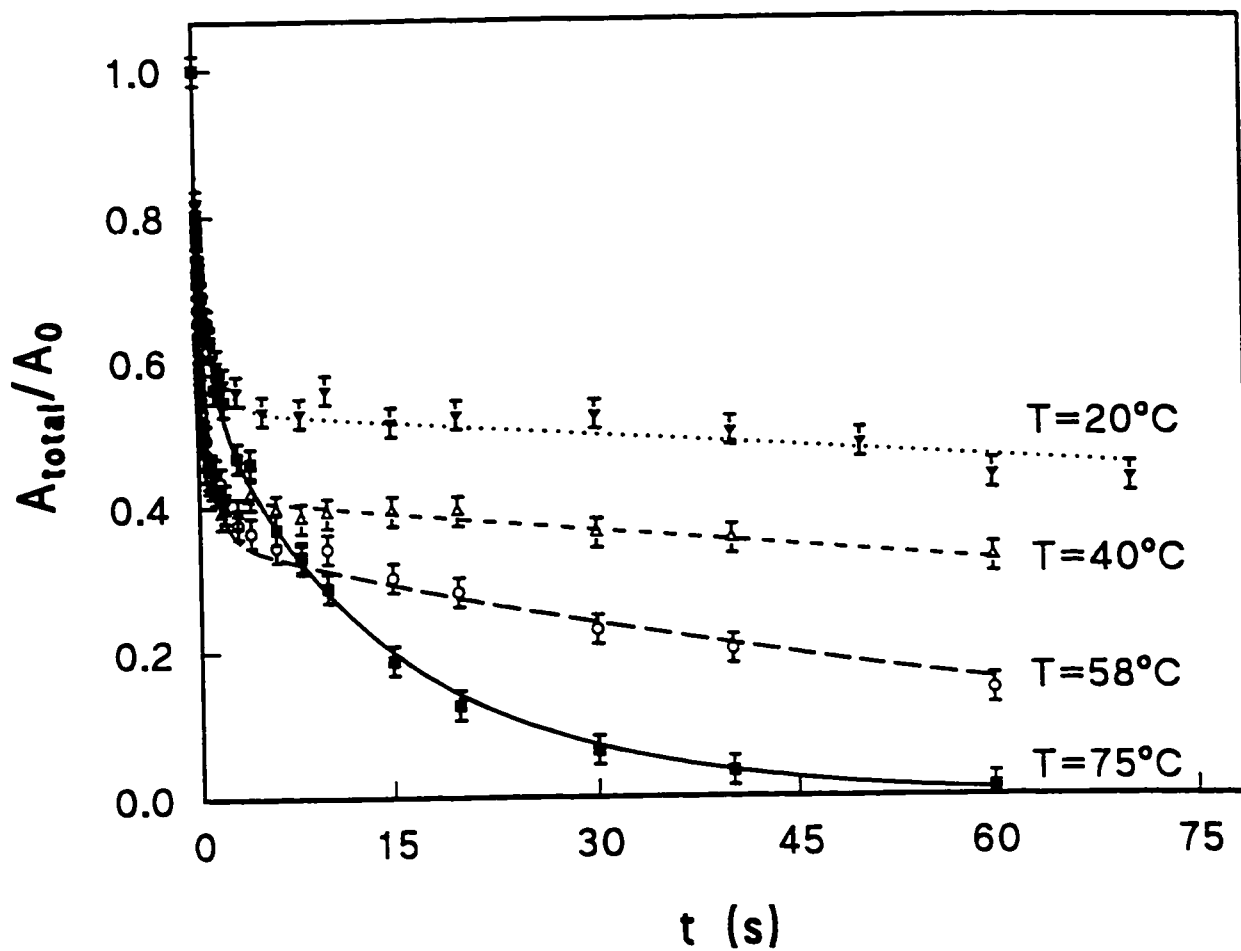


**Figure 28** Photodissociation kinetics for  $[(\text{CH}_3\text{CH}_2)_2\text{CO}]_2\text{H}^+$  at temperatures of  $20^\circ\text{C}$  (a),  $40^\circ\text{C}$  (b),  $58^\circ\text{C}$  (c),  $75^\circ\text{C}$  (d).  $I=9.9 \text{ W cm}^{-2}$ .

dissociation rate at long times can be attributed to either conversion from  $A_1$  to  $A_2$  *via* thermal repopulation of the absorbing species ( $A_2$ ) or a parallel purely unimolecular black body dissociation of the non-absorbing species ( $A_1$ ). The two processes cannot be distinguished from the observed kinetics.

The combination of the density of states calculation and the temperature dependence would seem to make a strong case for thermal vibrational bottlenecking. It should be noted, however, that a bottleneck caused by rotational hole burning could also exhibit temperature dependent dissociation kinetics. The Doppler linewidth, at 300 K, of the  $[(CH_3CH_2)_2O]_2H^+$  ion ( $m/z=149$ ) is 30 MHz and is expected to be the dominant line broadening mechanism. The Doppler width of an optical transition is proportional to  $T^{1/2}$ . Therefore, the fraction of ro-vibrational transitions which overlap the laser bandwidth would increase with increasing temperature. This would result in an increased dissociation yield which is in qualitative agreement with our data.

*Size Dependence.* A plot of the dissociation kinetics for  $(CH_3CH_2)_2OH^+$ ,  $[(CH_3CH_2)_2O]_2H^+$ ,  $[(CH_3CH_2)_2CO]_2H^+$  and  $[(CH_3CH_2CH_2CH_2)_2CO]_2H^+$  ions, obtained at laser intensities of  $9.8 \pm 0.1 \text{ W cm}^{-2}$ , is presented in Figure 29. The three dimer ions have bond dissociation enthalpies of approximately<sup>32</sup> 29 kcal mole<sup>-1</sup> and the ethylene elimination from protonated diethyl ether is 28.5 kcal mole<sup>-1</sup> endothermic.<sup>64</sup> Hence, differences due to energetic effects should be negligible. It can be seen from the figure that as the size of the ion increases, the initial dissociation rate increases but the fraction dissociated prior to the plateau decreases. For ions with the same bond

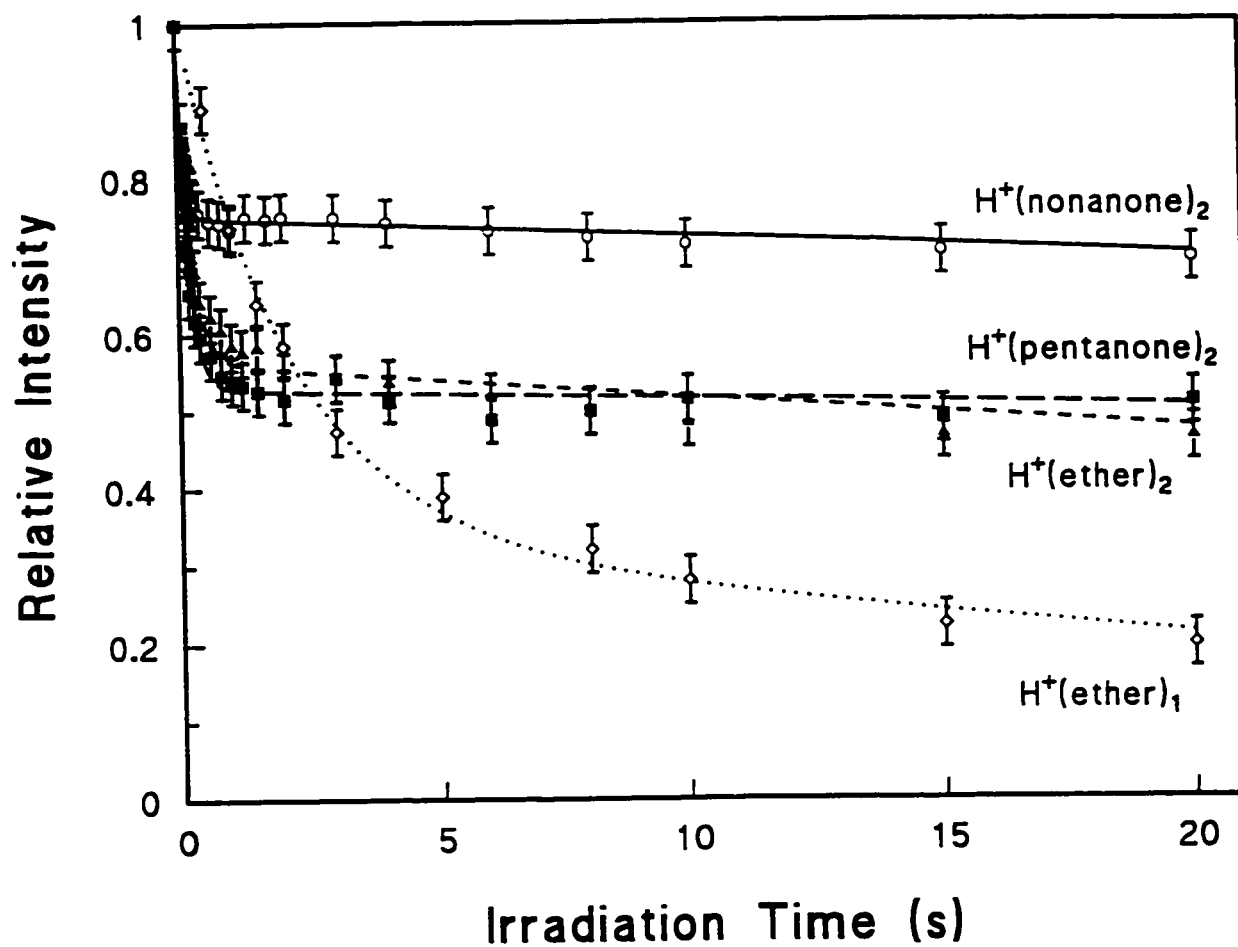


**Figure 29** The effect of ion size on IRMPD kinetics.  $I=9.8\pm0.1 \text{ W cm}^{-2}$ .

dissociation energy, the density of states at a given energy,  $\rho(E)$ , will be greater for the larger species, simply because of the increase in the number of vibrational modes. Thus, the quasi-continuum threshold is effectively shifted to lower energy for the larger species. The classical internal energy content also increases with the number of vibrational modes. Therefore, a greater fraction of the ions have internal energy in excess of  $E_{th}^{quasi}$ . Both of these factors suggest that the fraction of ions dissociated should increase with increasing size in obvious contradiction with the data. Therefore, the effect of ion size on the photodissociation kinetics is not consistent with a thermal vibrational bottleneck.

The observed size dependence would tend to support a late bottleneck rather than either type of early bottleneck, however, the existence of a rate limiting step at high levels of vibrational excitation is not consistent with the simplified model of IRMPD rates being proportional to the density of states. Quack has examined the master equation modelling of IRMPD with a late bottleneck.<sup>25</sup> Late bottlenecks may be observed for systems with slow dissociation rate constants,  $k_D(E)$ . Large molecules with energy just above threshold will have small values for  $k_D(E_{th})$  because the statistical probability of all of the energy finding its way into the correct dissociation channel, versus random distribution among the many other modes, approaches zero. In the extreme case, very large bio-molecules may have nearly infinite lifetimes  $\{\tau_{th}=k_D(E_{th})^{-1}\}$  just above threshold. Photodissociation with the low intensity CW laser used here has been shown to selectively produce only those fragment ions

resulting from the lowest dissociation channel.<sup>14</sup> An upper limit to the energy discrimination of this technique has been shown to be  $\Delta E \leq 3 \text{ kcal mole}^{-1}$  as discussed in Chapter 4. The decomposition step in these experiments, therefore, occurs when ions have energy no greater than one  $\text{CO}_2$  photon ( $2.7 \text{ kcal mole}^{-1}$ ) above threshold. The dissociation rate of the energized proton bound dimer ion of diethyl ether has been estimated at  $k_D = 10^3 \text{ s}^{-1}$  from radiative association reactions.<sup>65</sup> Since this rate is  $\sim 100$  times greater than the dissociation rates observed in the present experiments,  $k_D$  does not appear to be rate limiting. It should be noted, however, that the decomposition reaction which is observed in radiative association experiments may occur substantially above the dissociation threshold and that  $k_D$  increases rapidly with energy above the threshold. Thus, considering the size of the ions studied here and the evidence for near threshold fragmentation, it is reasonable to expect that  $k_D$  will be slow and that a subsequent late bottleneck may exist.

If the observed non-first order kinetics result from a late bottleneck,  $k_D$  may not be the only factor contributing to the size dependence. A complete description must also include spontaneous emission. The larger ions have more oscillators and hence absorption is more rapid, as evidenced by the faster initial dissociation rate. The spontaneous emission rate might also be expected to be faster for the same reason. Thus, a steady state of up and down pumping may be reached sooner as a result. This was demonstrated in calculations by Quack for weak field late bottleneck conditions.<sup>25</sup> This treatment did not specifically address an increased spontaneous emission rate but



instead defined an overall quenching rate. The quenching effect is expected to be the same for spontaneous emission as for quenching due to collisions, however.

*Pressure Dependence.* In an effort to probe quenching effects, the dissociation kinetics for  $[(\text{CH}_3\text{CH}_2)_2\text{O}]_2\text{H}^+$  were obtained with  $2.0 \times 10^{-9}$  mbar  $\text{CH}_4$ ,  $1.3 \times 10^{-7}$  mbar  $\text{CH}_4$  and  $2.9 \times 10^{-8}$  mbar diethyl ether added to the FT-ICR cell. The results are plotted in Figure 30. The initial dissociation rate is essentially unchanged by addition of the collision gasses but the *fraction* initially dissociated decreases.  $[\text{A}_2]_0$ , is 0.4, 0.3 and 0.2 respectively. Even though the diethyl ether pressure is lower than the methane pressure, the internal energy transferred per collision is expected to be more efficient for the larger molecule. Ligand switching with neutral diethyl ether molecules will also occur at approximately one half of the collision rate. Ligand switching with a thermally equilibrated bath gas will be a very efficient energy transfer mechanism. Thus, the observed pressure dependence of  $\text{A}_2$  is entirely at odds with either type of early bottleneck because increasing the bath gas pressure (or size) would be expected to increase the photolysis yield by either rotational hole filling or thermal repopulation of ions with  $E > E_{\text{th}}^{\text{quasi}}$ . The long time dissociation rate constant,  $k_1$ , does increase slightly with the addition of collision gas and could be attributed to either rotational hole filling or repopulation of higher energy vibrational states, however, the observed pressure dependence on  $\text{A}_2$  is consistent with collisional quenching and its effect will be much the same as the effect of an increased spontaneous emission rate proposed in the previous section.

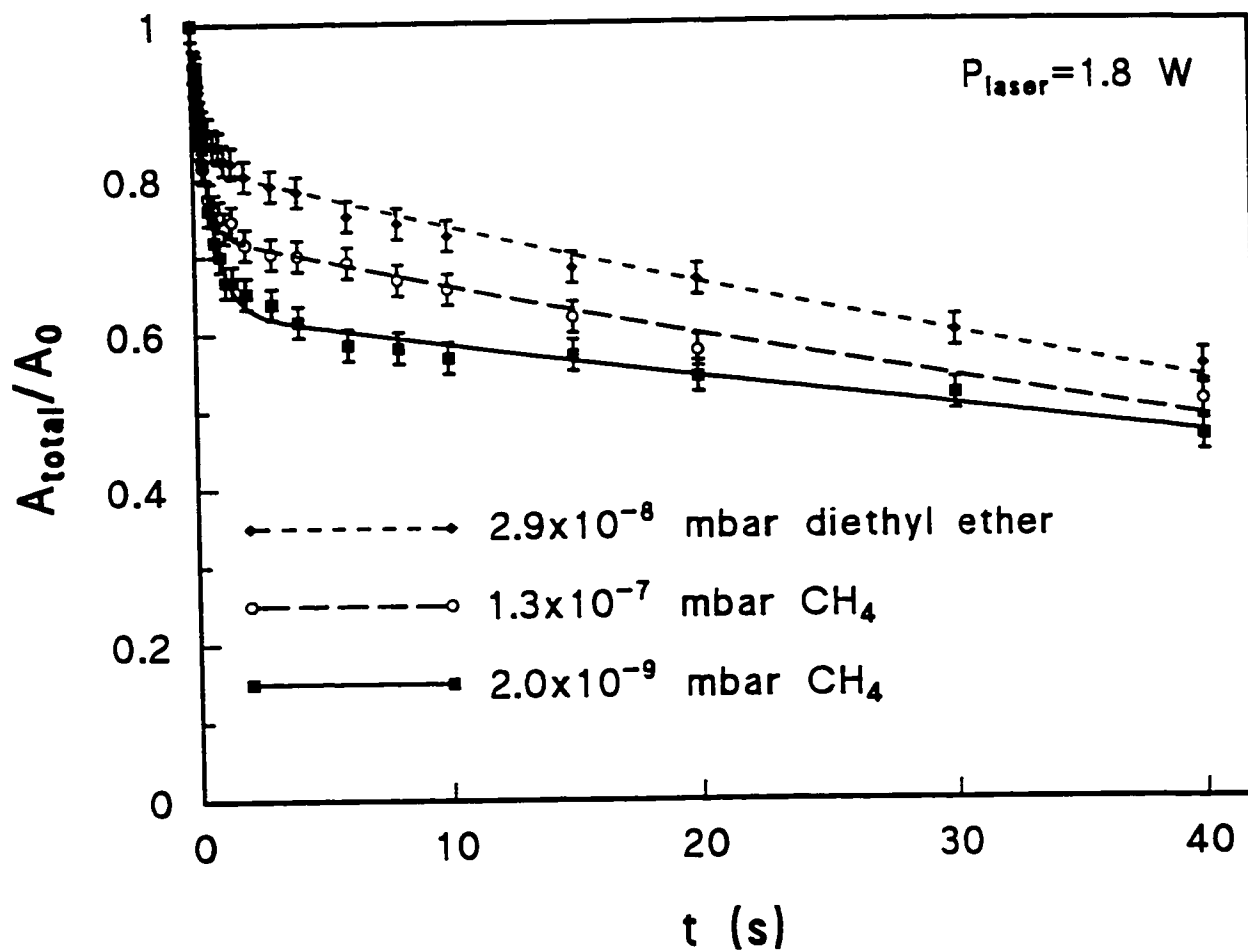


**Figure 30** The pressure dependence of the dissociation kinetics for  $[(\text{CH}_3\text{CH}_2)_2\text{O}]_2\text{H}^+$  with various bath gasses added to the FT-ICR cell.

*Bond Enthalpy.* For purposes of elucidating the origin of the non-linear kinetics, great care was taken to study species with comparable bond enthalpies. What would happen, however, if the bond were weaker? Several other systems with weaker bond enthalpies have been photodissociated using the same experimental methodology used in these experiments. The photodissociation kinetics of chloride-alkyl bromide  $S_N2$  complexes will be presented in Chapter 5 of this thesis. As mentioned in section 3.1, the photodissociation of  $H_3O^+(H_2O)_3$  has been studied previously.<sup>15</sup> Additionally, IRMPD experiments on chloride-alcohol clusters are currently underway.<sup>66</sup> Each of these cluster ions has a bond enthalpy in the range of 12-22 kcal mole<sup>-1</sup>. None of these cluster ions displayed the marked deviation from first order kinetics that was observed in the proton bound dimer ion experiments presented in this chapter. Furthermore, the  $Cl^-(i-C_3H_7OH)_2$  ion is close to the same size as the ions studied here which indicates that the bond enthalpy effect is real and not just necessarily related to the ion size effect reported.

*Induction Time.* No evidence of an induction time was observed in any of the results presented in this thesis. This differs from with the results of Beauchamp<sup>9, 21, 11a)</sup> *et al.* who observed induction times in the IRMPD of  $[(CH_3CH_2)_2O]_2H^+$  generated by electron impact of neutral diethyl ether in the ICR cell. Their reported induction times ranged from 20-100 ms for laser intensities of 20 and 4 W cm<sup>-2</sup> respectively. The minimum irradiation time possible with our current shutter configuration is 100 ms so an induction time shorter than this would not be observed. However, when

experiments were performed without the shutter, in which the ions were subjected to irradiation immediately upon entering the FT-ICR cell, more dissociation was initially observed, suggesting that there is no induction time in these experiments. One possible explanation for this discrepancy is that the neutral diethyl ether molecules, which are present in Beauchamp's experiment at pressures of  $\sim 10^{-7}$  torr, are absorbing IR laser radiation and subsequently transferring energy to the ions. Thus there would be an induction time necessary to heat up the bulk of the gas, after which a thermal unimolecular reaction occurs. Beauchamp and co-workers<sup>67</sup> also reported induction times for the IRMPD of benzyl anion while Brauman<sup>53</sup> *et al.* performed the same experiment and observed none. The source of this discrepancy is presently unclear.

*Relaxation.* Photodissociation kinetics at 20 °C were obtained for both  $[(\text{CH}_3\text{CH}_2)_2\text{O}]_2\text{H}^+$  and  $[(\text{CH}_3\text{CH}_2)_2\text{CO}]_2\text{H}^+$  ions using the double laser irradiation experiment described in section 3.2. The results are plotted in Figure 31 and Figure 32 respectively. Both experiments consisted of the following steps: 1) rf isolation of the parent ion, 2) an initial irradiation period, 3) rf re-isolation of the parent, 4) laser "OFF" delay (d4), 5) the second irradiation period, 6) detection. The kinetic plots were determined by plotting the normalized ion abundance against the time of the *second* irradiation period. The  $[(\text{CH}_3\text{CH}_2)_2\text{O}]_2\text{H}^+$  experiment used an initial irradiation period of 2 s and a 1 s d4 delay. The  $[(\text{CH}_3\text{CH}_2)_2\text{CO}]_2\text{H}^+$  experiment used an initial irradiation period of 5 s and a 1 s d4 delay.

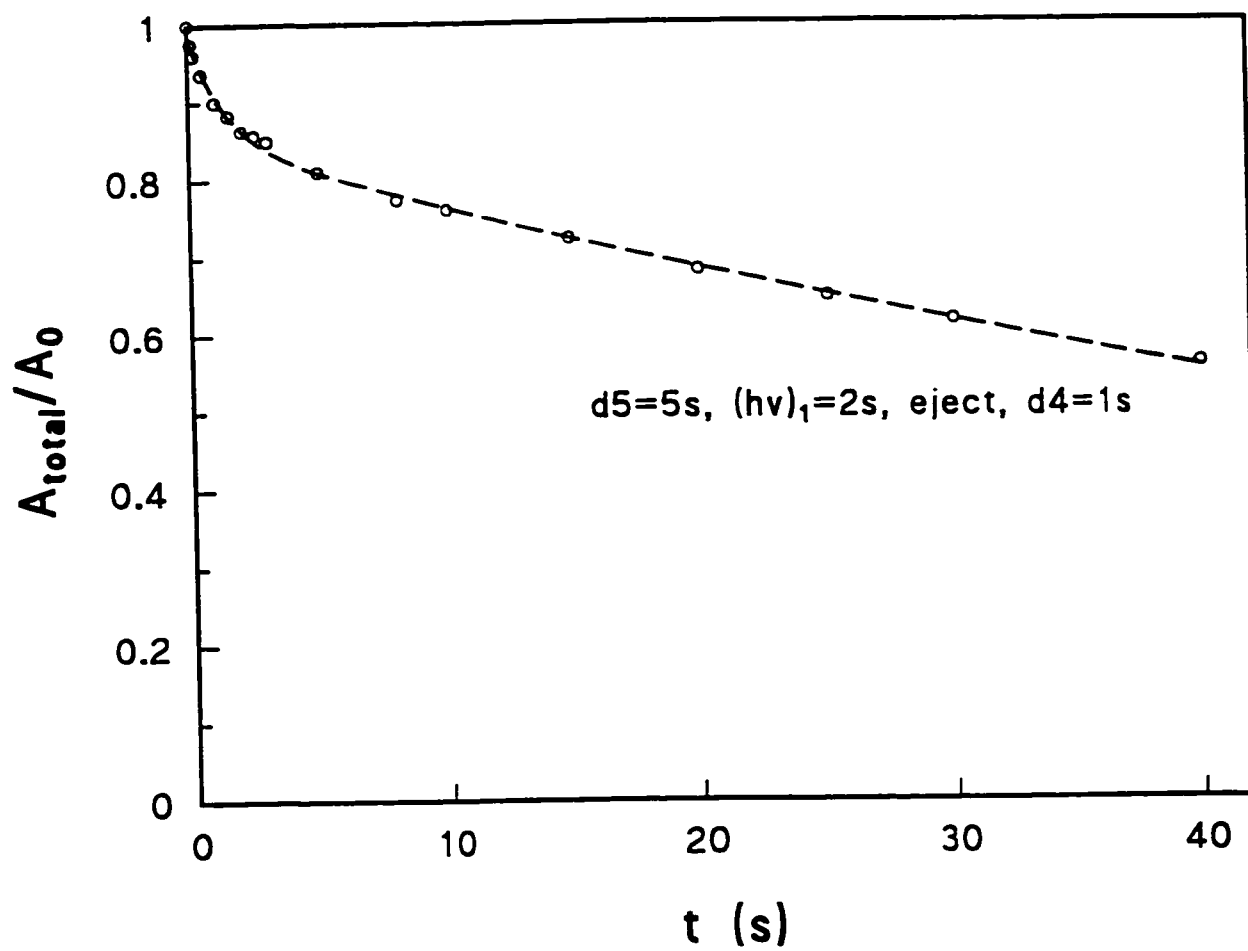


**Figure 31** The photodissociation kinetics of  $[(\text{CH}_3\text{CH}_2)_2\text{O}]_2\text{H}^+$  obtained from a double irradiation experiment.

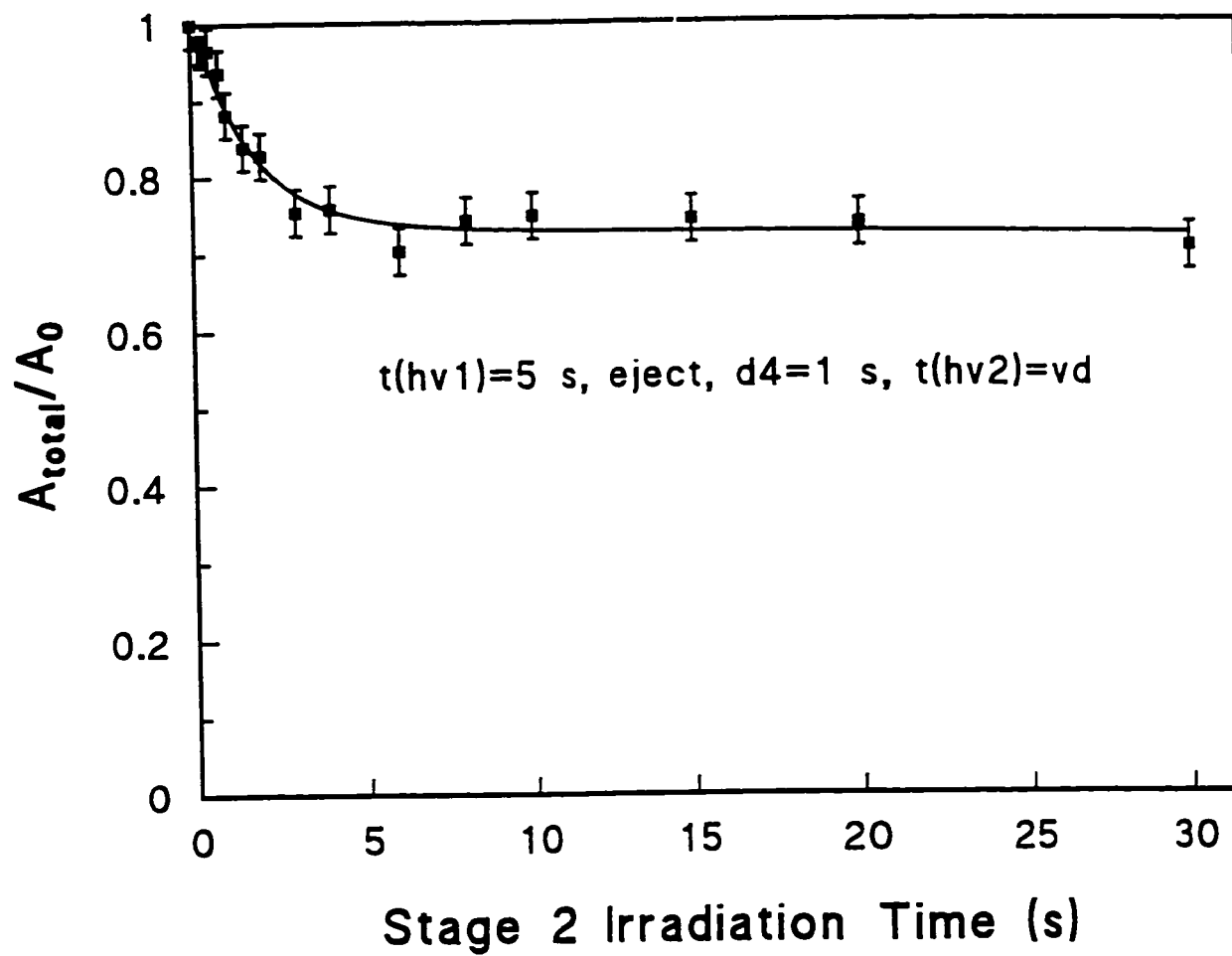


**Figure 32** The photodissociation kinetics of  $[(\text{CH}_3\text{CH}_2)_2\text{CO}]_2\text{H}^+$  obtained from a double irradiation experiment.

Both plots exhibit similar characteristics and therefore, will be discussed together. The plots contain a plateau in the curves similar to that observed in the single irradiation experiments. The rapid photodissociation yield for the double irradiation experiment,  $A_2^{\text{double}}$ , is substantially less than  $A_2^{\text{single}}$ . The irradiation time of the first laser event was sufficiently long to remove all of the rapidly dissociating ions. Therefore, all of the  $A_2$  ions in Reaction Scheme 2 have been photodissociated prior to recording the double irradiation photodissociation kinetics displayed in Figure 31 and Figure 32. If this remains true throughout the delay ( $d_4$ ), these plots should exhibit slow, first order dissociation consistent with the re-population rate constant,  $k_1$ . For an early bottleneck caused by rotational hole burning,  $k_1$  would correspond to rotational hole filling. For a thermal vibrational bottleneck,  $k_1$  would correspond to thermal re-population of the high energy portion of the distribution. Both of these processes are independent of whether the laser is ON or OFF. Since  $k_1 \leq 0.01 \text{ s}$  at  $20^\circ \text{C}$ , the extent of  $A_2 \rightarrow A_1$  conversion, during the 1 s delay, may be estimated at 1%. This is not sufficient to account for the ~15-20% of  $A_2$  that has been recovered in both Figure 31 and Figure 32. If, however, the laser is producing a "saturation" effect, in which the population inversion is caused by a slow  $k_D$  just above the dissociation threshold, the extent of relaxation when the laser is OFF for 1 s could be much greater. The combined quenching rate (collisional relaxation plus spontaneous emission) of highly excited ions is expected to be very rapid and, therefore, could easily relax the population out of this saturated condition when the

laser is OFF. Based upon this evidence, it appears likely that the "relaxation effect" observed in these double irradiation experiments, supports the proposed late bottleneck/saturation effect.

Attempts were made to duplicate this experiment at higher temperatures to increase the extent of repopulation by black body (for early bottlenecks). These experiments were impeded by the loss of total ion signal when the fragments from the initial photodissociation stage are ejected. Since the fraction of ions dissociated increases rapidly with temperature, the ion signal loss became prohibitive (at 50-60 °C) before a significant effect on the re-population rate was observed.

### **3.4.2 Non-Thermal Population Distribution**

The previous section (3.4.1) attempted to qualitatively assign the location and mechanism of the bottleneck in the IRMPD experiments by investigating the effects of changing several experimental parameters. For a quantitative analysis of the experimental data (section 3.3), a theoretical treatment of IRMPD using master equation modelling and random walk trajectory calculations would be required.<sup>25</sup> Such a calculation is beyond the scope of this thesis and may not even be accurate for such large systems. A question that *can* be addressed is whether the energy distribution is thermal? This question will be discussed by analogy to evidence presented in previous theoretical treatments, and some physical reasoning.

Dunbar has proposed that a truncated Boltzmann distribution (thermal model)



should be used to describe the internal energy of an ion population during photodissociation by low intensity CW monochromatic IR radiation.<sup>22,23,24</sup> Ironically, the current experiment shows that this model may not apply to very large molecules. Brauman *et al.* have shown that vibrational bottlenecking may occur during pulsed laser photolysis of relatively small ion-molecule complexes such as  $F^-(CH_3OH)$ .<sup>53</sup> Rapid photodissociation is observed only for those ions which were in excited vibrational states (above the bottleneck) prior to the laser pulse. In the extreme case where the discrete transitions are all far from resonant with the laser frequency, the lower energy ions will not dissociate. The resulting distribution of ion energies will be a truncated Boltzmann and the degree of truncation will depend upon the location of  $E_{th}^{quasi}$ . For small ions,  $E_{th}^{quasi}$  occurs at higher energy and only the hottest ions in the Boltzmann distribution can absorb and dissociate. The distribution then remains relatively unperturbed except for a small truncation in the tail end and the thermal model will be a good approximation. For large ions, the truncation will be much more severe, but still Boltzmann if the lowest energy ions remain unaffected by the laser.

The opposite situation occurs when the entire population of ions absorbs IR radiation from the laser and is, therefore, shifted to higher energy. As mentioned in section 3.1.2 of this thesis, this situation may occur if: 1) the intensity of the laser is sufficient to overcome the discrete state barrier as was observed during the pulsed laser photolysis of  $SF_6$  by Grant *et al.*<sup>39</sup> or 2) the ions are in the big molecule limit. The laser intensity used in these experiments is too low to power broaden all transitions,

but the density of states analysis in section 3.4.1. indicates that 30-70% of the ions in these experiments are within one photon of the quasicontinuum. Therefore, the big molecule limit is justified. There are two possible outcomes when the laser radiation is absorbed by the entire ion population. Either a higher temperature Boltzmann distribution of energy is produced or a non-thermal (but perhaps steady-state) energy distribution, peaked at high vibrational levels, results. If the ions are in thermal equilibrium, a temperature may be assigned to the ensemble, however, a truncated Boltzmann distribution requires that the rate of decomposition above the dissociation threshold ( $E_{th}^{diss}$ ) is fast compared to the rate of energization. This does not agree with the evidence for a late bottleneck (pressure and size dependence) discussed in section 3.4.1. Furthermore, the IR dissociation kinetics should be identical to a thermal unimolecular reaction (*i.e.* no break in the kinetics plots). A comparison of the initial photodissociation rate constant,  $k_2$ , with the rate constants determined from a separate ZTRID study allows the necessary temperature to be estimated at  $\sim 150^\circ\text{C}$ .<sup>32</sup>

If the rate of decomposition above  $E_{th}^{diss}$ , is slow and the ions strongly absorb IR radiation, then the population will accumulate in high energy states as shown by Quack<sup>25</sup> and Lee<sup>39</sup> for pulsed laser IRMPD experiments. The steady state population distributions calculated separately by Quack<sup>25</sup> and Lee<sup>39</sup> using master equation modelling are narrow and peaked below  $E_{th}^{diss}$ . Thus, an effect resembling saturation occurs and the resulting energy distributions are decidedly non-Boltzmann. Quack has repeatedly asserted that UNIMIR must be described by a microcanonical distribution

rather than a Boltzmann distribution as for thermal unimolecular reactions.<sup>25</sup> The exact shape, width and average energy of the steady state distribution will depend upon the relative strengths of the laser intensity, the quenching rate and the decomposition rate constant but we can draw qualitative conclusions from these models. It is easy to see why this process may exhibit a size dependence. The incoming radiation is directly exciting a single (or at most several degenerate) mode(s) but spontaneous radiation may be emitted by all modes. As the molecule or ion acquires more energy and moves up the vibrational manifold, the density of states increases dramatically. Fermi's golden rule states that the coupling rate of an isolated state to all other states is proportional to the density of states, so that molecules in highly excited vibrational states are expected to emit rapidly. The decreased photodissociation yield,  $A_2$ , observed with larger ions can, therefore, be attributed to an increased spontaneous emission rate. It is not obvious why a steady state population, decomposing with a rate constant,  $k_D$ , should exhibit the non-first order kinetics which we observe here. The explanation may be that the ions have exceeded the size limit in which the thermal approximation of low intensity IRMPD is valid and a full master equation calculation should be used instead. An accurate M.E. calculation may prove impossible for ions of this size, however.

### 3.5 Conclusions

In summary, we report the observation of a bottleneck in the IRMPD of large ions which causes the decay kinetics to deviate from first order. The complexity of the IRMPD process for ions with so many vibrational modes, has prohibited an absolute assignment of the cause of this deviation. The temperature dependence supports a vibrational bottleneck or possibly a rotational hole burning bottleneck (although the latter is supported by a weaker argument). The density of states calculation used to determine the location of the quasicontinuum threshold strongly supports a vibrational bottleneck (although again a rotational inhomogeneity in the quasicontinuum cannot be excluded with absolute certainty). The dependence of the observed kinetics on ion size, pressure and bond enthalpy would all suggest that the bottleneck occurs in the upper energy region of the vibrational manifold. The size dependence is probably because spontaneous emission, from excited vibrational levels, becomes increasingly competitive with up-pumping for the larger ions. In particular, the similar effects of increased ion size and increased collision gas pressure are strong indicators of the importance of quenching processes (spontaneous emission and collisional deactivation, respectively) to the photodissociation yield. This would be consistent with a non-thermal distribution of internal energy peaked around highly excited vibrational states just below the dissociation threshold. This "saturation" effect is a form of a population inversion caused by the slow dissociation rate of ions just above the dissociation threshold. The results of the double laser irradiation experiment

also support this saturation effect. The one second relaxation delay is too short for collisional relaxation to be effective but rapid spontaneous emission from ions which are very near threshold could easily relax the population out of this saturated condition. A future attempt at master equation modelling of these results would be useful for determining the effects of spontaneous emission and collisional quenching on the evolution of the ions through the quasi-continuum and over the dissociation threshold.

It seems that there is no single satisfactory explanation for the observed bottlenecking mechanism and perhaps a combination of early and late bottlenecks may be present. The tentative assignment of a late bottleneck may be the first such inhomogeneity observed in IRMPD studies and bears relevance to the IRMPD of large biologically significant molecules. Despite the difficulty encountered in assigning the cause of the non-first order kinetics, these experiments *have* shown conclusively that the thermal model of IRMPD does not universally apply to large molecules and ions.

### 3.6 References

1. Isenor, N. R.; Richardson, M. C. *Appl. Phys. Lett.* **1971**, 18, 225.
2. Isenor, N. R.; Merchant, V.; Hallsworth, R. S.; Richardson, M. C. *Can. J. Phys.* **1973**, 51, 1281.
3. Coggiola, M. J.; Schulz, P. A.; Lee, Y. T.; Shen, Y. R. *Phys. Rev. Lett.* **1977**, 38, 17.
4. Ambartzumyan, R. V.; Gorokhov, Yu. A.; Letokhov, V. S.; Makarov, G. N. *JETP Letts.* **1975**, 21, 375.
5. Lethokov, V. S.; Moore, C. B. *Sov. J. Quantum Electron.* **1976**, 129, 259.
6. Lyman, J. L.; Jensen, R. J.; Rink, J.; Robinson, G. P.; Rockwood, S. D. *Appl. Phys.* **1975**, 27, 87.
7. Bittenson, S.; Houston, P. L. *J. Chem. Phys.* **1977**, 67, 4819.
8. Woodin, R. L.; Bomse, D. S.; Beauchamp, J. L. *J. Am. Chem. Soc.* **1978**, 100, 3248-3250.
9. Bomse, D. S.; Woodin, R. L.; Beauchamp, J. L. *J. Am. Chem. Soc.* **1979**, 101, 5503-5512.
10. Jasinski, J. M.; Rosenfeld, R. N.; Meyer, F. K.; Brauman, J. I. *J. Am. Chem. Soc.* **1982**, 104, 652.
11. For example: (a) Bomse, D. S.; Berman, D. W.; Beauchamp, J. L. *J. Am. Chem. Soc.* **1981** 103, 3967-3971. (b) Uechi, G. T.; Dunbar, R. C. *J. Chem. Phys.* **1992** 96, 8897-8905. (c) Osterheld, T. H.; Brauman, J. I. *J. Am. Chem. Soc.* **1993** 115, 10311-10316. (d) Bensimon, M.; Rapin, J.; Gäumann, T. *Int. J. Mass Spectrom. Ion Processes* **1986** 72, 125-135.
12. Little, D. P.; Speir, J. P.; Senko, M. W.; O'Connor, P. B.; McLafferty, F. W. *Anal. Chem.* **1994**, 66, 2809-2815.
13. Little, D. P.; McLafferty, F. W., *J. Am. Soc. Mass Spectrom.* **1996**, 7, 209-210.
14. Tonner, D. S.; McMahon, T. B. *Anal. Chem.* **1997**, 69, 4735-4740.
15. Tonner, D. S.; *M.Sc. Thesis*, University of Waterloo, 1994.
16. Thölmann, D.; Tonner, D. S.; McMahon, T. B. *J. Phys. Chem.* **1994**, 98, 2002-2004.
17. Tonner, D. S.; Thölmann, D.; McMahon, T. B. *Chem. Phys. Lett.* **1995**, 223, 324-330.
18. Price, W. D.; Schnier, P. D.; Williams, E. R. *Anal. Chem.* **1996**, 68, 859-866.

19. Dunbar, R. C. *J. Phys. Chem.* **1994**, 98, 8705-8712.
20. Dunbar, R. C.; McMahon, T. B.; Thölmann, D.; Tonner, D. S.; Salahub, D. R.; Wei, D. *J. Am. Chem. Soc.* **1995**, 117, 12819-12825.
21. Dunbar, R. C. *J. Am. Chem. Soc.*, **1971**, 93, 4354-4358.
22. Dunbar, R. C.; Zaniwski, R. C., *J. Chem Phys.* **1992**, 96, 5069-5075.
23. Uechi, G. T.; Dunbar, R. C., *J. Chem Phys.* **1992**, 96, 8897-8905..
24. Dunbar, R. C., *J. Chem Phys.* **1991**, 95, 2537-2548.
25. Quack, M. *J. Chem. Phys.* **1978**, 69, 1282-1307.
26. Woodin, R. L.; Bomse, D. S.; Beauchamp, J. L. *J. Am. Chem. Soc.* **1978**, 100, 3248-3250.
27. Bomse, D. S.; Woodin, R. L.; Beauchamp, J. L. *J. Am. Chem. Soc.* **1979**, 101, 5503-5512.
28. Hoffman, T. L.; *M.Sc. Thesis*, University of Waterloo, 1997.
29. Hop, C. E. C. A; McMahon, T. B.; Willett, G. D. *Int. J. Mass Spectrom. Ion Processes* **1990**, 101 191-208.
30. Bensimon, M; Rapin, J.; Gäumann, T. *Int. J. Mass Spectrom. Ion Processes* **1986** 72,-125-135.
31. For a discussion of the use of HPMS Van't Hoff plots for determining the energetics of structural isomers, see: Norrman, K.; McMahon, T. B. *J. Am. Chem. Soc.* **1996** 118, 2449-2457 and the references contained therein.
32. Hoffman, T. L. *M.Sc. Thesis, University of Waterloo* **1997**.
33. Some reviews include: a) Ambartzumian, R. V.; Letokhov, V. S. in *Chemical and Biochemical Applications of Lasers*, C. B. Moore Ed., Academic, New York, 1977, Vol. III; b) Thorne, L. R.; Beauchamp, J. L. *Gas Phase Ion Chemistry*, Vol. 3, M. T. Bowers Ed., Academic, London, 1984, Chpt. 18.; c) Goodman, M. F.; Stone, J.; Thiele, E. *Multiple-Photon Excitation and Dissociation of Polyatomic Molecules*, D. Cantrell Ed., Springer, Heidelberg, 1980.
34. Chelkowski, S.; Bandrauk, A. D.; Corkum, P. B. *Phys. Rev. Lett.* **1990**, 65, 2355.
35. Steinfeld, J. I. *Molecules and Radiation* 2<sup>nd</sup> Ed., **1985**, MIT Press, Cambridge, p.428.
36. Quick, C. R.; Wittig, C. *J. Chem. Phys.* **1978**, 69, 4201.

37. Chekalin, N. V.; Letokhov, V. S.; Lokhman, V. N.; A. N. Shibanov *Chem. Phys.* **1979**, 36, 415.
38. Black, J. G.; Kolodner, P.; Shultz, M. J.; Yablonovitch, E.; Bloembergen, N. *Phys. Rev. A* **1979**, 19, 704.
39. Grant, E. R.; Schulz, P. A.; Sudbo, Aa. S.; Shen, Y. R.; Lee Y. T. *Phys. Rev. Lett.* **1978**, 40, 115.
40. Quack, M. *J. Chem. Phys.* **1978**, 70, 1069.
41. Quack, M.; Humbert, P.; van den Bergh, H. *J. Chem. Phys.* **1980**, 73, 247.
42. Carmelli, B.; Schek, I.; Nitzan, A.; Jortner, J. *J. Chem. Phys.* **1980**, 72, 1928.
43. Simpson, T.B.; Black, T. G.; Burak, I.; Yablonovitch, E.; Bloembergen, N. *J. Chem. Phys.* **1985**, 83, 628.
44. Barker, J. *J. Chem. Phys.* **1980**, 72, 3686.
45. Solomon, K. E.; Brauman, J. I. *J. Phys. Chem.* **1988**, 92, 6948.
46. Jasinski, J. M.; Rosenfeld, R. N.; Meyer, F. K.; Brauman, J. I. *J. Am. Chem. Soc.* **1982**, 104, 652.
47. Bomse, D. S.; Woodin, R. L.; Beauchamp, J. L. *J. Am. Chem. Soc.* **1979**, 101, 5503-5512.
48. Thorne, L. R.; Beauchamp, J. L. in *Gas Phase Ion Chemistry* Vol. 3, M. T. Bowers Ed., Academic, London, **1984**, p.71.
49. Stone, J.; Thiele, E.; Goodman, M. F.; Stephenson, J. C.; King, D. S. *J. Chem. Phys.* **1980**, 73, 2259.
50. Jetter, H.; Pearson, E. F.; Norris, C. L.; McGurk, J. C.; Flygare, W. H. *J. Chem. Phys.* **1973**, 59, 1796.
51. Marcoux, P. J.; Setser, D. W. *J. Phys. Chem.* **1978**, 82, 97.
52. Shultz, M. J.; Yablonovitch, E. *J. Chem. Phys.* **1978**, 68, 3007.
53. Salomon, K. E.; Brauman, J. I. *J. Phys. Chem.* **1988**, 92, 6948-6953.
54. Quack, M.; Humbert, P.; van den Bergh, H. *J. Chem. Phys.* **1980**, 73, 247-255.
55. For a description of 3 level lasers, see: Svelto, O. *Principles of Lasers* 3<sup>rd</sup> Ed., Plenum Press, New York, **1989**.



56. Kebarle, P. *Techniques for the Study of Ion-Molecule Reactions*; Wiley Interscience: New York, 1988; Chapter V.
57. Alleman, M.; Kellerhalls, H.; Wanczek, K.P. *Int. J. Mass Spectrom. Ion Phys.* **1983**, *46*, 139-142.
58. Kofel, P.; McMahon, T. B.; *Int. J. Mass Spectrom. Ion Proc.* **1990**, *98*, 1-24.
59. Simpson, T. B.; Black, J. G.; Burak, I.; Yablonovitch, E.; Bloembergen, N. *J. Chem. Phys.* **1985** *83*, 628-638.
60. Power broadening is estimated to be 1-10 MHz for transition dipole moments of 0.2 and 1.0 D, respectively. In comparison, collisional broadening, at  $10^{-9}$  torr, is almost non-existent, with a linewidth of 0.01 Hz and the lifetime broadening due to spontaneous infrared emission,  $\Delta\nu_{1/2}=A_{21}/2\pi$ , is also very small, on the order of 2 to 50 Hz (for  $\mu=0.2$  and 1.0 D, respectively) for a  $1000\text{ cm}^{-1}$  transition. It is important to note that the true lifetime broadening is likely much larger than that calculated from the Einstein coefficient for spontaneous emission,  $A_{21}$ . The coupling between ro-vibrational levels of different vibrational modes and overtones is expected to be very rapid as is the subsequent absorption or stimulated emission from any one of this set of coupled states. It is therefore impossible to accurately predict the linewidth due to lifetime broadening and in the absence of low pressure molecular beam spectra, the linewidth calculated from the spontaneous emission lifetime serves as a lower limit.
61. For laser intensity of  $10\text{ W cm}^{-2}$  and assuming a transition dipole moment between 0.01 and 0.2 D, the Rabi frequency is 0.5-10 MHz at  $1000\text{ cm}^{-1}$ .
62. Robinson, P. J.; Holbrook, K. A. *Unimolecular Reactions*; Wiley-Interscience: New York, 1972.
63. Dunbar, R. C. *J. Phys. Chem.* **1994** *98*, 8705-8712.
64. Lias, S. G.; Bartmess, J. E.; Liebman, J. F.; Holmes, J. L.; Levin, R. D.; and Mallard, W. G. *J. Phys. Chem. Ref. Data* **1988** *17*, Suppl. 1.
65. Fisher, J. J.; McMahon, T. B. *Int. J. Mass Spectrom. Ion Processes* **1990**, *100*, 701.
66. Jarvis, J. A.; McMahon, T. B. *unpublished results* **1998**.
67. Thorne, L. R.; Beauchamp, J. L. *Gas Phase Ion Chemistry*, Bowers, M. T., Ed.; Academic: Orlando, FL, **1984**; Vol. 3.

#### 4. CONSECUTIVE INFRARED MULTIPHOTON DISSOCIATIONS OF THE PROTON BOUND DIMER OF DIETHYL ETHER

*"We wish to suggest a structure for the salt of deoxyribose nucleic acid (D.N.A.). This structure has novel features which are of considerable biological interest."*

Watson and Crick, 1953

The results presented in this chapter describe a novel application of the IRMPD/FT-ICR technique, which was presented in Chapter 3, to analytical mass spectrometry. This work has attracted substantial interest because of its potential for obtaining sequence information of large bio-molecules and the bulk of this chapter has appeared in *Analytical Chemistry*.<sup>1</sup> The results demonstrate that consecutive infrared multiphoton dissociations (IRMPD) of ions may be observed in a Fourier transform ion cyclotron resonance mass spectrometer (FTICR). This is the IRMPD equivalent of previous MS<sup>n</sup> experiments using CID. This work presents a versatile technique, using a bi-stable shutter to gate ON and OFF a continuous-wave (CW) CO<sub>2</sub> laser for multiple irradiation periods of 0.1-1000 s duration. Consecutive photodissociations, up to MS<sup>4</sup>, are demonstrated for the proton bound dimer of diethyl ether and the resulting fragment ions. The photoproducts are formed close to the centre of the FTICR cell, resulting in high product ion recovery efficiency. This differs from CID products, which are formed throughout the FTICR cell causing re-isolation/detection problems. The fragmentation resulting from the use of low intensity, CW, infrared

laser radiation is shown to be much more energy selective than CID. Photodissociation of  $\text{C}_2\text{H}_5\text{OH}_2^+$  ion produces the lowest energy product ion exclusively, even though the two product channels differ only by  $\sim 5$  kcal/mole. Low energy CID, however, produces a mixture of  $\text{C}_2\text{H}_5^+$  and  $\text{H}_3\text{O}^+$  products in the ratio of 1.3:1. Hence, the *higher* energy pathway ( $\text{C}_2\text{H}_5^+$ ) is substantially favoured. The current results indicate that this IRMPD  $\text{MS}^n$  technique may be successfully applied to large bio-molecules prepared by electrospray or MALDI.

#### 4.1 Introduction

Tandem mass spectrometry (MS/MS) and multiple mass spectrometry ( $\text{MS}^n$ ) experiments have proven extremely powerful for identification and structural characterization of ions.<sup>2,3,4</sup> Additionally, it has been demonstrated that  $\text{MS}^n$  techniques can be applied to large (kDa), extensively protonated ions produced from electrospray ionization (ESI) because multiple protonation renders the ions more susceptible to dissociation. The use of the fragmentation information provided by  $\text{MS}^n$  techniques to directly sequence DNA and large protein molecules has gained much attention.<sup>5,6</sup> Of the various methods which exist for inducing fragmentation of ions, collision induced dissociation, (CID) is, perhaps, the most widely used. MS/MS experiments, incorporating CID, have been shown to provide substantial, and sometimes complete, sequence information for oligopeptide ions generated by ESI.<sup>7</sup>

Collisional induced dissociation (CID) of small molecules in a FTICR

spectrometer was demonstrated nearly two decades ago by Freiser and co-workers<sup>8</sup>. Translational excitation of the ions is accomplished by application of a radio frequency (r.f.) electric field at a frequency resonant with the ion cyclotron motion. Upon colliding with either a static<sup>9</sup> or pulsed<sup>10</sup> pressure of target gas, the ions undergo fragmentation. CID in a FTICR spectrometer differs from tandem or multi-sector instruments in that fragment ions are separated from parent ions temporally rather than spatially. Ion beam mass spectrometers use one electric, magnetic or quadrupole sector to separate the desired ionic species from the extraneous ions, and another sector to detect the fragmentation products. Hence, a MS<sup>n</sup> experiment requires "n" analyzer stages. In contrast, MS/MS experiments can be performed in a single FTICR spectrometer because ion isolation, excitation, collision and detection of the fragments all occur in the same FTICR cell. Extension of the FTICR experiment to produce consecutive CID events is then easily achieved, without additional hardware, simply by changing the pulse sequence in the FTICR software such that fragment ions are isolated and re-dissociated.<sup>11</sup> Quadrupole ion trap mass spectrometers (ITMS) are capable of producing MS/MS spectra by similar modifications in the pulse timing, however, these instruments require much higher operating pressures. Cooks and co-workers first demonstrated the MS/MS capability of ITMS in 1987.<sup>12</sup> An excellent comparison of the two techniques of trapped ion MS/MS is given by McLuckey *et al.*<sup>5</sup>

The efficiency of the FTICR MS<sup>n</sup> experiment is limited by several factors: 1) A low target gas pressure ( $<10^{-6}$  torr) is necessary to maintain optimum ion detection

conditions ( $<10^{-8}$  torr if high resolution detection is required); 2) The maximum translational energy imparted to the precursor ions is limited by the magnetic field and the size of the cell; 3) r.f. excitation takes the ions off-axis and consequently, forms fragmentation products away from the centre of the cell thereby decreasing the efficiency with which the ions can be re-isolated or detected.<sup>13</sup> Various improvements on the basic CID technique such as multiple excitation collisional activation (MECA),<sup>14</sup> sustained off-resonance irradiation collisionally activated dissociation (SORI-CAD),<sup>15,16</sup> very low energy collisionally activated dissociation (VLE-CAD)<sup>17,18</sup> and resonant amplitude modulated collisionally activated dissociation (RAM-CAD)<sup>6</sup> have been demonstrated. Using SORI-CAD, dissociation efficiencies greater than 90% have been reported for protonated ethyl acetate<sup>16</sup> and greater than 92% for large multiply charged ions.<sup>6</sup> Even though these techniques yield high dissociation efficiencies for an individual CID event, it is still difficult to obtain multiple MS events due to the production of fragment ions far from the centre of the cell.

Another powerful technique for dissociating ions in a mass spectrometer is photodissociation. Very early in the history of ICR spectrometers, the ion trapping capabilities of these instruments indicated their potential for photochemical studies of ions. Brauman and Smyth first demonstrated negative ion electron photodetachment in an ICR spectrometer in 1969.<sup>19</sup> Two years later, Dunbar performed the first photodissociation experiments in an ICR spectrometer using a monochromated Xenon

arc lamp to remove a chlorine atom from  $\text{CH}_3\text{Cl}^+$  ions.<sup>20</sup> In 1978, Beauchamp and co-workers first showed that low intensity ( $< 100 \text{ W/cm}^2$ ), continuous wave (CW),  $\text{CO}_2$  laser radiation could produce IRMPD of ions trapped at low pressure in an ICR cell.<sup>21,22</sup> The dissociation of weakly bound cluster ions by ambient black body radiation, termed Zero-pressure Thermal Radiatively Induced Dissociation (ZTRID), was demonstrated experimentally by McMahon and co-workers<sup>23,24</sup> with theoretical modelling provided by Dunbar.<sup>25</sup> Very recently, Williams and co-workers have extended this same technique to the higher temperatures necessary to achieve Black body Induced Radiative Dissociation (BIRD) with bio-molecule ions as large as ubiquitin.<sup>26</sup> Applications of UV,<sup>27</sup> IR<sup>28</sup>, and BIRD photodissociation techniques to large bio-molecules have, recently, been investigated as alternative methods to CID in MS/MS experiments.

To determine unimolecular reaction pathways (required for the sequencing of bio-molecules) or dissociation rates, the unambiguous assignment of the observed fragmentation products to the correct parent ion(s) is required. For consecutive reactions, mechanistic uncertainties may exist. For example, does a single step,  $\text{A} \rightarrow \text{C}$  reaction occur in parallel with a consecutive,  $\text{A} \rightarrow \text{B} \rightarrow \text{C}$  reaction? Since strong deviations from first order kinetics have been observed in FTICR photodissociation experiments<sup>29,30</sup>, it may be difficult to extract the reaction mechanism of a consecutive reaction from the observed kinetics. This process is greatly simplified if there is only one species present in the FTICR cell when the fragmentation event is

initiated. The IRMPD  $MS^n$  technique presented here is a powerful tool for the characterization of these reactions, because the dissociating ion in each step is isolated before the irradiation event. In a sense, this technique provides the ability to "stop" the reaction sequence at an arbitrary point, and observe the progress of the reaction, and/or instantly "purify" the resulting product(s) for further study. Similarly, the IRMPD  $MS^n$  experiment could be used to produce and trap a highly reactive species *via* photolysis of a stable ionic species. The reactive species, which perhaps could not be generated by other ionization methods, can then be isolated and fragmented, or reacted bimolecularly with the introduction of a pulsed reactant gas to the FTICR cell.

This study demonstrates a true, IRMPD analogue of previous  $MS^n$  experiments using CID. A bi-stable shutter (i.e. one TTL pulse to open, another to close) is used to gate the low power, CW laser beam before it enters the FTICR cell. Separating the "laser ON" periods by delays and/or ejection events facilitates multiple-stage, photodissociation experiments, with the extent of dissociation during each step being determined by the length of the irradiation period. Using this experimental procedure, we are able to observe  $MS^n$  spectra of externally generated  $[(C_2H_5)_2O]_2H^+$  ions at low pressures. Isolation and re-dissociation spectra up to  $MS^4$  are demonstrated and the final dissociation reaction (3) is compared to results obtained by CID.

## 4.2 Experimental

All experiments were performed on a Bruker CMS 47 Fourier transform ion cyclotron resonance (FTICR) spectrometer equipped with a 4.7 T superconducting magnet and a Bruker Infinity cell. The Waterloo FTICR spectrometer has been modified by the addition of an external, high pressure ion source similar to that found in a high pressure mass spectrometer (HPMS). A detailed explanation of HPMS has been given elsewhere.<sup>31</sup> The high pressure ion source permits the generation of weakly bound ion-molecule complexes which are thermalized by many collisions ( $\sim 10^5$ ) before exiting the source. Details of both the CMS 47<sup>32</sup> and the external ion source<sup>33</sup> have been published previously. Differential pumping is accomplished with 3 Balzers turbomolecular pumps. With 3.5 torr in the ion source, the pressure outside the source region is  $\sim 2 \times 10^{-4}$  torr while the base pressure in the FTICR cell is on the order of  $1 \times 10^{-9}$  torr at 20°C. CID experiments were performed with a static pressure ( $\sim 1 \times 10^{-7}$  torr) of either argon or methane in the FTICR cell. The  $[(C_2H_5)_2O]_2H^+$  ions were generated externally from a mixture of  $\sim 1\%$  reagent grade diethyl ether in methane. The gas mixture was flowed into the ion source at a pressure of  $\sim 3.5$  torr and was ionized by secondary electron impact ionization from 2 keV electrons.  $CH_5^+$  and  $C_2H_5^+$  ions formed by the ultra-high CI source pressures, subsequently proton transfer to the neutral diethyl ether molecules. Room temperature ionization conditions produced almost exclusively  $[(C_2H_5)_2O]_2H^+$  ions. Since the desired ion ( $m/z=149$ ) was so dominant initially, complete isolation was easily accomplished using standard r.f.



ejection techniques as shown in Figure 35a. No accidental CID of the parent ion, due to near-resonant excitation, was observed.

The methods and conditions for conducting CID experiments have been described in detail previously.<sup>8-10,34</sup> All CID experiments used the "ion excitation" pulse provided in the standard Bruker Xmass software. Ion excitation was accomplished by application of a single frequency r.f. pulse directly at the cyclotron frequency of the parent ion. The translational energy was controlled by varying the length and amplitude (controlled by attenuator settings) of the r.f. waveform. No off-resonant excitation experiments were performed as the purpose of the CID spectra presented here was simply to compare the fragmentation ratios with those produced by IRMPD.

The complete apparatus for the IRMPD MS<sup>n</sup> experiments is illustrated schematically in Figure 33. All IRMPD experiments were done with a SYNRAD Inc. 48-0-15W, CO<sub>2</sub> laser operating CW in TEM<sub>00</sub> modes with frequency at or near 10.6  $\mu\text{m}$  (10.55 to 10.65  $\mu\text{m}$ ).<sup>35</sup> Output power can be controlled up to a maximum of 10 W by changing the duty cycle from 5 to 98%. For these experiments, the duty cycle was fixed at approximately 40% so that the output laser power was 3.9 W. Further attenuation of laser power was accomplished by passing the beam through a static pressure (~1-10 torr) of ethylene gas contained in an attenuation cell equipped with AR coated zinc selenide windows (>99% transmission at 10.6  $\mu\text{m}$ ). The beam continues through a Newport 846HP bi-stable shutter with a 5.6 mm aperture and a maximum

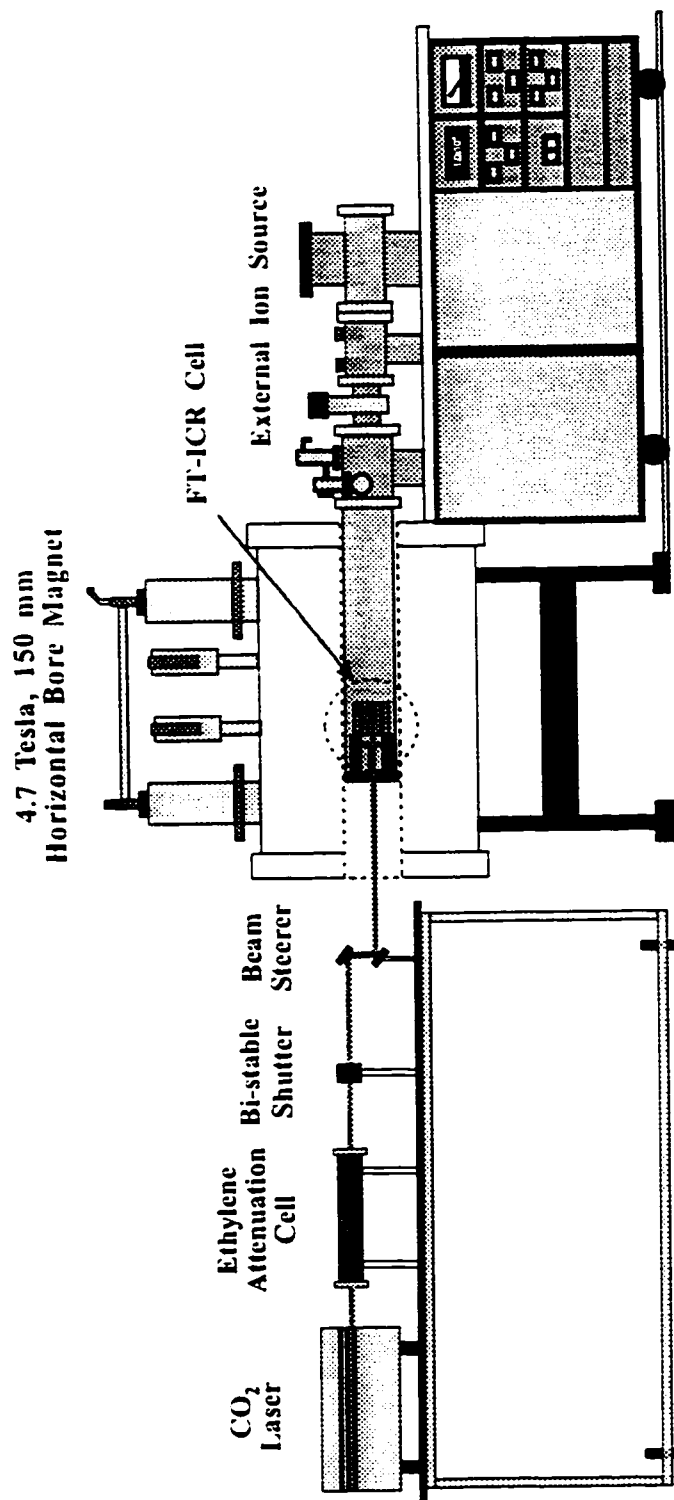


**Figure 33** Schematic representation of the apparatus used for IRMPD MS<sup>n</sup> experiments in a FTICR spectrometer.

incident beam power of 5 W. Positioning of the beam is accomplished with a Newport beam steerer using coated aluminum, first surface mirrors. Finally, the laser beam enters the rear of the FTICR cell through a 3x25.4 mm AR coated ZnSe window and passes through 6 mm restrictions at both the front and rear of the cell before being dissipated in the ion optics of the external source. Laser power was measured immediately behind the shutter with a Coherent 210 power meter. The laser beam profile, at the cell, was determined by translating a 1 mm aperture across the beam and measuring the transmitted power. The observed Gaussian beam profile had a full width half maximum (FWHM) value of 0.66 cm. Additionally, the power at the FTICR cell was measured and found to be less than that measured behind the shutter by a factor of approximately 0.87. The overall infrared laser intensity was determined by dividing the corrected laser power at the cell by the beam area (FWHM). The data presented here were collected with a laser power of 3.9 W (behind the shutter) which translates into an intensity of  $10 \text{ W/cm}^2$ .

The experimental timing was controlled by the Xmass data collection software running on a Silicon Graphics Inc. Indy work station. For a  $\text{MS}^3$  experiment, the pulse sequence presented in Figure 34 was used. The optical shutter was coupled to the Bruker data collection system via home-built electronics such that a TTL pulse from one auxiliary output would open the shutter which remains in this position until a TTL pulse from a second auxiliary output closes the shutter. Using this design, the shutter could be opened at any point in the experimental sequence and left open for any

## 2 Laser Irradiation Stages; MS<sup>3</sup> Experiment:

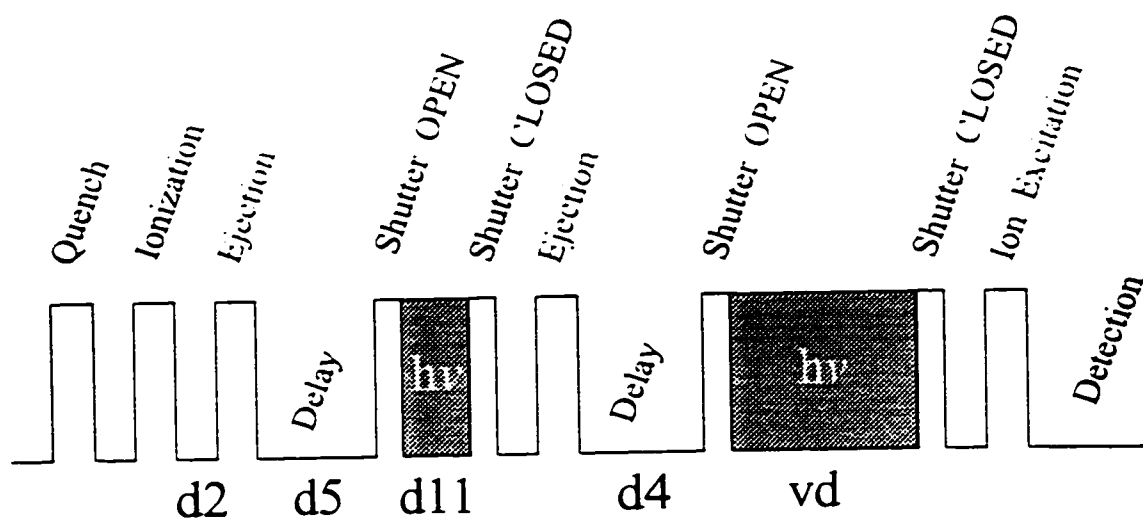


**Figure 34** The FTICR pulse sequence which controls the timing of MS<sup>n</sup> experiments. This example illustrates the MS<sup>3</sup> experiment used to obtain the mass spectrum shown in Figure 35d).

duration. By adding additional isolation and irradiation events with the appropriate delays to the software, multiple stage photodissociation experiments were accomplished.

### 4.3 Results and Discussion

The proton bound dimer ion of diethyl ether was an ideal system to illustrate the IRMPD  $MS^n$  technique because it undergoes a series of consecutive photodissociative reactions (discussed in detail in Reactions 1-3). Additionally, the cross-section for photodissociation of  $[(C_2H_5)_2O]_2H^+$  ions was known to be large,<sup>9, 21</sup> so that high conversion efficiencies for Reaction 1 could be expected. Finally, photogeneration of  $(C_2H_5)_2OH^+$  and  $C_2H_5OH_2^+$  provides a method of making these two ions which are ordinarily difficult to obtain from a high pressure ion source because the equilibrium constant for formation of the respective dimers,  $[(C_2H_5)_2O]_2H^+$  and  $(C_2H_5OH)_2H^+$ , is very large. An additional consideration is that  $(C_2H_5OH)_2H^+$  rapidly eliminates  $H_2O$  to form  $(C_2H_5)_2OH^+$  under high pressure conditions. Photodissociation of  $(C_2H_5OH)_2H^+$  also yields exclusively protonated diethyl ether ion *via* water elimination<sup>36</sup> and is, therefore, not a viable method of producing  $C_2H_5OH_2^+$  either. Ethyloxonium ion,  $C_2H_5OH_2^+$ , can be made in a conventional CI source, but care must be taken to minimize internal excitation of the ion from the exothermic proton transfer reaction. In contrast, photo-generation of  $C_2H_5OH_2^+$  from  $[(C_2H_5)_2O]_2H^+$  is quite facile and dissociation by low intensity photolysis has been shown to occur very nearly

at threshold,<sup>22</sup> producing fragments with less internal energy than from corresponding pulsed laser multiphoton dissociation.<sup>37</sup>

All of the mass spectra presented here were collected over the mass range 14.4-300 Da. Spectra out to 1000 Da were periodically examined to ensure that no interferences from higher mass ions were observed. The initial stage of the MS<sup>n</sup> experiment used r.f. ejection techniques to isolate the proton bound dimer ion of diethyl ether produced in the external ion source. The mass spectrum presented in Figure 35a contains, almost exclusively, the isolated  $[(C_2H_5)_2O]_2H^+$  ion at  $m/z=149$ . Single frequency ejection "shots" were used to remove unwanted ions after a 1 s post-ionization delay. The small peaks appearing at  $m/z=75.55$  and  $m/z=49.7$  are the second and third harmonics of  $m/z=149.1$  respectively. The ion appearing at  $m/z=147$ , corresponding to  $H_2$  elimination from  $m/z=149$ , was not ejected both to ensure no translational excitation of  $m/z=149$  and because it did not interfere with the observed diethyl ether reactions. Hence, each of the product ions shown in Figure 35 is accompanied by a small peak two Da below from the photodissociation of unejected  $m/z=147$ . The  $[(C_2H_5)_2O]_2H^+$  ion was found to be unreactive when trapped in the FTICR cell for a period of 500 s and did not undergo black body induced dissociation at room temperature. Irradiation of the  $[(C_2H_5)_2O]_2H^+$  ions for 0.4 s at a laser intensity of  $10\text{ W/cm}^2$  produces the spectrum shown in Figure 35b. Photodissociation of the  $[(C_2H_5)_2O]_2H^+$  ion results in the loss of a neutral diethyl ether, exclusively

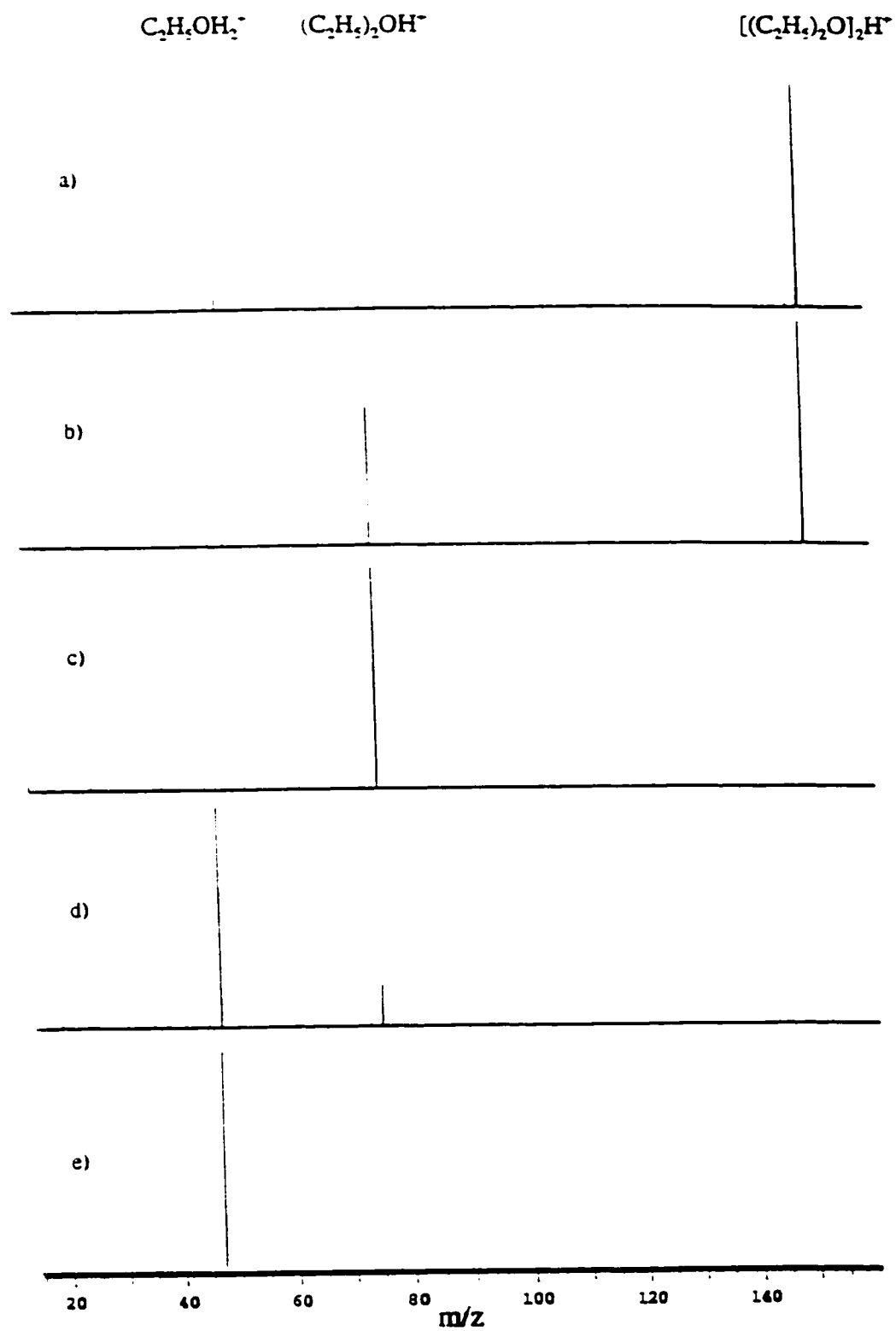
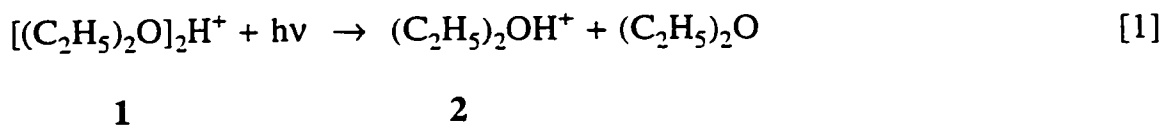
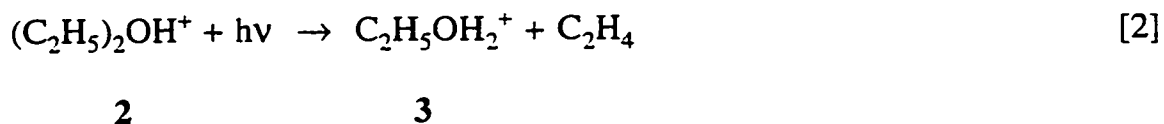


**Figure 35** Series of spectra illustrating the progression of the sequential photodissociation reactions of  $[(\text{C}_2\text{H}_5)_2\text{O}]_2\text{H}^+$  ion.

(Reaction 1). This reaction is known from HPMS equilibrium measurements to be 29.1 kcal/mole<sup>38</sup> endothermic.



The protonated diethyl ether monomer ion (**2**) produced in Reaction 1 was re-isolated with r.f. ejection shots and the resultant spectrum is given in Figure 35c. The small peaks occurring at  $m/z=37.5$  and  $m/z=25.0$  are the second and third harmonics of  $m/z=75.08$ , respectively. When the  $(\text{C}_2\text{H}_5)_2\text{OH}^+$  ion is subjected to a second photodissociation event (30 s, 10 W/cm<sup>2</sup>) the spectrum shown in Figure 35d is obtained. In this case, the protonated diethyl ether monomer undergoes a rearrangement to form ethyloxonium ion (**3**) *via* ethylene elimination (Reaction 2) which is 28.5 kcal/mole endothermic.<sup>39</sup> Since the precursor ion (**2**) for this reaction must be prepared through photolysis of **1**, the MS<sup>3</sup> pulse sequence, shown in Figure 34, represents the experimental procedure required to produce the mass spectrum shown in Figure 35d.



Reaction 2 proceeds much more slowly than Reaction 1 for the same laser intensities (the initial rate constants are  $k=0.5 \text{ s}^{-1}$  and  $k=4 \text{ s}^{-1}$  respectively). Beauchamp<sup>22</sup> observed that reactions 2 and 3 could only be observed with progressively higher laser intensities, but the irradiation times used were limited to less than 2 s because of back



reaction of **2** with the  $10^{-6}$  torr background pressure of neutral diethyl ether. The use of an external ion source in this work, yields a background diethyl ether pressure of  $\leq 1 \times 10^{-11}$  torr in the FTICR cell. Therefore, long irradiation times (up to 500 s) and hence, increased laser fluences are possible. The result is the observation of low intensity photodissociation of ions **2** and **3**.

When the ethyloxonium ion (**3**) is trapped and irradiated, (70 s, 10 W/cm<sup>2</sup>) H<sub>3</sub>O<sup>+</sup> (m/z=19) is the only fragmentation product observed, as shown in Figure 36a. This MS<sup>4</sup> experiment shows that photodissociation proceeds exclusively *via* ethylene elimination as illustrated in Reaction 3a. This is in contrast to the previous results of Bowers and co-workers in which both C<sub>2</sub>H<sub>5</sub><sup>+</sup> and H<sub>3</sub>O<sup>+</sup> fragment ions were produced from CID in a ratio of 1.2:1.<sup>40,41</sup> The dissociation of ethyloxonium ion to form C<sub>2</sub>H<sub>5</sub><sup>+</sup> *via* elimination of water is shown in Reaction 3b. When CID was performed on the ethyloxonium ion, in the Waterloo FTICR spectrometer, a mixture of products **4a** and **4b** was produced, as seen in Figure 36b. The observed ion intensities are in the ratio of 1.3:1, which is in good agreement with the results of Bowers.



**3**                      **4a**



**3**                      **4b**

According to the Lias compendium of thermochemical data, reactions 3a and 3b are endothermic by 32.5 kcal/mole and 36.8 kcal/mole respectively.<sup>39, 24</sup> Radom *et al.*

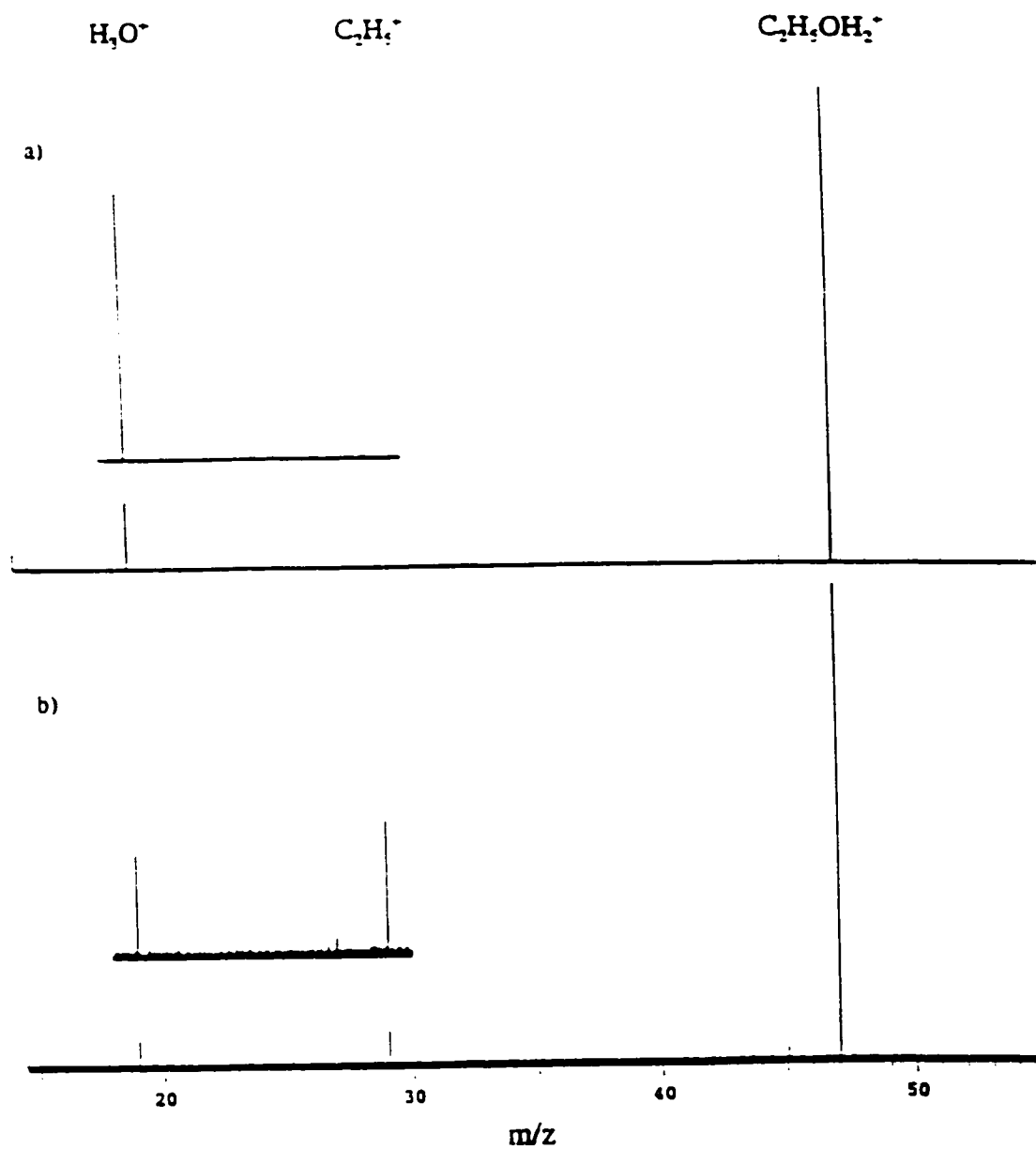


**Figure 36**  $MS^4$  spectra obtained by fragmenting the isolated  $C_2H_5OH_2^+$  ion using a) IRMPD; b) CID.

have calculated the relative energetics of reactions 3a and 3b to be 31.1 and 38.2 kcal/respectively<sup>42</sup> The reaction mechanism, complete with ion structures and enthalpy changes (from Lias *et al.*) is shown schematically in Figure 37.

The literature contains mixed results regarding the products of reaction 3 observed in *unimolecular* experiments. The metastable experiments by Bowers *et al.* reported observation of  $\text{H}_3\text{O}^+$  ion only,<sup>40,41</sup> while Smith and co-workers observed both  $\text{C}_2\text{H}_5^+$  and  $\text{H}_3\text{O}^+$  as unimolecular fragmentation products.<sup>43</sup> This discrepancy might be explained by the fact that the latter experiment sampled ions with greater than thermal translational energies. CID is an impulsive energy transfer method and the resulting products may not represent the lowest energy pathway. This is especially true if the lowest energy product requires a structural re-arrangement. Such reactions may have an entropic barrier governing the transition state which must be overcome prior to reaching the thermodynamically favoured product. Thus, the exclusive formation of  $\text{H}_3\text{O}^+$  from the photodissociation of ethyloxonium ion (3) shows that the IRMPD-MS<sup>n</sup> technique produces only the thermodynamically favoured product ion with an energy selectivity on the order of 5 kcal/mole or less. The CID MS<sup>n</sup> experiments performed here are clearly not energy selective since the *higher* energy process is favoured by a factor of 1.2-1.3. The ZTRID (or BIRD) technique is another very energy selective method which forms exclusively the lowest energy product but requires a large number of absorbing modes (many atoms) for dissociation of strongly bound ions. The dissociation of protonated diethyl ether (Reaction 2) and

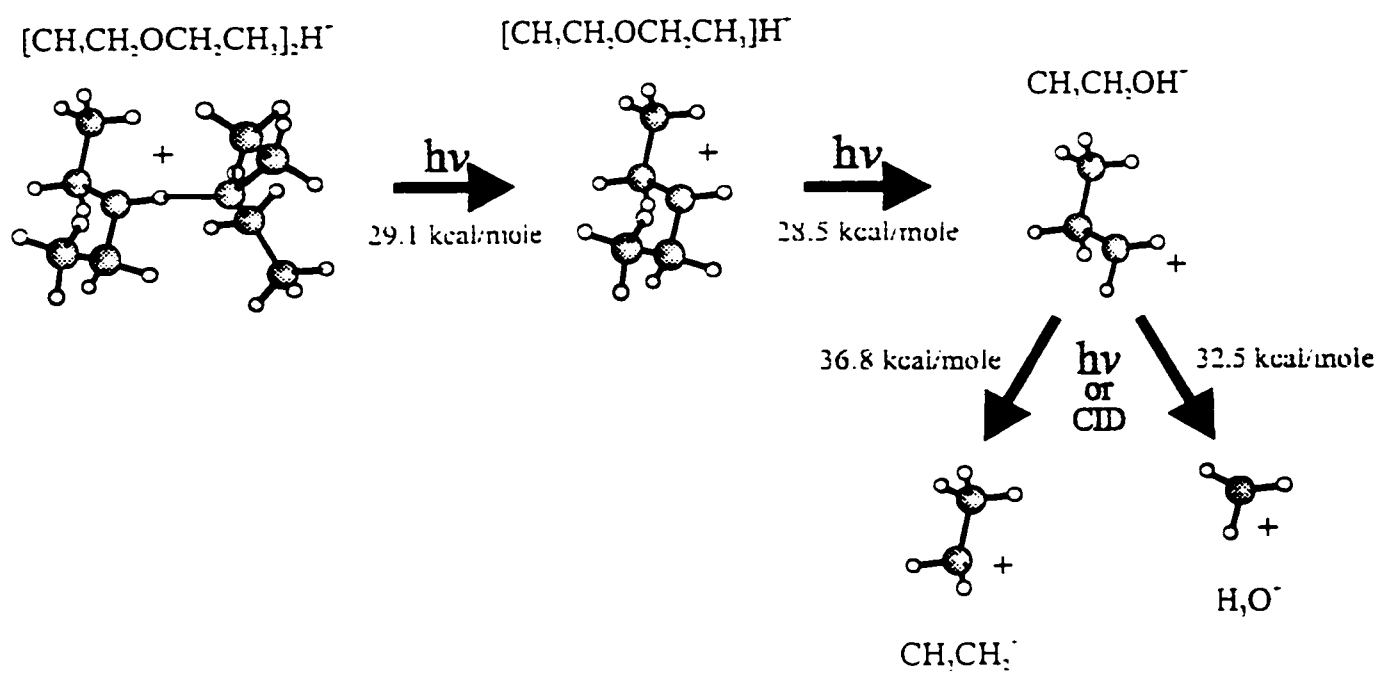


**Figure 37** Schematic Representation of the Ion Reaction Sequence used in IRMPD-MS<sup>n</sup> experiments

ethyloxonium ion (Reaction 3) are examples of reactions which cannot be observed *via* black body radiation (at least at  $T \leq 200$  °C) and again demonstrates the utility of the current technique.

It can be readily seen that the signal to noise ratios in the spectra of isolated **1**, **2** and **3** are still large. This is impressive in light of the fact that the observed maximum conversion efficiency for **1**  $\rightarrow$  **2** is approximately 50% due to the parasitic **2**  $\rightarrow$  **3** reaction and non-first order kinetics. The efficient recovery of ions, throughout the sequential MS stages, can be attributed to the very strong signal in the starting ion,  $[(C_2H_5)_2O]_2H^+$ , and to the formation of the photo-fragments close to the centre of the FTICR cell (along the laser axis). The difference in the S/N ratio between Figure 36a and Figure 36b illustrates the benefit of IRMPD over CID for efficient fragmentation of ions in an FTICR spectrometer. Increasing the length and/or amplitude of the r.f. excitation pulse, in an attempt to increase the fragmentation efficiency of the CID experiment, results in diminished signal because ions are either ejected from the cell or moved into a larger cyclotron orbit from which they are not detected as efficiently.

#### 4.4 Conclusions

A technique for obtaining  $MS^n$  spectra *via* infrared multi-photon dissociation has been demonstrated. Advantages of this method over analogous CID experiments, include better selectivity of the lowest enthalpy fragmentation pathway and increased throughput of product ions from previous MS events due to formation of photo-

fragments near the centre of the FTICR cell. Additionally, the internal energy deposition is limited only by the laser power, the irradiation time (both can be increased substantially from the present experiment) and the absorption cross-section of the ion at 10.6  $\mu\text{m}$ , (which is substantial for ions of moderate to large size) rather than by the physical dimensions of the cell and the magnetic field strength, as in CID experiments.

The superb energy selectivity, high product recovery efficiency, compatibility with external ionization sources, and potentially unlimited mass range indicate that this technique may be successfully applied to large bio-molecules prepared by electrospray or MALDI. Individual exploration of multiple fragmentation pathways should generate structural and qualitative, energetic information. Price *et al.* have applied Dunbar's modified Tholmann theorem approach to modelling IR absorption rates to large bio-molecules.<sup>44</sup> An extension of this treatment could produce quantitative energetic information regarding the fragmentation energetics of biomolecules observed by this technique.

## 4.5 References

1. Tonner, D. S.; McMahon, T. B. *Anal. Chem.* **1997**, 69, 4735-4740.
2. McLafferty, F. W. *Tandem Mass Spectrometry*, John Wiley and Sons: New York, 1983.
3. Busch, K. L.; Glush, G. L.; McLuckey, S. A. *Mass Spectrometry/Mass Spectrometry: Techniques and Applications of Mass Spectrometry*, VCH Publishers: New York, 1988.
4. de Hoffmann, E. *J. Mass Spectrom.* **1996**, 31, 129-137.
5. McLuckey, S. A.; Habibigoudarzi, S. J. *J. Am. Chem. Soc.* **1993**, 115, 12085-12095.
6. Senko, M. W.; Speir, J. P.; McLafferty F. W. *Anal. Chem.* **1994**, 66, 2801-2808.
7. Hunt, D. F.; Michel, H.; Dickinson, T. A.; Shabanowitz, J.; Cox, A. L.; Sakaguchi, K.; Appella, E.; Grey, H. M.; Sette, A. *Science* **1992** 256, 1817-1820.
8. Cody, R. B.; Freiser, B. S. *Int. J. Mass Spectrom. Ion Phys.* **1982**, 41, 199-204.
9. Cody, R. B.; Burnier, R. C.; Freiser, B. S. *Anal. Chem.* **1982**, 54, 96-101.
10. Carlin, T. J.; Freiser, B. S. *Anal. Chem.* **1983**, 55, 571- 574.
11. Cody, R. B.; Burnier, R. C.; Cassady, C. J.; Freiser, B. S. *Anal. Chem.* **1982**, 54, 2225-2228.
12. Louris, J. N.; Cooks, R. G.; Sycka, J. E. P.; Kelley, P. E.; Stafford Jr., G. C.; Todd, J. F. *J. Anal. Chem.* **1987** 59, 1677.
13. Guan, S.; Marshall, A. G.; Wahl, M. C. *Anal. Chem.* **1994**, 66, 1363-1367.
14. Lee, S. A.; Jiao, C. Q.; Huang, Y.; Freiser, B. S. *Rapid Commun. Mass Spectrom.* **1993**, 7, 819-821.
15. Heck, A. J. R.; de Koning, L. J.; Pinkse, F. A.; Nibbering, N. M. M. *Rapid Commun. Mass Spectrom.* **1991**, 5, 406-414.
16. Gauthier, J. W.; Trautman, T. R.; Jacobson, D. B. *Anal. Chim. Acta* **1991**, 246, 211-225.
17. Boering, K. A.; Rolfe, J.; Brauman, J. I. *Rapid Commun. Mass Spectrom.* **1992**, 6, 303-305.
18. Boering, K. A.; Rolfe, J.; Brauman, J. I. *Int. J. Mass Spectrom. Ion Processes* **1992**, 117, 357-386.

19. Brauman, J. I.; Smyth, K. C. *J. Am. Chem. Soc.* **1969**, *91*, 7778-7780.
20. Dunbar, R. C. *J. Am. Chem. Soc.*, **1971**, *93*, 4354-4358.
21. Woodin, R. L.; Bomse, D. S.; Beauchamp, J. L. *J. Am. Chem. Soc.* **1978**, *100*, 3248-3250.
22. Bomse, D. S.; Woodin, R. L.; Beauchamp, J. L. *J. Am. Chem. Soc.* **1979**, *101*, 5503-5512.
23. Thölmann, D.; Tonner, D. S.; McMahon, T. B. *J. Phys. Chem.* **1994**, *98*, 2002-2004.
24. Tonner, D. S.; Thölmann, D.; McMahon, T. B. *Chem. Phys. Lett.* **1995**, *223*, 324-330.
25. Dunbar, R. C. *J. Phys. Chem.* **1994**, *98*, 8705-8712.
26. Price, W. D.; Schnier, P. D.; Williams, E. R. *Anal. Chem.* **1996**, *68*, 859-866.
27. Williams, E. R.; Furlong, J. J. P.; McLafferty, F. W. *J. Am. Soc. Mass Spectrom.* **1990**, *1*, 288-294.
28. Little, D. P.; Speir, J. P.; Senko, M. W.; O'Connor, P. B.; McLafferty, F. W. *Anal. Chem.* **1994**, *66*, 2809-2815.
29. Tonner, D. S.; McMahon, T. B. *J. Phys. Chem.*, *Submitted* **1998**.
30. Riveros, J. M.; *Personal Communication*, **1997**.
31. Kebarle, P. *Techniques for the Study of Ion-Molecule Reactions*; Wiley Interscience: New York, 1988; Chapter V.
32. Alleman, M.; Kellerhalls, H.; Wanczek, K.P. *Int. J. Mass Spectrom. Ion Phys.* **1983**, *46*, 139-142.
33. Kofel, P.; McMahon, T. B.; *Int. J. Mass Spectrom. Ion Proc.* **1990**, *98*, 1-24.
34. Hop, C. E. C. A.; McMahon, T. B.; Willett, G. D. *Int. J. Mass Spectrom. Ion Proc.* **1990**, *101*, 191-208.
35. SYNRAD Inc. *Infrared Gas Lasers Instruction Manual*.
36. Bomse, D. L.; Beauchamp, J. L. *J. Am. Chem. Soc.* **1981**, *103*, 3292-3296.
37. Jasinski, J. M.; Rosenfeld, R. N.; Meyer, F. K.; Brauman, J. I. *J. Am. Chem. Soc.* **1982**, *104*, 652-658.
38. Hoffman, T. L.; McMahon, T. B. *Unpublished results*, **1996**.



39. Lias, S. G.; Bartmess, J. E.; Liebman, J. F.; Holmes, J. L.; Levin, R. D.; and Mallard, W. G. *J. Phys. Chem. Ref. Data* **1988** *17*, Suppl. 1.
40. Jarrold, M. F.; Illies, A. J.; Kirchner, N. J.; Bowers, M. T. *Org. Mass Spectrom.* **1983**, *18*, 388.
41. Jarrold, M. F.; Kirchner, N. J.; Lin, S.; Bowers, M. T. *J. Phys. Chem.* **1986**, *90*, 78-83.
42. Swanton, D. J.; Marsden, D. C. J.; Radom, L. *Org. Mass Spectrom.* **1991**, *26*, 227-234.
43. Smith, S. C.; McEwan, M. J.; Giles, K.; Smith, D.; Adams, N. G. *Int. J. Mass Spectrom. Ion Processes* **1990**, *96*, 77-96.
44. Price, W. D.; Schnier, P. D.; Jockusch, R. A.; Strittmatter, E. F.; Williams, E. R. *J. Am. Chem. Soc.* **1996**, *118*, 10640-10644.

## 5. THE DYNAMICS OF CHLORIDE-ALKYL BROMIDE $S_N2$ REACTIONS

*Gott würfelt nicht. (God does not play dice.)*  
Albert Einstein

### 5.1 Introduction

The study of reaction mechanisms is of universal importance to all branches of chemistry. A thorough understanding of a chemical reaction mechanism allows a chemist to manipulate the relative efficiency of product formation, classify reactions and predict the products of new reactions. A detailed study of the gas phase dynamics of chloride-alkyl bromide  $S_N2$  reactions will be presented in this chapter.

Ions in solution exhibit an intrinsic reactivity because of the charge on the ion, but this reactivity can be modified by the stabilizing effect of the solvent. For some reactions, there may be immense solvent effects and the separation of the intrinsic chemical reactivity of a species from the solvent effect may be impossible. Studies of gaseous cluster ion reactivity attempt to bridge the gap between isolated gas phase reaction mechanisms and reactions in bulk solution. An extreme example of solvation effects on a microscopic scale may be seen in the ingenious experiments of Lineberger and co-workers. Recombination of the separated  $I^-$  and  $I$  species, due to solvent "caging" effects, has been observed in the photodissociation of the multiply solvated cluster ions  $I_2^-(CO)_n$  and  $I_2^-(Ar)_n$ .<sup>1,2</sup> Before addressing the demanding question of

how a solvent affects the mechanism of a chemical reaction, it is desirable to study the dynamics of the reaction in an isolated environment and gas phase reactions provide the ideal medium. Reaction dynamics of neutral species are typically probed by optical techniques such as absorption, fluorescence or emission spectroscopy. These techniques are capable of giving precise state-to-state reaction cross sections but require a minimum number density of molecules (and, therefore, minimum pressure) for optical detection. Gas phase studies of ionic reactions have the advantage that the charged species may be isolated from neutral molecules by performing the experiment at very low pressure. Ions can be separated from other ions, according to their mass to charge ratio, through the use of electric and/or magnetic fields. In modern mass spectrometers, the detection of ions is very sensitive. This is critical because the number density of ions is limited by space-charge considerations which makes the study of ion dynamics difficult by optical techniques. Thus, state-to-state reaction dynamics are difficult to obtain for ionic reactions and often must be inferred from macroscopic observables such as reaction rates, branching ratios or photodissociation yields. Despite the experimental difficulty, some vibrationally state selected unimolecular<sup>3</sup> and bi-molecular<sup>4</sup> reaction rates have been investigated. Also, a new technique for generating ion pairs may enable the formation of rotationally resolved, state selected negative ions.<sup>5</sup> These techniques are, however, currently limited to very small reaction systems. In addition to the difficulties involved in obtaining microscopic experimental data, full quantum scattering calculations of polyatomic

reaction dynamics are limited by the size of the system, therefore, statistical reaction theories are often applied. "The basic assumptions of all statistical theories is that the rate constant  $k(E,J)$  depends only on the total energy  $E$  and the total angular momentum  $J$ . It is assumed that the energy does not depend upon where the energy is initially located and that a microcanonical ensemble is maintained as the molecule dissociates."<sup>6a)</sup> Despite advances in both classical<sup>18</sup> and quantum<sup>28,27</sup> approaches, accurate treatments of reaction dynamics can prove surprisingly difficult for moderately sized systems. In particular, reactions which exhibit incomplete energy randomization among the vibrational modes of the molecule or ion prior to reaction are incompletely described by statistical reaction theories such as RRKM<sup>7</sup> theory. This is because "the final RRKM equation derives its simplicity from the neglect of all dynamical aspects and from the treatment of the system in terms of only the molecular and transition state properties."<sup>6b)</sup> The first experimental example of non-RRKM behaviour was reported by Rynbrandt and Rabinovitch.<sup>8</sup> In their experiment,  $\text{CD}_2$  was added across the double bond of  $c\text{-CF}_2\text{CH}_2\text{CF-CF=CF}_2$  to form a molecule which consisted of two distinguishable, partially fluorinated cyclopropane rings. A preferential opening of the chemically activated (deuterium labelled) ring was observed at short (ns) times. In this classic example of non-statistical behaviour, the molecule retains a "memory" of which ring is excited because it dissociates more rapidly than intramolecular vibrational energy redistribution (IVR) can occur. Such reactions are characterized by poor coupling between some or all of the vibrational modes. One indication of poor

coupling is when the photodissociation lifetime depends on the vibrational mode being excited. Perhaps the most compelling evidence of non-statistical behaviour has been observed for the photodissociation of the van der Waals dimer of hydrogen fluoride. Excitation of the intramolecular H-F bond in  $\text{H-F}\cdots\text{H-F}$  resulted in a significantly increased lifetime compared to direct excitation of the van der Waals (intermolecular)  $\text{H}\cdots\text{F}$  bond.<sup>9</sup> This bottleneck in the IVR rate results because the coupling between the high frequency modes of the individual HF molecules and the low frequency intermolecular mode is weak. Photodissociation of a van der Waals dimer constitutes a particularly clear example of a reaction in which the intramolecular vibrational modes are decoupled from the reaction co-ordinate because of large differences in the respective vibrational frequencies. Trajectory calculations have suggested that the  $\text{Cl}^-$  ( $\text{CH}_3\text{Cl}$ ) complex, which is an intermediate in the  $\text{Cl}^- + \text{CH}_3\text{Cl}$   $\text{S}_{\text{N}}2$  reaction, also exhibits non-statistical behaviour because the intermolecular coupling between the closed shell  $\text{Cl}^-$  ion and the  $\text{CH}_3\text{Cl}$  is weak.<sup>10</sup> This prediction of non-statistical behaviour in an  $\text{S}_{\text{N}}2$  reaction is particularly interesting because  $\text{S}_{\text{N}}2$  reactions are fundamental to organic chemistry and thus constitute a "real world" system as opposed to the rather specialized case of a van der Waals dimer.

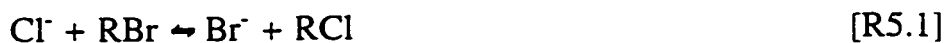
A novel application of non-statistical reaction dynamics is the use of laser light to influence the outcome of a chemical reaction. A reaction in which the product yield is influenced by the excitation of a specific bond or vibrational mode is said to exhibit "vibrational mode specific" behaviour. Since uranium isotope separation was

successfully accomplished by isotope selective laser ionization, chemists have tried to use lasers to selectively break bonds and control the products of chemical reactions. Rapid intramolecular vibrational energy redistribution (IVR), however, defeated all attempts prior to 1990,<sup>11</sup> when a successful mode specific reaction was first observed by Crim and co-workers for the photolysis of monodeuterated water, H-O-D.<sup>12</sup> The mode specific behaviour exists in HOD because the H-O and O-D vibrations are sufficiently decoupled that the molecule dissociates before energy can "leak" between modes. More recently, mode specific control of the products of bimolecular ion-molecule reactions of  $C_2H_2^+$ <sup>13</sup> and  $NH_3^+$ <sup>14</sup> ions has been observed. As mentioned above, halide-methyl halide  $S_N2$  reactions have shown indications of non-statistical reaction dynamics but, thus far, attempts to induce mode-selective reactivity in this reaction have not succeeded.

Many experimental<sup>15</sup> and theoretical<sup>16</sup> studies of gas phase  $S_N2$  reactions have been reported in the two decades since Brauman proposed that such reactions proceed via a double minimum potential energy surface.<sup>21</sup> A trio of communications to the editor of *J. Am. Chem. Soc.*<sup>17</sup>, in 1991, demonstrated that stable  $S_N2$  reaction intermediates could be isolated, energized and induced to react. These experiments also indicated that the reaction exhibited non-statistical behaviour. This experimental evidence was supported by detailed theoretical trajectory calculations by Vande Linde and Hase.<sup>18</sup> A fascinating result of these calculations was the prediction that "the unimolecular reaction dynamics of the  $Cl(CH_3Br)$  complex were "highly mode

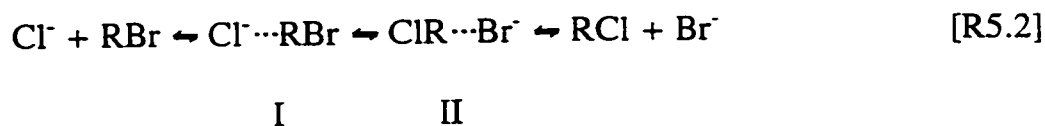
specific. When the low frequency  $\text{Cl}^{\cdots}\text{C}$  stretch and  $\text{Cl}^{\cdots}\text{CH}_3\text{Br}$  bending modes of the complex are excited, the predominant event is dissociation to form  $\text{Cl}^- + \text{CH}_3\text{Br}$ . However, this is a negligible pathway when the higher frequency modes of the complex are excited." <sup>19</sup> This prediction has elicited an increased interest in the dynamics of the  $\text{S}_{\text{N}}2$  reaction and the structure of the reaction intermediates. The search for direct experimental evidence of mode specific reaction dynamics in  $\text{S}_{\text{N}}2$  reactions was a motivating factor in the current study. The chloride-alkyl bromide systems are particularly attractive because of the asymmetrical potential energy surface (PES) and the ease of differentiating the two products,  $\text{Br}^-$  and  $\text{Cl}^-$ .

Halide-alkyl halide reactions are traditionally considered to occur by a concerted bimolecular nucleophilic substitution, or  $\text{S}_{\text{N}}2$ , mechanism. The generic form of this reaction is shown in reaction R5.1:



Following the convention of organic chemistry textbooks, R has been used to designate any alkyl group. For this study R is limited to  $\text{CH}_3$ ,  $\text{C}_2\text{H}_5$  or  $i\text{-C}_3\text{H}_7$  groups. The R group can, in principle, be any organic substituent, however, the  $\text{S}_{\text{N}}2$  reaction probability rapidly decreases as the size of R increases due to steric hindrance.<sup>20</sup> In the gas phase, the  $\text{Cl}^{\cdots}\text{RBr}$  and  $\text{ClR}^{\cdots}\text{Br}^-$  moieties constitute bound ion-molecule complexes. Therefore, the gas phase analogue of reaction R5.1 must proceed through

the ion-dipole complexes  $\text{Cl}^- \cdots \text{RBr}$  and  $\text{ClR} \cdots \text{Br}^-$  which function as reaction intermediates in reaction R5.2.



For all of the reactions discussed in this chapter, the chloride-alkyl bromide ion will be referred to as complex I and the bromide-alkyl chloride complex will be referred to as complex II. The terms "entrance complex" and "exit complex" will also be used to describe I and II, respectively, by analogy to the bimolecular  $\text{Cl}^- + \text{RBr}$  reaction as written in R5.1. Because of the ability to form two distinct intermediates, Brauman proposed that  $\text{S}_{\text{N}}2$  reactions are best described by a double well potential energy surface<sup>21</sup> like that shown in Figure 38. The entrance and exit complexes are labelled I and II in this Figure and the well depths correspond to the stabilization energy of the  $\text{Cl}^- \cdots \text{RBr}$  and  $\text{ClR} \cdots \text{Br}^-$ , respectively. A previous study of the thermochemistry of this reaction has shown that the well depths increase with increasing substitution of methyl groups for hydrogen atoms (methyl to ethyl to isopropyl to t-butyl) which reflects the increase in the polarizability of R.<sup>22</sup> The central barrier on the  $\text{S}_{\text{N}}2$  PES corresponds to the transition state of the reaction and is denoted by  $\text{TS}^\ddagger$ . The enthalpy change between the reactants and the transition state is labelled  $\Delta\text{H}^\ddagger$  in Figure 38. The back-dissociation of complexes I and II to the reactant species ( $\text{Cl}^-$  and  $\text{Br}^-$



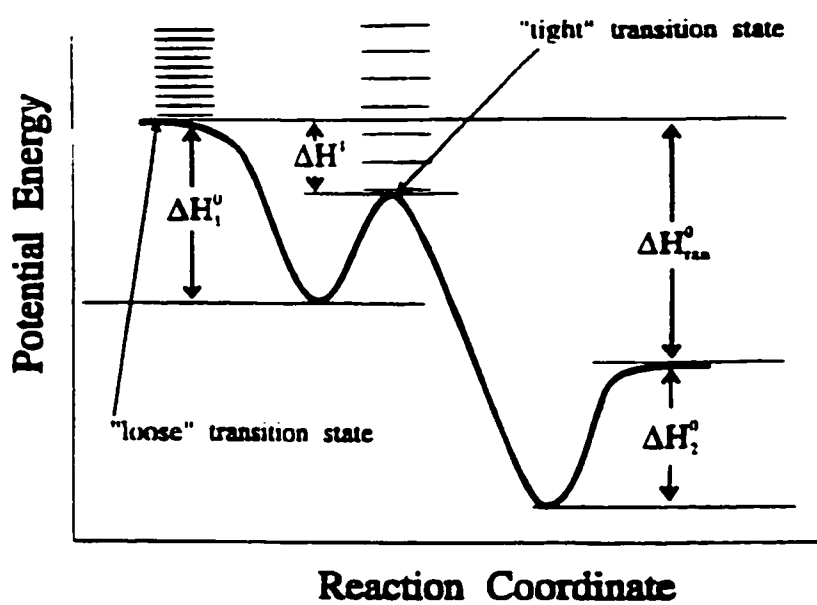
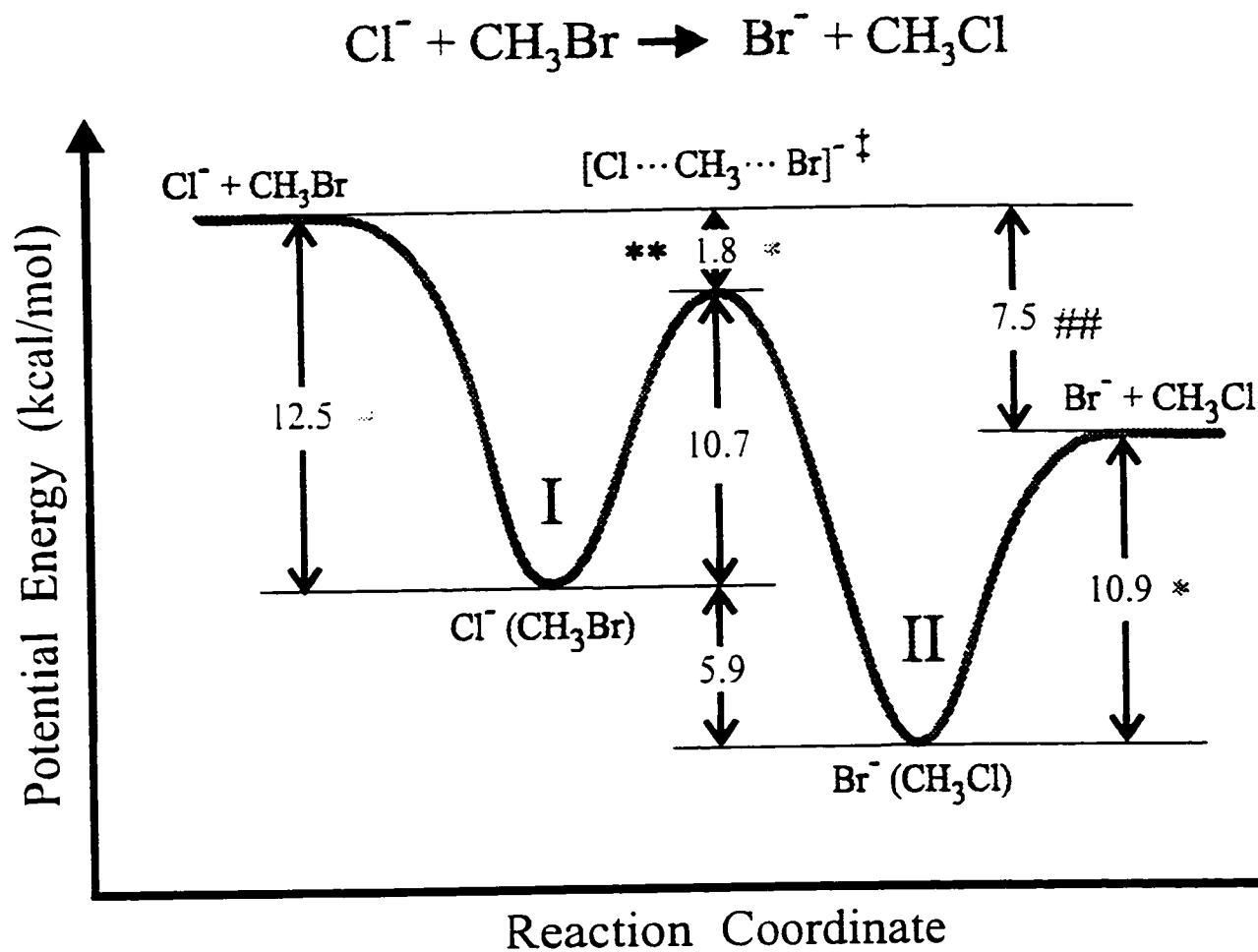


**Figure 38** Schematic representation of the double minimum potential energy surface for a  $S_N2$  reaction.

respectively) is a direct cleavage of the electrostatic  $X^-$ -C bond and, therefore, proceeds through a "loose" transition state (*ie.* the density of states is large at the transition state). The reaction of complex I to form  $Br^-$ , however, must cross the central barrier and is accompanied by an inversion around the central carbon atom. Such a rearrangement is entropically constrained and the transition state is described as "tight" because of the sparse density of states at the col, as shown in Figure 38.

The bimolecular  $Cl^- + RBr$  reaction has a central barrier which lies below the energy of the separated reactants for methyl, ethyl or n-propyl groups but above for isopropyl and t-butyl groups.<sup>22</sup> McMahon *et al.* found that substitution of a methyl group for a hydrogen atom generally raises the barrier height by  $\sim 2$ -3 kcal mole<sup>-1</sup>.<sup>22</sup> The exception is the  $Cl^- + CH_3Br$  reaction, for which the barrier would have to be lowered to fit the trend. Since the barrier height was determined using transition state theory, it may be inaccurate because the reaction is believed to be non-statistical. This would agree with recent results from a study of thermal unimolecular dissociation of  $Cl(CH_3Br)$ , conducted by Viggiano *et al.*, which suggest that the barrier for this reaction should be lowered to 5.4 kcal mole<sup>-1</sup>.<sup>46</sup> The bimolecular  $Cl^- + RBr$  reactions in which the barrier lies below the reactants will exhibit a negative energy dependence as seen for the  $Cl^- + CH_3Br$  reaction.<sup>28,23</sup> The potential energy surface for the  $Cl^- + CH_3Br$  reaction is shown in Figure 39. The relative enthalpies of the stationary points were primarily taken from the PHPMS work of McMahon *et al.*<sup>22</sup> Additional and/or unreported values were obtained from Viggiano and co-workers<sup>23</sup> or Lias *et*



\* HPMS; McMahon *et al.*, JACS 1996, 118, 9369.

## LIAS tables, 1988.

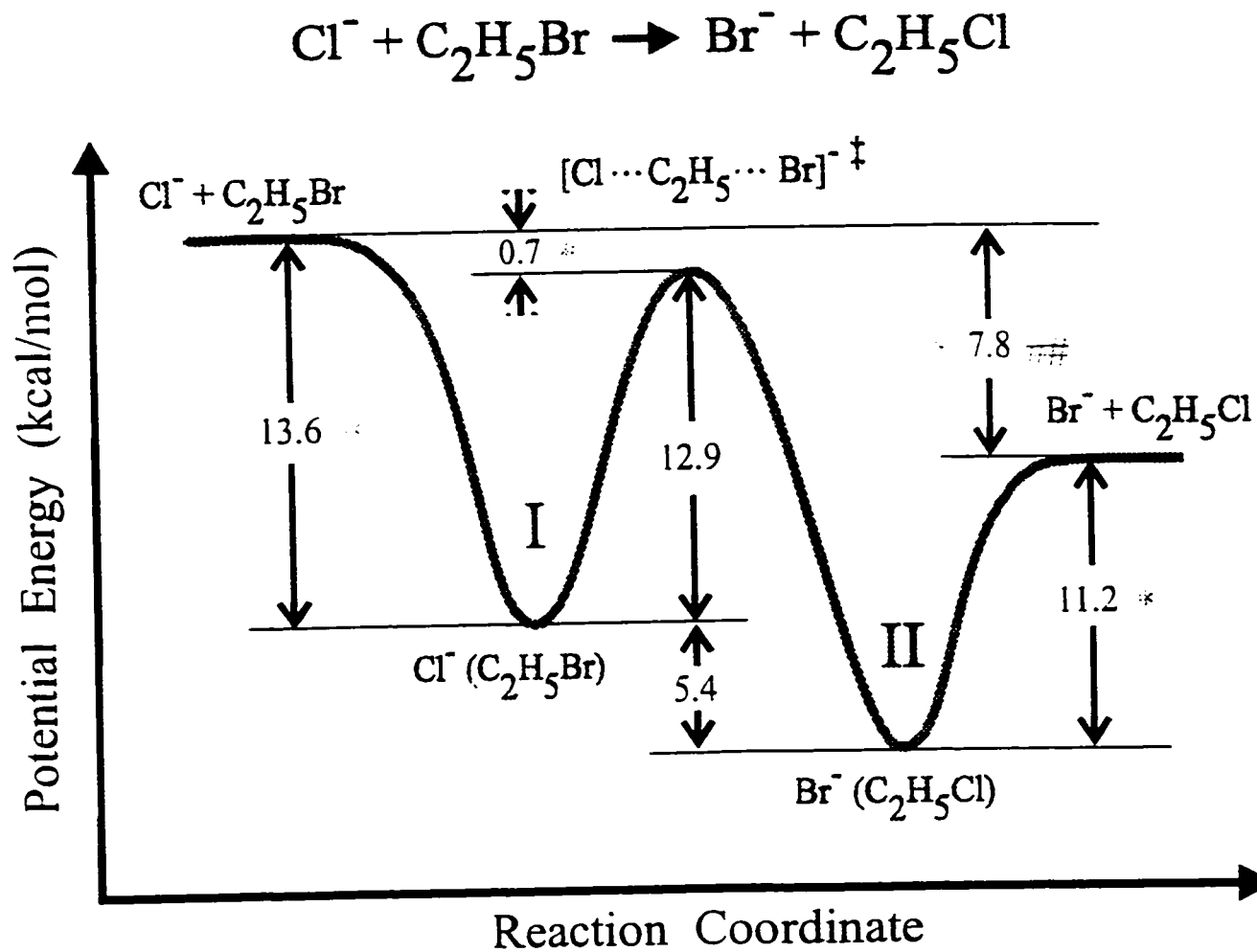
\*\* Viggiano *et al.*, JACS 1992, 114, 10477.

**Figure 39** The potential energy surface for the  $\text{Cl}^- + \text{CH}_3\text{Br}$  reaction.

*al.*<sup>24</sup> as indicated in the figure.

Although the  $\text{Cl}^- + \text{CH}_3\text{Br}$  reaction is one of the simplest cases of a "complex" polyatomic chemical reaction involving structural re-arrangement, an accurate treatment of the reaction dynamics has proven to be difficult. One of the main problems is that statistical reaction theories such as RRKM have proven to be inadequate for this reaction.<sup>23,19,25,46</sup> A recent development may help to shed light on this problem. Clary has developed a quantum scattering method which, although it involves approximations, explicitly treats the C-Cl, C-Br and the umbrella vibrations.<sup>26,27</sup> This method has been used to calculate the temperature dependence of the bimolecular  $\text{Cl}^- + \text{CH}_3\text{Br}$  reaction<sup>28</sup> but not unimolecular dissociation of the  $\text{Cl}^-(\text{CH}_3\text{Br})$  complex which is the primary goal of this study. It will be interesting to see if future quantum calculations from Clary's group will confirm Hase's classical prediction of mode specific behaviour in the  $\text{Cl}^- + \text{CH}_3\text{Br}$  reaction.

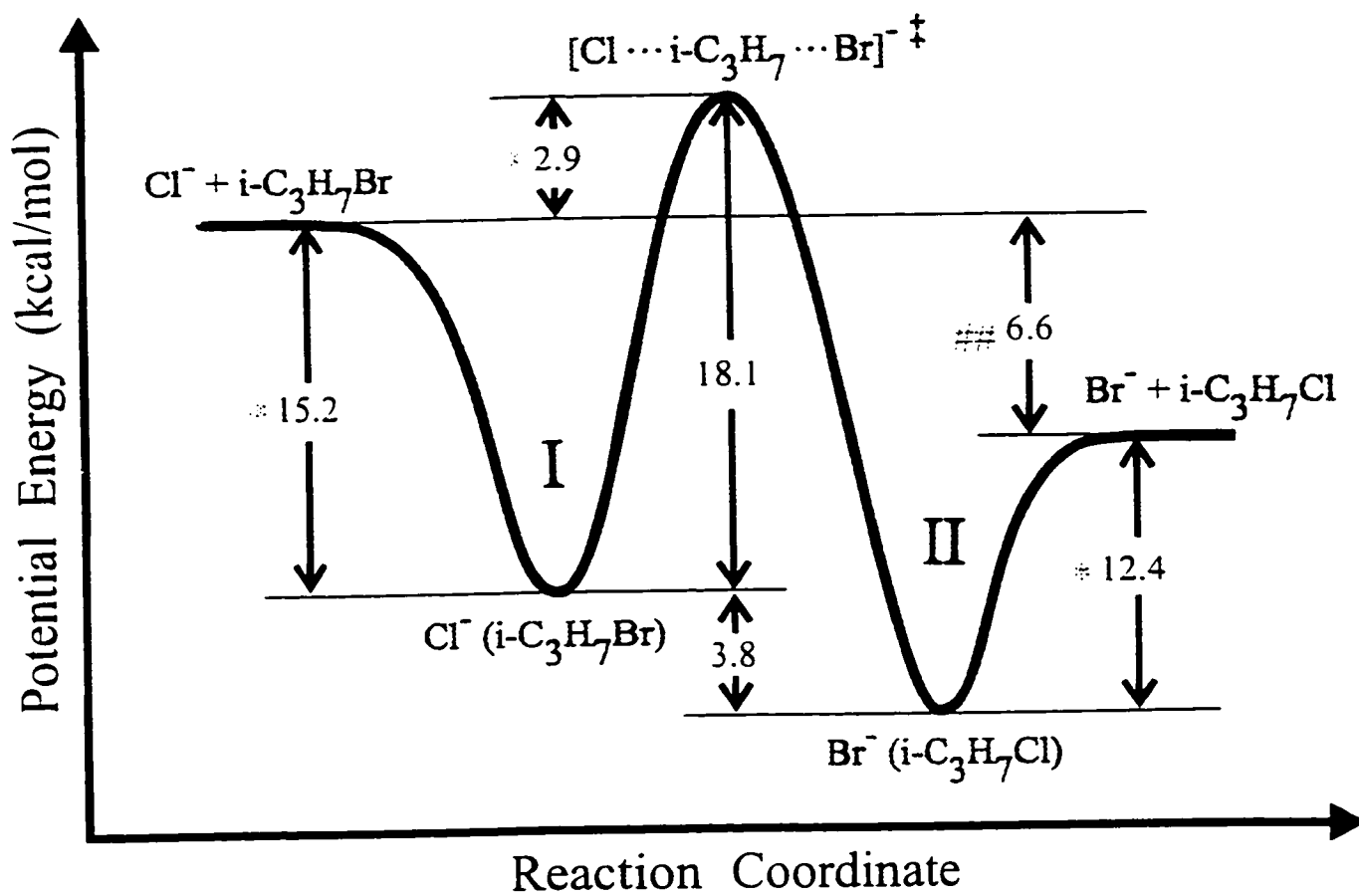
The potential energy surfaces for the  $\text{Cl}^- + \text{C}_2\text{H}_5\text{Br}$  and  $\text{Cl}^- + i\text{-C}_3\text{H}_7\text{Br}$  reaction are shown in Figure 40 and Figure 41. As noted for the chloride-methyl bromide PES, the relative enthalpies of the stationary points were taken primarily from the work of McMahon *et al.*<sup>22</sup> and the sources of other values are indicated on the figure. The central barrier of the  $\text{Cl}^- + \text{C}_2\text{H}_5\text{Br}$  reaction is only 0.7 kcal mole<sup>-1</sup> below the energy of the separated reactants compared to the barrier in the  $\text{Cl}^- + \text{CH}_3\text{Br}$  reaction which is 1.8 kcal mole<sup>-1</sup> below the energy of the reactants. Therefore, the rate of  $\text{Br}^-$  production from the bimolecular reaction of  $\text{Cl}^- + \text{C}_2\text{H}_5\text{Br}$  will be slower and the



\* HPMS measurements: McMahon *et al.* JACS 1996, 118, 9360.

# LIAS tables, 1988.

**Figure 40** The potential energy surface for the  $\text{Cl}^- + \text{C}_2\text{H}_5\text{Br}$  reaction.



\* HPMS measurements: McNahan *et al.* JACS 1996, 118, 9560.

## LLAS tables, 1988.

**Figure 41** The potential energy surface for the  $\text{Cl}^- + i\text{-C}_3\text{H}_7\text{Br}$  reaction.

efficiency of trapping complex I will be higher than for the chloride-methyl bromide reaction. The central barrier of the  $\text{Cl}^- + i\text{-C}_3\text{H}_7\text{Br}$  reaction is  $2.9 \text{ kcal mole}^{-1}$  above the reactants. Thus, the rate of  $\text{Br}^-$  production from the bimolecular reaction of  $\text{Cl}^- + i\text{-C}_3\text{H}_7\text{Br}$  at room temperature is negligible and complex I is easily trapped.

## 5.2 Experimental

All of the black body dissociation and IRMPD experiments presented in this chapter were performed on the Waterloo FT-ICR spectrometer and all of the ions were generated in an external high pressure ion source. The techniques of trapping and isolating ions generated in the high pressure ion source were described in chapter 2. The only difference between the negative and positive ion experiments is that the ion optics of the external source were switched to positive voltages in order to achieve acceleration and focussing of the negative ions. The end trapping plates of the FT-ICR cell also were switched to negative voltages to contain the negative ions. The methodology described in chapter 3 also applies to the IRMPD of  $\text{S}_{\text{N}}2$  complexes presented in this chapter. Where relevant, the pulse sequences and delays for individual experiments are discussed in section (5.3) of this chapter.

All of the chloride ions in this experiment were generated by 2 keV electron impact ionization on a mixture of approximately 1% carbon tetrachloride in methane bath gas. The reaction for  $\text{Cl}^-$  production is shown in R5.3.



The chloride-ethyl bromide and chloride-isopropyl bromide entrance channel complexes (complex I) were produced by clustering of the chloride ion onto the alkyl bromide neutral as shown in reaction R5.4. A mixture of ~1%  $\text{CCl}_4$ , 5-10 %  $\text{RBr}$  ( $\text{R}$ =ethyl or isopropyl) and ~1000 torr methane bath gas was used for these experiments.

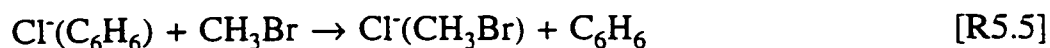


The chloride-methyl bromide complex (complex I) was much more difficult to make. Since the central barrier for the reaction is  $1.8 \text{ kcal mole}^{-1}$  below the reactant energy, the bimolecular reaction of  $\text{Cl}^- + \text{CH}_3\text{Br} \rightarrow \text{Br}^- + \text{CH}_3\text{Cl}$  rapidly goes to completion and the dominant ion produced from the source was  $\text{Br}^-$ . Attempts to make the  $\text{Cl}^-(\text{CH}_3\text{Br})$  complex by reaction R5.4 failed (the FT-ICR spectrum contained a negligible amount of the complex). An intermediate reaction was necessary to produce the  $\text{Cl}^-(\text{CH}_3\text{Br})$  complex. A large excess of benzene (~ 50 torr) was added to a mixture of ~0.1%  $\text{CCl}_4$ , ~1%  $\text{CH}_3\text{Br}$  and ~1000 torr methane bath gas. The clustering reaction of chloride ion onto benzene (R5.5) is  $8.8 \text{ kcal mole}^{-1}$  exothermic.





Termolecular collisions with the bath gas in the ion source stabilized the  $\text{Cl}^-(\text{C}_6\text{H}_6)$  complex. The chloride ion was then transferred from  $\text{Cl}^-(\text{C}_6\text{H}_6)$  to  $\text{CH}_3\text{Br}$  as shown in reaction R5.6.



The transfer reaction is  $\sim 3.7 \text{ kcal mole}^{-1}$  exothermic. This method resulted in a "softer" ion formation process and produced a small amount of the desired  $\text{Cl}^-(\text{CH}_3\text{Br})$  species ( $\leq 5\%$  of the total ion intensity).

All of the bromide-alkyl chloride ions (complex II) were prepared by electron impact ionization of bromoform (R5.7) and subsequent clustering to the alkyl chloride neutral molecules (R5.8).



Since the central barrier for all of the reverse reactions,  $\text{Br}^- + \text{RCl} \rightarrow \text{Cl}^- + \text{RBr}$ , is  $\geq 6 \text{ kcal mole}^{-1}$  higher than the energy of the separated reactants, the rate of the reverse bimolecular  $\text{S}_{\text{N}}2$  reaction was negligible. Therefore,  $\text{Br}^-(\text{RCl})$  was efficiently stabilized by termolecular collisions in the high pressure ion source and the bromide-alkyl chloride complexes (II) were easier to produce in usable quantities.

## 5.3 Results

### 5.3.1 $\text{Cl}^-(\text{CH}_3\text{Br})$

The  $\text{Cl}^-(\text{CH}_3\text{Br})$  ions studied in this section were produced using the experimental methodology described in section 5.2 of this thesis. Both the reactant concentrations and the instrumental parameters were optimized to produce the maximum possible intensity of  $\text{Cl}^-(\text{CH}_3\text{Br})$ . Figure 42 was obtained by summing 64 scans which were acquired without rf ejection in order to determine the relative abundance of each ion produced in the high pressure external source. The spectrum shows that  $\text{Cl}^-(\text{CH}_3\text{Br})$  constitutes a minor fraction of the total ion intensity. Thus, rf *sweep* ejection was required to achieve clean isolation of the  $\text{Cl}^-(\text{CH}_3\text{Br})$  ion. The efficiency of the rf sweep isolation is demonstrated by the FT-ICR mass spectrum which is presented in Figure 43. This spectrum was collected immediately after isolation and is the sum of 8 scans. The  $m/z=131, 133$  ions could not be reliably ejected without translational excitation of the complex and the  $\text{Cl}^-(\text{CH}_3\text{Br})$  ions were found to be particularly sensitive to translational energy as will be discussed in detail in section 5.4. The three isotopomers ( $m/z=129, 131, 133$ ) were isolated using a wide ( $\sim 60\text{-}80$  kHz) notch or "safety belt" in the rf frequency sweep and the total  $\text{Cl}^-(\text{CH}_3\text{Br})$  intensity was obtained by adding the integrated intensity of all three peaks. When the isolated  $\text{Cl}^-(\text{CH}_3\text{Br})$  ions were trapped in the FT-ICR cell in the presence of ambient black body infrared radiation, unimolecular dissociation was observed. The mass

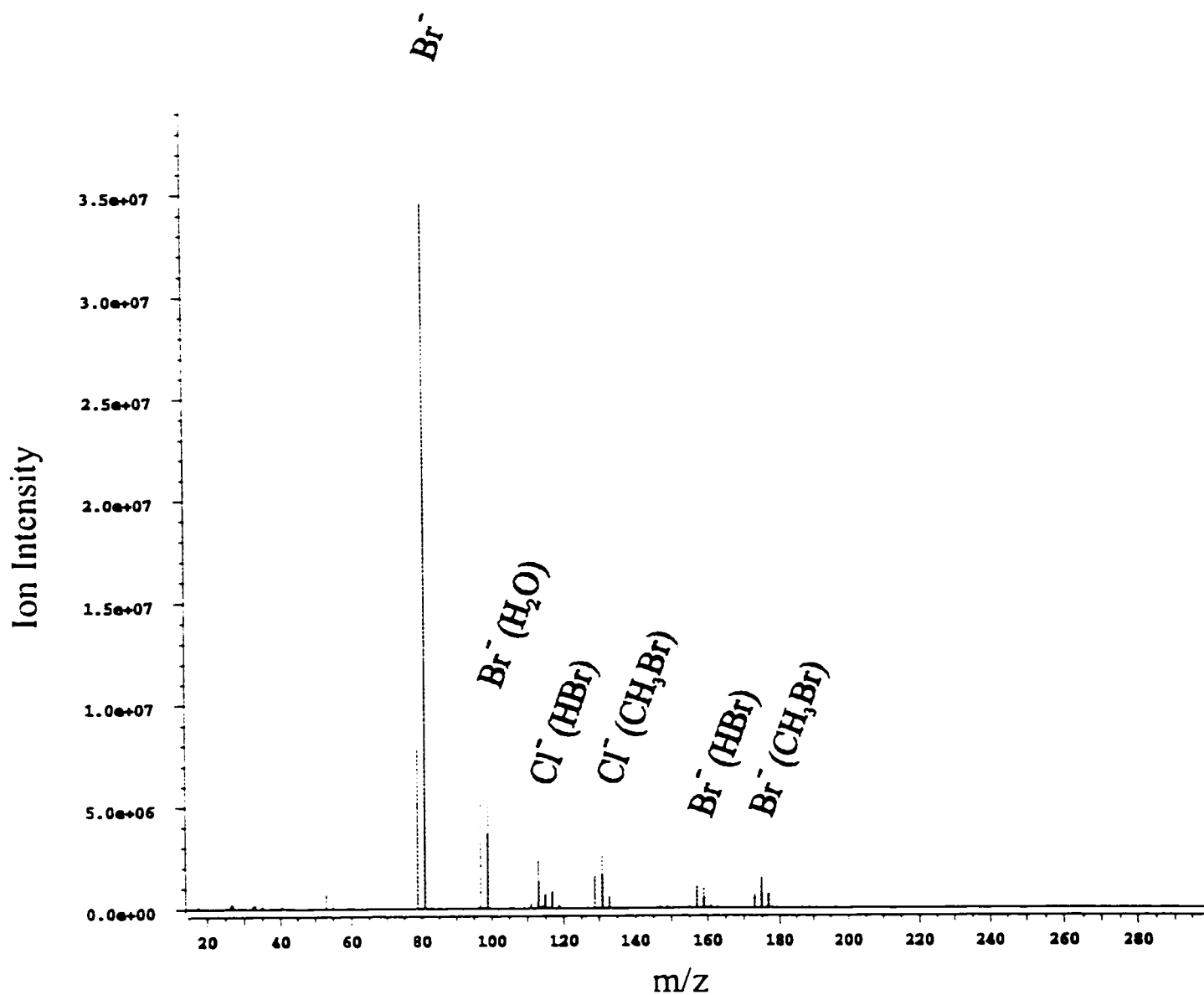


**Figure 42** Un-ejected FT-ICR mass spectrum of ions produced in the high pressure external ion source during the  $\text{Cl}^- + \text{CH}_3\text{Br}$  reaction.

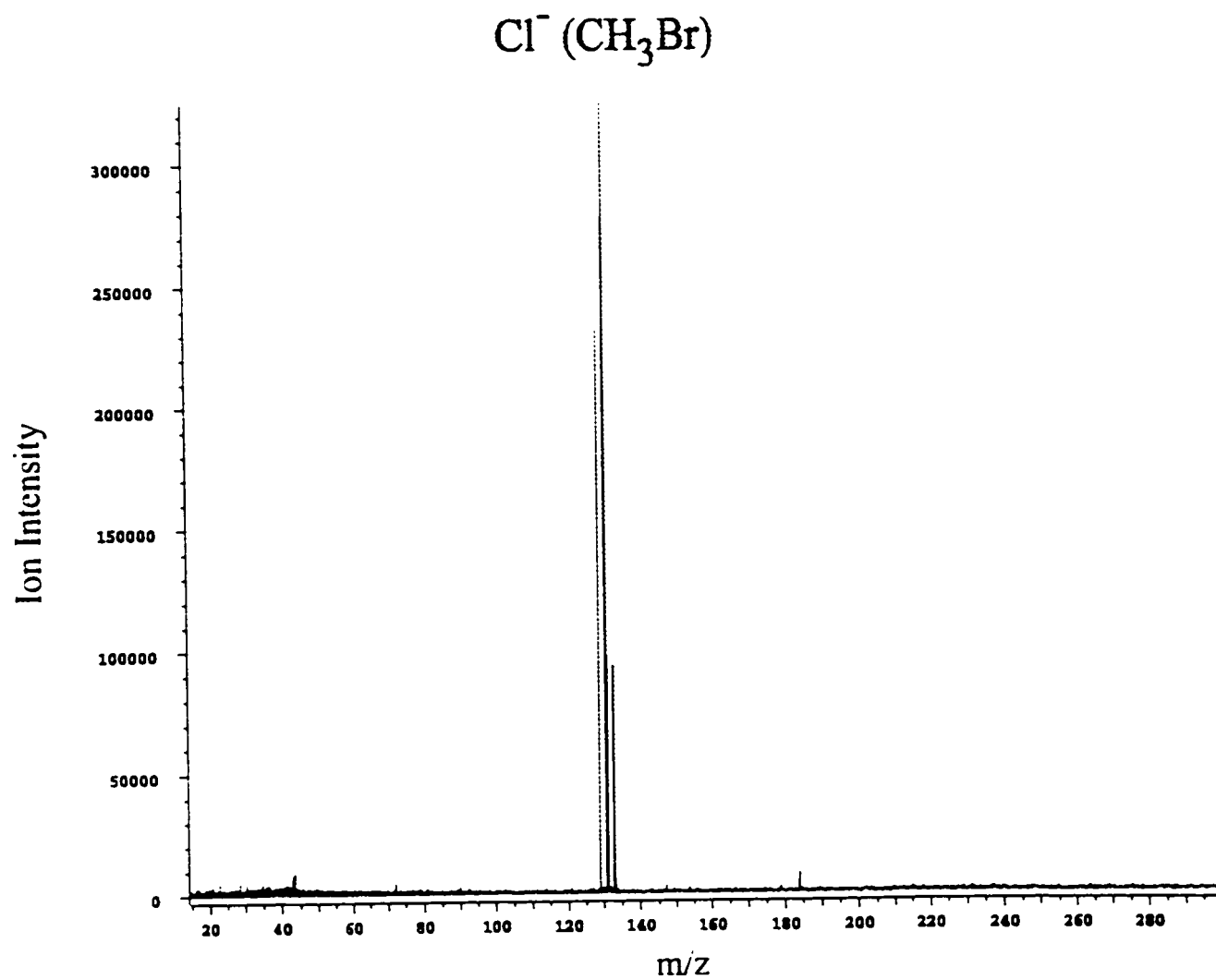


**Figure 43** FT-ICR mass spectrum of the  $\text{Cl}^-(\text{CH}_3\text{Br})$  complex after rf isolation.

spectrum shown in Figure 47b) was obtained by trapping the ions for a period of 15 s following isolation, at 20 °C. 64 scans were co-added. The observed products are  $\text{Cl}^-$ ,  $\text{Cl}^-(\text{H}_2\text{O})$  and  $\text{Br}^-$ . The  $\text{Br}^-$  ion is more abundant than the  $\text{Cl}^-$  ion which qualitatively agrees with the  $\text{Cl}^-(\text{CH}_3\text{Br})$  PES shown in Figure 39 because the  $\text{Br}^-$  product is the thermochemically favoured reaction channel. The  $\text{Cl}^-(\text{H}_2\text{O})$  ion arises from a bimolecular exchange reaction between the  $\text{Cl}^-(\text{CH}_3\text{Br})$  ion and background water (estimated to be on the order of  $5 \times 10^{-11}$  torr) in the UHV chamber where the FT-ICR cell is located. The association reaction of  $\text{Cl}^- + \text{H}_2\text{O} \rightarrow \text{Cl}^-(\text{H}_2\text{O})$  has an enthalpy change,  $\Delta H = -14.3 \text{ kcal mole}^{-1}$ ,<sup>29</sup> therefore, the  $\text{Cl}^-$  exchange reaction from  $\text{CH}_3\text{Br}$  to  $\text{H}_2\text{O}$  is approximately  $1.8 \text{ kcal mole}^{-1}$  exothermic. Thermoneutral or slightly exothermic exchange reactions are very efficient under the low pressure conditions of the FT-ICR cell, thus, the  $\text{Cl}^-$  exchange reaction rate will proceed at a rate which approaches the Langevin collision rate.<sup>30</sup>

A series of mass spectra was obtained with reaction delays (vd) ranging from 0.1 s to 40 s at 21 °C. Each experiment had a 15 s relaxation delay (d5) following the rf sweep isolation of  $\text{Cl}^-(\text{CH}_3\text{Br})$ . The products formed in the 15 s period were then ejected with rf shots prior to the variable reaction delay. A plot of the ion intensity vs. reaction delay (vd) is shown in Figure 44. The  $\text{Cl}^-(\text{CH}_3\text{Br})$  decay curve was calculated from a least squares fit of the data to a first order rate equation, which yielded a value for the unimolecular dissociation rate constant,  $k_{\text{uni}}$ , of  $0.045 \text{ s}^{-1}$ . Since the  $\text{H}_2\text{O}$  pressure is constant during any experiment, the rate of  $\text{Cl}^-(\text{H}_2\text{O})$  formation

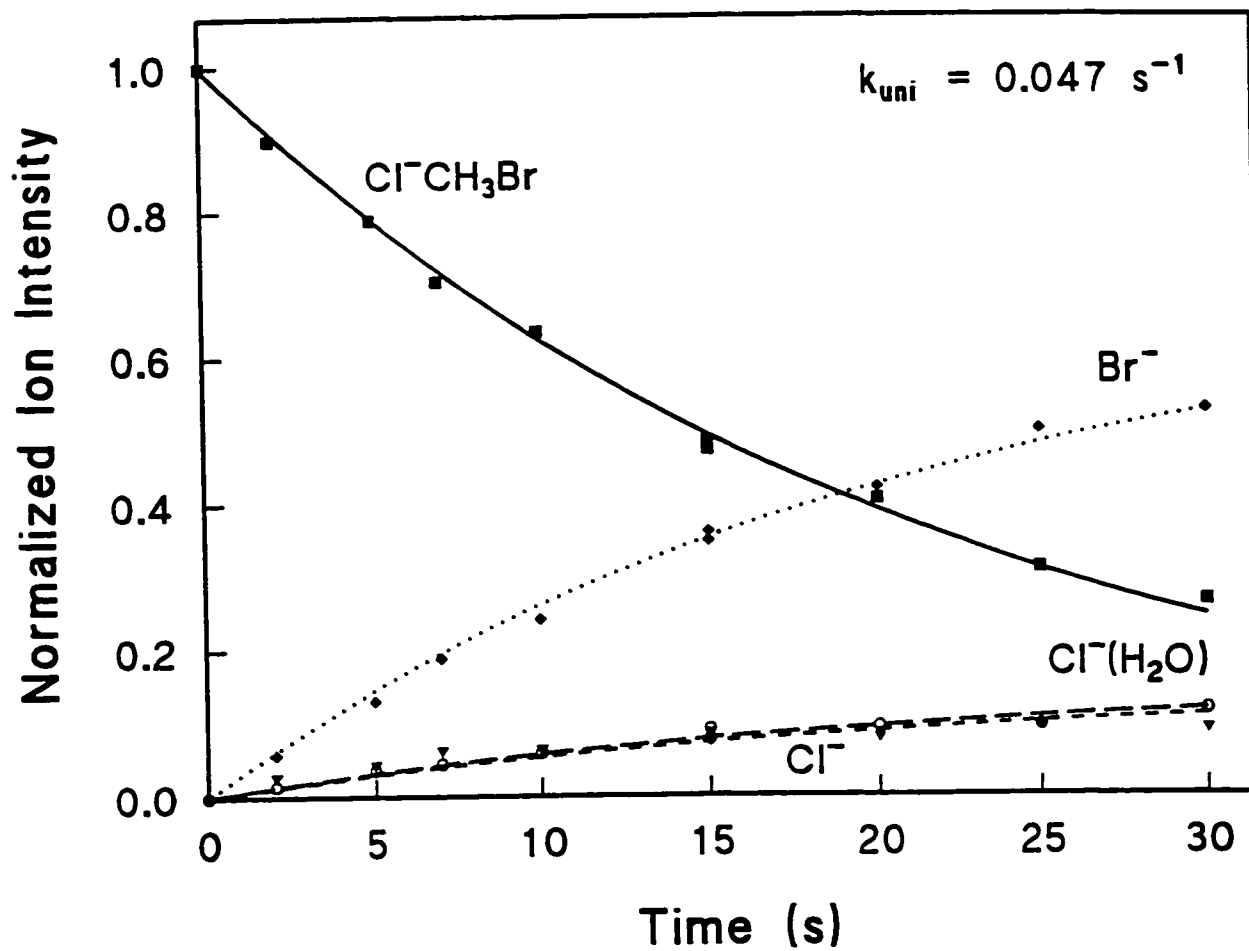


**Figure 44** Black body dissociation kinetics of  $\text{Cl}^-(\text{CH}_3\text{Br})$  at 21 °C.

will be pseudo-first order and the formation of the product ions may be treated as parallel first order reactions. If there are no product ions present initially, then the ratio of the rate constants  $k_{Br^-}:k_{Cl^-}:k_{Cl^-(H_2O)}$  governing formation of the  $Br^-$ ,  $Cl^-$  and  $Cl^-(H_2O)$  products, respectively, is equal to the ratio of the relative abundances of each of the species,  $[Br^-]:[Cl^-]:[Cl^-(H_2O)]$ .<sup>31</sup> If the total number of products is  $i$ , then:

$$\sum_i k_i = k_{uni} \quad (42)$$

and the kinetics for each of the product ions,  $X_i$ , may be described by:

$$[X_i]_t = B_i (1 - [A]_t) = B_i (1 - [A]_0 e^{-k_{uni}t}) \quad (43)$$

where the co-efficient,  $B_i$ , is defined as:

$$B_i = \frac{k_i}{k_{uni}} \quad ; \quad \sum_i B_i = 1 \quad (44)$$

The curves for the product ions were fit to equation (43) and the rate constants for the  $Br^-$ ,  $Cl^-$  and  $Cl^-(H_2O)$  products are shown in Table 5.1 as  $k_{Br^-}$ ,  $k_{Cl^-}$  and  $k_{Cl^-(H_2O)}$ , respectively. This experiment was repeated at 33, 50 and 70 °C in order to examine the effect of temperature on the black body dissociation kinetics of  $Cl^-(CH_3Br)$ . The rate constants  $k_{uni}$ ,  $k_{Br^-}$ ,  $k_{Cl^-}$  and  $k_{Cl^-(H_2O)}$  and the branching ratio of the halide products,

$k_{Br}/k_{Cl}$  are reported in Table 5.1. The relaxation delay,  $d_5$ , had to be reduced from 15 s for the higher temperature experiments and is included in Table 5.1 because there is evidence that it may affect the branching ratio. The temperature dependence of the individual rate constants,  $k_{Br}$  and  $k_{Cl}$ , may be used to determine the activation energy for each process from the Arrhenius equation (45), provided the activation energy is independent of temperature.<sup>32</sup>

$$k = A_{Arr} e^{-\frac{E_a}{RT}} \quad (45)$$

If an Arrhenius plot of  $\ln k$  vs.  $T^{-1}$  is constructed, the activation energy,  $E_a$ , and the Arrhenius pre-exponential factor,  $A_{Arr}$ , can be obtained from the slope and intercept respectively. Since the formation of  $Cl^-$  and  $Br^-$  from  $Cl^-(CH_3Br)$  is treated as parallel reactions, the activation energy for each reaction must be determined from the temperature dependence of the individual rate constants  $k_{Br}$  and  $k_{Cl}$ , respectively. No attempt was made to determine the Arrhenius parameters,  $E_a^{ClW}$  and  $A_{Arr}^{ClW}$  because the pressure of the water vapour could not be measured and increased with increasing temperature. Figure 45 is a plot of  $\ln k_{Br}$  vs.  $T^{-1}$ , from which  $E_a^{Br}$  was determined to be  $5.4 \text{ kcal mole}^{-1}$  and  $A_{Arr}^{Br}=365$ . Similarly, the plot of  $\ln k_{Cl}$  vs.  $T^{-1}$  presented in Figure 46 yielded the values  $E_a^{Cl}=6.7 \text{ kcal mole}^{-1}$  and  $A_{Arr}^{Cl}=665$ . The activation energies are much lower than the  $\Delta H$  values shown on the potential energy surface in Figure 39 and the Arrhenius A factors are  $\sim 10^{10}$  times too small.<sup>33</sup> For unimolecular



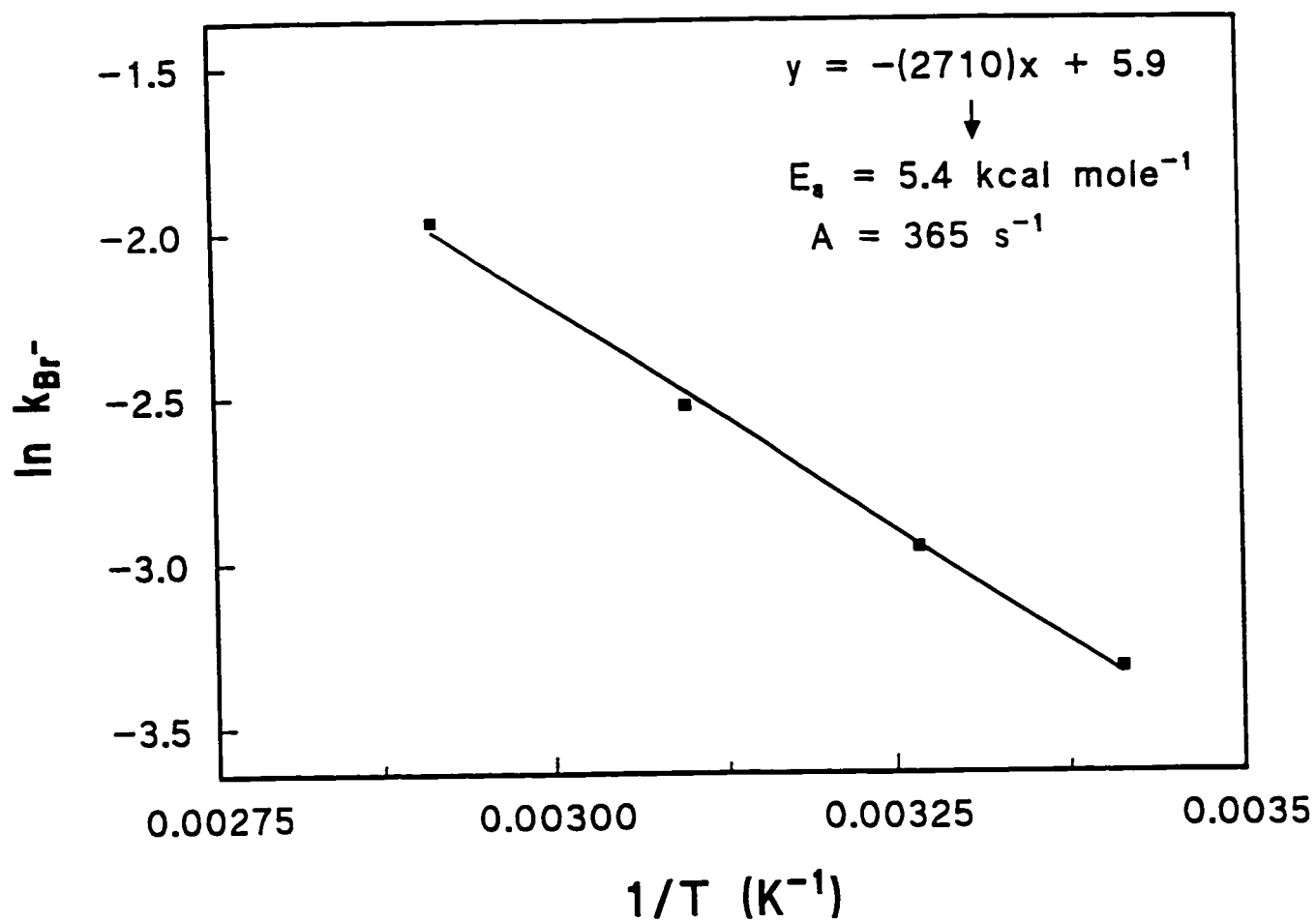


**Figure 45** Arrhenius plot of  $\ln k_{Br}$  vs.  $T^{-1}$  for black body induced dissociation of  $Cl^-(CH_3Br)$ .

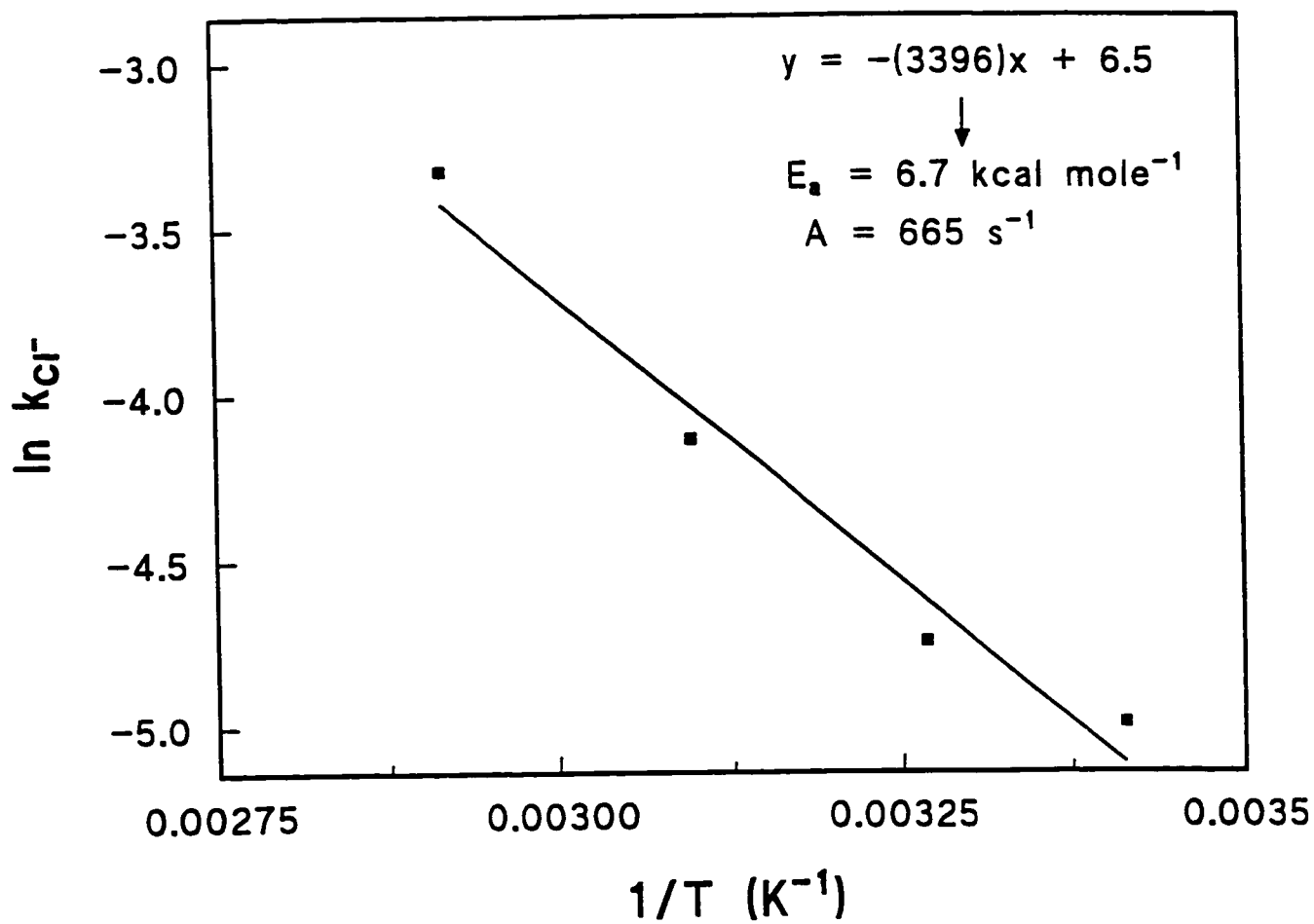


**Figure 46** Arrhenius plot of  $\ln k_{\text{Cl}}$  vs.  $T^{-1}$  for black body induced dissociation of  $\text{Cl}(\text{CH}_3\text{Br})$ .

dissociation induced by black body radiation, only ions which are large enough to be in the rapid energy exchange (REX) limit<sup>34</sup> are expected to yield Arrhenius activation energies which agree with the true bond dissociation enthalpy.<sup>35,36,37</sup> The ions described here are too small to be in the REX limit. Thus, the underestimated values of  $E_a$  and  $A_{Arr}$  obtained in this study are a reflection of the fact that the rate of photon absorption is the limiting factor in these experiments and not the dissociation rate of energized species.

The  $Cl^-(CH_3Br)$  ion was irradiated with 10.6  $\mu m$  CW infrared radiation from the  $CO_2$  laser and the FT-ICR spectrum of the photodissociation product ions was recorded. The spectrum shown in Figure 47a) resulted from irradiation with 9.9 W  $cm^{-2}$  for 15 s. 64 scans were summed. The background (black body dissociation) spectrum at 20 °C was obtained with all parameters and delays identical to Figure 47a), and is shown in Figure 47b). *Both* the unimolecular dissociation rate of the  $Cl^-(CH_3Br)$  ion *and* the  $Br^-/Cl^-$  ratio were significantly enhanced in the presence of the laser. Subtraction of the raw "laser OFF" transient (Figure 47b) from the raw "laser ON" transient (Figure 47a) yields a difference spectrum which is presented in Figure 48. No normalization was used to produce this difference spectrum. The peak intensities in the difference spectrum represent only the products formed (positive) and the reactants consumed (negative) by IRMPD of  $Cl^-(CH_3Br)$ . The difference spectrum "tracks" (*ie.* total reactant intensity is equal to total product intensity) within ~10% error using subtraction of the raw transients. Fluctuations in absolute intensity are

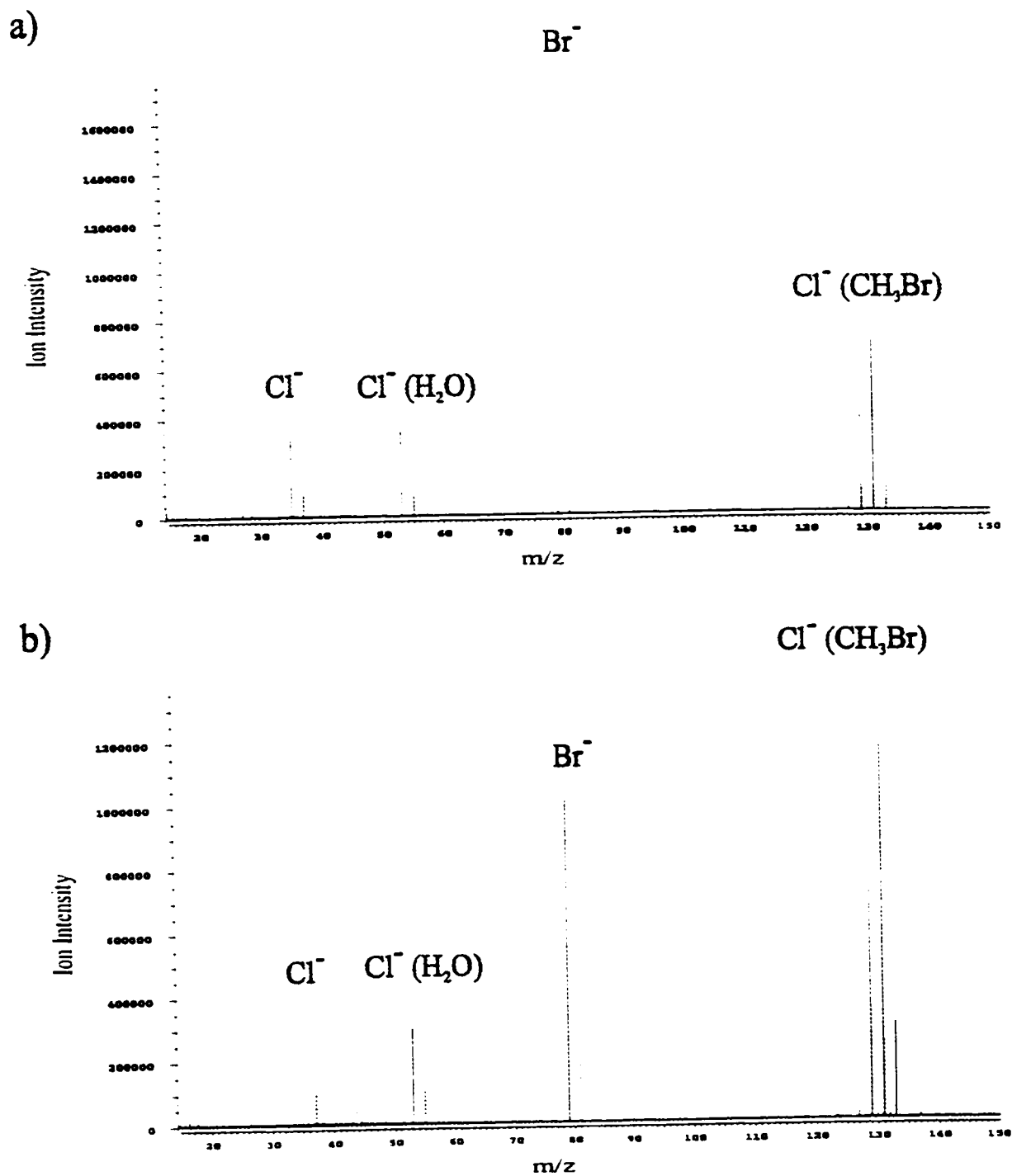


**Figure 47** FT-ICR mass spectra resulting from 15 s exposure of isolated  $\text{Cl}^- (\text{CH}_3\text{Br})$  to a)  $9.9 \text{ W cm}^{-2}$  IR laser radiation; b) black body radiation,  $20^\circ \text{C}$ .

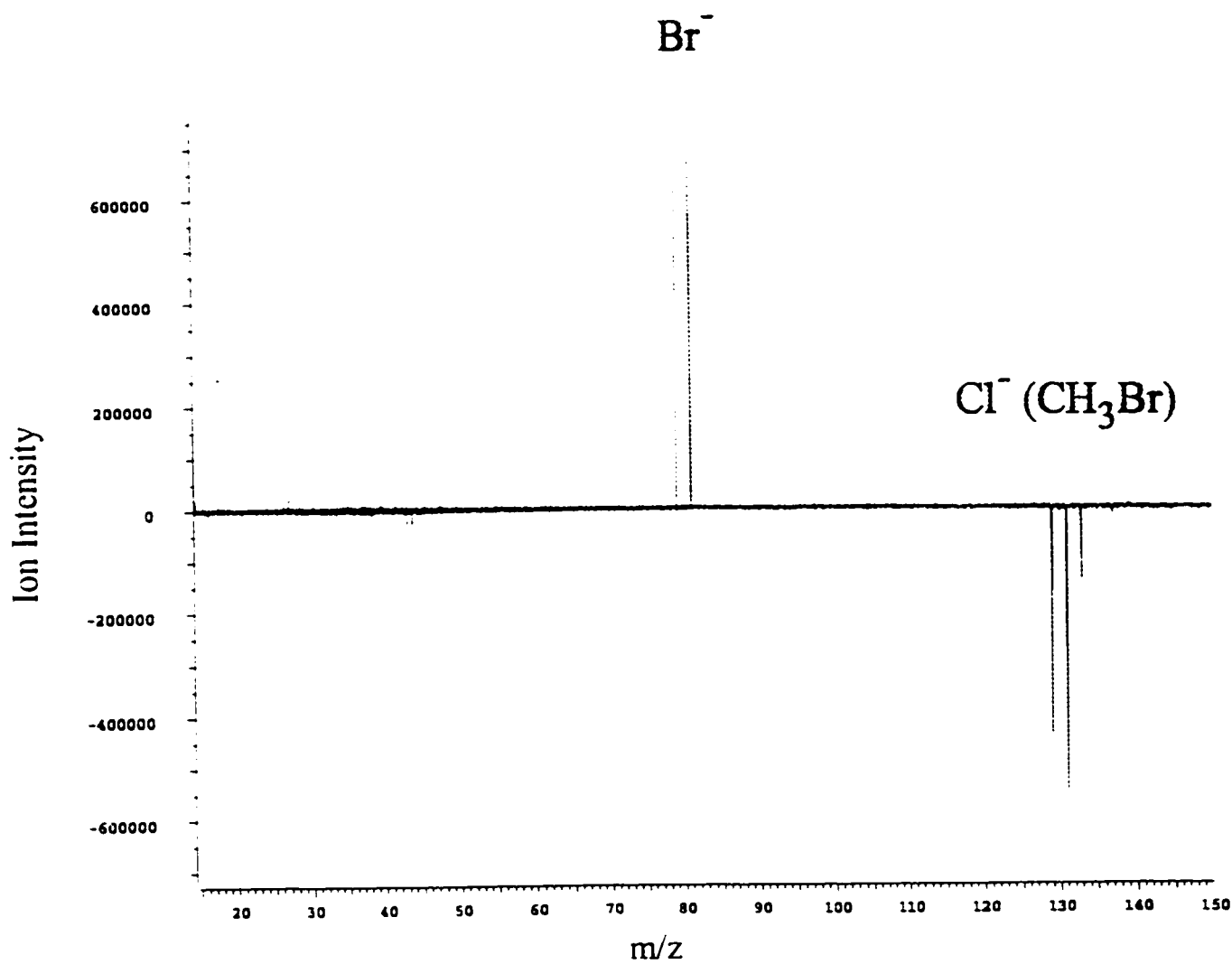


**Figure 48** Difference spectrum (laser ON-laser OFF) for  $\text{Cl}^-(\text{CH}_3\text{Br})$  photodissociation.

commonly observed in FT-ICR spectra in which the ions are generated externally, however the relative intensities of the ions are constant. Ion intensities are, therefore typically normalized to the total ion intensity when determining dissociation kinetics. The difference spectrum was obtained by subtraction of the raw transients which led to a greater uncertainty than if the individual transients had been normalized prior to subtraction. Future versions of XMASS software will allow the transients to be normalized to identical total ion intensities, prior to subtraction, which may improve the tracking of the difference spectra. Even though  $\text{Br}^-$  accounts for 100% of the observed product yield from IRMPD of  $\text{Cl}^-(\text{CH}_3\text{Br})$ , there is a 10% tracking error and a noise hump at low mass which may obscure small amounts of  $\text{Cl}^-$ . Therefore, the  $\text{Br}^-$  ion yield may only be reported confidently at  $\geq 90\%$  of the observed product yield.

The difference spectrum in Figure 48 indicates that all four isotopic variants of  $\text{Cl}^-(\text{CH}_3\text{Br})$  are dissociated by the infrared laser radiation and that the rates of dissociation are approximately equal. Irradiation of ions with a narrow bandwidth IR laser might be expected to show isotopic selectivity. Beauchamp *et al.* have shown that low-power multiphoton dissociation of dimethyl chloronium ions displayed no observable difference in the dissociation rates of the  $^{35}\text{Cl}$  and  $^{37}\text{Cl}$  isotopes.<sup>38</sup> Deuterium substitution, however, *did* produce a significant isotope effect (only the completely deuterium substituted ion,  $(\text{CD}_3)_2\text{Cl}^+$  was dissociated). Since the relative difference in the frequency of the C-Br stretch for the  $^{79}\text{Br}$  and  $^{81}\text{Br}$  isotopes will be less than the shift in the C-Cl stretch frequency between  $^{35}\text{Cl}$  and  $^{37}\text{Cl}$  isotopes, the

lack of an observed chlorine isotope effect should also preclude the existence of a bromine isotope effect on the photodissociation kinetics of  $\text{Cl}^-(\text{CH}_3\text{Br})$ .

The enhancement in  $\text{Cl}^-(\text{CH}_3\text{Br})$  dissociation rate and  $\text{Br}^-$  production may also be observed by comparing the kinetics of the IRMPD and black body experiments. The dissociation kinetics resulting from irradiation of the ions by a  $9.9 \text{ W cm}^{-2}$  infrared laser and a  $21^\circ\text{C}$  black body source are presented in Figure 49a) and b), respectively.

The bimolecular reaction of  $\text{Cl}^- + \text{CH}_3\text{Br}$  was also studied. Bare chloride ion was produced in the external high pressure ion source and trapped in the FT-ICR cell where it was allowed to react with a static pressure of  $\text{CH}_3\text{Br}$  gas which was introduced through molecular leak valves. The kinetics for the reaction are shown in Figure 50. The curve represents a least squares fit of the data to a first order rate equation. The pseudo-first order rate constant,  $k' = k_{\text{bi}}[\text{CH}_3\text{Br}]$ , obtained from the fit, is equal to  $4.8 \times 10^{-2} \text{ s}^{-1}$  with  $1.1 \times 10^{-7} \text{ mbar}$  (uncorrected ion gauge pressure) in the FT-ICR cell. The bimolecular  $\text{S}_{\text{N}}2$  rate has been extensively studied in the past using flowing afterglow techniques and is reported as  $k_{\text{bi}} = (2.5 \pm 0.3) \times 10^{-11} \text{ cm}^3 \text{ s}^{-1}$ .<sup>23</sup> The excellent fit to the data in Figure 50 indicates that the kinetics are completely first order for the duration of the reaction (70 s) which confirms that neither ion loss or mass discrimination is occurring. The reactants were also irradiated with a CW  $\text{CO}_2$  laser in order to investigate the effects of vibrational excitation of neutral  $\text{CH}_3\text{Br}$  on the bimolecular reaction rate. No observable difference in the reaction rate was observed. This is possibly because the neutral methyl bromide molecule does not have

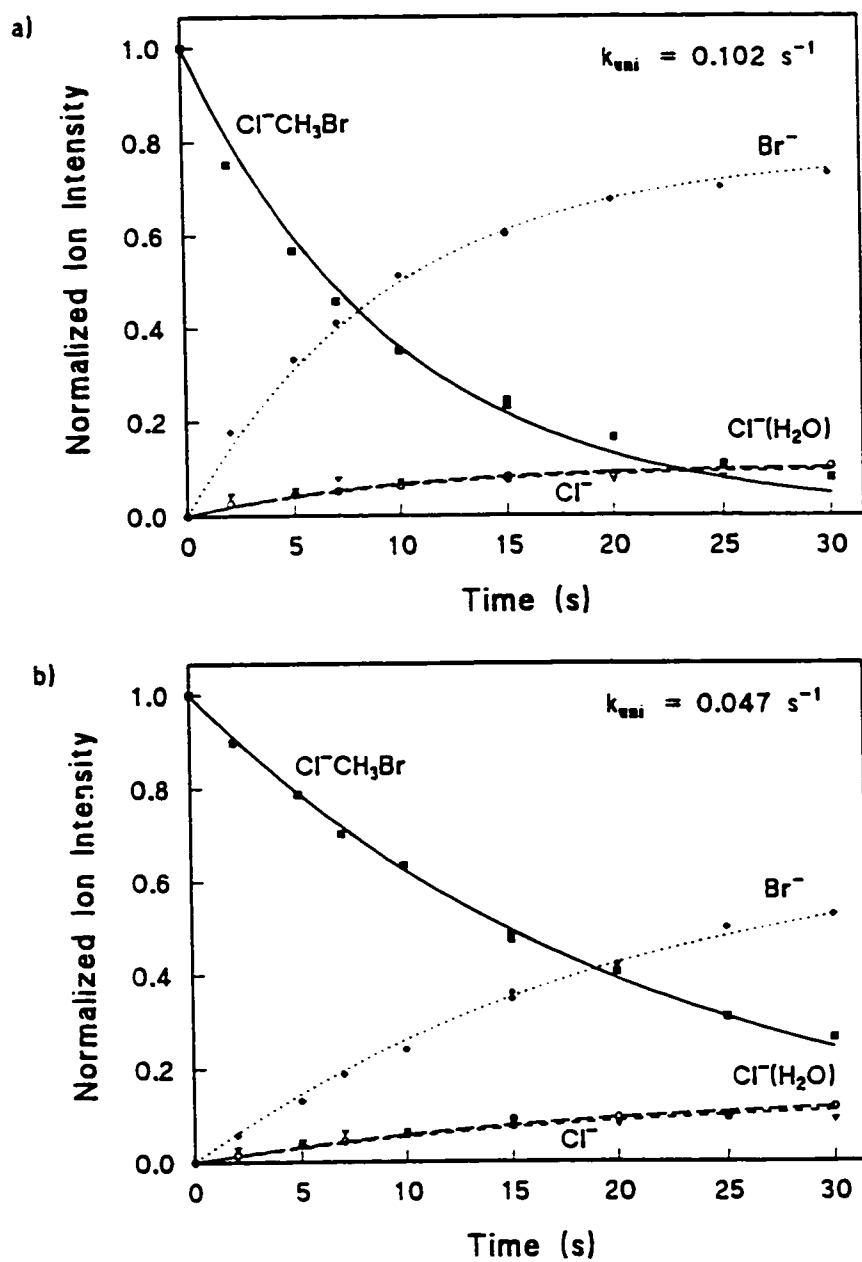


**Figure 49** Dissociation kinetics of  $\text{Cl}^-(\text{CH}_3\text{Br})$  from; a)  $9.9 \text{ W cm}^{-2}$  IR laser radiation; b) black body IR radiation at  $20^\circ\text{C}$ .



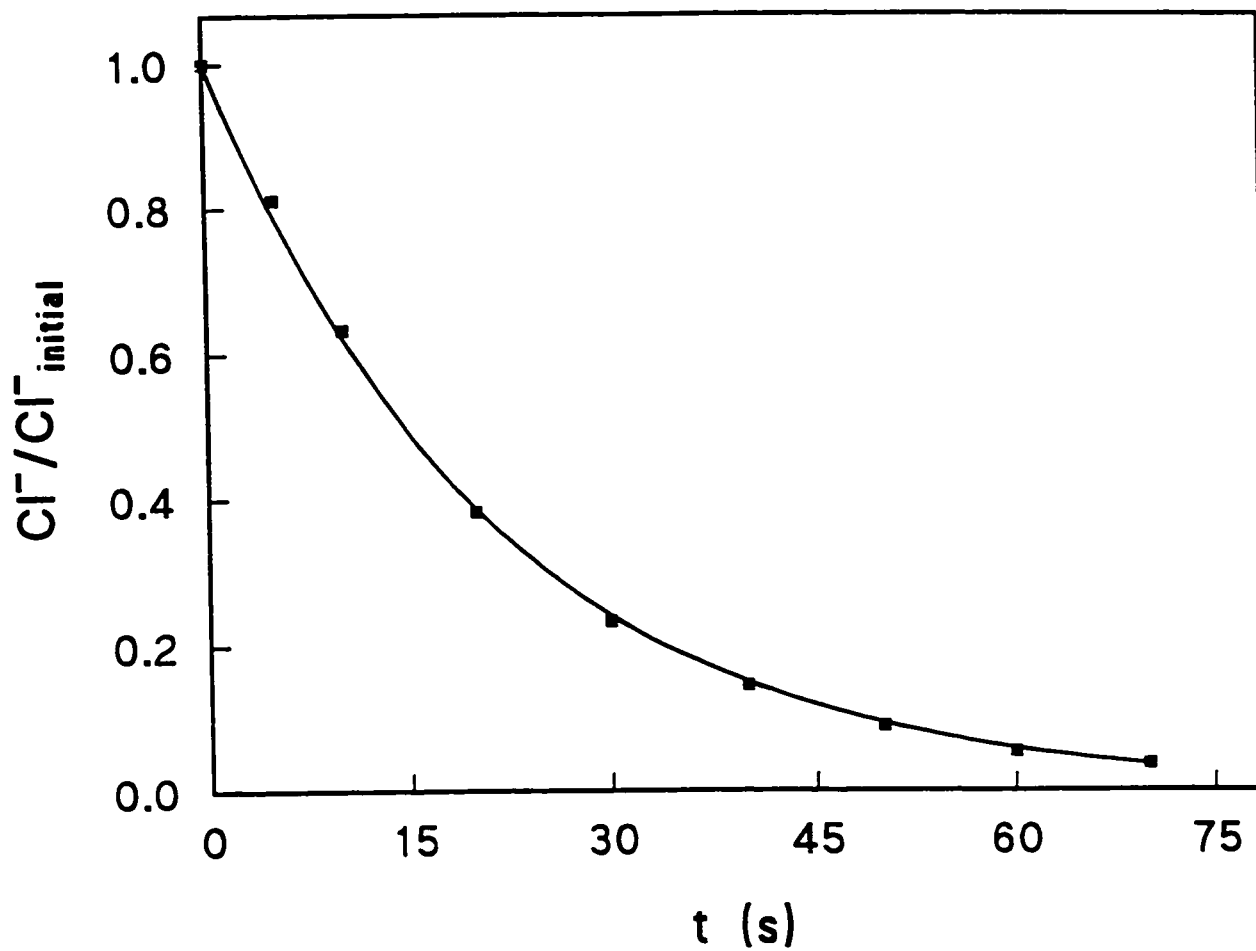


**Figure 50** Kinetics plot for the bimolecular reaction of  $\text{Cl}^- + \text{CH}_3\text{Br}$  at 20 °C. The uncorrected ion gauge pressure of  $\text{CH}_3\text{Br}$  was  $1.1 \times 10^{-7}$  mbar.

an infrared absorption at the laser frequency, however, the change in the frequency of the methyl rock vibration in going from the neutral  $\text{CH}_3\text{Br}$  to the  $\text{Cl}^-(\text{CH}_3\text{Br})$  complex is small.<sup>19</sup> Another possibility which exists is that the  $\text{CH}_3\text{Br}$  is being vibrationally excited without a change in the reaction rate. Viggiano and co-workers have shown that a change in temperature and, therefore, internal energy does not affect the bimolecular reaction rate if the center of mass kinetic energy is fixed.<sup>23</sup> The present experiment cannot resolve which of these two reasons is responsible for the lack of bimolecular reaction enhancement upon infrared irradiation.

**Table 5.1** Data obtained from the dissociation kinetics of  $\text{Cl}^-(\text{CH}_3\text{Br})$ .

a) Black Body

T (°C)	$k_{\text{uni}}$ ( $\text{s}^{-1}$ )	$k_{\text{Br}}$ ( $\text{s}^{-1}$ )	$k_{\text{Cl}}$ ( $\text{s}^{-1}$ )	$k_{\text{ClW}}$ ( $\text{s}^{-1}$ )	$k_{\text{Br}}/k_{\text{Cl}}$	d5 (s)
21	$4.5 \times 10^{-2}$	$3.6 \times 10^{-2}$	$6.8 \times 10^{-3}$	$2.4 \times 10^{-3}$	5.3	15
33	$6.4 \times 10^{-2}$	$5.2 \times 10^{-2}$	$8.7 \times 10^{-3}$	$3.4 \times 10^{-3}$	5.9	15
50	0.10	$8.0 \times 10^{-2}$	$1.6 \times 10^{-2}$	$7.9 \times 10^{-3}$	5.1	10
70	0.21	0.14	$3.6 \times 10^{-2}$	$2.7 \times 10^{-2}$	4.0	5

b) IRMPD

I ( $\text{W cm}^{-2}$ )	$k_{\text{uni}}$ ( $\text{s}^{-1}$ )	$k_{\text{Br}}$ ( $\text{s}^{-1}$ )	$k_{\text{Cl}}$ ( $\text{s}^{-1}$ )	$k_{\text{ClW}}$ ( $\text{s}^{-1}$ )	$k_{\text{Br}}/k_{\text{Cl}}$	d5 (s)
9.9	0.10	$7.9 \times 10^{-2}$	$1.1 \times 10^{-2}$	$1.0 \times 10^{-2}$	7.4	15

### 5.3.2 $\text{Br}^-(\text{CH}_3\text{Cl})$

The  $\text{Br}^-(\text{CH}_3\text{Cl})$  ion was isolated in the FT-ICR cell and both the black body dissociation and the IRMPD of the complex were studied. As mentioned in section 5.2 of this thesis, the barrier for the bimolecular back reaction,  $\text{Br}^- + \text{CH}_3\text{Cl} \rightarrow \text{Cl}^- + \text{CH}_3\text{Br}$ , is too large for the reaction to occur at ambient temperatures. Therefore, the complex could be isolated without an intermediate halide transfer reaction as was used to generate the  $\text{Cl}^-(\text{CH}_3\text{Br})$  ion (see reaction R5.5). The  $\text{Br}^-(\text{CH}_3\text{Cl})$  ion was isolated using rf shot ejection and a 10 s relaxation delay ( $d_5=10$  s) was employed before re-isolation. At 21 °C, a reaction delay of 60 s resulted in the FT-ICR spectrum shown in Figure 51a). The black body induced unimolecular dissociation of  $\text{Br}^-(\text{CH}_3\text{Cl})$  produced only  $\text{Br}^-$  and  $\text{Br}^-(\text{H}_2\text{O})$ . No  $\text{Cl}^-$  is produced because the central barrier is too large to overcome (16.6 kcal mole<sup>-1</sup>). The IRMPD of  $\text{Br}^-(\text{CH}_3\text{Br})$  resulted in an increased extent of dissociation compared to the black body experiment. The FT-ICR spectrum presented in Figure 51b) was recorded after 60 s of irradiation at a laser intensity of 9.9 W cm<sup>-1</sup> with all delays and parameters the same as for the black body dissociation spectrum in Figure 51a). Full kinetics plots for black body dissociation and IRMPD over a 60 s period are presented in Figure 52a) and b) respectively. The rate constants for both the black body dissociation and IRMPD kinetics plots were determined by fitting to a first order equation. The black body dissociation plot in Figure 52a) produced a unimolecular dissociation rate constant,  $k_{\text{uni}}=1.2 \times 10^{-2} \text{ s}^{-1}$  and

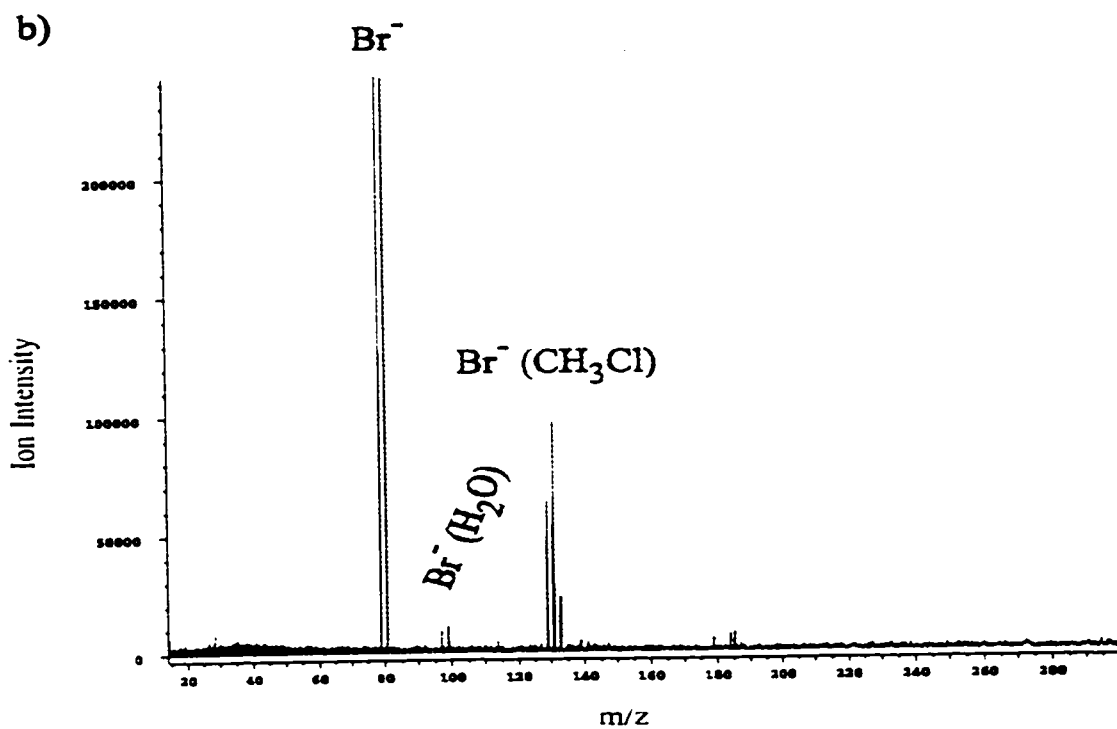
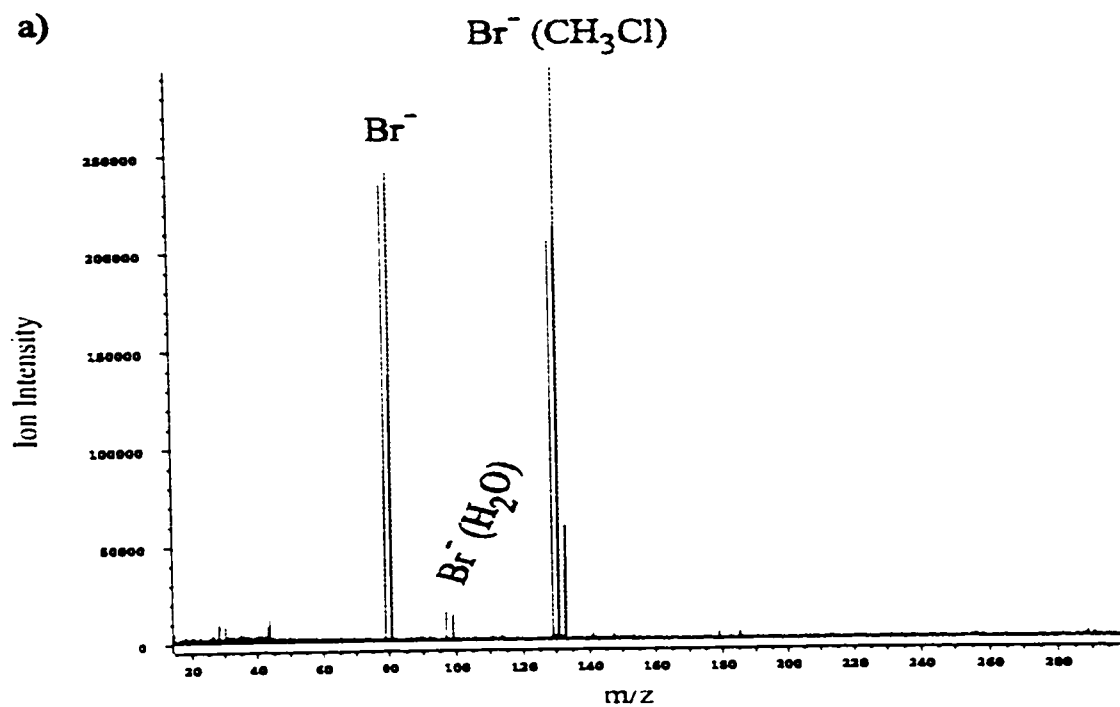


**Figure 51** FT-ICR spectrum recorded after 60 s exposure of  $\text{Br}^-(\text{CH}_3\text{Cl})$  to a) black body radiation;  $T=21^\circ\text{C}$ , b) IRMPD; laser intensity= $9.9\text{ W cm}^{-2}$ .

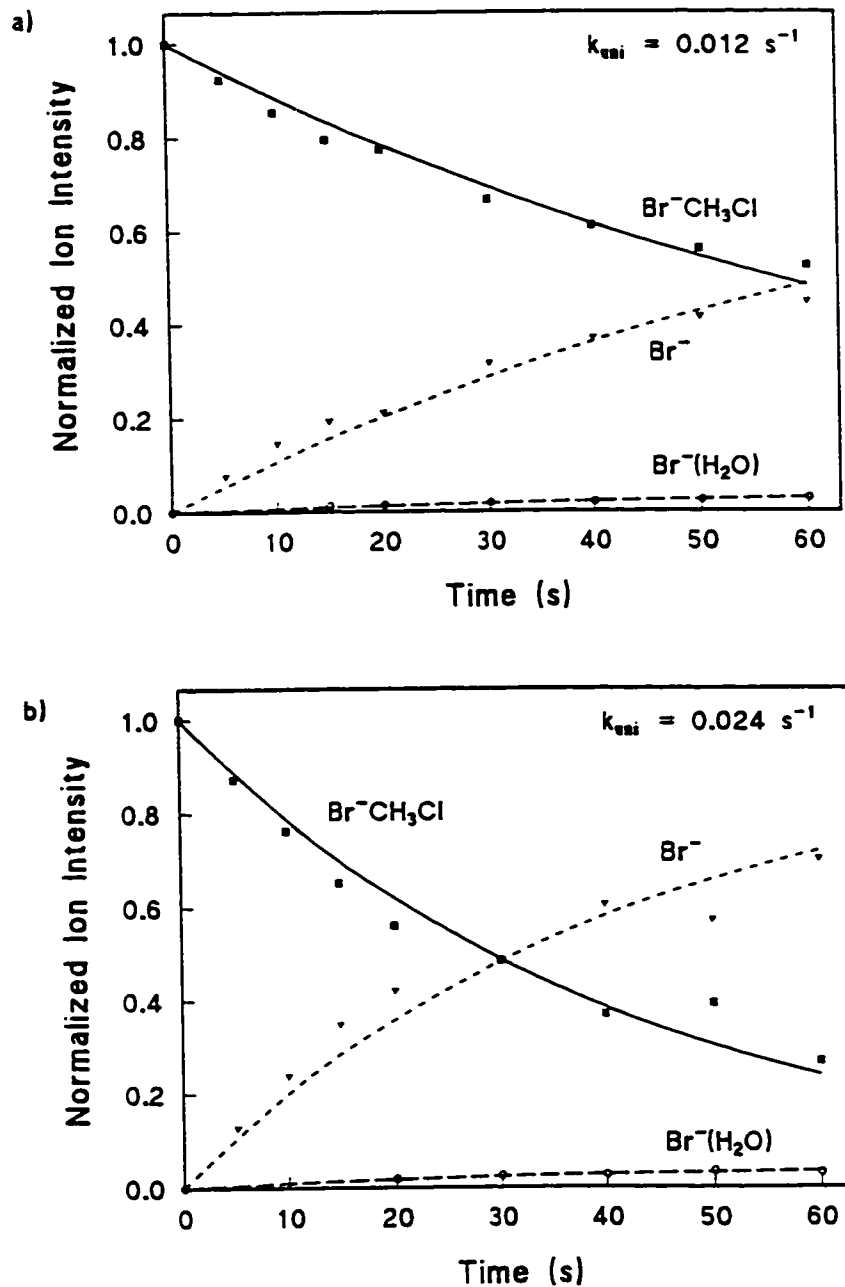


**Figure 52** Kinetics plots for the dissociation of  $\text{Br}^-(\text{CH}_3\text{Cl})$  by a) black body infrared radiation;  $T=21 \text{ }^\circ\text{C}$ , b) IRMPD; laser intensity=  $9.9 \text{ W cm}^{-2}$ .

a rate constant for  $\text{Br}^-$  production,  $k_{\text{Br}}=1.1 \times 10^{-2} \text{ s}^{-1}$  (using the equations for kinetics of parallel reaction which were described in section 5.3.1). The IRMPD kinetics plot in Figure 52b) yielded rate constants,  $k_{\text{uni}}=2.4 \times 10^{-2} \text{ s}^{-1}$  and  $k_{\text{Br}}=2.3 \times 10^{-2} \text{ s}^{-1}$ . It is worth noting that both  $\text{Cl}^-(\text{CH}_3\text{Br})$  and  $\text{Br}^-(\text{CH}_3\text{Cl})$  exhibit approximately the same enhancement in dissociation rate when going from black body dissociation at 20 °C to IRMPD with a laser intensity of  $9.9 \text{ W cm}^{-2}$ . It should also be noted that the rate of  $\text{Br}^-$  production from  $\text{Cl}^-(\text{CH}_3\text{Br})$  is approximately 4 times faster than the rate of  $\text{Br}^-$  production from  $\text{Br}^-(\text{CH}_3\text{Cl})$ , despite the fact that the potential energy surface indicates that the enthalpy changes are almost identical. This point is discussed in more detail in the discussion of the  $\text{Cl}^-(\text{CH}_3\text{Br})$  barrier height in section 5.4 of this thesis.

### 5.3.3 $\text{Cl}^-(\text{C}_2\text{H}_5\text{Br})$

The  $\text{Cl}^-(\text{C}_2\text{H}_5\text{Br})$  ions studied in this section were produced using the experimental methodology described in section 5.2. The concentrations of the reactants and the instrumental parameters were optimized to produce the maximum possible intensity of the  $\text{Cl}^-(\text{C}_2\text{H}_5\text{Br})$  ion. The central barrier for this reaction is closer to the reactant energy ( $\Delta H^\ddagger=-0.7 \text{ kcal mole}^{-1}$ ) than the barrier in the methyl reaction ( $\Delta H^\ddagger=-1.8 \text{ kcal mole}^{-1}$ ). Therefore, the probability of stabilizing the  $\text{Cl}^-(\text{C}_2\text{H}_5\text{Br})$  intermediate, rather than directly forming a  $\text{Br}^-$  product *via* the bimolecular  $\text{S}_{\text{N}}2$  reaction, is much greater than for the methyl reaction. The  $\text{Cl}^-(\text{C}_2\text{H}_5\text{Br})$  ion was the dominant ion produced from the high pressure ion source and the number of interfering

ions was dramatically less than for the  $\text{Cl}^-(\text{CH}_3\text{Br})$  ion. Thus, rf *shot* ejection was sufficient to achieve clean isolation of the four isotopomers ( $m/z=143, 145, 147$ ) of  $\text{Cl}^-(\text{C}_2\text{H}_5\text{Br})$  as shown by the spectrum presented in Figure 53. This spectrum was obtained immediately after isolation and is the sum of 16 scans. The  $m/z=143, 145$  ionic isotopes were not ejected to avoid the possibility of translational excitation of the complex. Since no isotope effects were observed, the total  $\text{Cl}^-(\text{C}_2\text{H}_5\text{Br})$  intensity was taken as the sum of the integrated intensity of all three peaks. When the isolated  $\text{Cl}^-(\text{C}_2\text{H}_5\text{Br})$  ions were trapped in the FT-ICR cell in the presence of ambient black body infrared radiation, unimolecular dissociation was observed. The observed product ions were  $\text{Cl}^-$ ,  $\text{Cl}^-(\text{H}_2\text{O})$  and  $\text{Br}^-$ . The  $\text{Br}^-$  ion was more abundant than the  $\text{Cl}^-$  ion but the relative enhancement was less than was observed for the  $\text{Cl}^-(\text{CH}_3\text{Br})$  black body dissociation. This result is consistent with the fact that the barrier is not as far below the reactant energy. A series of mass spectra were obtained with reaction delays ( $\nu d$ ) ranging from 0 s to 100 s at 31 °C. Each spectrum had a 10 s relaxation delay ( $d5$ ) following the initial rf sweep isolation of  $\text{Cl}^-(\text{C}_2\text{H}_5\text{Br})$ . The products formed in the 10 s period were then ejected using a second set of rf shots prior to the variable reaction delay. A plot of the ion intensity vs. reaction delay ( $\nu d$ ) is shown in Figure 54. The  $\text{Cl}^-(\text{C}_2\text{H}_5\text{Br})$  decay curve was fit to a first order rate equation, which yielded a value for the unimolecular dissociation rate constant,  $k_{\text{uni}}$ , of  $2.3 \times 10^{-2} \text{ s}^{-1}$ . The curves representing the product ions were fit to the equations for parallel first order reactions (see section 5.3.1) and the resulting rate constants are  $k_{\text{Br}^-}=1.4 \times 10^{-2} \text{ s}^{-1}$ ,  $k_{\text{Cl}^-}=5.1 \times 10^{-3}$



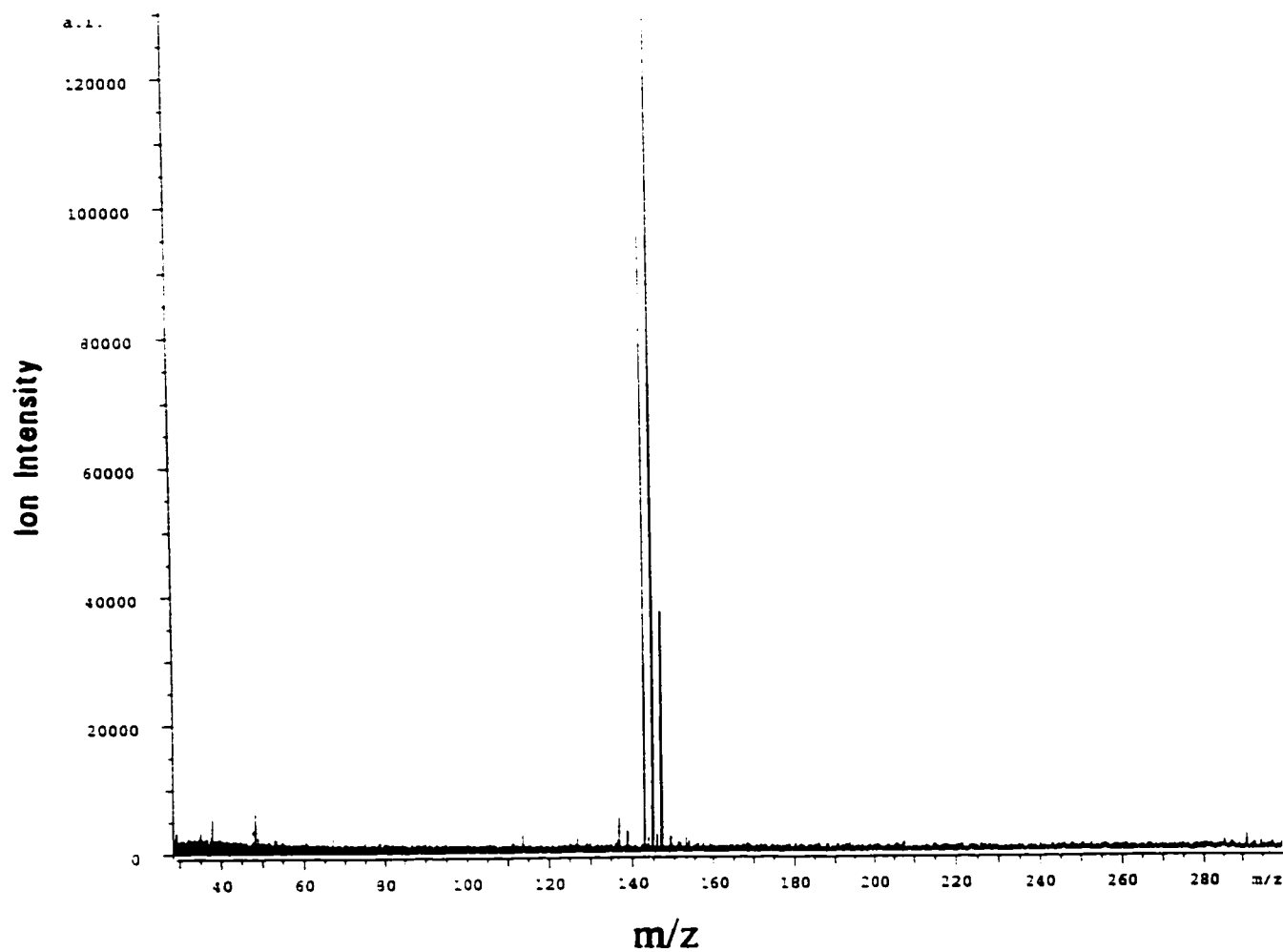


**Figure 53** FT-ICR mass spectrum of the  $\text{Cl}^-(\text{C}_2\text{H}_5\text{Br})$  complex after rf isolation.

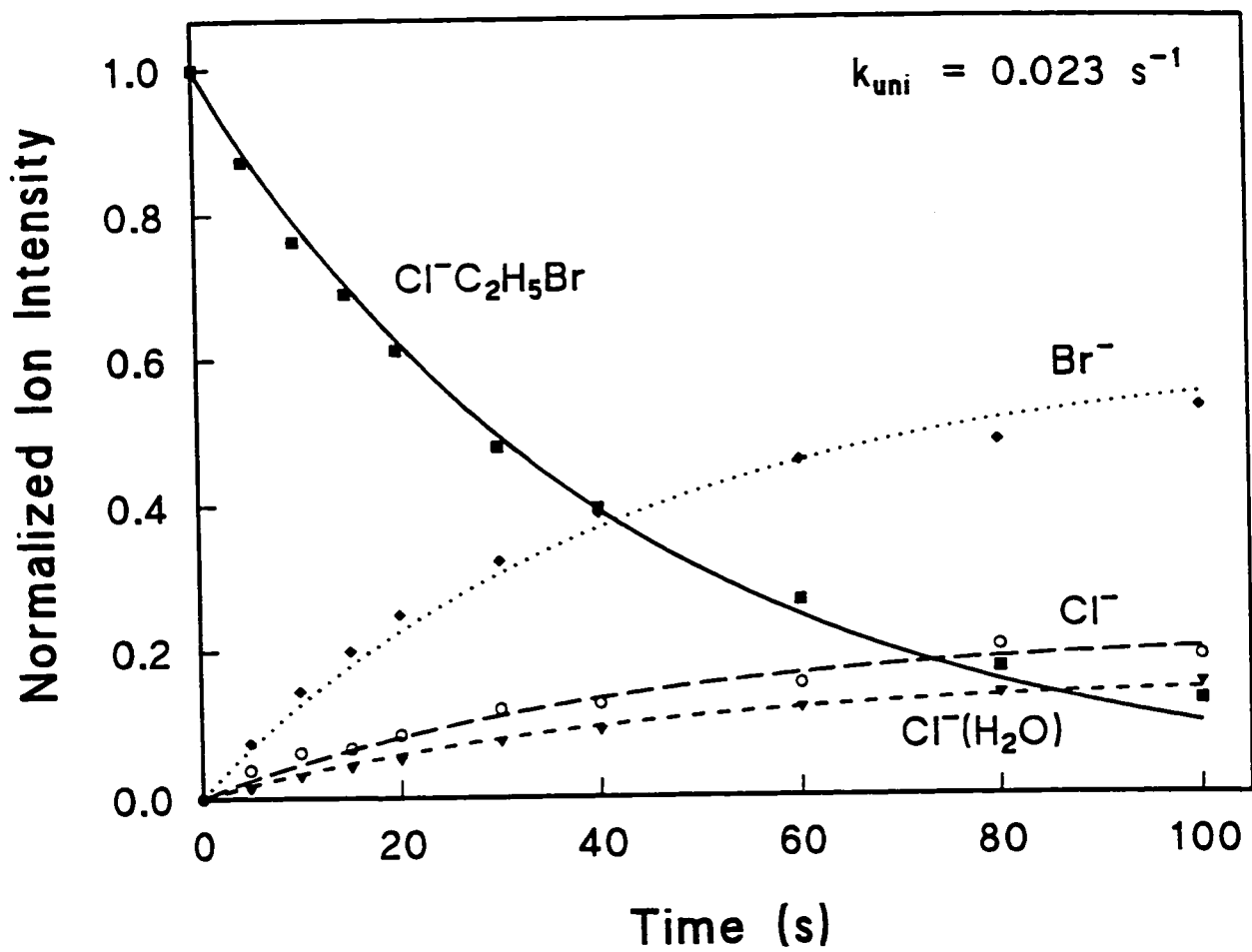


**Figure 54** Black body dissociation kinetics of  $\text{Cl}^-(\text{C}_2\text{H}_5\text{Br})$  at  $31^\circ\text{C}$ .

$\text{s}^{-1}$  and  $k_{\text{ClW}}=3.7 \times 10^{-3} \text{ s}^{-1}$ . The resulting ratio of bromide to chloride ions is  $k_{\text{Br}}/k_{\text{Cl}}=2.8$ . This experiment was repeated at 21, 40, 56 and 77 °C and the resulting rate constants and product branching ratios are summarized in Table 5.2. The relaxation delay,  $d_5$ , had to be reduced from 10 s for the higher temperature experiments and is included in Table 5.2 because, as explained in section 5.2, it may affect the branching ratio. Since the production of  $\text{Cl}^-$  and  $\text{Br}^-$  from  $\text{Cl}^-(\text{C}_2\text{H}_5\text{Br})$  is treated as parallel reactions, the activation energy for each reaction must be determined from the temperature dependence of the individual rate constants  $k_{\text{Br}}$  and  $k_{\text{Cl}}$ , respectively, using the Arrhenius equation (45). The Arrhenius parameters for the  $\text{Cl}^-(\text{H}_2\text{O})$  channel,  $E_{\text{a}}^{\text{ClW}}$  and  $A_{\text{Arr}}^{\text{ClW}}$ , were not determined because the pressure of the water vapour could not be measured and varies with temperature. Figure 55 is a plot of  $\ln k_{\text{Br}}$  vs.  $T^{-1}$ . From it,  $E_{\text{a}}^{\text{Br}}$  was determined to be  $10.2 \text{ kcal mole}^{-1}$  and  $A_{\text{Arr}}^{\text{Br}}=3 \times 10^5 \text{ s}^{-1}$ . Similarly, the plot of  $\ln k_{\text{Cl}}$  vs.  $T^{-1}$  presented in Figure 56 yielded the values  $E_{\text{a}}^{\text{Cl}}=10.5 \text{ kcal mole}^{-1}$  and  $A_{\text{Arr}}^{\text{Cl}}=2 \times 10^5 \text{ s}^{-1}$ . In contrast to the results of the methyl reactions, the values obtained for  $E_{\text{a}}^{\text{Br}}$  and  $E_{\text{a}}^{\text{Cl}}$  are now approaching the actual values for enthalpy of activation ( $\Delta H=12.9$  and  $13.6 \text{ kcal mole}^{-1}$ , respectively) which are shown in Figure 40. Also, the Arrhenius A factors are now only  $\sim 10^6$  smaller than expected.<sup>33</sup> Thus, the underestimation of the Arrhenius parameters for this reaction is less severe than was observed in the methyl reactions (section 5.3). This is a reflection of the fact that larger ions are stronger absorbers of black body radiation because the number of oscillators has increased. Therefore,  $\text{Cl}^-(\text{C}_2\text{H}_5\text{Br})$  is closer to being in the

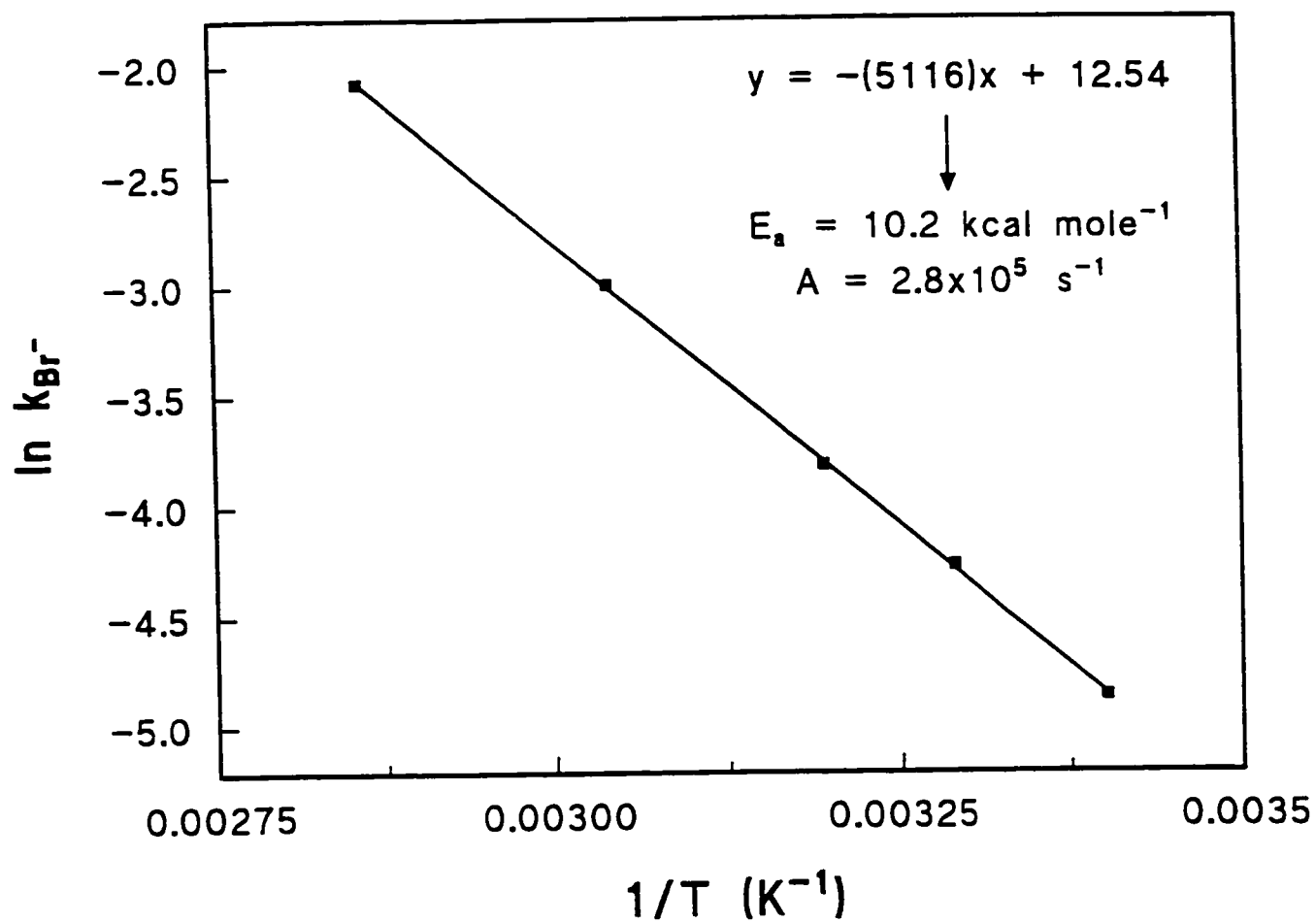


**Figure 55** Arrhenius plot of  $\ln k_{Br^-}$  vs.  $T^{-1}$  for black body induced dissociation of  $Cl^-(C_2H_5Br)$ .

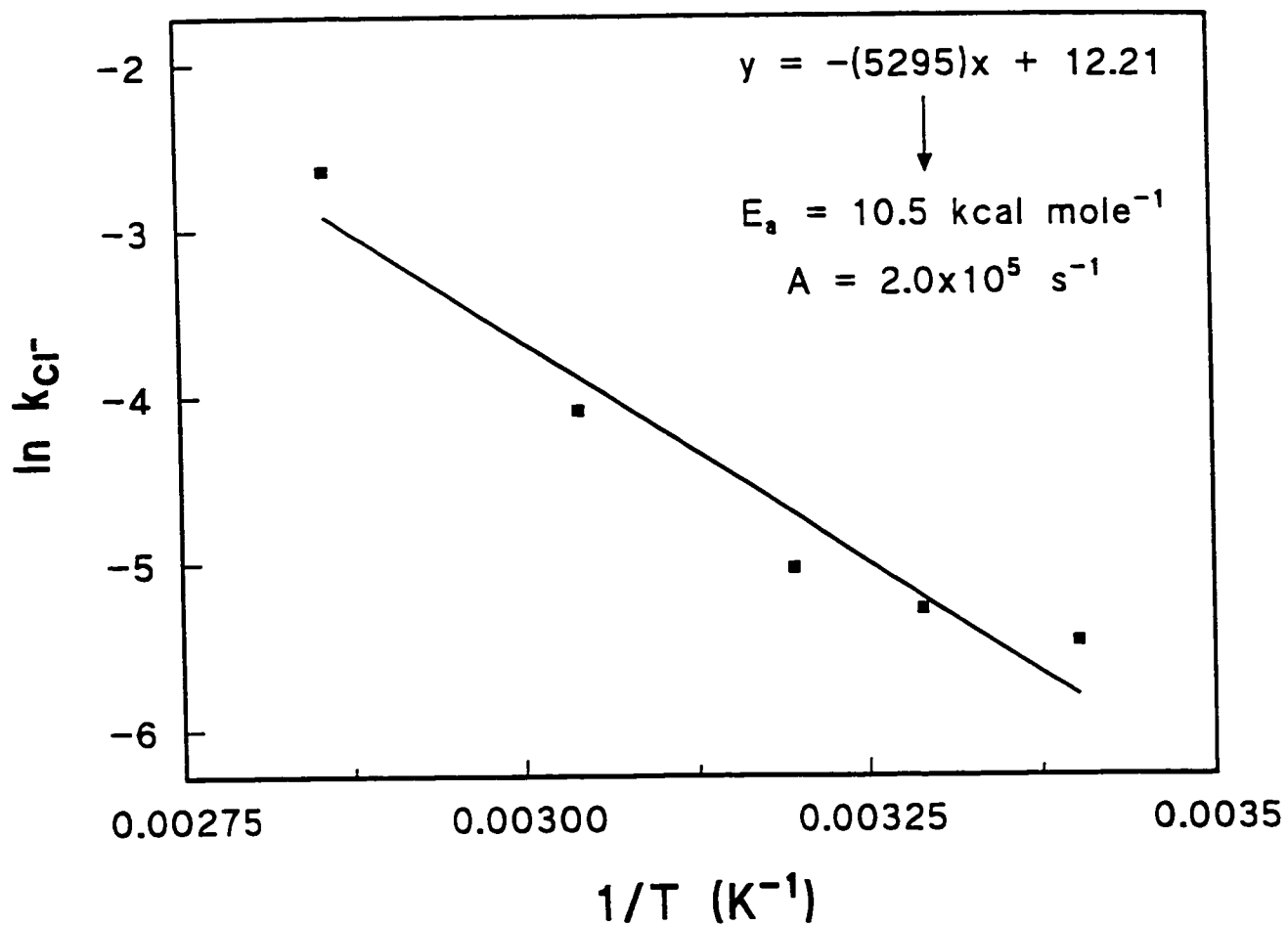


**Figure 56** Arrhenius plot of  $\ln k_{Cl}$  vs.  $T^{-1}$  for black body induced dissociation of  $Cl(C_2H_5Br)$ .

rapid energy exchange (REX) limit (but is still too small) required for the black body dissociation experiments to yield correct Arrhenius activation parameters.

Although the activation energies may be in error, an analysis of the average product branching ratio will indicate the difference in activation energies between the  $\text{Cl}^-$  and  $\text{Br}^-$  paths. The average branching ratio of the bromide to chloride product ions from the black body dissociation of  $\text{Cl}^-(\text{C}_2\text{H}_5\text{Br})$  at the five temperatures is  $\langle k_{\text{Br}^-}/k_{\text{Cl}^-} \rangle = 2.6 \pm 0.8$ . Comparison of the branching ratios with the  $d_5$  values, reported in Table 5.2, indicates that there may be an increase in the  $k_{\text{Br}^-}/k_{\text{Cl}^-}$  ratio with longer relaxation times. This observation was reported for the black body dissociation of the  $\text{Cl}^-(\text{CH}_3\text{Br})$  ion and was attributed to the preferential formation of  $\text{Cl}^-$  product ion from collisional processes. Therefore, the correct value for the branching ratio of a purely radiative dissociation is probably closer to 3 since  $k_{\text{Br}^-}/k_{\text{Cl}^-}$  values of  $3.1 \pm 0.3$  were obtained from the kinetics which had the longest relaxation delays ( $d_5 = 10$  s). Using  $k_{\text{Br}^-}/k_{\text{Cl}^-} = 2.6$  and  $3.1$  respectively, a simple calculation of the difference in the Arrhenius activation energies, using equation (45) with  $A_{\text{Arr}}^{\text{Br}} = A_{\text{Arr}}^{\text{Cl}}$ , yields  $E_a^{\text{Br}} - E_a^{\text{Cl}} = -0.6$  and  $-0.7$  respectively. This difference in activation energies is in good agreement with the value of  $\Delta H^\ddagger = -0.7$  kcal mole $^{-1}$  obtained from the PHPMS study of the bimolecular  $\text{Cl}^- + \text{C}_2\text{H}_5\text{Br}$  reaction reported by McMahon and co-workers.<sup>22</sup> This agreement suggests that the dynamics of the  $\text{Cl}^- + \text{C}_2\text{H}_5\text{Br}$  reaction behave statistically.

The  $\text{Cl}^-(\text{C}_2\text{H}_5\text{Br})$  ion was exposed to 10.6  $\mu\text{m}$  infrared radiation from the  $\text{CO}_2$  laser and the photodissociation kinetics at 21  $^\circ\text{C}$  were determined. The kinetics plots obtained at laser intensities of 9.9 and 3.3  $\text{W cm}^{-2}$  are presented in Figure 57 and Figure 58 respectively. The rate constants were determined by fitting the data to a first order equation with parallel product formation. The data obtained from the fit is included in Table 5.2. It can be seen that the unimolecular dissociation rate was increased substantially over the ambient black body dissociation rate indicating that the  $\text{Cl}^-(\text{C}_2\text{H}_5\text{Br})$  has a strong IR absorption at 10.6  $\mu\text{m}$ . The rate constant,  $k_{\text{uni}}$ , also increased with increasing laser intensity ( $k_{\text{uni}}=0.22$  and  $0.85$  for 3.3 and 9.9  $\text{W cm}^{-2}$ , respectively). The product ion ratio was constant,  $\text{Br}^-/\text{Cl}^-=3.2$ , for both experiments. This is essentially unchanged from the ratio observed from the black body dissociation experiments. The insensitivity of the  $\text{Br}^-/\text{Cl}^-$  branching ratio to changes in internal energy, whether affected by a temperature change or a laser intensity change, suggests that the  $\text{Cl}^- + \text{C}_2\text{H}_5\text{Br}$  reaction exhibits none of the non-statistical behaviour observed for the  $\text{Cl}^- + \text{CH}_3\text{Br}$  reaction.

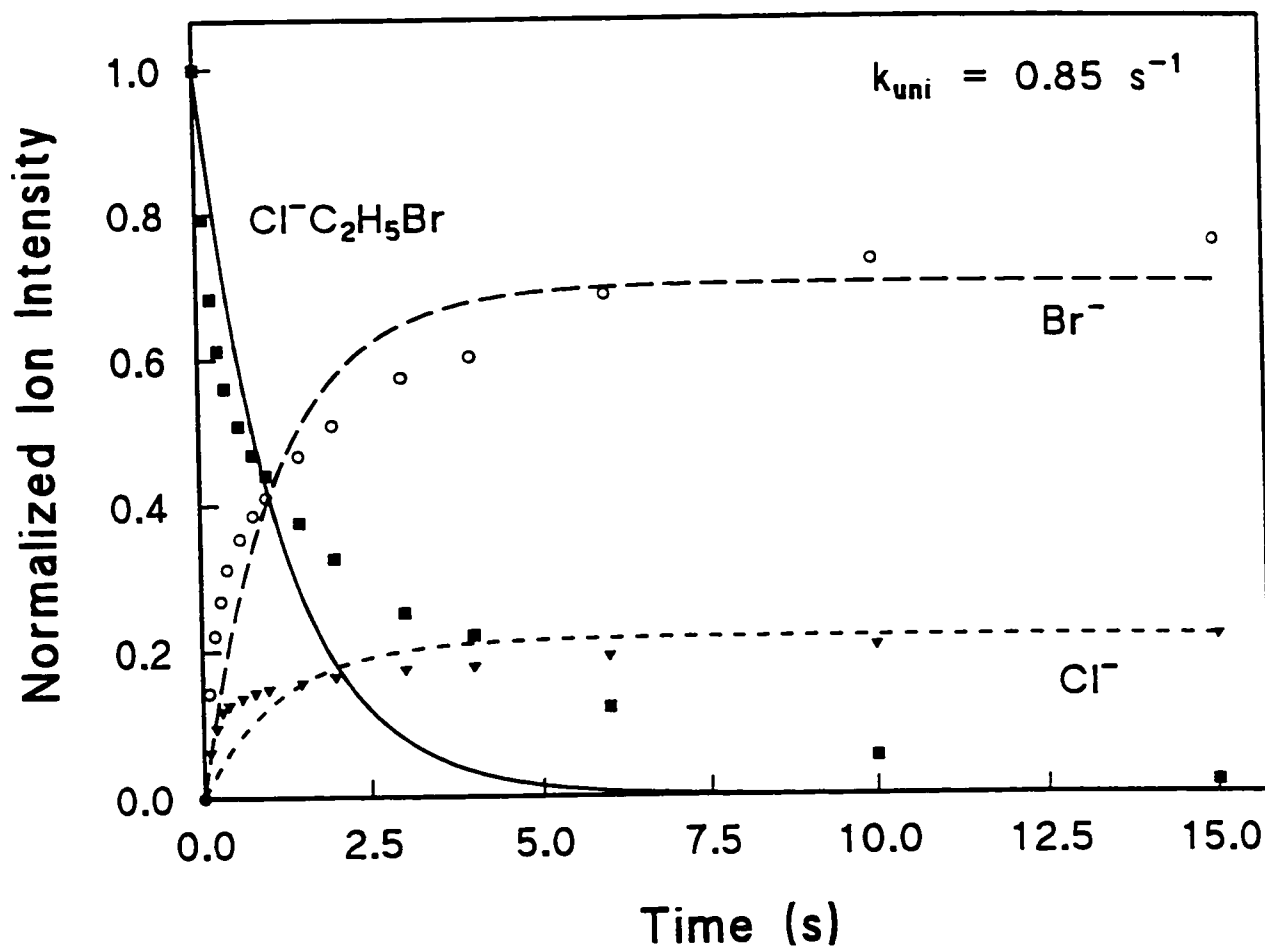


**Figure 57** IRMPD kinetics of  $\text{Cl}^-(\text{C}_2\text{H}_5\text{Br})$  at a laser intensity of  $9.9 \text{ W cm}^{-2}$ .



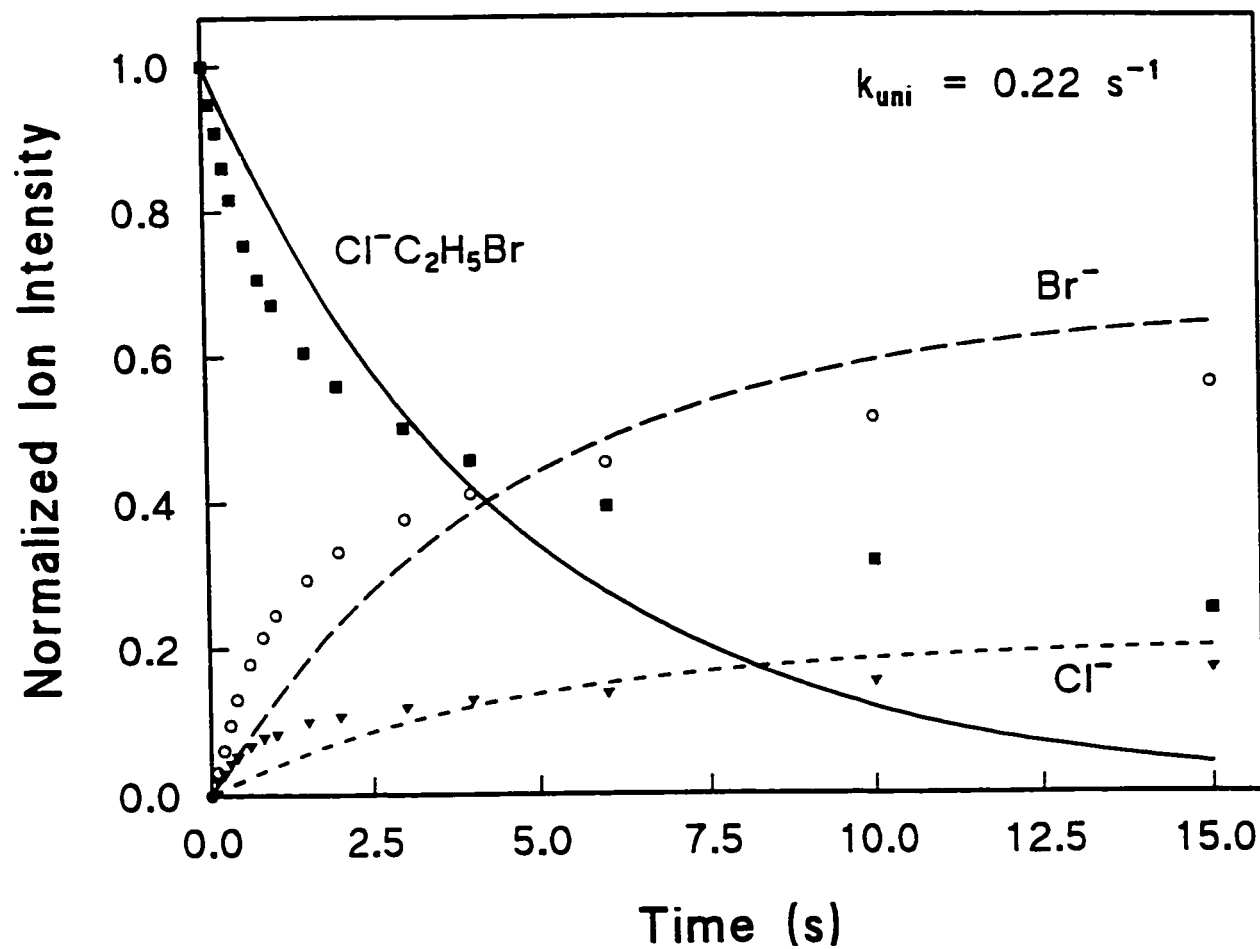


**Figure 58** IRMPD kinetics of  $\text{Cl}^-(\text{C}_2\text{H}_5\text{Br})$  at a laser intensity of  $3.3 \text{ W cm}^{-2}$ .

**Table 5.2 Data Obtained from the Dissociation kinetics of  $\text{Cl}^-(\text{C}_2\text{H}_5\text{Br})$ .****a) Black Body Dissociation**

T (°C)	$k_{\text{uni}}$ ( $\text{s}^{-1}$ )	$k_{\text{Br}}$ ( $\text{s}^{-1}$ )	$k_{\text{Cl}}$ ( $\text{s}^{-1}$ )	$k_{\text{ClW}}$ ( $\text{s}^{-1}$ )	$k_{\text{Br}}/k_{\text{Cl}}$	d5 (s)
21	$1.5 \times 10^{-2}$	$7.7 \times 10^{-3}$	$4.2 \times 10^{-3}$	$2.3 \times 10^{-3}$	1.8	5
31	$2.3 \times 10^{-2}$	$1.4 \times 10^{-2}$	$5.1 \times 10^{-3}$	$3.7 \times 10^{-3}$	2.8	10
40	$3.5 \times 10^{-2}$	$2.2 \times 10^{-2}$	$6.5 \times 10^{-3}$	$6.2 \times 10^{-3}$	3.4	10
56	$8.4 \times 10^{-2}$	$5.0 \times 10^{-2}$	$1.7 \times 10^{-2}$	$1.7 \times 10^{-2}$	3.0	5
77	0.28	0.13	$7.1 \times 10^{-2}$	$7.9 \times 10^{-2}$	1.8	2

**b) IRMPD**

I ( $\text{W cm}^{-1}$ )	$k_{\text{uni}}$ ( $\text{s}^{-1}$ )	$k_{\text{Br}}$ ( $\text{s}^{-1}$ )	$k_{\text{Cl}}$ ( $\text{s}^{-1}$ )	$k_{\text{ClW}}$ ( $\text{s}^{-1}$ )	$k_{\text{Br}}/k_{\text{Cl}}$	d5 (s)
3.3	0.22	0.14	$4.5 \times 10^{-2}$	$\sim 4 \times 10^{-3}$	3.2	2
9.9	0.85	0.59	0.19	$\sim 9 \times 10^{-3}$	3.2	2

#### 5.3.4 $\text{Br}^-(\text{C}_2\text{H}_5\text{Cl})$ , $\text{Cl}^-(\text{i-C}_3\text{H}_7\text{Br})$ and $\text{Br}^-(\text{i-C}_3\text{H}_7\text{Cl})$

The unimolecular dissociation kinetics and IRMPD of the bromide-ethyl chloride, chloride-isopropyl bromide and bromide-isopropyl chloride complexes have been studied. These three species are discussed together in this section because two of the three isotopomers were ejected in each case. This ejection may have translationally excited the remaining ions. Since translational energy effects were observed in the  $\text{Cl}^- + \text{CH}_3\text{Br}$  and  $\text{Cl}^- + \text{C}_2\text{H}_5\text{Br}$  reactions, only qualitative conclusions will be reported for the  $\text{S}_{\text{N}}2$  reactions in this section. Both the black body unimolecular dissociation and IRMPD of  $\text{Br}^-(\text{C}_2\text{H}_5\text{Cl})$ ,  $\text{Cl}^-(\text{i-C}_3\text{H}_7\text{Br})$  and  $\text{Br}^-(\text{i-C}_3\text{H}_7\text{Cl})$  produced only  $\text{Br}^-$ ,  $\text{Cl}^-$ ,  $\text{Br}^-$  and the corresponding monohydrated halide ions, respectively. The formation of the halide-water cluster ions by a halide transfer reaction and confirms that only the desired ion-molecule complex (I or II) is being formed in each reaction. The lack of  $\text{Cl}^-$ ,  $\text{Br}^-$  and  $\text{Cl}^-$  ions, respectively indicates that none of these reactions had sufficient energy to cross the central barrier. The translational excitation of these ions by ejection of the isotopes prevents a meaningful comparison of the relative rates of unimolecular dissociation with the rates of the other  $\text{S}_{\text{N}}2$  complexes reported here. The lack of this information is not critical, however, because all of these ions result in a single halide product. These reactions are, therefore, expected to behave in much the same way as any other ion-molecule dissociation and the dynamics are predictable.

## 5.4 Discussion

The results obtained in this study demonstrate the ability of the Waterloo FT-ICR spectrometer to selectively generate either the entrance (I) or exit (II) complex of a chloride-alkyl bromide reaction and then examine the dynamics of these gas phase  $S_N2$  reactions with a combination of IR/MPD and ZTRID techniques. The dynamics of  $Cl^- + CH_3Br$  reaction are of the greatest interest because of the potential for non-RRKM behaviour, and the uncertainty in the height of the central barrier. The other  $S_N2$  systems seem to be well described by statistical reaction theory since the branching ratio of  $Br^-/Cl^-$  is consistent with a simple Arrhenius analysis of the relative barrier heights for each channel as determined by the thermochemical study of McMahon and co-workers.<sup>22</sup> Thus, most of the discussion presented in this section is focussed on the  $Cl^- + CH_3Br$  reaction dynamics.

*Structural Confirmation* All of the chloride-alkyl bromide  $S_N2$  systems in this study, ( $R = CH_3, C_2H_5, i-C_3H_7$ ) exhibited a bimolecular reaction in which a halide ion,  $X^-$ , is transferred to background water vapour. This reaction produced exclusively the halide-water cluster ion that corresponds to the separated reactant ion for that complex (*i.e.*  $Cl^-(RBr)$  produced  $Cl^-(H_2O)$  and  $Br^-(RCl)$  produced  $Br^-(H_2O)$ ). These results demonstrate conclusively that the chloride-alkyl bromide  $S_N2$  ions formed in these experiments were synthesized entirely in either the entrance or exit complex (I or II, respectively) and that no interconversion between the two complexes occurs. Johnson and co-workers have shown that the entrance and exit complexes in the chloride-

methyl bromide reaction could be distinguished by the fact that II displays electron photodetachment at 312 nm while I does not,<sup>17b)</sup> and that collisional activation of  $\text{Cl}^-(\text{CH}_3\text{Br})$ , produced both  $\text{Cl}^-$  and  $\text{Br}^-$  ions, while  $\text{Br}^-(\text{CH}_3\text{Cl})$ , yielded exclusively  $\text{Br}^-$  ion. Additionally, Olmstead and Brauman showed that  $\text{Cl}^-(\text{CH}_3\text{Br})$  could transfer a  $\text{Cl}^-$  but not a  $\text{Br}^-$  ion to acetonitrile and 1,1 difluoroethane.<sup>39</sup> The results presented here are perhaps the most convincing evidence of complete control of gas phase  $\text{X}^-\text{RY}$  synthesis for a variety of reactions. Additionally, the long time scale of these experiments proves that zero conversion between complexes I and II occurs.

*Temperature Dependence.* The unimolecular dissociation of both the  $\text{Cl}^-(\text{CH}_3\text{Br})$  and  $\text{Cl}^-(\text{C}_2\text{H}_5\text{Br})$  ions was observed to occur with a positive temperature dependence (*ie.*  $k_{\text{uni}}$  increases with increasing T). The positive temperature dependence agrees with all previous examples of black body induced unimolecular dissociation of cluster ions and with the results of Viggiano *et al.* who have observed a positive temperature dependence for the thermal unimolecular decomposition of the  $\text{Cl}^-(\text{CH}_3\text{Br})$  complex in an ion flow tube.<sup>46</sup> In contrast, the bimolecular  $\text{Cl}^- + \text{CH}_3\text{Br}$  reaction has been shown to exhibit a strong negative temperature dependence<sup>28,23</sup> which is common for bimolecular  $\text{S}_{\text{N}}2$  reactions for which the central barrier lies below the reactant energy.<sup>40</sup> Even though the barrier for the bimolecular experiments is lower, than the reactant energy,  $E_{\text{a}}(\text{bi}) < 0$ , the unimolecular dissociation starts from the stabilized complex and, therefore,  $E_{\text{a}}(\text{uni}) > 0$ . As mentioned in section 5.3.1, the values for the activation energies,  $E_{\text{a}}^{\text{Br}}$  and  $E_{\text{a}}^{\text{Cl}}$ , calculated from the Arrhenius plots are well below

the respective bond enthalpies for the dissociation of the  $\text{Cl}^-(\text{CH}_3\text{Br})$  complex because the ions are not large enough to be in the REX limit. Although the larger  $\text{Cl}^-(\text{C}_2\text{H}_5\text{Br})$  ions are still nowhere near the REX limit, the activation energies obtained for this ion are closer to the known values of the bond enthalpy in agreement with the present understanding of the ZTRID mechanism. It can be seen that the rate of unimolecular dissociation of the  $\text{Cl}^-(\text{CH}_3\text{Br})$  ion is faster than the rate of  $\text{Cl}^-(\text{C}_2\text{H}_5\text{Br})$ . In this case, the increase in rate due to the weaker bond in the methyl reaction is more important than the increased number of absorption modes for the ethyl complex. Since the molecules are not in the REX limit, the dissociation energies cannot be determined directly from the experimentally measured values of  $E_a$ . Dunbar *et al.*<sup>41</sup> have shown that master equation modelling of black body dissociation reactions, for which accurate infrared absorption frequencies and intensities are known, can yield reliable estimates of bond strengths. Since many detailed *ab initio* calculations have been performed on the  $\text{Cl}^-(\text{CH}_3\text{Br})$  complex, the temperature dependence of the black body dissociation kinetics of  $\text{Cl}^-(\text{CH}_3\text{Br})$ , presented in this chapter may be an ideal candidate for master equation modelling. Since the well depths of complexes I and II are known from PHPMS measurements, the activation energies for simple bond cleavage to form  $\text{Cl}^-$  and  $\text{Br}^-$ , respectively, would not be of sufficient use to justify the effort of master equation modelling. The activation energy for the barrier crossing unimolecular reaction,  $\text{Cl}^-(\text{CH}_3\text{Br}) \rightarrow \text{Br}^- + \text{CH}_3\text{Cl}$ , however, might prove useful to help establish the height of the central barrier which is in dispute because of conflicting results and the

statistical assumptions used to determine some reported values. It is entirely possible, however, that quantum scattering calculations may be required to accurately describe this non-RRKM reaction.

*Non-Statistical Reaction Dynamics.* The most striking result of the experiments presented here, is the exclusive formation of  $\text{Br}^-$  upon vibrational excitation of the intramolecular  $\text{CH}_3\text{Br}$  modes of the  $\text{Cl}^-(\text{CH}_3\text{Br})$  complex. This effect was previously predicted by Hase and co-workers,<sup>19</sup> but the results presented in this chapter are the first experimental evidence to support the prediction. The difference spectrum shown in Figure 48, unambiguously shows that irradiation of the  $\text{Cl}^-(\text{CH}_3\text{Br})$  ion with infrared laser radiation at  $943\text{ cm}^{-1}$ , produces  $\geq 90\%$   $\text{Br}^-$  ion. This spectrum was obtained from a background subtraction experiment. Therefore, it is not affected by uncertainties in the kinetic and/or internal energy of the ions since the only difference between the two experiments is the presence of the laser radiation. The laser radiation is almost certainly exciting the "methyl rock" vibration of the  $\text{Cl}^-(\text{CH}_3\text{Br})$  complex.<sup>42</sup> Hase and co-workers have calculated the "scaled" frequency of this vibrational mode to be  $943\text{ cm}^{-1}$ , using a HF/SV4PP/6-31G\* level of theory.<sup>43</sup> The  $\text{CO}_2$  laser frequency is  $943 \pm 5\text{ cm}^{-1}$ . It should be pointed out that, despite the apparent exact agreement of the laser and vibrational frequencies, there is enough uncertainty in each that excitation is expected to be off-resonant. This is supported by the slow rate of IRMPD observed for the weakly bound  $\text{Cl}^-(\text{CH}_3\text{Br})$  ion compared with much more strongly bound ions, such as the proton bound dimers of diethyl ether and pentanone, which were studied

in chapter 3 of this thesis. The lack of frequency tunability in the current CO<sub>2</sub> laser prevented a study of the wavelength dependence of the photodissociation rate. Since an infrared spectrum of the Cl<sup>-</sup>(CH<sub>3</sub>Br) ion is not available, the exact ro-vibrational transition being excited is not known. Thus, caution must be exercised before presenting this result as a clear case of a mode-specific S<sub>N</sub>2 reaction. It is believed that the data presented here constitutes the strongest evidence to date supporting the predicted non-statistical reaction dynamics of the Cl<sup>-</sup> + CH<sub>3</sub>Br reaction. Hase has suggested that: "The unimolecular dynamics of the Cl<sup>-</sup>(CH<sub>3</sub>Br) complex are highly mode specific" and that excitation of the low frequency Cl<sup>-</sup>- C stretch and Cl<sup>-</sup>- CH<sub>3</sub>Br bend modes will produce predominantly Cl<sup>-</sup> while excitation of the higher frequency (intramolecular) modes will produce almost entirely Br<sup>-</sup>.<sup>19</sup> With the long time scale of this experiment (seconds) it is difficult to determine how much of the energy deposited into the methyl rock mode "leaks" into other vibrational modes prior to dissociation. A detailed study of the effects of internal energy on the Br<sup>-</sup>/Cl<sup>-</sup> branching ratio would help to resolve whether the observed Br<sup>-</sup> enhancement is the evidence of true mode specific behavior or non-RRKM behaviour of internally excited ions. Therefore, the discussion of the effects of temperature on the ZTRID rate which follows is relevant to this discussion of non-statistical behaviour.

The dynamics of the Cl<sup>-</sup> + C<sub>2</sub>H<sub>5</sub>Br reaction appears to behave statistically because the Br<sup>-</sup>/Cl<sup>-</sup> ratio obtained from the black body unimolecular dissociation of Cl<sup>-</sup>(C<sub>2</sub>H<sub>5</sub>Br) agrees well with the barrier height previously established by McMahon and



co-workers<sup>22</sup> using bimolecular PHPMS experiments. The statistical nature of the reaction is confirmed by the fact that infrared photodissociation of  $\text{Cl}^-(\text{C}_2\text{H}_5\text{Br})$  increases the unimolecular dissociation rate but does not produce an enhancement in the  $\text{Br}^-$  yield as was observed for the non-statistical  $\text{Cl}^-(\text{CH}_3\text{Br})$  dissociation reaction. Craig and Brauman have recently reported that the  $\text{S}_{\text{N}}2$  reaction of chloride ion and chloroacetonitrile exhibited statistical reaction dynamics when translationally excited.<sup>44</sup> Their agreement between RRKM theory and experiment is in contrast to the bulk of the literature on  $\text{S}_{\text{N}}2$  reaction dynamics. The chloroacetonitrile molecule,  $\text{ClCH}_2\text{CN}$  is similar to ethyl bromide in size and structure. Therefore, the observation of statistical behaviour for the  $\text{Cl}^- + \text{C}_2\text{H}_5\text{Br}$  and  $\text{Cl}^- + \text{ClCH}_2\text{CN}$  reactions may indicate that these reactions represent the upper limit of molecular size for which non-statistical  $\text{S}_{\text{N}}2$  dynamics will occur.

*Branching Ratio; Translational vs. Internal Energy.* Having already established that laser irradiation of the  $\text{Cl}^-(\text{CH}_3\text{Br})$  ion results in a definite enhancement of the  $\text{Br}^-$  product ion, an important question remains to be answered. Is this a mode specific effect or an internal energy effect? If the photon energy which is deposited into the methyl rock mode "leaks" into other vibrational modes prior to dissociation, then the effect is not mode specific but may still be non-statistical. In this case, the same  $\text{Br}^-$  enhancement observed with IR laser radiation, should be produced by increasing the temperature of a thermal unimolecular reaction and, therefore, increasing the internal energy of the system. Viggiano and co-workers<sup>46</sup> did not report a change in the  $\text{Br}^-$

/Cl<sup>-</sup> ratio with T in the thermal unimolecular decomposition of Cl<sup>-</sup>(CH<sub>3</sub>Br), however, it is not clear that their experiment is sensitive enough to observe small changes in the Cl<sup>-</sup> intensity. Also, Hase has found that angular momentum is critical to the mode specific behaviour of the Cl<sup>-</sup> + CH<sub>3</sub>Br reaction and that sufficient rotational excitation can "wash out" the effects of vibrational excitation.<sup>19</sup> Therefore, the ZTRID experiment, by nature of the low collision frequency, may be a better method of exploring unimolecular temperature effects than thermal decomposition in an ion flow tube, which should continually re-establish a thermal distribution of rotational states. When the data in Table 5.1 is examined, a consistent increase in the Br<sup>-</sup>/Cl<sup>-</sup> branching ratio with increasing temperature is NOT observed for the black body dissociation of Cl<sup>-</sup>(CH<sub>3</sub>Br). From Table 5.1, the average branching ratio, <Br<sup>-</sup>/Cl<sup>-</sup>>, from the black body induced unimolecular dissociation of Cl<sup>-</sup>(CH<sub>3</sub>Br) is 5±1, indicating some scatter in the data points. The <Br<sup>-</sup>/Cl<sup>-</sup>>=5 ratio is less than observed in the thermal unimolecular dissociation experiment of Viggiano and co-workers.<sup>46</sup> This may be because the observed temperature effect seems to be convoluted with translational energy effects and relaxation delay effects. A study of the Br<sup>-</sup>/Cl<sup>-</sup> ratio obtained with a fixed reaction time using various relaxation delays (d5) and collision gas pressures has shown that both increased d5 and increased pressure produce greater Br<sup>-</sup>/Cl<sup>-</sup> ratios.<sup>45</sup> This seems to indicate that some of the Cl<sup>-</sup> produced in the unimolecular dissociation is caused by excess translational energy (greater than thermal) which is relaxed by collisions with the background gas if d5 is sufficiently long and the

pressure sufficiently high. The fact that the branching ratio increases as the ion is relaxed indicates that  $\text{Br}^-$  production is favoured in a true thermal dissociation while  $\text{Cl}^-$  is preferentially formed by collisional processes as seen in previous experiments.<sup>17a),b)</sup> This is confirmed by low energy collision induced dissociation (CID) experiments performed in the FT-ICR spectrometer. The  $\text{Cl}^-(\text{CH}_3\text{Br})$  ion was isolated and then translationally excited with resonant rf excitation in a static pressure of  $1.6 \times 10^{-8}$  mbar of neon gas. The resultant spectrum is shown in Figure 59 and the  $\text{Br}^-/\text{Cl}^-$  ratio is  $\sim 0.2$  compared to  $\sim 5$  for the ZTRID experiments. The observation of increased  $\text{Cl}^-$  production from translationally excited  $\text{Cl}^-(\text{CH}_3\text{Br})$  ions is in agreement with the trajectory calculations of Hase and co-workers which showed that "intermolecular" excitation of the  $\text{Cl}^- \cdots \text{C}$  stretch or the  $\text{Cl}^- \cdots \text{CH}_3\text{Br}$  bend modes predominantly results in dissociation of the  $\text{Cl}^-(\text{CH}_3\text{Br})$  complex to form  $\text{Cl}^-$  ion.<sup>19</sup> Collisions of the complex with the surrounding neutral molecules are expected to preferentially excite these intermolecular modes rather than the "intramolecular"  $\text{CH}_3\text{Br}$  modes because the predominantly electrostatic  $\text{Cl}^- \cdots \text{C}$  bond is longer ( $\sim 60\%$  longer) and less rigid than the covalent  $\text{C}-\text{Br}$  bond. Thus, if the  $\text{Br}^-/\text{Cl}^-$  ratio from the black body experiments reported here is artificially low due to excess kinetic energy producing  $\text{Cl}^-$ , then the branching ratio for a true thermal dissociation will be larger than 5:1 and may approach Viggiano's reported yield of  $\geq 90\%$   $\text{Br}^-$ .

The assertion that  $\text{Cl}^-$  and  $\text{Br}^-$  may be preferentially produced by kinetic and internal energies, respectively, is re-enforced by a comparison of the relative linearity

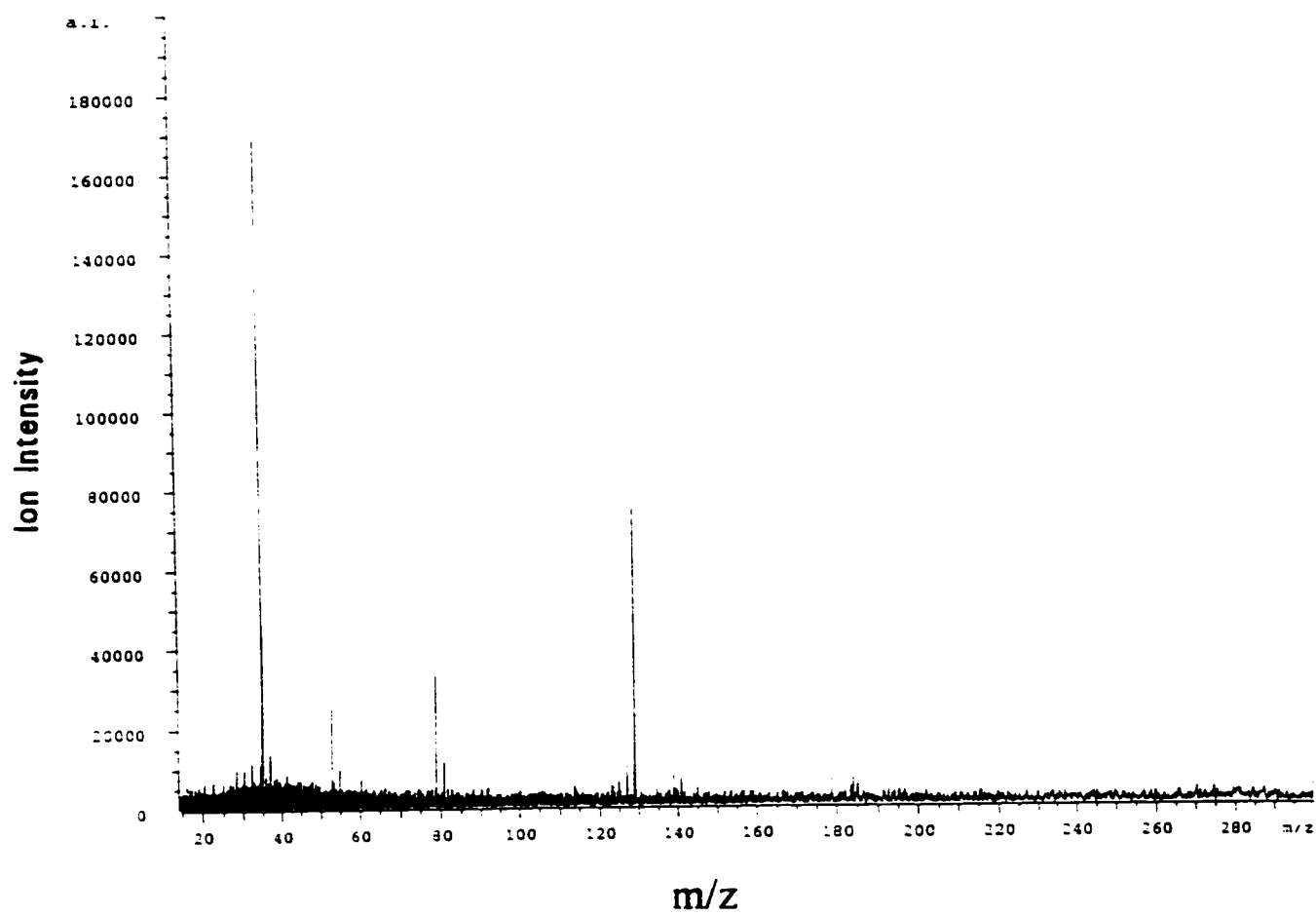


**Figure 59** Low energy CID of  $\text{Cl}^-\text{CH}_2\text{Br}$  ion in  $1.6 \times 10^{-8}$  mbar neon.

of the Arrhenius plots for  $\text{Br}^-$  and  $\text{Cl}^-$  production. For both  $\text{Cl}^-(\text{CH}_3\text{Br})$  and  $\text{Cl}^-(\text{C}_2\text{H}_5\text{Br})$  ions, the plots of  $\ln k_{\text{Br}}$  vs.  $T^{-1}$  are very linear ( $r^2=0.997$  and  $0.9998$  respectively). The plots of  $k_{\text{Cl}}$  vs.  $T^{-1}$ , however show upwards curvature ( $r^2=0.970$  and  $0.938$  respectively). It is not surprising that a true thermal dissociation, which is thought to favour the  $\text{Br}^-$  mechanism, would depend only on temperature while the collisional mechanism for  $\text{Cl}^-$  production is affected by the kinetic energy and pressure which, due to experimental limitations cannot be held constant when changing the temperature. Consideration of the reduced d5 times (see Table 5.1) used at higher temperatures (necessary to maintain some parent ion intensity at the end of the relaxation delay) suggests that an increase in the  $\text{Br}^-/\text{Cl}^-$  branching ratio with temperature may be occurring. A detailed study of the temperature dependence of the  $\text{Cl}^-(\text{CH}_3\text{Br})$  dissociation at *thermal* translational energy would be very useful for resolving the issue of mode specificity, however, this was not possible with the current limitations on  $\text{Cl}^-(\text{CH}_3\text{Br})$  ion signal. A  $10^{-6}$  torr pulse of methane has been used previously in this laboratory to thermalize cluster ions prior to black body dissociation. This technique could be applied to the study of the  $\text{Br}^-/\text{Cl}^-$  branching ratio if the initial  $\text{Cl}^-(\text{CH}_3\text{Br})$  intensity could be increased. Cooling of the ion source or, perhaps, a better halide transfer reagent than benzene are two possible methods for improving the  $\text{Cl}^-(\text{CH}_3\text{Br})$  ion signal which would allow better separation of the temperature and translational energy effects in this reaction.

*Barrier Heights.* The results of the kinetics and laser dissociation of the ethyl

and isopropyl  $S_N2$  systems are consistent with the thermochemical data and barrier heights reported by McMahon and co-workers.<sup>22</sup> The fact that the central barrier is  $\Delta H^\ddagger = +2.9$  kcal mole<sup>-1</sup> above the reactant energy prevents  $Cl^-(i-C_3H_7Br)$  from forming any  $Br^-$  and the  $\Delta H^\ddagger = -0.7$  kcal mole<sup>-1</sup> barrier proposed for the  $Cl^- + C_2H_5Br$  reaction yields the correct branching ratio of  $Br^-/Cl^-$  from  $Cl^-(C_2H_5Br)$ . These results are not surprising since the larger systems are expected to be better described by the statistical reaction theory used by McMahon and co-workers<sup>22</sup>. The height of the reaction barrier for the  $Cl^- + CH_3Br$  reaction, however, has been the source of much debate recently. Previous experiments determined the barrier from the temperature dependence of the bimolecular reaction<sup>15c)-f)</sup> and these results were consistent with calculated values of the barrier height<sup>16</sup> and the phase space calculations put forth by Bowers and co-workers to explain their kinetic energy release measurements.<sup>17a)</sup> Viggiano *et al.*,<sup>46</sup> however, recently reported that thermal decomposition reactions of  $Cl^-(CH_3Br)$  produced >90%  $Br^-$  which could be accounted for by RRKM theory only if the central barrier height is reduced to 5.4 kcal mole<sup>-1</sup> compared with the previously accepted barrier height of approximately 10.7 kcal mole<sup>-1</sup> as shown in Figure 39. The previous barrier height, obtained from bimolecular experiments, was calculated using transition state theory (TST) and, therefore, may be in considerable error if the reaction is indeed non-statistical. As discussed in the previous section, the  $E_a^{Br^-}$  values for complex I are not representative of the true activation energy but could, perhaps, be converted with master equation modelling. The relative rates of bromide ion production, however,

from the black body induced dissociation of the  $\text{Cl}^-(\text{CH}_3\text{Br})$  and  $\text{Br}^-(\text{CH}_3\text{Cl})$  complexes may help to elucidate the true central barrier height. No comparison of the IRMPD rates between the two complexes will be attempted because of the likelihood that the IR absorption intensities for monochromatic laser light at  $10.6\ \mu\text{m}$  will differ substantially between complexes I and II. The calculated vibrational frequencies of the two complexes are quite similar,<sup>19</sup> however, and therefore, the overall energy absorption from a broad band infrared excitation source should not be significantly different for complexes I and II. The infrared absorption *intensities* of each of the vibrational modes in complexes I and II have not been reported and could cause a difference in the observed black body dissociation rates if found to be substantially different. If, however, the infrared absorption intensities are assumed to be relatively similar, the differences in  $k_{\text{Br}^-}$  from complexes I and II will be an indication of the relative activation energies for each reaction. The rate constants for formation of bromide ion,  $k_{\text{Br}^-}$ , from complexes I and II are  $0.036\ \text{s}^{-1}$  and  $0.011\ \text{s}^{-1}$ , respectively. Thus, the black body rate of  $\text{Br}^-$  production at  $21\ ^\circ\text{C}$  from complex I is approximately 3 times faster than the rate of  $\text{Br}^-$  production from complex II at the same temperature, despite the fact that the barrier to reaction is almost identical in both cases (see the PES in Figure 39). This observation would seem to support Viggiano's assertion that the barrier in the  $\text{Cl}^- + \text{CH}_3\text{Br}$  reaction should be lowered from  $10.7\ \text{kcal mole}^{-1}$ . This evidence is even more convincing since the reaction of  $\text{Cl}^-(\text{CH}_3\text{Br})$  to produce  $\text{Br}^-$  must proceed through an entropically unfavourable "tight" transition state compared with the

direct cleavage of the  $\text{Br}^-$ -C bond for the dissociation of  $\text{Br}^-(\text{CH}_3\text{Cl})$ . Absolute comparisons between the individual black body dissociation rates of complexes I and II in the  $\text{Cl}^- + \text{CH}_3\text{Br}$  reaction should be made cautiously because the control of translational energy is limited in these experiments and kinetic energy may have a significant effect on the reaction rates. Thus, there is expected to be some error associated with each rate constant but not enough to account for the factor of three difference in the observed dissociation rates of the  $\text{Br}^-(\text{CH}_3\text{Cl})$  and  $\text{Cl}^-(\text{CH}_3\text{Br})$  complexes.

*Bimolecular Reaction.* Viggiano and co-workers have previously shown that the bimolecular reaction rate is insensitive to changes in temperature if  $E_{\text{com}}$  was held constant. Therefore, thermal internal energy does not promote the bimolecular reaction.<sup>23</sup> In the current study, irradiation of the bimolecular  $\text{Cl}^- + \text{CH}_3\text{Br}$  reaction produced no change in observed reaction rate. These results, however, are not absolute proof that internal energy has no effect on the bimolecular reaction rate since the  $\text{CH}_3\text{Br}$  molecule may not absorb IR radiation at  $10.6\ \mu\text{m}$ , as mentioned in section 5.3.1.



## 5.5 Conclusions

In conclusion, the Waterloo FT-ICR spectrometer and high pressure ion source have proven to be a powerful tool for the study of chloride alkyl bromide  $S_N2$  reactions dynamics. IRMPD of the bound ion-molecule complex,  $\text{Cl}^-(\text{CH}_3\text{Br})$  has produced the first experimental indication of the theoretically predicted mode specific behaviour for the  $\text{Cl}^- + \text{CH}_3\text{Br}$  reaction.  $\text{CO}_2$  laser excitation of the methyl rock vibrational mode of  $\text{Cl}^-(\text{CH}_3\text{Br})$ , at  $943\text{ cm}^{-1}$ , has produced exclusively the  $\text{Br}^-$  product. This result agrees with the theoretical prediction that vibrational excitation of the intramolecular  $\text{CH}_3\text{Br}$  modes in the  $\text{Cl}^-(\text{CH}_3\text{Br})$  complex would cause enhancement of the  $\text{Br}^-$  product. The prediction of  $\text{Cl}^-$  product enhancement by excitation of the intermolecular vibrational modes ( $\text{Cl}\cdots\text{C}$  stretch and  $\text{Cl}\cdots\text{CH}_3\text{Br}$  bend) was also supported by the observation of preferential  $\text{Cl}^-$  formation from collisional processes in these experiments. These results provide the most convincing experimental evidence to date for the existence of non-statistical reaction dynamics in the  $\text{Cl}^- + \text{CH}_3\text{Br}$  reaction because the low frequency vibrations ( $\text{Cl}\cdots\text{C}$  stretch and  $\text{Cl}\cdots\text{CH}_3\text{Br}$  bend) are clearly de-coupled from the higher frequency intramolecular  $\text{CH}_3\text{Br}$  modes. Whether the  $\text{Cl}^- + \text{CH}_3\text{Br}$  reaction dynamics are mono-mode specific could not be determined from the current experiment. The slow reaction rate suggests that the  $\text{Br}^-$  enhancement may be the result of overall vibrational excitation of the intramolecular  $\text{CH}_3\text{Br}$  modes rather than purely mode specific excitation of the methyl rock mode because coupling to other vibrational modes is expected during this time.

The temperature dependence of the black body dissociation rate was measured to determine the effect of thermal internal energy on the  $\text{Br}^-/\text{Cl}^-$  branching ratio, however, the effects of translational energy on the branching ratio interfered. Relaxation of this translational energy with a collision gas could not be accomplished with the limited  $\text{Cl}^-(\text{CH}_3\text{Br})$  ion signal currently available. Thus, separation of the temperature effect on the true thermal branching ratio from the kinetics energy effects could not be accomplished with the current experiment. A qualitative interpretation of the black body results supports a previous study which says that the central barrier to the  $\text{Cl}^- + \text{CH}_3\text{Br}$  reaction should be lowered. The bimolecular  $\text{S}_{\text{N}}2$  reaction,  $\text{Cl}^- + \text{CH}_3\text{Br}$ , was also studied by allowing bare  $\text{Cl}^-$  ions to react with a static pressure of methyl bromide gas in the FT-ICR cell. This reaction did not show an enhancement in the reaction rate upon laser irradiation. Due to the possibility that the  $\text{CH}_3\text{Br}$  does not absorb at  $943\text{ cm}^{-1}$ , this observation may or may not confirm a previous determination that the bimolecular reaction is temperature insensitive. In contrast to the methyl system, the  $\text{Cl}^- + \text{C}_2\text{H}_5\text{Br}$  reaction was found to be completely statistical, in agreement with a recent study on the  $\text{Cl}^- + \text{ClCH}_2\text{CN}$  reaction which was also found to be statistical.

## 5.6 References

1. Papanikolas, J. M.; Gord, J. R.; Levinger, N. E.; Ray, D.; Vorsa, V.; Lineberger, W. C. *J. Phys. Chem.* **1991**, 95, 8028-8040.
2. Vorsa, V.; Nandi, S.; Campagnola, P. J.; Larsson, M.; Lineberger, W. C. *J. Chem. Phys.* **1997**, 106, 1402-1410.
3. a) Baer, T.; Booze, J. A.; Weitzel, K. M. in *Vacuum Ultraviolet Photoionization and Photodissociation of Molecules and Clusters*, Ng, C. Y., Ed. World Scientific; Singapore: **1991**, 259. b) Baer, T. *Adv. Chem. Phys.* **1986**, 64, 111. c) Durant, J. L.; Rider, D. M.; Anderson, S. L.; Prochm F. D.; Zare, R. N. *J. Chem. Phys.* **1984**, 80, 1817.
4. de Gouw, J. A.; Ding, L. N.; Frost, M. J.; Kato, S.; Bierbaum, V. M.; Leone, S. R. *Chem. Phys. Lett.* **1995**, 240, 362.
5. Martin, J. D. D.; Hepburn, J. W. *Phys. Rev. Lett.* **1997**, 79, 3154.
6. a) Baer, T.; Hase, W. L. *Unimolecular Reaction Dynamics; Theory and Experiments*; Oxford University Press: New York, **1996**, p. 189. b) *ibid* p. 194.
7. Marcus, R. A.; Rice, O. K. *J. Phys. Colloid Chem.* **1951**, 55, 894.
8. a) Rynbrandt, J. D.; Rabinovitch, B. S. *J. Chem. Phys.* **1970**, 74, 4175. b) *ibid* **1971**, 75, 2164.
9. Huang, Z. S.; Jucks, K. W.; Miller, R. E. *J. Chem. Phys.* **1986**, 85, 3338.
10. Cho, Y. J.; Vande Linde, S. R.; Zhu, L.; Hase, W. L. *J. Chem. Phys.* **1992**, 96, 8275.
11. Flam, F. *Science*, **1994**, 266, 215.
12. a) Crim, F. F. *Science* **1990**, 249, 1387. b) Crim, F. F. *Ann. Rev. Pys. Chem.* **1993**, 44, 397.
13. a) Chiu, Y.; Fu, H.; Huang, J.; Anderson, S. L. *J. Chem. Phys.* **1994**, 101, 5410. b) Chiu, Y.; Yang, B.; Anderson, S. L. *ibid.* **1995**, 102, 1188. c) Chiu, Y.; Fu, H.; Anderson, S. L. *ibid.* **1995**, 102, 1199.
14. Guettler, R. D.; Jones, G. C.; Zare, R. N.; *Science*, **1994**, 266, 259.
15. (a) G. Caldwell, T.F. Magnera and P.J. Kebarle *J. Am. Chem. Soc.* **106** (1984) 959. (b) J.M. Riveros, S.M. Jose and K. Takashima *Adv. Phys. Org. Chem.* **21** (1985) 197. (c) S. Gronert, C.H. DePuy and V.M. Bierbaum *J. Am. Chem. Soc.* **113** (1991) 4010. (d) C.H. DePuy, S. Gronert, A. Mullin and V.M. Bierbaum *J. Am. Chem. Soc.* **112** (1990) 8650. (e) V.M. Bierbaum, J.J. Grabowski and C.H. DePuy *J. Phys. Chem.* **88** (1984) 1389. (f)

- D.K. Bohme, A.B. Raksit *Can. J. Chem.* **63** (1985) 3007. (g) D.K. Bohme, A.B. Raksit *J. Am. Chem. Soc.* **106** (1984) 3447. (h) D.K. Bohme, G.I. Mackay and J.D. Payzant *J. Am. Chem. Soc.* **96** (1974) 4027.
16. (a) S.C. Tucker, D.G. Truhlar, *J. Am. Chem. Soc.* **112** (1990) 3338. (b) J.D. Evanseck, J.F. Blake and W.L. Jorgenson, *J. Am. Chem. Soc.* **109** (1987) 2349. (c) K. Ohta and K. Morokuma, *J. Am. Chem. Soc.* **89** (1985) 5845.
  17. (a) S.T. Graul and M.T. Bowers *J. Am. Chem. Soc.* **113** (1991) 9696. (b) D.M. Cyr, L.A. Posey, F.A. Bishea, C.C. Han and M.A. Johnson *J. Am. Chem. Soc.* **113** (1991) 9697. (c) J.L. Wilbur and J.I. Brauman *J. Am. Chem. Soc.* **113** (1991) 9699.
  18. (a) S.R. Vande Linde and W.L. Hase, *J. Phys. Chem.* **94** (1990) 6148. (b) S.R. Vande Linde and W.L. Hase, *J. Phys. Chem.* **94** (1990) 2778. (c) S.R. Vande Linde and W.L. Hase, *J. Chem. Phys.* **93** (1990) 7962. (d) S.R. Vande Linde and W.L. Hase, *J. Am. Chem. Soc.* **111** (1989) 2349.
  19. Wang, H.; Peslherbe, G. H.; Hase, W. L. *J. Am. Chem. Soc.* **1994**, 116, 9644.
  20. Streitweiser Jr., A.; Heathcock, C. H. *Introduction to Organic Chemistry* 3<sup>rd</sup> Ed., Macmillan: New York **1985**.
  21. (a) W.E. Farneth and J.I. Brauman, *J. Am. Chem. Soc.* **98** (1976) 5546. (b) W.N. Olmstead and J.I. Brauman, *J. Am. Chem. Soc.* **99** (1977) 4219.
  22. Li, C.; Ross, P.; Szulejko, J. E.; McMahon, T. B. *J. Amer. Chem. Soc.* **1996** 118, 9360.
  23. Viggiano, A. A.; Morris, R. A.; Paschkewitz, J. S.; Paulson, J. F. *J. Amer. Chem. Soc.* **1992** 114, 10477.
  24. Lias, S. G.; Bartmess, J. E.; Liebman, J. F.; Holmes, J. L.; Levin, R. D.; Mallard, W. G. "Gas Phase Ion and Neutral Thermochemistry" *J. Phys. Chem. Ref. Data*, Vol. 17, Suppl. 1, **1988**.
  25. Wang, H.; Hase, W. L. *J. Am. Chem. Soc.* **1995**, 117, 9347.
  26. Clary, D. C. *J. Phys. Chem.* **1994** 98, 10678.
  27. Clary, D. C.; Palma, J. *J. Chem. Phys.* **1997** 106, 575.
  28. Le Garrec, J-L; Rowe, B. R.; Queffelec, J. L.; Mitchell, J. B. A.; Clary, D. C. *J. Chem. Phys.* **1997** 107, 1021.
  29. Szulejko, J. E.; McMahon, T. B. *unpublished results*.

30. Weston Jr., R. E.; Schwartz, H. A. *Chemical Kinetics*, Prentice-Hall: New Jersey: **1972**, 65.
31. Szabo, Z. G.; *Kinetic Characterization of Complex Reaction Systems* Chapter 1 in *Comprehensive Chemical Kinetics* Vol. 2, C. H. Bamford and C. F. H. Tipper Eds., Amsterdam; New York: Elsevier, **1969**.
32. Laidler, K. J. *Chemical Kinetics*; 3<sup>rd</sup> Ed., Harper and Row: New York, 1987, p.39.
33. Typical first order decomposition or re-arrangement reactions have  $A_{\text{Arr}}$  on the order of  $10^{13} \text{ s}^{-1}$ . See, for instance: Atkins, P. W. *Physical Chemistry*, 4<sup>th</sup> Ed.; W. H. Freeman and Co.: New York, **1990**, p.793.
34. The rapid energy exchange or REX limit is explained in section 1.2.
35. Hoffman, T. L. *M.Sc. Thesis*, University of Waterloo, **1997**.
36. Price, W. D.; Schnier, P. D.; Jockusch, R. A.; Strittmatter, E. F.; Williams, E. R. *J. Am. Chem. Soc.* **1996**, 118, 10640.
37. Dunbar, R. C.; McMahon, T. B. *Science* **1998**, 279, 194.
38. Thorne, L. R.; Beauchamp, J. L. in *Gas Phase Ion Chemistry* Vol. 3; Bowers, M. T., Ed.; Academic: Orlando, **1984**, 82.
39. Olmstead, W. N.; Brauman, J. I. *J. Amer. Chem. Soc.* **1976** 99, 4219.
40. Magnera, T. F.; Kebarle, P. In *Ionic Processes in the Gas Phase*; Almoester Ferreira, M. A., Ed.; Reidel Publishing: Boston, 1984; pp 135-157.
41. Dunbar, R. C.; McMahon, T. B.; Thölmann, D.; Tonner, D. S.; Salahub, D. R.; Wei, D. *J. Am. Chem. Soc.* **1995**, 117, 12819-12825.
42. Hase, W. L. *Personal Communication*.
43. Peslherbe, G. H.; Wang, H.; Hase, W. L. *J. Am. Chem. Soc.* **1996**, 118, 2257.
44. Craig, S. L.; Brauman, J. I. *Science* **1997**, 276, 1536.
45. Tonner, D. S.; McMahon, T. B. *unpublished results*.
46. Seeley, J. V.; Morris, R. A.; Viggiano, A. A.; Wang, H.; Hase, W. L. *J. Amer. Chem. Soc.* **1997**, 119, 577.

## 6. SUMMARY AND FUTURE EXPERIMENTS

A detailed study of the infrared photodissociation kinetics of cluster ions in a low pressure environment has been completed. The ions were dissociated using a low intensity CW CO<sub>2</sub> laser controlled by a shutter to allow full control of one or more sequential irradiation periods. A bottleneck in the IRMPD of large ions was observed. This bottleneck caused the decay kinetics of the parent ion to deviate from first order. The relevant IRMPD bottleneck mechanisms have been discussed and compared with the effects of temperature, laser intensity, pressure, ion size and bond enthalpy. The complexity of the IRMPD process, in ions as large as those studied here, has prevented the satisfactory explanation of the results by a single bottlenecking mechanism. The results support the existence of a late bottleneck which is related to ion size and pressure because of the quenching effects of spontaneous emission and collisional quenching respectively. This study is fundamentally important because it is the first study of low intensity IRMPD of large ions trapped in the UHV pressure regime ( $\leq 10^{-9}$  mbar) where collisions do not dominate the redistribution of internal energy. The observation of increased quenching effects in larger ions suggests that spontaneous emission and increased dissociation lifetime may limit the effectiveness of low intensity IRMPD in very large (kDa) ions. This result has important implications to the growing field of biomolecule analysis *via* IRMPD of very large electrosprayed ions. The single most important addition to the following work would be the ominous task of master equation modelling the IRMPD of these large cluster ions with state-to-

state coupling terms calculated or approximated by *ab initio* methods.

The study of IRMPD and bottlenecking laid the foundation for two novel applications of the current experimental apparatus. Chapter four of this thesis describes a new technique for performing sequential IRMPD of large ions. This experiment is the IRMPD equivalent of the existing  $MS^n$  experiment in FT-ICR. IRMPD is shown to be a very soft fragmentation method (*i.e.* always yields the lowest energy product) compared to CID. The combination of soft fragmentation and the high mass resolution of the FT-ICR makes this technique uniquely suited for the structural assignment of large multiply protonated ions produced from an electrospray ion source. The reduced centre of mass energy, for collisions of heavy ions, limits the energy deposition and, hence, the effectiveness of CID. Alternately, large ions have so many vibrational modes that strong IR absorptions at 10.6  $\mu\text{m}$  are almost always observed. Therefore, the IRMPD experiment offers significant advantages over current CID techniques for  $MS^n$  studies of large ions derived from biopolymers and future work on this experiment would be most suited to the large, multiply protonated ions produced from an electrospray ion source.

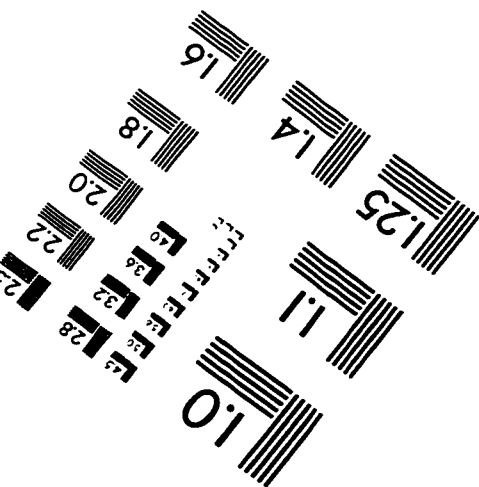
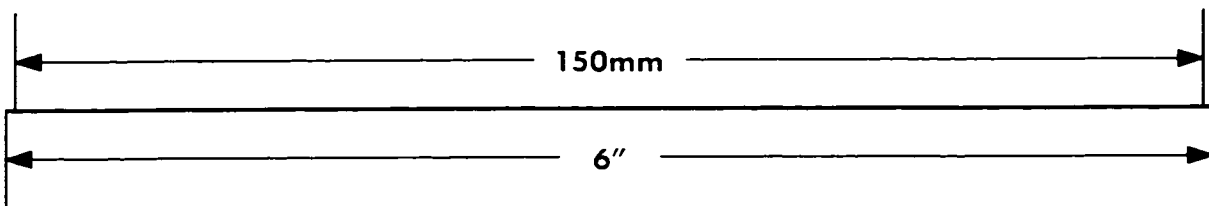
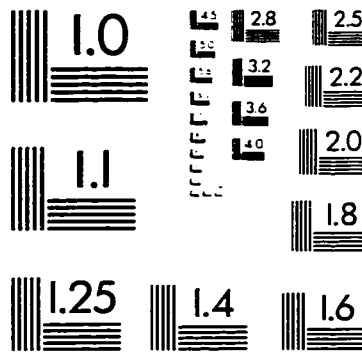
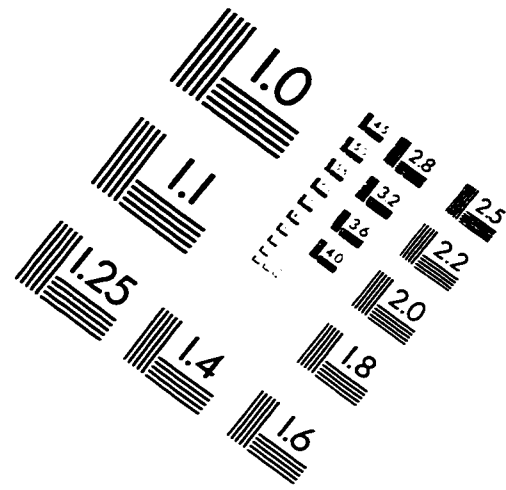
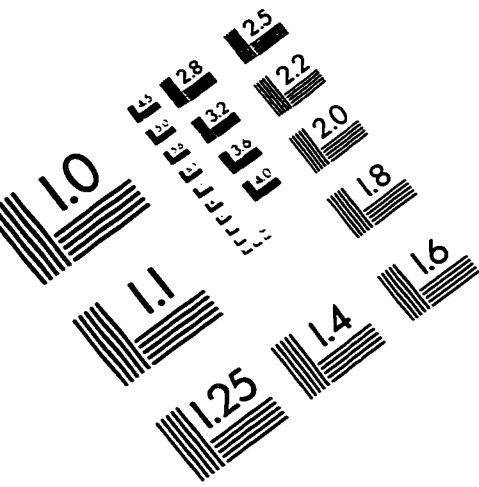
The FT-ICR/IRMPD experiment was also applied to the study of chloride alkyl bromide  $S_N2$  reactions. There has been considerable effort devoted recently to the search for experimental confirmation of the theoretically predicted mode specific behaviour of the  $\text{Cl}^- + \text{CH}_3\text{Br}$  reaction. In the work presented in this thesis, IRMPD of the  $\text{Cl}^-(\text{CH}_3\text{Br})$  complex resulted in exclusive formation of the  $\text{Br}^-$  product. These

results provide the most convincing experimental evidence to date for the existence of non-statistical reaction dynamics in the  $\text{Cl}^- + \text{CH}_3\text{Br}$  reaction. The  $\text{CO}_2$  laser radiation was used to excite the methyl rock vibrational mode ( $943\text{ cm}^{-1}$ ) of the  $\text{Cl}^-(\text{CH}_3\text{Br})$  complex which was one of the intramolecular  $\text{CH}_3\text{Br}$  modes predicted to cause enhancement of the  $\text{Br}^-$  product. Since the  $\text{Cl}^-(\text{CH}_3\text{Br})$  complex exhibited a weak IR absorption at  $943\text{ cm}^{-1}$ , the dissociation lifetime was on the order of 10 seconds and the extent of energy leakage to other vibrational modes during this time is undetermined. Thus, the exact mode specificity of the  $\text{Cl}^- + \text{CH}_3\text{Br}$  reaction dynamics could not be determined. Temperature dependent black body dissociation experiments were undertaken to attempt to resolve the effect of thermal internal energy on the  $\text{Br}^-/\text{Cl}^-$  branching ratio. However, small amounts of translational energy were observed to produce preferential  $\text{Cl}^-$  formation by collisions with background gas. Relaxation of this translational energy with a collision gas could not be accomplished with the limited  $\text{Cl}^-(\text{CH}_3\text{Br})$  ion signal currently available. Thus, separation of the temperature effect on the true thermal branching ratio from the kinetics energy effects could not be accomplished with the current experiment. A qualitative interpretation of the black body results supports a previous study which says that the central barrier to the  $\text{Cl}^- + \text{CH}_3\text{Br}$  reaction should be lowered. In contrast to the methyl system, the  $\text{Cl}^- + \text{C}_2\text{H}_5\text{Br}$  reaction was found to be completely statistical, in agreement with a recent study on the  $\text{Cl}^- + \text{ClCH}_2\text{CN}$  reaction which was also found to be statistical. An important future experiment would be the study of the  $\text{Br}^-/\text{Cl}^-$  ratio from the black body



dissociation of the  $\text{Cl}^-(\text{CH}_3\text{Br})$  complex at *thermal* translational energy. This experiment will be possible if the fraction of  $\text{Cl}^-(\text{CH}_3\text{Br})$  ions leaving the high pressure source can be increased so that translational relaxation of the ions inside the FT-ICR cell can be performed using a pulsed collision gas. The discovery of a better chloride transfer reagent than benzene may provide the necessary signal increase. Alternately, increased pumping in the source chamber would allow a bath gas pressure greater than 4 torr to be used which should increase the fraction of ions trapped in the entrance well by stabilizing collisions. Cooling of the ion source usually helps stabilize weakly bound ion-molecule complexes, however, the inverse temperature dependence of the competing bimolecular reaction, may prevent source cooling from being effective.

# IMAGE EVALUATION TEST TARGET (QA-3)



APPLIED IMAGE, Inc.  
1653 East Main Street  
Rochester, NY 14609 USA  
Phone: 716/482-0300  
Fax: 716/288-5989

© 1993, Applied Image, Inc., All Rights Reserved

